Algorithms, Models, and Methods for SDSS-V Wide-field Robotic Fiber Spectroscopy

Conor Sayres

A dissertation
submitted in partial fulfillment of the
requirements for the degree of

Doctor of Philosophy

University of Washington

2023

Reading Committee:

Sarah Tuttle, Chair

Andrew Connolly

Michael Blanton

Program Authorized to Offer Degree:
Astronomy

©Copyright 2023
Conor Sayres

University of Washington

Abstract

Algorithms, Models, and Methods for SDSS-V Wide-field Robotic Fiber Spectroscopy

Conor Sayres

Chair of the Supervisory Committee:
Professor Sarah Tuttle
Astronomy

The field of astronomy has entered an age of big data, and this being driven by dedicated telescopes and instruments built for the sole purpose of conducting broad surveys to catalog the night sky. The highly successful space-based Gaia mission has already cataloged the broadband colors, 3D locations, and trajectories for nearly 2 billion astronomical sources. The much anticipated Legacy Survey of Space and Time (LSST) is projected to catalog an order of magnitude more objects. Imaging surveys like these are providing an unprecedented number of sources available for spectroscopic followup. Spectroscopy reveals a wealth of astrophysical information that imaging alone cannot, but spectroscopy is an inherently slow process. To spectroscopically observe even a small fraction of what is currently available, observations need to be performed as quickly and efficiently as possible.

Robotic fiber positioners are a relatively new technology designed to speed up spectroscopic data collection. The fifth iteration of the Sloan Digital Sky Survey (SDSS-V) has built a pair of instruments each with 500 robots carrying optical fibers for multi-object spectroscopy. The first instrument operates from Apache Point Observatory (APO) in New Mexico and saw first light in December 2021. The second instrument operates from Las Campanas Observatory (LCO) in Chile and saw first light in August 2022. These instruments are designed to perform a spectroscopic survey of 6 million sources in a survey duration of five years. Operationally these instruments are complex, and they are required to perform at very high precision. This work describes the

mathematics, algorithms, analysis, and general calibration strategies we have developed to make these instruments operational.

A robot's fundamental task is to position a 120 μm diameter optical fiber in the focal plane of the telescope to capture light from an astronomical source. The `coordio` software package was developed to perform the calculations for determining where an astronomical source will land in the focal plane of the telescope and how a robot should be moved to collect light from that object. This package defines a series of coordinate systems and transforms and provides a computational backbone for many pieces of SDSS-V's survey operations and infrastructure codes.

SDSS-V has chosen a spatially-aggressive layout for the robotic fiber positioner array in which the physical workspace for a robot heavily overlaps with its neighbors. This layout grants more sky coverage to each robot but introduces a high risk of collision between robots during reconfiguration. The `kaiju` software package was developed to compute safe paths for every robot while moving from one spectroscopic target to the next. This path planning algorithm was an important success for the project, and it allowed the instrument to realize its full potential in using every available robot in every spectroscopic exposure.

Once instrument assembly was completed, a period of lab testing and calibration was performed. A lab test camera was used to measure positions of back-lit optical fibers as robots were moved through many reconfigurations. From this process we derived a kinematic model unique to each robot for use in `coordio` routines to accurately predict fiber locations. This period also served to test and tune `kaiju` path planning parameters while operating the robot array at full scale, ensuring proper operation prior to shipping the instrument to the telescope.

After lab calibration, each instrument was installed at the telescope where a Fiber View Camera (FVC) is used to measure and adjust fiber positions during array reconfiguration. A series of camera distortion models were derived to reach sufficient FVC measurement accuracy. On-sky instrument commissioning consisted of spectroscopic observations of Gaia sources using a telescope dither technique, which allowed us to estimate on-sky fiber position errors. Analysis of these

data informed additional layers of instrument calibration which improved overall fiber positioning accuracy.

The instrument at APO was commissioned first, and is currently placing robotic fibers with an RMS error of 21 μm relative to astrophysical sources in the focal plane. Spectroscopic targets are generally well centered within the 120 μm fiber aperture, and normal survey operations are proceeding. We expect that ongoing efforts will further improve survey efficiencies and fiber positioning performance with an end goal of limiting fiber placement error to $\sim$17 μm. The instrument at LCO is currently in the commissioning and science verification phase, but initial indications suggest that fiber throughput will be sufficient for achieving SDSS-V science goals.

SDSS-V is the third project worldwide to successfully deploy a robotic fiber positioner instrument to conduct a multi-year spectroscopic survey, and several other projects of comparable scale are nearing deployment. Throughout the process of designing, building, and using these instruments, we have developed a number of strategies and techniques that are directly applicable to contemporary instruments today. Robotic fiber positioner arrays will likely continue to grow in importance, and proposals for building instruments with tens of thousands of robots on large aperture telescopes are already in place. The solutions derived from today's robotic multi-object spectrosopic surveys will directly influence the feasibility and design of future projects.

TABLE OF CONTENTS

LIST OF FIGURES

LIST OF TABLES

GLOSSARY

APO: Apache Point Observatory.

APOGEE: SDSS near-infrared spectrograph.

BHM: Black Hole Mapper.

BOSS: SDSS optical spectrograph.

CCD: charge-coupled device.

CDF: cumulative distribution function.

CMM: coordinate-measuring machine.

CNC: computer numerical control.

COORDIO: SDSS-V software package for coordinate system transformations.

DEC: declination.

DESI: Dark Energy Spectroscopic Instrument.

FOV: field of view.

FPS: Focal Plane System, the SDSS-V robotic fiber positioning instrument.

FVC: Fiber View Camera.

FWHM: full width at half maximum, a measure of PSF spread.

GC: Greedy choice, a flavor of the kaiju algorithm

GFA: Guide Focus Acquisition camera.

KAIJU: SDSS-V software/algorithm for robotic path planning.

LCO: Las Campanas Observatory.

LOOCV: leave-one-out cross-validation.

LSST: Legacy Survey of Space and Time.

LTC: Lab Test Camera.

MC: Markov chain, a flavor of the kaiju algorithm.

MOS: multi-object spectroscopy.

MWM: Milky Way Mapper.

PID: proportional-integral-derivative, a feedback-driven control loop.

PSF: point spread function.

RA: right ascension.

RFP: robotic fiber positioner.

RM: reverberation mapping.

RMS: root mean square, an error metric.

SDSS: Sloan Digital Sky Survey.

SDSS-V: fifth iteration of SDSS.

SOFA: Standards of Fundamental Astronomy.

ZB: Zhao-Burge, a set of 2D vector polynomials.

ACKNOWLEDGMENTS

The work presented here was done in close collaboration with many other individuals, and I will use the word "we" throughout this dissertation to reinforce that this project has been (and continues to be) a collaborative effort.

First and foremost I would like to thank my graduate advisor Sarah Tuttle and my dissertation committee members Andrew Connolly and Michael Blanton. Their advice, direction, and encouragement extends far beyond the boundaries of this project. I would also like to thank Russell Owen, who has provided many years of mentorship and set me on my current trajectory in this field.

José Sánchez-Gallego, Jon Holtzman, Michael Blanton, David Hogg, Douglas Finkbeiner, Andrew Saydjari, and Dustin Lang all contributed to software, mathematical modeling, and the extensive troubleshooting associated with this project.

The optical/electrical/mechanical design and assembly for SDSS-V's robotic fiber positioner instrument was a joint effort between teams from the Ohio State University, École Polytechniqe Fédérale de Lausanne (EPFL), and the Univeristy of Washington made up of individuals: Richard Pogge, Mark Derwent, Tom O'Brien, Colby Jurgenson, Dan Pappalardo, Michael Engleman, Christopher Brandon, Julia Brady, Jean-Paul Kneib, Mohamed Bouri, Ricardo Araujo, Luzius Kronig, Loic Grossen, Sarah Tuttle, Emily Farr, Travis Mandeville, Rishi Pahuja, and Kal Kadlec.

On-sky data collection was largely performed by the excellent team of observing specialists at both Apache Point Observatory and Las Campanas Observatory, and observatory staff were (and continue to be) critical for the successful deployment of this instrument and survey.

David Schlegel, Eddie Schlafly and the DESI collaboration provided aid in the form of technical advice and code. SDSS-V has directly benefitted from the lessons learned from the DESI team's

experience deploying and calibrating their robotic spectroscopy instrument.

A final thank you to SDSS-V Director Juna Kollmeier who has supported myself and the whole team in this effort. Funding for the Sloan Digital Sky Survey V has been provided by the Alfred P. Sloan Foundation, the Heising-Simons Foundation, the National Science Foundation, and the Participating Institutions. SDSS acknowledges support and resources from the Center for High-Performance Computing at the University of Utah. The SDSS web site is www.sdss.org.

SDSS is managed by the Astrophysical Research Consortium for the Participating Institutions of the SDSS Collaboration, including the Carnegie Institution for Science, Chilean National Time Allocation Committee (CNTAC) ratified researchers, the Gotham Participation Group, Harvard University, Heidelberg University, The Johns Hopkins University, L'Ecole polytechnique fédérale de Lausanne (EPFL), Leibniz-Institut für Astrophysik Potsdam (AIP), Max-Planck-Institut für Astronomie (MPIA Heidelberg), Max-Planck-Institut für Extraterrestrische Physik (MPE), Nanjing University, National Astronomical Observatories of China (NAOC), New Mexico State University, The Ohio State University, Pennsylvania State University, Smithsonian Astrophysical Observatory, Space Telescope Science Institute (STScI), the Stellar Astrophysics Participation Group, Universidad Nacional Autónoma de México, University of Arizona, University of Colorado Boulder, University of Illinois at Urbana-Champaign, University of Toronto, University of Utah, University of Virginia, Yale University, and Yunnan University.

Chapter 1

INTRODUCTION

1.1 The Demand for Massively-Multiplexed Spectroscopy

The landscape of observational astronomy has rapidly evolved over the past 20 years. The field is shifting focus from PI-based proposal-driven observations to dedicated observatories performing astronomical surveys. Recent large-footprint and time-domain photometric surveys (e.g, Gaia Gaia Collaboration et al. 2016, TESS Ricker et al. 2014, DES The Dark Energy Survey Collaboration 2005, ZTF Bellm et al. 2019, and soon Rubin/LSST Ivezić et al. 2019) are providing a wealth of targets for spectroscopic follow up. The combination of massive increases in target volumes and real-time alerts now streaming from survey-based telescopes have driven the need for new technologies in multi-object spectroscopic (MOS) surveys (National Research Council, 2015), specifically fast-moving and highly-multiplexed spectroscopic instruments with low operational overheads. To achieve this, virtually all MOS surveys and instruments (now and future) are adopting robotic fiber positioners.

Robotic fiber positioner arrays remain a relatively risky technology. LAMOST (Cui et al., 2012) was the first highly-multiplexed robotically-positioned spectroscopic instrument on sky. In 2011 LAMOST launched a 9 month pilot survey in which half of their spectra were unusable (Luo et al., 2012). LAMOST challenges were related to accuracy issues in fiber positioning and metrology. The LAMOST survey was ultimately forced to re-scope to match the capabilities of the instrument (Luo et al., 2015). This early LAMOST experience emphasizes the operational challenges inherent in deploying a robotic fiber positioning system. Despite these initial challenges, LAMOST's observational efficiencies have continued to improve over the last decade, and their eighth data release contains over 10 million spectra (Yan et al., 2022).

A new generation of robotic MOS systems has arrived for the 2020s. DESI (DESI Collaboration et al., 2016) and SDSS-V (Kollmeier et al., 2017) are currently in survey operations. WEAVE (Dalton et al., 2012) has just begun instrument commissioning, and a slew of other contemporary instruments should all see first light in 2023 (4MOST de Jong et al. 2019, MOONS Cirasuolo et al. 2011, PFS Sugai et al. 2015). These projects sample a distribution of science goals, robot design, robot arrangement, metrology systems, survey implementation, and telescope apertures. Although

variations are present, these MOS projects all are functionally similar, and will inevitably face similar challenges throughout their operational lifetimes. Solutions found by any project will be of interest to other projects. Common solutions to broad problems in this domain are already emerging.

Looking ahead, MOS instruments will continue to grow in importance, and the 2030s will see MOS instruments on larger aperture telescopes with even larger numbers of fibers. New MOS projects are being developed in anticipation of LSST imaging, which will require massively multiplexed MOS systems on large aperture telescopes to specroscopically survey even a small percentage of the available photometric sample. Most MOS facilities today exist on 2-4m class telescopes in the Northern Hemisphere, and may not be for suited LSST follow up. Notable next generation MOS projects include: MSE (Hall et al., 2019), MegaMapper (Schlegel et al., 2019), FOBOS (Bundy et al., 2019), and pre-concepts such as SpecTel (Ellis and Dawson, 2019). The Rubin Observatory may even see a MOS retrofit in the future (Jha et al., 2019).

As astronomical observation moves into highly multiplexed and automated modes, spectra for millions of sources will be collected on incredibly short timescales. SDSS-V will target over 6 million objects and DESI will target over 40 million objects in the span of 5 years. MOS spectroscopy may be on a Moore's law trajectory (Schlegel et al., 2019). This new domain of robotic MOS spectroscopy is ripe for innovation. The problems solved and the lessons learned in the current era of MOS development will directly inform and influence the feasibility, design, and execution of next-generation of MOS surveys.

1.2 SDSS-V Survey and Instrumentation

The Sloan Digital Sky Survey (SDSS I/II; York et al. 2000) has recently started its fifth phase of operations. For nearly two decades, SDSS has continuously served high quality, well documented, and accessible data. The project has evolved over the years, beginning with SDSS I/II, which provided multiband photometry from a large camera that now resides at the Smithsonian (Gunn et al., 1998) and multi-object optical spectroscopy (Smee et al., 2013) using plug plates at Apache Point Observatory (APO). SDSS-III (Eisenstein et al., 2011) included new instrumentation at APO for

conducting a near-infrared multi-object spectroscopic survey APOGEE (Majewski et al., 2017), a radial velocity planet finding survey MARVELS (Ge et al., 2009), and increased total fiber capacity of the optical spectographs. SDSS-IV (Blanton et al., 2017) saw the inclusion of the MaNGA integral field unit (IFU) survey of nearby galaxies (Bundy et al., 2015), and built out infrastructure and instrumentation to extend the APOGEE survey to the southern hemisphere at Las Campanas Observatory (LCO).

SDSS-V (Kollmeier et al., 2017) is an all-sky, multi-epoch spectroscopic mapping survey, operating for five years from both hemispheres. Two of SDSS-V's main science programs use a use a robotic fiber positioning array: the Black Hole Mapper (BHM) and the Milky Way Mapper (MWM). The BHM and MWM surveys operate in tandem, sharing a common robotic focal plane system (FPS, Pogge et al. 2020). One FPS is installed on the 2.5 meter $f/5$ Sloan Foundation Telescope at APO (Gunn et al., 2006). The second FPS is installed on the 2.5 meter $f/7.5$ du Pont Telescope at LCO (Bowen and Vaughan, 1973).

The BHM is a very-wide area dual hemisphere survey to obtain multi-epoch optical spectroscopy of accreting black holes. It will provide comprehensive follow-up of X-ray sources from the recently launched eROSITA space telescope (Predehl et al., 2010). With its multi-epoch capability, BHM will provide black hole masses for supermassive black holes using the reverberation mapping technique (Shen et al., 2015) and will probe the dynamics of black hole environments by obtaining multi-epoch spectroscopy for quasars and AGN with sensitivity to variability on timescales ranging from decades to months when combined with legacy SDSS datasets.

The MWM science program is an all-sky survey targeting over 6 million stars in the Milky Way for multi-epoch optical and near-infrared spectroscopy. The survey will measure fundamental stellar characteristics (e.g. age, chemistry, kinematics), yielding a dataset well-suited for investigating the history and evolution of the Galaxy's structure. The MWM aims to double the number of spectroscopically observed objects from all previous SDSS cycles in a span of five years. This target volume increase would be impossible to accomodate using the original SDSS plug plate system, which required approximately 20 minutes of operational overhead to move between fields. The combined MWM and BHM target volume drove the need for a nimble robotic fiber positioning

system in SDSS-V.

To carry out the BHM and MWM surveys, a pair of SDSS-V robotic fiber positioning systems were constructed. At APO the robotic fibers cover a $\sim$5 deg^2 field of view. At LCO the robotic fibers cover a $\sim$2 deg^2 field of view. At both telescopes FPS units are mounted to an instrument rotator at Cassegrain focus. Each FPS consists of 500 robotic fiber positioners, 6 guide-focus-acquisition (GFA) cameras, and 60 fixed fiducials mounted upon a dished surface termed the "wok". The wok's top surface has been machined to match the telescope's very slight focal plane curvature such that GFAs and science fibers remain in focus across the telescope's field of view.

Within the wok, robots are installed into a hexagonally-packed grid pattern with fiducials and environmental sensors interspersed among them. Each robot carries a 120 μm diameter APOGEE, BOSS and metrology fiber in a common ferrule. All 500 positioners feed the BOSS optical spectrograph (Smee et al., 2013), while a subset of 298 robots additionally feed the APOGEE near-infrared spectrograph (Wilson et al., 2019). The BOSS and APOGEE spectrographs have a capacity of 500 and 300 fibers respectively, so not every robot will be available for near-infrared targeting. Two fibers on the APOGEE spectrograph are reserved for a new Fabry-Perot interferometer which will increase the precision of APOGEE radial velocity measurements (Wilson et al., 2022).

A new three element wide-field corrector was designed and commissioned for SDSS-V operations at the APO Sloan Foundation Telescope (Barkhouser et al. 2022, Gray et al. 2022). The new corrector makes the infrared and optical focal planes parfocal and telecentric, a necessity for optimally feeding the robotically positioned fibers of the FPS. Additionally the new corrector has optimized coatings for near-infrared transmission which has improved APOGEE throughput by $>$30% at APO.

Each telescope is equipped with a Fiber View Camera (FVC, Jurgenson et al. 2020). This camera measures the centroids of back-lit fiducial and metrology fibers in the positioner field to measure and correct the placement of fibers in the focal plane when reconfiguring robots for science fields. The FVC accomplishes this in an unusual fashion by using the telescope in reverse. The camera images a small section of the primary mirror to capture rays originating from the telescope's focal plane via their reflection off the secondary mirror.

The changes brought on by new instrumentation and survey modes in SDSS-V have required a near total reconfiguration of operations at APO and LCO (Sánchez-Gallego et al., 2020), affecting all levels of survey implementation from target selection to data release. The content presented here describes strategies and solutions to several fundamental challenges SDSS-V has faced when taking our new hardware and making it work. We also emphasize the challenges that still remain.

1.3 Overview of Content

In Chapter 2 we derive and describe the exact models and mathematics used in SDSS-V to calculate how to position a robot to receive photons from astrophysical targets with coordinates provided from an astronomical catalog. The main product of this work (besides documenting its underlying methods) is a software package `coordio`, which provides fundamental utilities necessary for organizing, optimizing, and deploying many pieces of the SDSS-V codebase and survey. In Chapter 3 we describe a novel algorithm that allows us to freely move robots between science configurations without colliding with one another. Our methods are implemented in a software package `kaiju`, which frees our robots to actually do their job despite their crowded environment. Chapters 4 and 5 describe the calibration strategy for the FPS and FVC instruments in the lab and later on sky. These chapters also serve to test and verify the (until recently) theoretical methods discussed in Chapters 2 and 3.

Chapter 2

COORDIO: COORDINATE SYSTEMS AND TRANSFORMATIONS

Portions of this chapter were originally published in the Society of Photo-Optical Instrumentation Engineers (SPIE) for 2022 Astronomical Telescopes and Instrumentation (Sayres et al., 2022, SPIE, Vol. 12184, 121847K; 2022 © SPIE, DOI: 10.1117/12.2630507), and are reproduced below with the permission of the SPIE.

2.1 Introduction

Here we describe the mathematical framework behind the SDSS-V robotic Focal Plane System operations. This is organized into a set of coordinate systems and transforms used to propagate locations of targets from astronomical catalogs to coordinates on a robotically positioned fiber or guide camera. Specifically the tasks of this chapter are to (1) calculate where a spectroscopic target lands in "wok" coordinates, and (2) determine the robot's $(\theta_\alpha, \theta_\beta)$ positioner coordinates that will align a science fiber with that source. The calculation for determining a guide star's location on a guide chip proceeds along analogous lines. Figure 2.1 shows the complete stack of coordinate systems and conversions we have defined for this task, and the mathematics for the traversal of this stack are detailed in Sections 2.2 - 2.8.

Accurate metrology is a prerequisite for accurate coordinate transforms. We require precise knowledge of the location and orientation of a robot or GFA on the wok, and we need precise knowledge of where a fiber is on a robot. A key component of the FPS metrology system is the Fiber View Camera (FVC). The FVC coordinate system and transform (dashed box in Figure 2.1) is built using distortion modeling techniqes detailed in Sections 5.3.3, 5.3.4, and 5.4.7. We omit FVC details from this chapter and return to it in Chapter 5. Fiber positioning has continued to improve at APO and LCO largely due to continuing improvements in our ability to measure where a fiber is, and these general topics of FPS metrology and calibration are derived in Chapters 4 and 5.

The complete suite of FPS transforms (in both forward and reverse directions) have been implemented in SDSS-V's `coordio`[1] software package. `coordio` is written in Python and Python-

[1] https://github.com/sdss/coordio

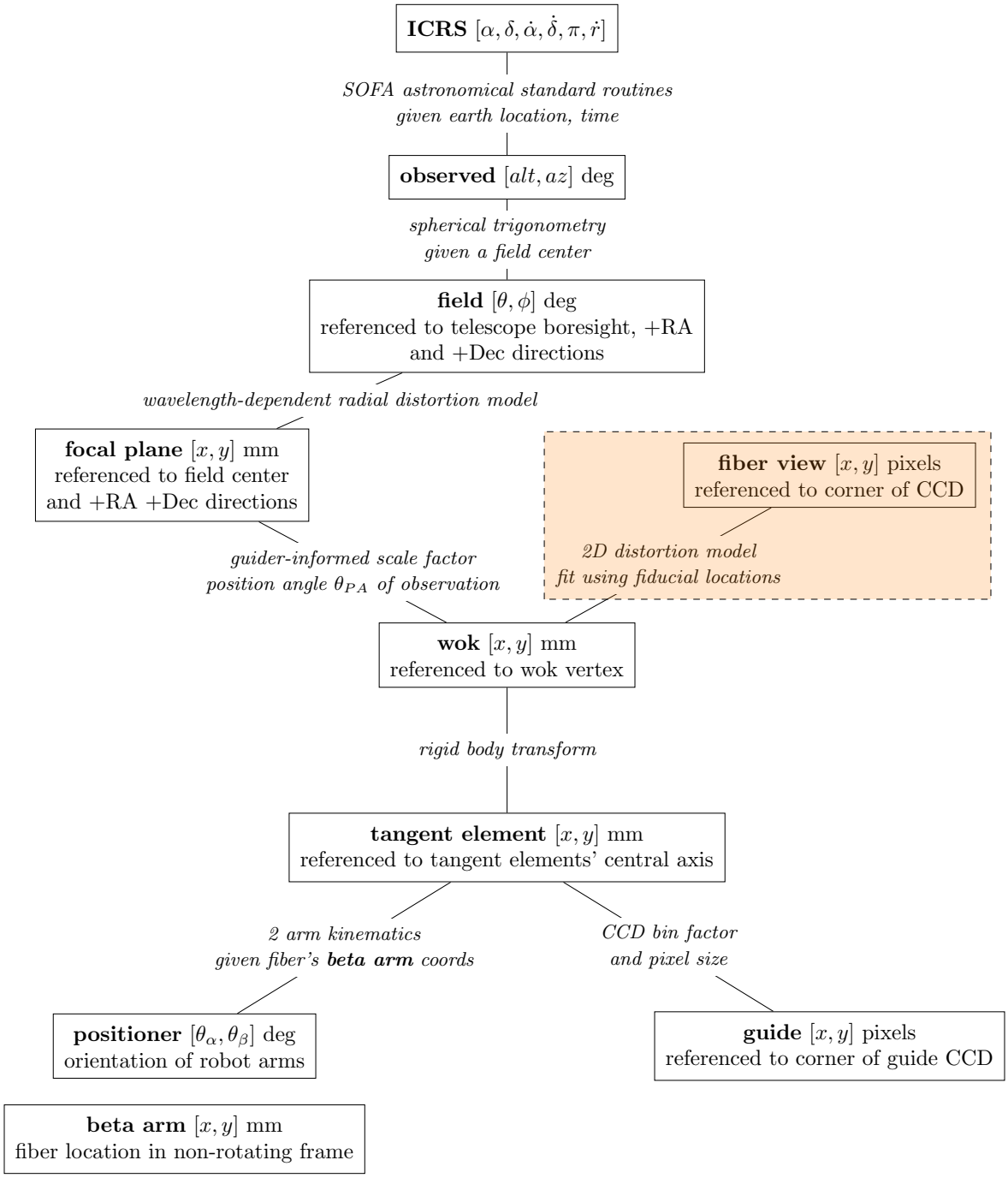

Figure 2.1 – The coordinate transformation stack for the SDSS-V FPS. Coordinate systems are boxed nodes, and edges represent a transform between coordinate systems. The transform between fiber view and wok coordinates (dashed and highlighted) is detailed in Chapter 5.

wrapped C/C++. It provides a common backbone for many other SDSS-V software products including those concerned with survey design and target assignment[2], robot path planning (Chapter 3; Sayres et al. 2021), and nightly operations[3]. `coordio` makes use of SOFA[4] routines for certain astronomical calculations.

2.2 Catalog (ICRS) to observed (Alt, Az) coordinates

SDSS-V targets are selected from published astronomical catalogs. Prior to observation each target must be associated with (1) a site (APO or LCO), (2) a field center (telescope pointing, or boresight), (3) a position angle on sky, and (4) a specific fiber on a robot. Both target and boresight ICRS coordinates are converted to observed (Alt, Az) coordinates using SOFA's `iauAtco13` routine which handles refraction, proper motion, parallax, stellar aberration, Earth orientation, and nutation. The relevant inputs and outputs of this routine are shown in Table 2.1. Figure 2.2 shows an example of target and boresight coordinates in the observed coordinate system.

2.3 Observed (Alt, Az) to field (ϕ_{FC}, θ_{FC}) coordinates

Field coordinates are a spherical coordinate system that specify the location of a target with respect to the telescope boresight. ϕ_{FC} is the angular on-sky separation between the boresight and the target. θ_{FC} is the on-sky direction from the boresight to the target, measured from +RA through +Dec. The conversion from observed to field coordinates involves constructing a 3D rotation matrix M_B derived from the boresight's observed coordinates:

---

[2] https://github.com/sdss/robostrategy

[3] https://github.com/sdss/jaeger

[4] https://www.iausofa.org/

Table 2.1 – . iauAtco13 inputs and outputs.

Inputs	
ra	ICRS right ascension at J2000.0
dec	ICRS declination at J2000.0
pmra	RA proper motion
pmdec	Dec proper motion
px	parallax
rv	radial velocity
lat	latitude of site
lon	longitude of site
el	elevation of site
epoch	time of observation
wl	wavelength of observation
rh	relative humidity
temp	temperature
Outputs	
Alt	Altitude angle positive above the horizon
Az	Azimuthal angle measured eastward from north

$$\theta_B = -\mathrm{Az_B} + 2\pi \tag{2.1}$$

$$\phi_B = \frac{\pi}{2} - \mathrm{Alt_B} \tag{2.2}$$

$$M_1 = \begin{bmatrix} \cos(\frac{\pi}{2}+\theta_B) & \sin(\frac{\pi}{2}+\theta_B) & 0 \\ -\sin(\frac{\pi}{2}+\theta_B) & \cos(\frac{\pi}{2}+\theta_B) & 0 \\ 0 & 0 & 1 \end{bmatrix} \tag{2.3}$$

$$M_2 = \begin{bmatrix} 1 & 0 & 0 \\ 0 & \cos(\phi_B) & \sin(\phi_B) \\ 0 & -\sin(\phi_B) & \cos(\phi_B) \end{bmatrix} \tag{2.4}$$

$$M_3 = \begin{bmatrix} \cos(q) & \sin(q) & 0 \\ -\sin(q) & \cos(q) & 0 \\ 0 & 0 & 1 \end{bmatrix} \tag{2.5}$$

$$M_B = M_3 M_2 M_1 \tag{2.6}$$

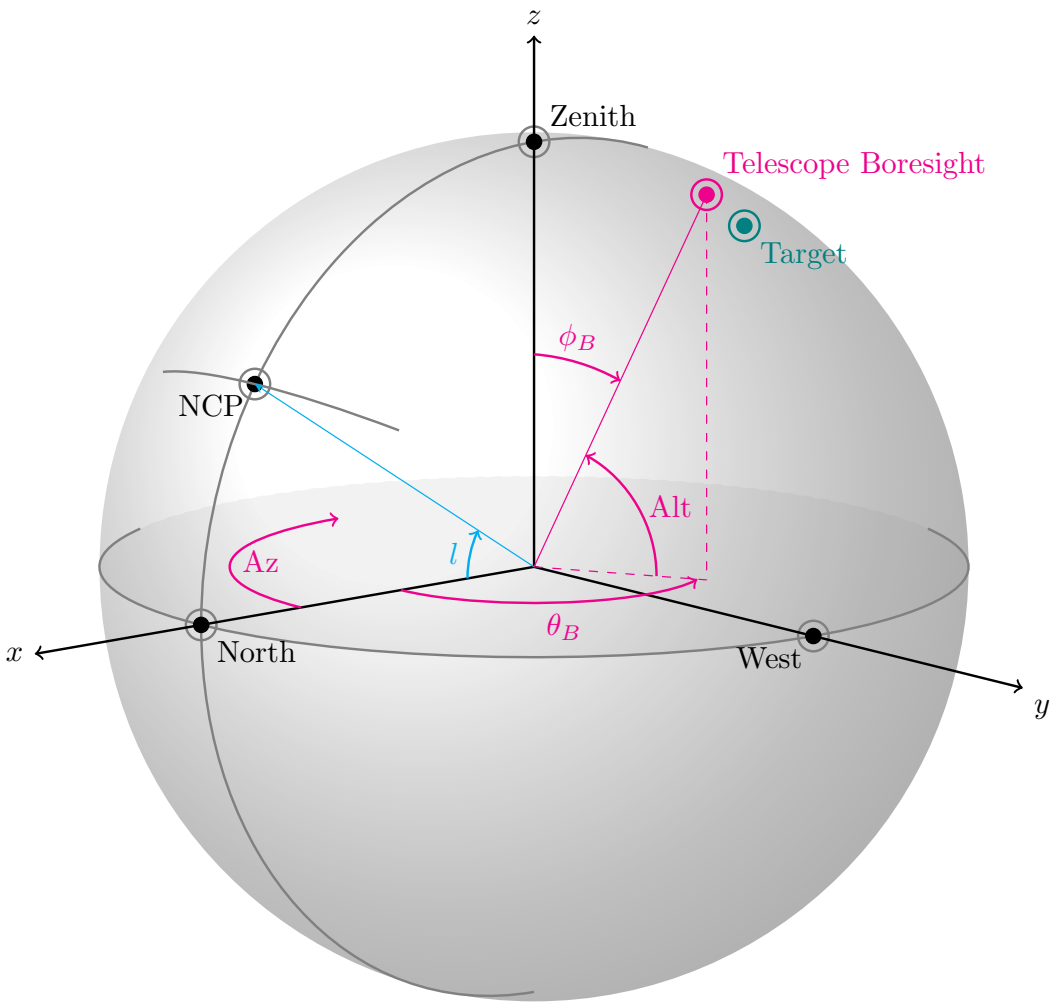

Figure 2.2 – The observed (Alt, Az) coordinate system. NCP is north celestial pole.

The parallactic angle q in Equation 2.5 is computed using SOFA's `iauHd2pa` routine. Figure 2.3 provides a visualization of the series of coordinate system rotations M_1, M_2, and M_3. The bottom right panel of the figure shows the end result of the final coordinate system rotation when viewed along the boresight direction: +y' points along +Dec and +x' points along +RA. Finally, to convert a target from observed to field coordinates:

$$\theta_T = -\mathrm{Az_T} + 2\pi \tag{2.7}$$

$$\phi_T = \frac{\pi}{2} - \mathrm{Alt_T} \tag{2.8}$$

$$\begin{bmatrix} x_T \\ y_T \\ z_T \end{bmatrix} = \begin{bmatrix} \cos(\theta_T)\sin(\phi_T) \\ \sin(\theta_T)\sin(\phi_T) \\ \cos(\phi_T) \end{bmatrix} \tag{2.9}$$

$$\begin{bmatrix} x'_T \\ y'_T \\ z'_T \end{bmatrix} = M_B \begin{bmatrix} x_T \\ y_T \\ z_T \end{bmatrix} \tag{2.10}$$

$$\begin{bmatrix} \phi_{FC} \\ \theta_{FC} \end{bmatrix} = \begin{bmatrix} \arccos(z'_T) \\ \arctan 2(y'_T, x'_T) \end{bmatrix} \tag{2.11}$$

2.4 Field (ϕ_{FC}, θ_{FC}) to focal plane (x_{FPC}, y_{FPC}) coordinates

Focal plane coordinates are 2D Cartesian with units of mm. +x points along +RA and +y points along +Dec. Figure 2.4 shows the geometric relationship between field and focal plane coordinates. Converting from field to focal plane coordinates involves a wavelength-dependent radial distortion model. The focal plane is modeled as a spherical surface projected onto the xy plane. The incoming field angle ϕ_{FC} is related to the outgoing focal plane angle ϕ'_{FPC} by an odd-order polynomial. The conversion from field coordinates to focal plane coordinates is given by:

$$\phi'_{FPC} = c_0\phi_{FC} + c_1\phi_{FC}^3 + c_2\phi_{FC}^5 + c_3\phi_{FC}^7 + c_4\phi_{FC}^9 \tag{2.12}$$

$$\begin{bmatrix} x_{FPC} \\ y_{FPC} \end{bmatrix} = R\sin(\pi - \phi'_{FPC}) \begin{bmatrix} \cos(\theta_{FC}) \\ \sin(\theta_{FC}) \end{bmatrix} \tag{2.13}$$

Polynomial coefficients and focal plane surface radii were determined by least squares fits to

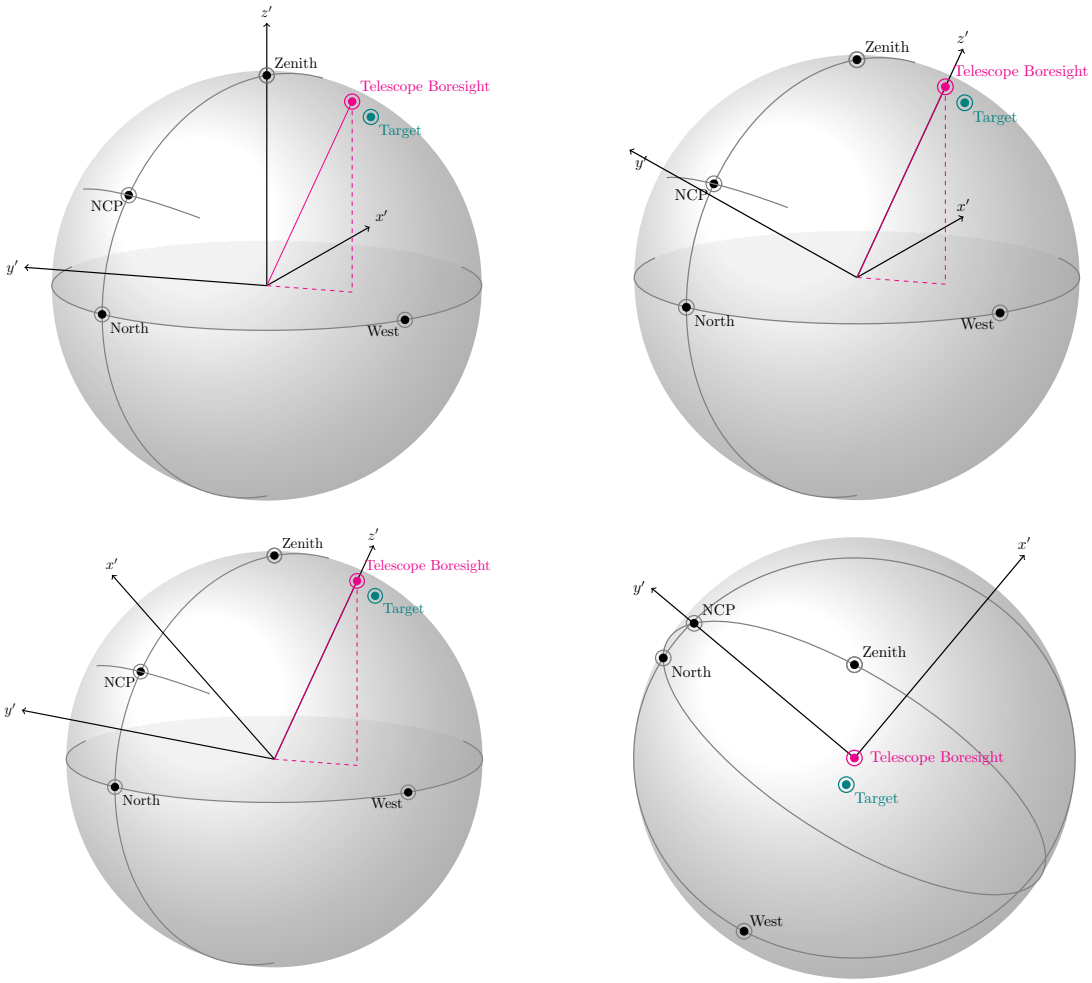

Figure 2.3 – Visualizations of coordinate system rotations in Equations 2.3-2.6. Top left: M_1 rotation. Top right: M_2M_1 rotation. Bottom left: $M_3M_2M_1$ rotation. Bottom right $M_3M_2M_1$ rotation viewed from the boresight direction.

ZEMAX ray traces for each telescope at several wavelengths of interest. These parameters are tabulated in Table 2.2. Polynomial coefficients were calculated for ϕ_{FC} and ϕ'_{FPC} in degrees. The model is only valid for $\phi_{FC} < 1.5^{\circ}$ at APO and $\phi_{FC} < 1.1^{\circ}$ at LCO because these were the maximum field angles for which ray traces were performed. At the focal plane, this polynomial model has an RMS accuracy of 0.1 μm.

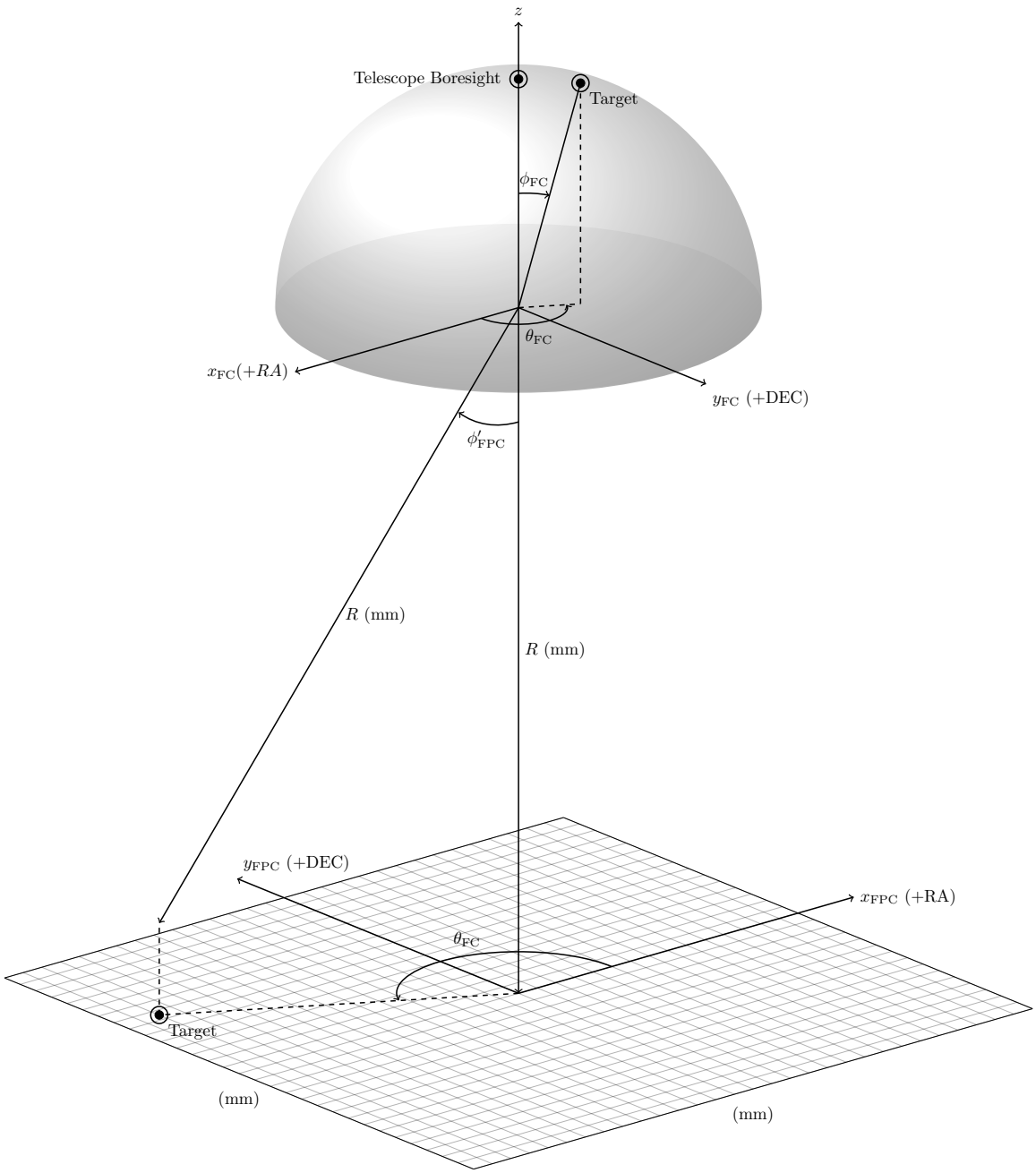

Figure 2.4 – The geometric relationship between field and focal plane coordinates. The focal plane angle ϕ'_{FPC} is a polynomial function of field angle ϕ_{FC}. The focal plane is modeled as a spherical surface with radius R and projected onto the xy plane.

Table 2.2 – . Focal plane distortion model parameters.

site	λ (μm)	R (mm)	c_0	c_1	c_2	c_3	c_4
APO	1.66	8939	1.40708	6.13779e-03	7.25138e-04	-3.28007e-06	-1.65995e-05
APO	0.54	9208	1.36580	6.09425e-03	6.54926e-04	2.62176e-05	-2.27106e-05
APO	0.6231	9164	1.37239	6.09825e-03	6.67511e-04	2.14437e-05	-2.17330e-05
LCO	1.66	8905	2.11890	1.40826e-02	1.27996e-04	6.99967e-05	0
LCO	0.54	9938	1.89824	1.31773e-02	1.04445e-04	5.77341e-05	0
LCO	0.6231	9743	1.93618	1.33536e-02	9.17031e-05	6.58945e-05	0

2.5 Focal plane (x_{FPC}, y_{FPC}) to wok (x_{wok}, y_{wok}) coordinates

Wok coordinates are 2D Cartesian with units of mm. Generally, +x points between GFA3 and GFA4 and +y points toward GFA2 (right panel Figure 2.5). Technically, the wok coordinate axes are defined by the grid of xy fiducial locations for which precise CMM measurements were obtained.

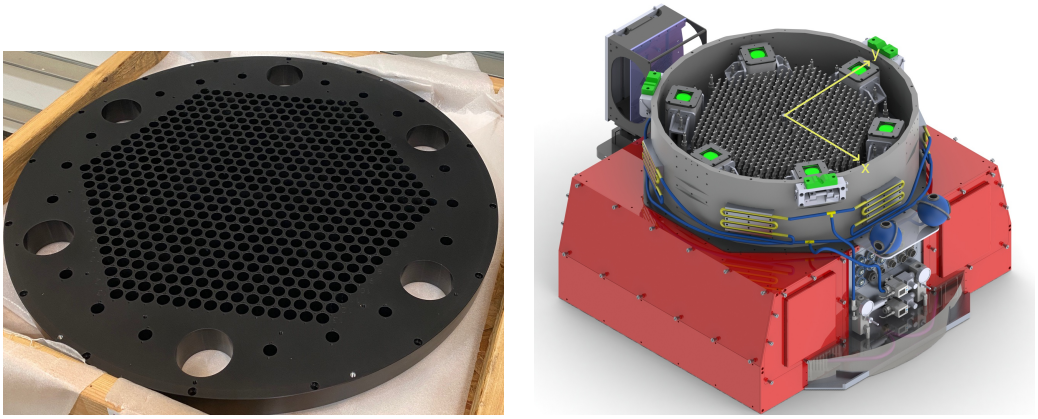

Figure 2.5 – Left panel: the bare wok mounting plate. Right panel: solid model rendering of instrument after robots, fiducials, and GFAs have been mounted in the wok. Wok coordinate axes are indicated in yellow.

The conversion from focal plane to wok coordinates involves a rotation by θ_{PA} (the desired position angle of observation) and a scale. Scale is measured and applied throughout the night

using GFA camera feedback. Figure 2.6 shows the relationship between focal plane and wok coordinates. The conversion is defined as:

$$\begin{bmatrix} x_{\text{wok}} \\ y_{\text{wok}} \end{bmatrix} = \frac{1}{\text{scale}} \begin{bmatrix} \cos(\theta_{PA}) & \sin(\theta_{PA}) \\ -\sin(\theta_{PA}) & \cos(\theta_{PA}) \end{bmatrix} \begin{bmatrix} x_{FPC} \\ y_{FPC} \end{bmatrix} \tag{2.14}$$

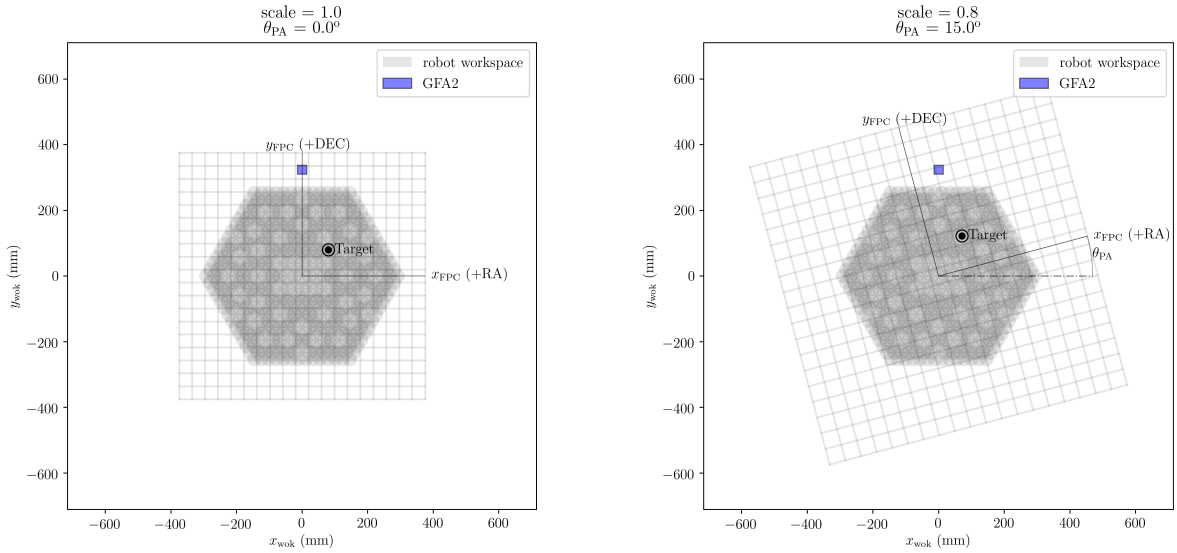

Figure 2.6 – Wok coordinates are related to focal plane coordinates by a rotation (desired position angle) and scale. Small variations in scale are tracked and adjusted throughout the night using the GFA camera on-sky measurements.

2.6 Wok (x_{wok}, y_{wok}) to tangent (x_{TC}, y_{TC}) coordinates

Tangent coordinates are 2D Cartesian with units of mm. Each element on the wok has a unique tangent coordinate system. The tangent coordinate origin is located at either (1) the center of a robot's work space or (2) the center of a GFA CCD. The transform from wok to tangent coordinates is given by:

$$\begin{bmatrix} \mathrm{x}_{TC} \\ \mathrm{y}_{TC} \end{bmatrix} = \begin{bmatrix} \hat{x} \\ \hat{y} \end{bmatrix} \left(\begin{bmatrix} \mathrm{x}_{wok} \\ \mathrm{y}_{wok} \end{bmatrix} - \begin{bmatrix} x_b \\ y_b \end{bmatrix} \right) \tag{2.15}$$

where $\hat{x}$ and $\hat{y}$ are 2D orthogonal unit vectors that specify the direction of the tangent x and y axes in wok coordinates, and (x_b, y_b) specify the origin of the tangent element in wok coordinates. For positioners $\hat{x}$ points along the $\theta_\alpha = 0$ axis, which is $\sim [0, -1]$ for all positioners. For GFAs $\hat{x}$ is parallel to CCD rows. $\hat{x}$ is is $\sim [1, 0]$ for GFA2 and $\sim [-1, 0]$ for GFA5. The precise values for $\hat{x}$, $\hat{y}$, x_b, and y_b are carefully measured for each robot and GFA installed in the wok.

2.7 Tangent (x_{TC}, y_{TC}) to guide (x_{CCD}, y_{CCD}) coordinates

Guide coordinates are 2D Cartesian with units of pixels. The origin of the guide coordinate frame is the lower left corner of the lower left pixel of the CCD. The GFA CCDs are (2048,2048) square devices with 13.5 μm pixels. The tangent to guide coordinate conversion is specified as:

$$x_{CCD} = \frac{1}{\mathrm{bin}_x} \left[\frac{1000}{13.5} x_{TC} + 2048/2 \right] \tag{2.16}$$

$$y_{CCD} = \frac{1}{\mathrm{bin}_y} \left[\frac{1000}{13.5} y_{TC} + 2048/2 \right] \tag{2.17}$$

where bin_x and bin_y are the column and row CCD bin factors.

2.8 Positioner (θ_α, θ_β) to tangent (x_{TC}, y_{TC}) coordinates

Positioner coordinates are specified by two angles (θ_α, θ_β). θ_α is a rotation about the robot's alpha axis, θ_β is a rotation about the robot's beta axis. The alpha and beta axes are separated by a length $l_\alpha \sim 7.4$ mm (a measured quantity for each robot). Figure 2.7 shows the orientation of robot arms and the axes of rotation. The wok coordinate frame and tangent coordinate frame are indicated in the figure. The robot's alpha and beta arms are unequal lengths, which leads to an annular patrol

zone for fibers carried in the beta arm.

Each robot carries three fibers on beta arm: a metrology fiber, an APOGEE fiber, and a BOSS fiber. Fiber coordinates are specified in the beta arm frame (x_β, y_β) in mm. These Cartesian fiber coordinates can be represented in a polar coordinates (r_F, θ_F) via:

$$\theta_F = \arctan 2(y_\beta, x_\beta) \tag{2.18}$$

$$r_F = \sqrt{x_\beta^2 + y_\beta^2} \tag{2.19}$$

By definition, the origin of the beta arm frame is at the beta axis of rotation and +x points to the metrology fiber center. Fiber positions in the beta arm frame are shown in in Figure 2.8.

The robot kinematic equation defining the location of a fiber in tangent coordinates is:

$$\begin{bmatrix} x_{TC} \\ y_{TC} \end{bmatrix} = \begin{bmatrix} \cos(\theta_\alpha) & \cos(\theta_\alpha + \theta_\beta + \theta_F) \\ \sin(\theta_\alpha) & \sin(\theta_\alpha + \theta_\beta + \theta_F) \end{bmatrix} \begin{bmatrix} l_\alpha \\ r_F \end{bmatrix}. \tag{2.20}$$

2.9 Discussion and Conclusion

Omitting the FVC, this chapter shows the complete suite of coordinate systems and transforms SDSS-V has chosen for survey design and operations with the FPS instruments. The coordinate system mapping is shown graphically in Figure 2.1 and mathematically in Sections 2.2 - 2.8. In each section, the transform is only shown in one direction. Most of the transforms we have derived are algebraically invertible, with the exception of a few that deserve mention.

In Section 2.2, the reverse transform from (Alt, Az) observed coordinates to ICRS coordinates directly employs SOFA's `iauAtoc13` routine. In Section 2.4, the reverse transform from (x_{FPC}, x_{FPC}) focal plane coordinates to (ϕ_{FC}, θ_{FC}) field coordinates involves a separate set of polynomial coefficients c_0-c_4 to compute:

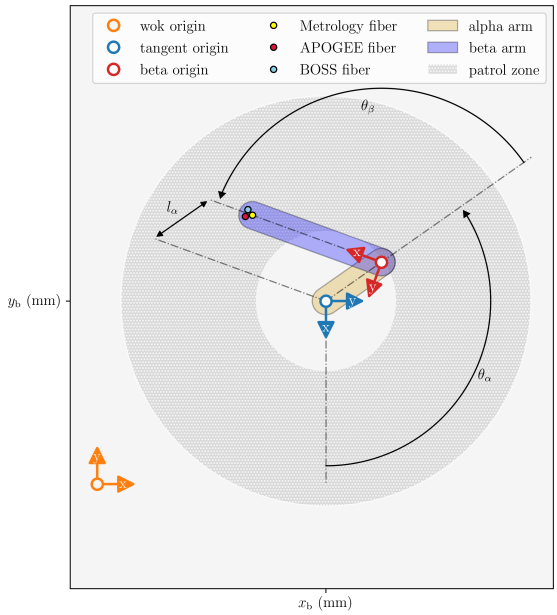

Figure 2.7 – Two arm kinematics for SDSS-V robots. θ_α is the rotation of the alpha arm, θ_β is the rotation of the beta arm. Wok and tangent coordinate frames are indicated by orange and blue axes. Red axes indicate the beta arm coordinate frame.

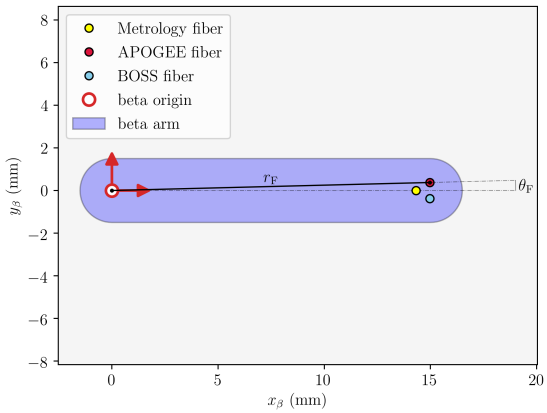

Figure 2.8 – The beta arm coordinate frame. Origin is set to the center of beta arm rotation, +x points to the metrology fiber. (x_β, y_β) fiber locations in mm are specified in this frame.

$$\phi_{FC} = c_0\phi'_{FPC} + c_1\phi'^3_{FPC} + c_2\phi'^5_{FPC} + c_3\phi'^7_{FPC} + c_4\phi'^9_{FPC}, \tag{2.21}$$

and this inverse model yields an RMS of 1-2 milliarcseconds on sky when tested against ZEMAX raytraces.

In Section 2.8, it is of common interest to compute the inverse kinematics: (θ_α, θ_β) positioner coordinates given (x_{TC}, y_{TC}) tangent coordinates. Solutions to this problem only exist for (x_{TC}, y_{TC}) points within the robot's workspace. Our procedure for this task was adapted from an online source[5] and is explicitly shown in Chapter 4 Equations 4.21-4.25.

A self-contained technical description of coordinate systems and their transformations has both

[5] https://motion.cs.illinois.edu/RoboticSystems/InverseKinematics.html

organized and simplified SDSS survey planning and operations code. SDSS-V's `coordio` software package has implemented coordinate transforms as described here, allowing conversions between any two coordinate systems in the stack. `coordio` has become a key tool used throughout the SDSS-V survey's growing code base.

Chapter 3

KAIJU: COLLISION-FREE PATH PLANNING FOR ROBOTIC FIBER POSITIONERS

Portions of this chapter were originally published in the January 2021 edition of the Astronomical Journal (Sayres et al., 2021, AJ*, Vol. 161, 92; 2021 © American Astronomical Society, DOI: 10.3847/1538-3881/abd0f2), and are reproduced below with the permission of the American Astronomical Society.*

Summary

Robotic fiber positioner (RFP) arrays are becoming heavily adopted in wide field massively multiplexed spectroscopic survey instruments. RFP arrays decrease nightly operational overheads through rapid reconfiguration between fields and exposures. In comparison to similar instruments, SDSS-V has selected a very dense RFP packing scheme where any point in a field is typically accessible to three or more robots. This design provides flexibility in target assignment, but the task of collision-less trajectory planning is especially challenging. We present two multi-agent distributed control strategies that are highly efficient and computationally inexpensive for determining collision-free paths for RFPs in heavily overlapping workspaces. We demonstrate that a reconfiguration path between two arbitrary robot configurations can be efficiently found if "folded" state, in which all robot arms are retracted and aligned in a lattice-like orientation, is inserted between the initial and final states. Although developed for SDSS-V, the approach we describe is generic and so applicable to a wide range of RFP designs and layouts. Robotic fiber positioner technology continues to advance rapidly, and in the near future ultra-densely packed RFP designs may be feasible. Our algorithms are especially capable in routing paths in very crowded environments, where we see efficient results even in regimes significantly more crowded than the SDSS-V RFP design.

3.1 Introduction

Robotic fiber positioners are emerging as a promising technology in the today's landscape of wide-field multi-object spectroscopic instruments and surveys. Many projects (e.g. LAMOST Cui et al. 2012, PFS Sugai et al. 2015, DESI Abareshi et al. 2022, MOONS Cirasuolo et al. 2011, 4MOST de Jong et al. 2019, SDSS-V Kollmeier et al. 2017) have adopted densely packed positioner arrays patrolling the telescope's focal plane to obtain massively multiplexed spectroscopic observations

of hundreds to thousands of objects in a field. These arrays minimize operational overhead through rapid reconfigurations between fields and exposures. Generally, each robotic fiber positioner will patrol a relatively small circular zone of the focal plane. To obtain complete focal plane coverage, RFP patrol zones or workspaces necessarily overlap. A system in which RFPs may physically interfere must therefore have a motion planning strategy ensuring that robots do not collide, wedge, or deadlock during reconfiguration.

The difficulty of the reconfiguration problem scales with the number of positioners able to physically occupy the same workspace. Both SDSS-V and MOONS have chosen densely packed fiber positioner layouts that exhibit a large amount of workspace overlap when compared to similar instruments. For example, a point in the DESI focal plane will typically be accessible to only a single positioner, whereas any point in the SDSS-V focal plane will typically be accessible to 3 or 4 positioners. A heavily shared workspace increases flexibility in target assignment at the cost of a heightened chance of collision during reconfiguration. The challenge posed by RFP reconfiguration is a type of "Cocktail Party Problem" (Lumelsky and Harinarayan, 1997), in which mobile agents must navigate around each other in a crowded environment to reach a destination; an analogous situation to the trajectory planning problem humans subconsciously solve when moving around at a crowded cocktail party.

The Cocktail Party Problem lies in the general field of distributed multi-agent coordination and control, sometimes called swarm control. Cao et al. (2012) and Rossi et al. (2018) provide comprehensive overviews of this rapidly advancing subject. The swarm control objective is to model how collective behavior (e.g. pattern formation, motion planning, synchronization) emerges from networks of individual agents following relatively simple protocols. As the number of agents in a network increases, a global (or centralized) optimization strategy becomes computationally prohibitive. Distributed control strategies often alleviate this computational burden by delegating the decision-making to the agents themselves, who then act according to the state of their immediate environments. Distributed control is well-suited for real-time optimization and decision making in large networks, and scales well as additional agents are added. Applications in the field are typically focused on coordinated robotics problems like remote sensor and surveillance net-

works or unmanned aerial vehicle coordination. The algorithms are diverse with strategies ranging from game-theory approaches (Arslan et al., 2007), to Markov-based processes (Emenheiser et al., 2016), to biologically-inspired artificial potential function (APF) models (Olfati-Saber, 2006).

Makarem et al. (2014) approached the RFP navigation challenge using control laws based on artificial potential functions. For array layouts with slightly overlapping fiber patrol zones (e.g. DESI or PFS), this strategy demonstrates the successful convergence of robots to targets. However, this algorithm struggles when directly applied to heavily overlapping RFP layouts like those of SDSS-V: large fractions of positioners experience a deadlocked state, where progress toward the target halts due to the inability of combinations of positioners to move past one another. Tao et al. (2018) injected additional control layers to the existing algorithm to detect and mitigate deadlock situations. Using this augmented APF algorithm they report convergence increases from $\sim$65% to $\sim$80% for SDSS-V geometries. Recently, Macktoobian et al. (2019) further improved the APF strategy with the introduction of cooperative fields, in which they demonstrate completely successful path solutions for SDSS-V positioner geometries in grids of various sizes in a set of 12 simulations.

In this work we present an alternative and simplified approach to the RFP navigation problem with a pair of closely related algorithms that are directly applicable to the majority of existing RFP systems today. The first algorithm is a greedy heuristic, and the second algorithm is a Markov chain variant of the greedy heuristic. Collecting statistics from thousands of simulations, we measure the efficiency of each algorithm as the fraction of targets assigned to targets acquired under collision-avoidance constraints. In parameter spaces relevant to SDSS-V, we find the efficiency of the greedy heuristic to be $\sim 99.2\%$ and efficiency of the Markov variant to be $> 99.9\%$. The high efficiencies of these routines are largely attributable to a reverse path generation strategy, rather than overall algorithmic complexity. We discuss tradeoffs between operational overheads and overall targeting efficiency in the context of each algorithm. We explore the limits of each algorithm by scaling up the relative size of the robots within the array to simulate overly crowded environments. The results suggest that high efficiency paths can be found for positioner arrays that are significantly more crowded than the SDSS-V positioner array. This work provided important feedback for the

SDSS-V positioner design, so these algorithms serve as useful tools for vetting the feasibility of current and future RFP instrument designs.

This chapter is organized as follows. In Section 3.2, we describe the physical layout and robot arm kinematics for which the algorithms presented here have been developed. In Section 3.3 we present the generic algorithms followed by a detailed analysis in Section 3.4. In Section 3.5 we discuss methods for the effective deployment of these algorithms in the presence realistic hardware constraints. Finally, in 3.6 we discuss these algorithms in context of overall survey optimization and comment on the general relevance of this work. Pseudocode for all routines is provided in Section A.1, and SDSS-V's `kaiju`[1] package contains source code for the algorithms we present.

3.2 Focal Plane System Layout

The following subsections describe the layout and kinematics of the SDSS-V RFP array. In this chapter we make three benign simplifications: (1) each robot carries a single fiber, (2) the xy coordinate system of the focal plane is rotated by 90 degrees with respect to the positioner's internal coordinate system, and (3) the only obstacles within the robot array are other robots. Omitting certain SDSS-V specific details allows us to present a more generic formulation of the algorithms.

3.2.1 Positioner Kinematics

A rendering of the SDSS-V RFP is shown in the upper inset of Figure 3.1. The lower panel of this figure shows the relative packing of positioners in the focal plane when viewed edge on. Fiber positioning in the focal plane is achieved through the rotations of two arms about two axes. The alpha arm (lower arm, indicated in gold) rotates about the alpha axis. The alpha axis is collinear with the lower body of the robot. The beta arm (upper arm, indicated in blue), rotates about a beta axis near the edge of the alpha arm. The distance between the alpha axes of neighboring robots we call the pitch. The beta arm carries the optical fiber and risks collisions with the beta arms of neighboring robots. Alpha arms cannot collide with one another. The left two robots in the lower

[1] https://github.com/sdss/kaiju

panel of Figure 3.1 are in an orientation of closest approach between alpha arms, showing the tight clearance between them. Beta arms cannot collide with alpha arms, as they exist in different planes along the optical axis.

To visualize how a robot positions a fiber, a focal plane view is helpful. Figure 3.2 shows the focal plane projection of a fiber positioner centered at the robot's xy base position $(x_\mathrm{b}, y_\mathrm{b})$. Robot arms and rotation axes are indicated on the figure. The alpha arm length (l_α) is the distance from the alpha axis to beta axis (7.4 mm for SDSS-V). The beta arm length (l_β) is the distance from the beta axis to the fiber center (15 mm for SDSS-V). The robot may position a fiber anywhere in the annular patrol zone through the specification of the alpha angle (θ_α) and beta angle (θ_β). This coordinate conversion is:

$$\begin{bmatrix} x_\mathrm{f} \\ y_\mathrm{f} \end{bmatrix} = \begin{bmatrix} x_\mathrm{b} \\ y_\mathrm{b} \end{bmatrix} + \begin{bmatrix} \cos\theta_\alpha & \cos(\theta_\alpha + \theta_\beta) \\ \sin\theta_\alpha & \sin(\theta_\alpha + \theta_\beta) \end{bmatrix} \begin{bmatrix} \mathrm{l}_\alpha \\ \mathrm{l}_\beta \end{bmatrix}, \tag{3.1}$$

where $(x_\mathrm{f}, y_\mathrm{f})$ corresponds to the position of the fiber in the xy focal plane.

The physical limits of travel for the SDSS-V positioner are roughly between -5^o and 365^o for both the alpha and beta axes. This permits each axis slightly more than one full rotation between hard stops. Operationally we enforce slightly more restrictive limits of travel during path planning: each axis must remain in the range $[0^\mathrm{o}, 360^\mathrm{o})$.

Notice that the orientation in Figure 3.2 resembles a human's view of a right arm, and increasing θ_β beyond 180^o would resemble a left arm. Every point in a positioner's workspace is physically achievable by both a left and right arm conformation. We will limit targeting to right-armed configurations, though positioners may potentially take on left-armed configurations while maneuvering. This choice does not impact a positioner's ability to cover the available workspace, but it will eliminate an alternative positioning option during target assignment. The elimination of the left arm targeting configuration serves two practical purposes in SDSS-V.

The first purpose is to avoid degenerate solutions. When the FPS system is deployed, a fiber viewing metrology system is used to determine a robot's orientation by measuring the centroid of a back-lit fiber. If the option of a left arm configuration is eliminated there is only one pos-

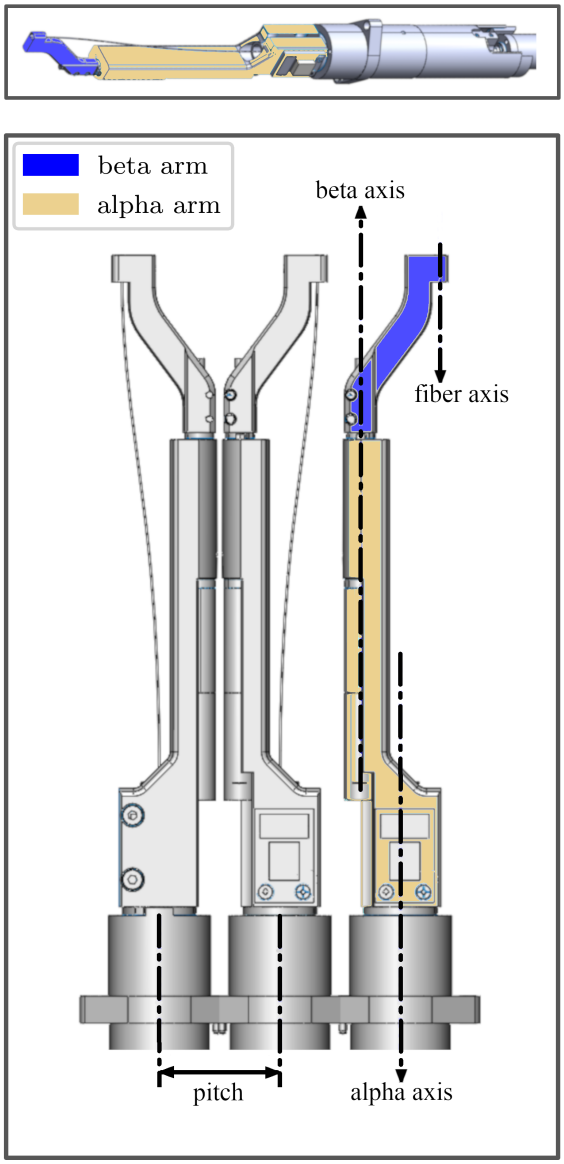

Figure 3.1 – Renderings of SDSS-V robots. The upper panel shows a single RFP unit, the lower panel shows the relative packing of three units at the focal plane viewed edge on at the nominal SDSS-V pitch, where the pitch is the distance between robot centers. The alpha arm (lower arm) is colored gold, the beta arm (upper arm) is colored blue and holds the optical fiber. Fiber positioning is accomplished through a rotation of the alpha arm about the alpha axis, and a rotation of the beta arm about the beta axis. Beta arms risk collision with one another, but alpha arms do not. The left two positioners in the bottom panel show the level of clearance between alpha arms in an orientation of closest approach.

sible solution for $(\theta_\alpha, \theta_\beta)$ given a measurement of (x_f, y_f). This is important when considering a malfunctioning robot that cannot report its absolute position. The robot array will be powered down during science integrations to minimize heat at the focal plane. If we enforce that robots are only powered down in right arm configurations, this will minimize confusion that could arise due to a malfunction after a power cycle. While robots remain powered, their absolute positions are frequently reported.

The second purpose is of mechanical nature, rather than mathematical. We achieve higher fiber positioning accuracy when $0^\text{o} \leq \theta_\beta \leq 180^\text{o}$. This is due to an interaction between the beta axis preload spring and the direction of torque imparted by the optical fiber itself. In right arm configurations, the fiber torque and preload work together. In left arm configurations, the fiber torque and preload oppose each other, leading to slightly higher variance in absolute positioning when operating in especially cold weather.

3.2.2 Positioner Arrangement

To obtain full focal plane coverage the robots are spaced at a pitch of $\mathrm{l}_\alpha + \mathrm{l}_\beta$ in a hexagonal array (22.4 mm for SDSS-V). This allows a robot's neighbor to patrol its central exclusion zone, leading to heavily overlapping patrol zones between a robot and its neighbors. Figure 3.3 shows the overlapping patrol zones for an array of 19 SDSS-V positioners, indicating the areas covered by 1, 2, 3, and 4 fibers in the focal plane. Scaling up the hexagonal array to hundreds of positioners, the majority of the focal surface will be covered by 3 or more fibers. Only the perimeter of the hexagonal array will have single fiber coverage with some gaps. The axes in the lower left of the figure indicate the orientation of θ_α with respect to the hexagonal grid.

The SDSS-V specifications for l_α, l_β, and pitch were chosen to maximize the patrol area for each positioner under present constraints of the telescope and spectrograph. The BOSS spectrograph has a 500 fiber capacity, dictating the total number of robots. Evenly distributing 500 robots over the telescope's field of view yields a desired pitch of 22.4 mm. Given the pitch, a 7.4 mm alpha arm length grants the largest possible reach while ensuring that alpha arms cannot physically collide with one another. With pitch and alpha arm length selected, a 15 mm beta arm length is

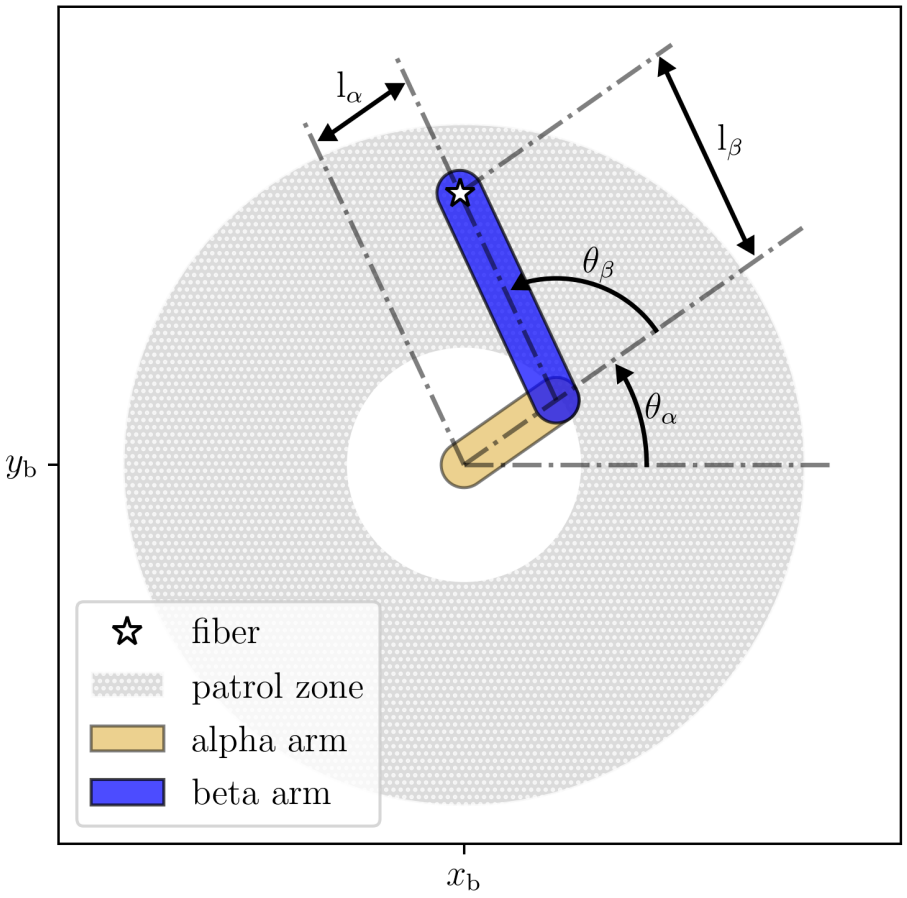

Figure 3.2 – A focal plane projection of an SDSS-V robot, showing the annular patrol zone in gray. Fiber position in the focal plane (white star) is achieved through the specification of two angular rotations θ_α and θ_β of the alpha and beta arms. Alpha and beta arms are colored gold and blue. l_α, l_β indicate the alpha and beta arm lengths.

required to ensure gap-less coverage of the focal plane. Hörler et al. (2018) provide further discussion on the general topic of RFP design and arrangement, including the densely-packed arangement selected for SDSS-V.

3.2.3 Collision Formalism

All physical interference between robots in the grid happens between beta arms. We use a relatively simple strategy to represent a beta arm geometry in Cartesian space. The beta arm is modeled

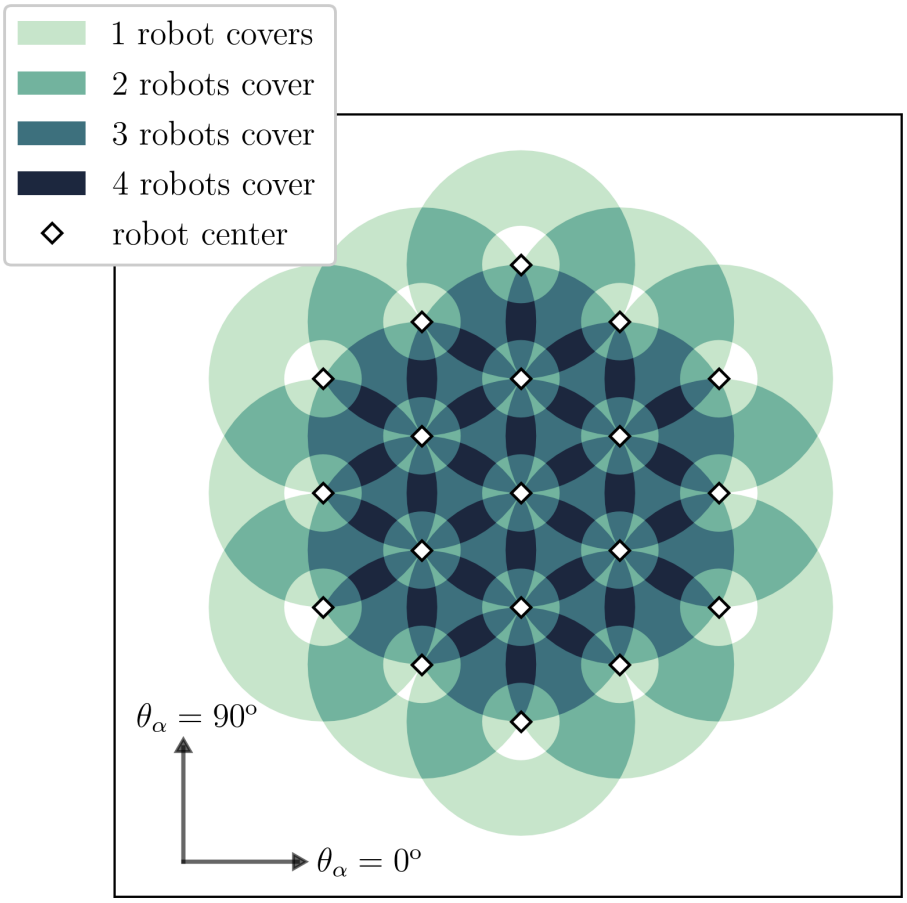

Figure 3.3 – A 19 positioner hexagonal array, showing the high packing density of SDSS-V RFPs. The area is shaded according to the number of positioners that patrol the space. The six surrounding neighbors may occupy the space at a robot's center (white diamonds). Generally the area is covered by 3-4 positioners. Only the array's perimeter is covered by fewer than three robots. The direction of θ_α is labeled to indicate the orientation of the robot's coordinate system with respect to the grid.

by two elements: (1) a line segment and (2) a collision buffer ($\sigma_{\rm cb}$). The beta line segment is constructed between two points $(x_{\rm f}, y_{\rm f})$, and $(x_{\rm e}, y_{\rm e})$. The former point is given in Equation 3.1. The coordinates of the latter point (elbow point) describe the position of the beta axis:

$$\begin{bmatrix} x_{\rm e} \\ y_{\rm e} \end{bmatrix} = \begin{bmatrix} x_{\rm b} \\ y_{\rm b} \end{bmatrix} + \begin{bmatrix} {\rm l}_\alpha \cos\theta_\alpha \\ {\rm l}_\alpha \sin\theta_\alpha \end{bmatrix} \tag{3.2}$$

The orientation of the beta line segment will depend on a positioner's $(\theta_\alpha, \theta_\beta)$ coordinates which vary during motion. A positioner's base position $(x_\mathrm{b}, y_\mathrm{b})$ and arm lengths $(\mathrm{l}_\alpha, \mathrm{l}_\beta)$ remain fixed.

We measure the proximity between two beta arms by computing the minimum distance between beta arm segments. The procedure for this calculation is provided in Appendix A.1 and was adapted from an online source[2]. We label the minimum distance between beta arm segments for positioners i and j as D_{ij}.

The collision buffer (σ_cb) specifies a radius from the beta line segment that safely encloses the physical extent of the beta arm. We refer to this buffered line segment as the collision envelope, which is a cigar shaped area. We say robots i and j are collided when:

$$\mathrm{D}_{ij} \leq 2\sigma_\mathrm{cb} \tag{3.3}$$

Figure 3.4 constructs the geometric representation of the beta arm segment (dashed gold line), σ_cb (gold arrow), and collision envelope (blue area) for two colliding RFPs. The red area in the figure indicates the collided area between the two positioners, where the inequality in Equation 3.3 is satisfied.

The two dimensional collision envelope we have drawn is conservative when considering the three dimensional shape of the beta arm. Certain robot orientations would allow the head of a beta arm hover directly above a neighbor's beta axis without suffering a physical collision between beta arms. Consider the view in Figure 3.1 and imagine the central positioner's beta arm floating rightward. Such an orientation would not be allowed in the focal plane projected view of Figure 3.4, as the area around the elbow joint is encompassed within the collision envelope. The extent of the collision buffer was chosen to completely allocate the space below a beta arm as belonging to the optical fiber, eliminating any chance of physical interaction between a fiber and a neighboring robot body. Reserving all space below the beta arm is perhaps unnecessarily greedy, as the fiber is tugged closer to the beta arm body when the arm is extended. The allowance of some amount of safe physical overlap between beta arms could be accomplished by either reducing the length

[2] http://geomalgorithms.com/a07-_distance.html

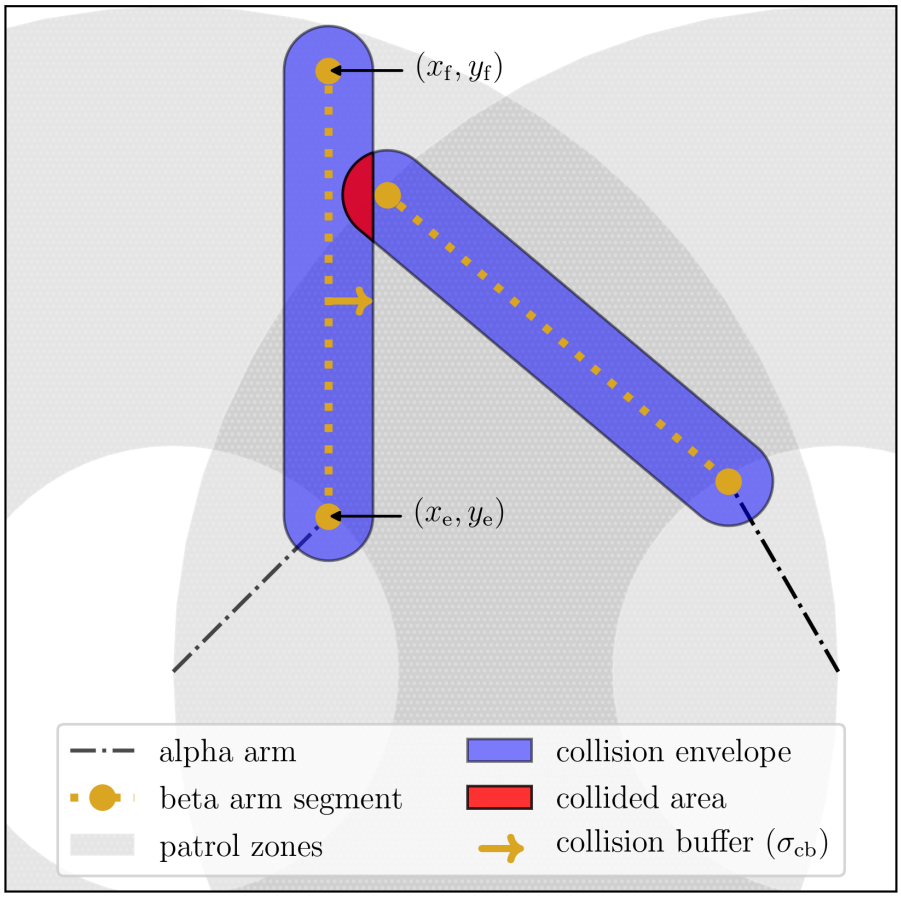

Figure 3.4 – Geometric representation of collided beta arms. The beta arm is described by a line segment constructed of two points (x_e, y_e), (x_f, y_f) and a collision buffer σ_{cb} (gold arrow), where $\sigma_{cb} = 1.5$ mm in this view. The area generated by the line segment and σ_{cb} is the blue-colored collision envelope, which contains the physical extent of the beta arm. When collision envelops intersect (Equation 3.3, indicated as red in the figure), the two robots are collided. The overlapping patrol zones are shown in light gray.

of the beta arm segment to yield space around the elbow, or modeling the beta arm as a segment or curve in three dimensional space. Permitting beta arm overlap would provide additional real estate for both target assignment and path generation which might prove beneficial. We adopt the collision buffer as described in this section for SDSS-V operations. However, the algorithms we present do not necessarily depend on a specific collision buffer length or width.

3.3 Algorithms

We present two algorithms for the SDSS-V RFP reconfiguration problem: a Greedy Choice (GC) algorithm, and a Markov Chain (MC) algorithm. Both algorithms carve paths in a stepwise fashion through a series of discrete state transitions by selecting next-state options from a set of small perturbations about the current alpha and beta angles. The two algorithms vary in their implementation: the GC algorithm selects moves "greedily" according to a simple heuristic, while the MC algorithm injects a tunable level of randomness into the GC routine. These algorithms are best classified as Distributed Model Predictive Control (i.e. Camponogara et al. 2002), where positioner's choice of move depends only on the current state of its immediate spatial neighbors. As a heuristic, this simple distributed approach requires minimal computation and results in quickly solved solutions.

The algorithms that follow generically assume a "perfect" fiber positioner possessing infinite acceleration and no positional uncertainty. We describe a post-processing strategy that allows for path-adaptation to realistic hardware constraints in Section 3.5.

3.3.1 Definitions

We first introduce the parameters, metrics, and general ingredients before describing the procedures of the GC and MC algorithms. We focus our analysis using SDSS-V geometries, although the definitions that follow are generic and can be applied to any layout of RFPs with similar kinematics.

Arm Angles: θ_α, θ_β The alpha and beta axis angles define the physical orientation of a robot. The range of motion for each axis is $[0^\circ, 360^\circ)$, as described in Section 3.2.1

Arm Lengths: l_α, l_β The lengths of the alpha and beta arms. In this work we use SDSS-V positioner values of l_α = 7.4 mm and l_β = 15 mm.

Collision Buffer: σ_{cb} This parameter sets the relative size of the beta arm, a radial distance from the beta arm line segment (see Section 3.2.3). We vary σ_{cb} between 1.5 and 3.5 mm. A 1.5 mm

$\sigma_{\rm cb}$ value exactly encloses the physical envelope of an SDSS-V RFP. A $\sigma_{\rm cb}$ between 2 and 2.5 mm maintains a generous amount positioner separation during motion, providing an extra safety buffer for both (1) real-time RFP positional uncertainties along trajectories and (2) path post-processing and simplification. We touch on these two topics further in Section 3.5. In deployment for the SDSS-V FPS, values of $\sigma_{\rm cb}$ greater than 2.5 mm are unreasonably large. However this parameter space will show the potential of these algorithms to achieve high efficiency solutions in regimes more crowded than our specific application.

Figure 3.5 shows the minimum, mean, and maximum $\sigma_{\rm cb}$ we investigate, emphasizing the crowding effect with increasing $\sigma_{\rm cb}$. A $\sigma_{\rm cb}$ of 1.5, 2.5, and 3.5 mm correspond to roughly 6%, 12%, and 20% of the focal plane area occupied by the collision envelopes of positioners when packed into a SDSS-V layout containing 547 positioners.

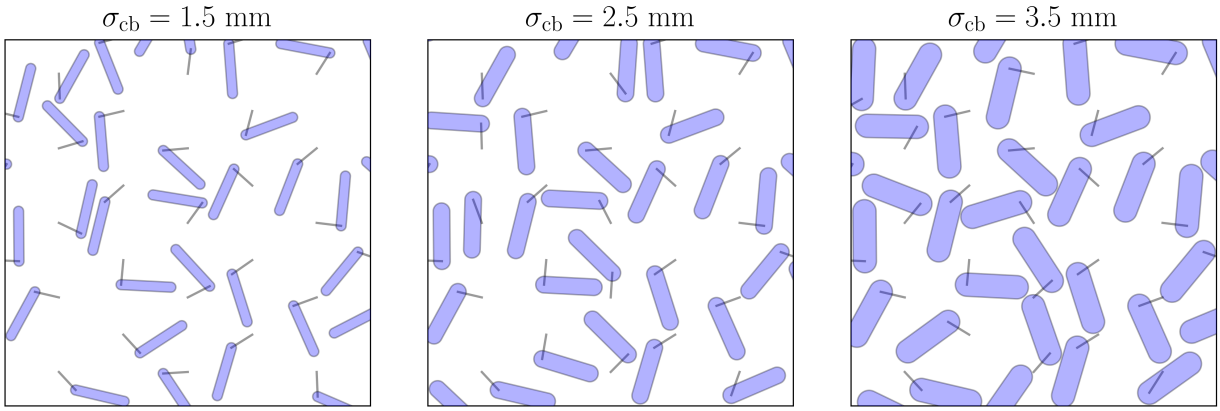

Figure 3.5 – Minimum, mean, and maximum $\sigma_{\rm cb}$ we consider. With increasing $\sigma_{\rm cb}$ available free space in the focal plane decreases. $\sigma_{\rm cb}$ = 1.5, 2.5, 3.5 mm occupy roughly 6%, 12%, and 20% of the focal plane area for 547 RFP grid. A $\sigma_{\rm cb} = 1.5$ mm represents the physical size of an SDSS-V RFP. A $\sigma_{\rm cb} = 2.5$ mm isolates a large safe zone around an SDSS-V RFP. A $\sigma_{\rm cb} = 3.5$ mm takes up an unreasonable amount of space for an SDSS-V application, but serves to test our algorithms in extremely cramped environments.

Robot Centers: $\vec{b}_i = (x_{\rm b}, y_{\rm b})$ Base position in the grid for positioner i. For this work we consider hexagonal grids with a pitch of 22.4 mm, matching the pitch of the SDSS-V FPS. We vary the number of positioners in the grid.

Robot Neighbors: N_i The set of robot neighbors for positioner i. Two robots are considered neighbors only if they risk collision with one another: when their center-to-center distance is less than twice the sum of their arm lengths and collision buffer σ_{cb}. If G is the set of all robots in the grid, the set of neighbors for positioner i is:

$$N_i = \{j \in G, j \neq i \mid \|\vec{\boldsymbol{b}}_i - \vec{\boldsymbol{b}}_j\| \leq 2(\text{l}_\alpha + \text{l}_\beta + \sigma_{\text{cb}})\} \tag{3.4}$$

Initial Coordinates: $\vec{\boldsymbol{\theta}}_i^{\text{I}} = (\theta_\alpha, \theta_\beta)$ The initial alpha and beta angle coordinates for a positioner i, a starting point for the routine. Initial coordinates must be non-colliding.

Destination Coordinates: $\vec{\boldsymbol{\theta}}_i^{\text{D}} = (\theta_\alpha, \theta_\beta)$ The desired alpha and beta axis angles for a positioner i. The algorithms seek to drive a positioner from its initial coordinates to its destination coordinates, while avoiding collisions with neighbors. Destination coordinates must be non-colliding.

Current Coordinates: $\vec{\boldsymbol{\theta}}_i^{\text{C}} = (\theta_\alpha, \theta_\beta)$ The current alpha and beta axis angles for a positioner i. These coordinates evolve with program step, and their history defines the path followed by a positioner.

Source Coordinates: $\vec{\boldsymbol{\theta}}_i^{\text{S}} = (\theta_\alpha, \theta_\beta)$ The source coordinates specify the alpha and beta axis angles for a positioner to receive light from an astronomical source. In this work a robot's source coordinates are drawn uniformly from the annular fiber patrol zone. Source coordinates must be non-colliding. All source coordinates are right-armed (Section 3.2.1). If an initial source coordinate assignment creates a collision with a previously assigned robot, source coordinates are redrawn iteratively until the collision vanishes. In a **forward** path solution, the source coordinates for positioner i are the destination coordinates, $\vec{\boldsymbol{\theta}}_i^{\text{D}}$. In a **reverse** path solution, the source coordinates serve as the initial coordinates, $\vec{\boldsymbol{\theta}}_i^{\text{I}}$.

Angular Step: $\Delta\theta$ The angular step parameter specifies the step size of the routine: a maximum angular perturbation of a robot's current coordinates $\vec{\boldsymbol{\theta}}^{\text{C}}$ at each program step. This parameter may

be converted into a time step, Δt by:

$$\Delta t = \frac{\Delta\theta}{\dot{\theta}}, \tag{3.5}$$

where $\dot{\theta}$ is the angular speed of the positioner's alpha and beta axes (30 deg/sec for SDSS-V RFPs). Smaller angular step values produce more densely sampled paths at the cost of increased program runtime.

Maximum Steps The maximum number of steps for the routine. For this work we set a limit of $1000^{\mathrm{o}}/\Delta\theta$ steps. This corresponds to 1000 degrees of motion, or roughly 33 seconds of motion assuming a 30 degree/sec angular speed for an SDSS-V RFP.

Minimum Approach Distance This distance designates the the closest allowed approach between any two beta arm segments in the routine. For a positioner i with a set of neighbors N_i we enforce the inequality:

$$\min\{j \in N_i \mid D_{ij}\} > 2\sigma_{\mathrm{cb}} + \mathrm{MD}, \tag{3.6}$$

where MD is a bound on the maximum displacement for a beta arm in a single program step. We choose a conservative value for MD: the displacement of the fiber $(x_{\mathrm{f}}, y_{\mathrm{f}})$ with beta arm at full extension ($\theta_\beta = 0$), when rotated $2\Delta\theta$ about the positioner's central axis:

$$\mathrm{MD} = (\mathrm{l}_\alpha + \mathrm{l}_\beta)\sin(2\Delta\theta) \tag{3.7}$$

The inclusion of the maximum displacement term protects against "tunneling collisions", where one positioner may completely jump through a collided orientation in a single step. Smaller values of $\Delta\theta$ permit closer approaches between positioners, and thus allow more options for maneuvering.

Cost: C_i The cost metric is minimized throughout the routine for each positioner. It measures a distance between a positioner's destination coordinates ($\vec{\boldsymbol{\theta}}_i^{\mathrm{D}}$) and current coordinates ($\vec{\boldsymbol{\theta}}_i^{\mathrm{C}}$). Note

this metric is not equal to the Euclidean distance between a fiber and its destination in the xy focal plane. For a positioner i we define the cost as:

$$C_i = \|\vec{\boldsymbol{\theta}}_i^{\mathrm{C}} - \vec{\boldsymbol{\theta}}_i^{\mathrm{D}}\| \tag{3.8}$$

When the cost is zero, the positioner has arrived at its destination.

Energy: E_i Energy is a measure of local crowding: the sum of inverse square distances to a set of neighbors. We define the energy for a positioner i with neighbors N_i as:

$$E_i = \sum_{j \in N_i} \left(\frac{1}{D_{ij}} \right)^2 \tag{3.9}$$

This metric is only used in the MC algorithm.

Phobia Phobia is a scalar between 0 and 1, used only in the MC algorithm. It represents the weighting of relative importance between the energy metric E_i and the cost metric C_i. A weight of 0 produces a positioner insensitive to crowding. A phobia weight of 1 produces a positioner only sensitive to crowding and it will seek to separate from neighbors above all else.

Greed Greed is a scalar between 0 and 1 used only in the MC algorithm. It represents how much weight a positioner will place on taking the best move when minimizing the E_i or C_i metrics. A greed value of 1 introduces no stochasticity in a positioner's move selection sequence, while a greed value of 0.5 resembles a random, undirected walk. A greed value of 0 produces a robot that will remain stationary.

Neighbor Encroachment Neighbor encroachment is a proximity threshold that is only considered in the MC algorithm. A positioner i with neighbors N_i will remain stationary only while its cost C_i = 0 and the following inequality is satisfied:

$$\min\{j \in N_i \mid D_{ij}\} > 2\sigma_{\mathrm{cb}} + 3\mathrm{MD} \tag{3.10}$$

This provides a similar constraint to the minimum approach distance outlined in Equation 3.6, but is sensitive over a slightly longer distance. This will cause any robot currently at rest at its destination to be kicked awake by any neighboring robot entering its horizon.

3.3.2 The Greedy Choice Algorithm

The GC algorithm is a stepwise process. At each iteration, each robot i in a grid of G is visited in turn and presented with a set of nine options from which to select its next state. The options consist of the combination of $\{-\Delta\theta, 0, \Delta\theta\}$ perturbations applied to the current alpha and beta coordinates $\vec{\boldsymbol{\theta}}_i^{\mathrm{C}}$. Perturbations are modified if limits of travel are violated or destination coordinates are overshot. The robot will choose the option that both (1) minimizes its cost (Equation 3.8), and (2) satisfies the minimum approach criterion (Equation 3.6). The routine terminates when either (1) all robots have reached their destination coordinates ($\sum_{i \in G} C_i = 0$) or (2) the max iteration limit is reached.

3.3.3 The Markov Chain Algorithm

The MC algorithm is an extension of the GC algorithm. In contrast to the GC algorithm, the MC algorithm selects subsequent states probabilistically rather than greedily, where the level of stochasticity is controlled by the greed parameter. Additionally, we construct a control policy that jointly minimizes both the cost and energy metrics, where relative weighting between cost and energy is controlled by the phobia parameter. Greed, phobia, cost, and energy are described in Section 3.3.1.

At each program step a positioner must first select whether or not to consider a move. If the positioner is at its destination coordinates and the inequality in Equation 3.10 is satisfied, it will remain stationary until the next program step, otherwise it will consider a move.

If a positioner considers a move, it must next choose a metric to minimize: either cost or energy. The probability of selecting the energy metric is equal to the phobia parameter. With a metric selected, a positioner will visit each of the nine next-state candidates in a random order,

where these options are the combinations of $\{-\Delta\theta, 0, \Delta\theta\}$ perturbations applied to the current alpha and beta coordinates. Perturbations are modified if limits of travel are violated or destination coordinates are overshot. As each state is visited, a positioner will choose to accept or reject the proposed state. A positioner accepts the proposed state with a probability equal to the greed parameter if the following two criteria are met: (1) this state represents the minimum value of the selected metric seen at this step (by measure of Equation 3.8 or 3.9), and (2) this state satisfies the minimum approach criterion (Equation 3.6). If no state is selected, it defaults to remain in its current state until the next program step.

The routine terminates when either (1) all robots have reached their destination coordinates ($\sum_{i \in G} C_i = 0$) or (2) the max iteration limit is reached.

The GC algorithm represents perhaps the simplest possible control law in the framework we have described. The MC algorithm extends upon the GC algorithm through the inclusion of two additional features: (1) the injection of stochasticity in a robot's decision making process, and (2) a mechanism for robots to sense and avoid crowded spaces. The greed and phobia parameters provide a tuning knob for these MC features. When greed approaches 1 and phobia approaches 0, the MC algorithm becomes identical to the GC algorithm. In the analysis that follows, we fix greed and phobia parameters to 0.9 and 0.3. This choice of MC parameter setting is not necessarily intended to represent an optimal tuning, but rather to provide a point of comparison between the two approaches.

A complete pseudocode implementation for the GC/MC routine is provided in Section A.1.

3.4 Analysis

We begin our analysis using a grid of 19 positioners with σ_{cb} = 3.5 mm. This small, crowded grid will serve to both visualize the algorithm's behavior, and motivate a reverse path solve strategy. Further analysis will implement the reverse solve strategy in large grids, comparing behavior between the GC and MC algorithms at various parameter settings and grid sizes. We largely focus on

547 positioner grids, as this matches the size of SDSS-V FPS layout[3].

SDSS-V's `kaiju`[4] package is an open source Python-wrapped C++ package implementing the collision avoidance algorithms. The results we present here were obtained using the `kaiju` package (tag 0.5.0) compiled with clang++ (version 10.0.1) using an -O3 optimization flag running in a single thread on a 2.9 GHz Intel Core i9 CPU.

3.4.1 Motivating the Reverse Solver

The performance of the GC and MC algorithms can be highly dependent on direction of solved motion. Consider two array configuration states between which we want find collision-less paths for all robots. The first state $\vec{\boldsymbol{\theta}}_i^{\mathrm{F}} = (0^{\mathrm{o}}, 180^{\mathrm{o}})$ represents a "folded" state in which all robot arms are retracted and aligned in a lattice-like orientation. The second state is a randomized source coordinate configuration $\vec{\boldsymbol{\theta}}_i^{\mathrm{S}}$ which approximates an orientation of RFPs positioned to receive light from astronomical sources in a field. When solving the **forward** path from initial coordinates $\vec{\boldsymbol{\theta}}^{\mathrm{F}}$ to destination coordinates $\vec{\boldsymbol{\theta}}^{\mathrm{S}}$ a vast number of positioners will deadlock and never their destination. However, if we swap the initial and destination coordinates and solve the **reverse** path $\vec{\boldsymbol{\theta}}^{\mathrm{S}} \rightarrow \vec{\boldsymbol{\theta}}^{\mathrm{F}}$, we find our routines yield near-perfect convergence of robots to their desired destinations.

To demonstrate the forward and reverse solutions we use the GC algorithm, a 19 positioner grid, and a step size $\Delta_\theta = 0.5$ deg. We set $\sigma_{\mathrm{cb}} = 3.5$ mm to simulate an abnormally large level interference between positioners. Non-colliding source coordinates for each positioner are selected randomly from their respective patrol zones. Initial coordinates are set such that the robots begin their journey from a folded position, $\vec{\boldsymbol{\theta}}_i^{\mathrm{I}} = \vec{\boldsymbol{\theta}}_i^{\mathrm{F}}$. Destination coordinates are set to be the source coordinates $\vec{\boldsymbol{\theta}}_i^{\mathrm{D}} = \vec{\boldsymbol{\theta}}_i^{\mathrm{S}}$.

Figure 3.6 shows three snapshots in robot-travel time when forward motion is propagated according to the GC algorithm. The first panel shows the initial folded state of the positioners, the second panel shows an intermediate state in the routine, and the third panel shows the final state.

[3] As described in Section 1.2, the FPS will carry only 500 robots. For simulations here we elect to fill every available spot with a positioner.

[4] https://github.com/sdss/kaiju

Stars indicate the source coordinate locations, circles indicate the fiber position at the end of the beta arm. When the fiber is aligned with the source, the positioner has reached its destination. Robots at their destination are colored tan, robots in motion are colored blue. Curved streaks drawn behind the fiber indicate the path the fiber has followed through previous program steps.

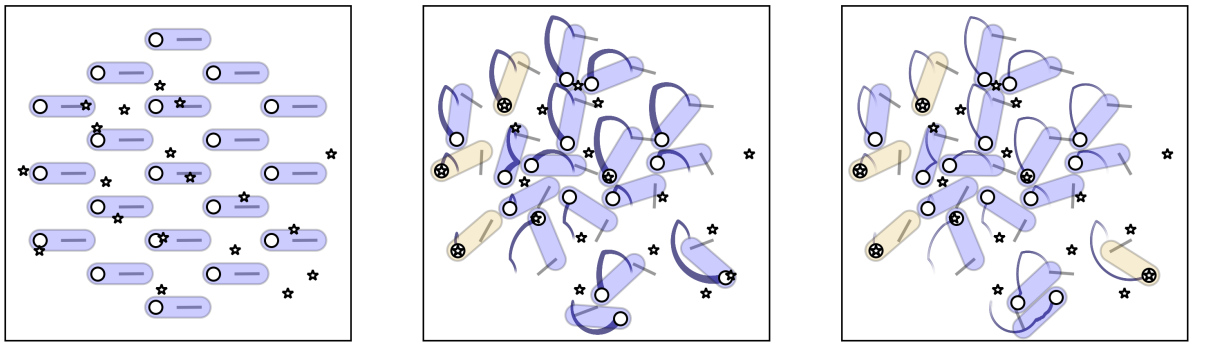

starting configuration | 7 seconds of motion | 33 seconds of motion (max step limit)

Figure 3.6 – A 19 positioner grid solved with the GC algorithm in the **forward** direction using $\Delta_\theta = 0.5$ deg. We set $\sigma_{\rm cb} = 3.5$ mm to simulate an environment more crowded than SDSS-V, which increases the optimization challenge. Panels from left to right show the starting configuration, an intermediate state of motion, and the final state. Stars indicate source coordinates and open circles indicate the fiber. When a star aligns with its fiber, the robot has reached its destination, and is colored tan. Streaks behind the fibers indicate the path followed by a fiber through previous program steps. In this example, the maximum step limit is hit with only 4 positioners reaching their destination (right panel), the remainder of positioners are in deadlock.

In this example, only 4 of 19 positioners arrive at their destination before the routine's iteration limit is reached. The remaining positioners are in a deadlocked state where all progress is halted due to inability of robots to navigate beyond their collective blockade.

The next demonstration uses identical configurations to those of the previous example with the following modification: initial coordinates are set to the source coordinates $\vec{\boldsymbol{\theta}}_i^{\rm I} = \vec{\boldsymbol{\theta}}_i^{\rm S}$, and destination coordinates are set to the folded configuration $\vec{\boldsymbol{\theta}}_i^{\rm D} = \vec{\boldsymbol{\theta}}_i^{\rm F}$. When solved with the GC algorithm, robots will begin from a source coordinate orientation, and carve out paths toward a folded configuration. In this case we are solving exactly the same problem as the previous example (a path between a folded and source orientation), by simply reversing the direction of robot-arm

propagation.

Figure 3.7 shows the results of the reverse GC solve, an analogous sequence to that presented in Figure 3.6. Positioners begin aligned with source coordinates, and step toward a folded destination. In this experiment we find that all positioners successfully navigate to their destinations after 12 seconds of motion. This result is striking when contrasted with the forward example in which only a small subset of positioners were able to obtain their desired destination. This pair of examples demonstrates that the reverse path strategy is a surprisingly good approach.

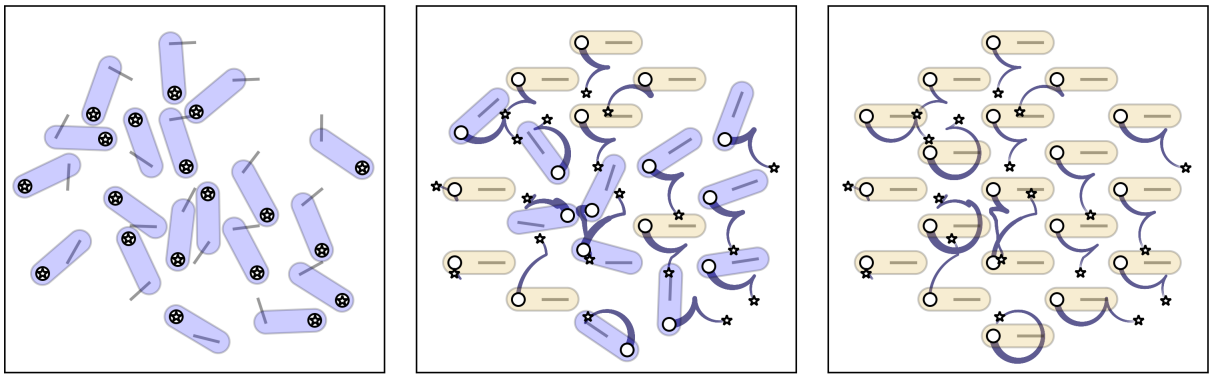

Figure 3.7 – A **reverse** direction GC solution to the configuration presented in Figure 3.6. The initial state of the routine is set to the source coordinate configuration (left panel) in which all fibers are aligned with astronomical targets. The program steps toward a folded destination (right panel). Here all 19 positioners successfully navigate to the folded destination in 12 seconds of motion. A forward path may be obtained by reflecting the reversely solved path in time, providing a route for positioners to go out and back from a folded state when visiting this field of science targets.

The irreversible behavior of the algorithm raises eyebrows (the author's included), yet it provides unique leverage in solving our path routing problem. Consider the two following points. First, paths are trivially reversible. If a reverse path solution is found, we can obtain a forward path solution by simply reflecting trajectories of all robots. Second, by building all paths between any source coordinate state and a common folded state, transitioning between any two source coordinate states is also trivial given that reconfigurations always route through the folded state.

The reverse path approach was discovered serendipitously through experimentation, and moti-

vated by the following thought experiment: is it easier to tie a complex knot, or untie a complex knot? Presumably the latter task is easier, and if one carefully recorded the steps taken while performing the latter task, then the reversal of those steps yields a solution to the former task. Regrettably, we do not currently have a theoretical justification as to why the reverse process works so well in the context of our problem, though we find the behavior interesting and provide some further discussion in Section 3.6. In further sections we rely on statistics gathered from large numbers of simulations to gain confidence in the quality of our solutions.

3.4.2 Measuring Efficiency with Source Coordinate Replacement

Here we formulate a statistical measure of algorithmic efficiency for the layout described in Section 3.4.1. We repeat GC forward/backward pair analysis in a set of 5000 trials, where source coordinates are randomized between trials. Figure 3.8 shows the resulting histogram of positioner deadlock frequencies for both strategies. The forward strategy will always result in deadlock that typically involves half of the positioners, whereas the reverse strategy only rarely suffers a deadlock. In these rare cases of reverse path deadlock, only a few positioners are involved. The chance of deadlock in the reverse solution is small, but non-negligible.

For the reverse solution to be viable, we require a deadlock-free path for every positioner in the grid. The full reconfiguration sequence from source coordinates A to subsequent source coordinates B requires two steps: (step 1) the array moves from A to an intermediate folded state, then (step 2) the array moves from the folded state to B. If any single positioner deadlocks during reverse path generation, the array has not made it to the transition state, and thus the set of paths cannot be used. Having a strategy for eliminating deadlocks is a necessary feature for the reverse path solver.

We adopt a brute-force method of deadlock resolution. If a grid is deadlocked, we randomly select a single deadlocked robot, replace its source coordinates, and re-run the path generator. Replacing a source coordinate results in the loss of the original astronomical source. In large grids of positioners, deadlocks are typically isolated in small groups throughout the array. For these cases we may simultaneously replace one robot from each deadlocked group, which minimizes the

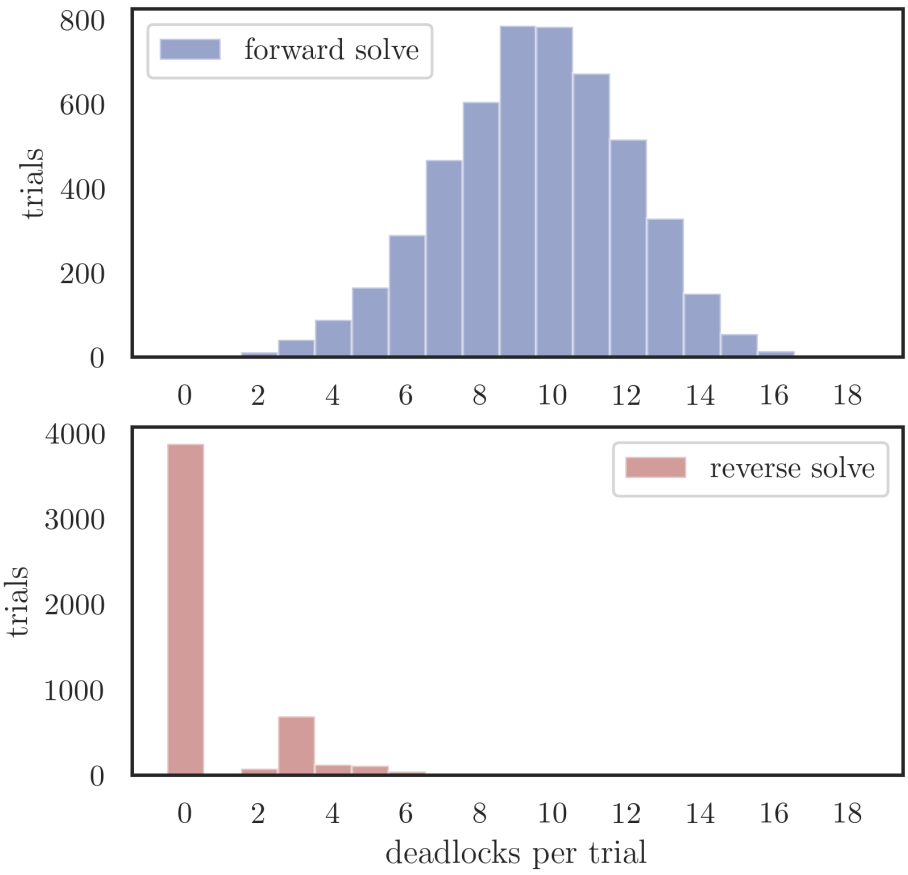

Figure 3.8 – Histograms comparing deadlock frequencies between the forward and reverse solve methods for abnormally crowded grids. Histograms are generated from 5000 trials using the GC algorithm, a 19 positioner grid, $\sigma_{\text{cb}} = 3.5$ mm, and $\Delta_\theta = 0.5$ deg. Essentially we have repeated the trajectory comparisons between Figures 3.6 and 3.7 with source coordinates randomized between trials. In forward solutions (upper panel), every trial experienced a deadlock, and the typical deadlock involved many positioners. For reverse solutions (lower panel), the large majority of trials suffered no deadlock, and those that did typically involved only a few positioners. From this example, the reverse path solution is well motivated.

number of iterations required of the path generator, and improves the total runtime.

This brute force replacement strategy is illustrated in Figure 3.9. The top three panels show a sequence of reverse-solved motion that results in a four positioner deadlock. The lower three panels show the results obtained after replacing a single positioner's source coordinates to a new random position. The array now completely converges to a folded orientation in 12 seconds of

motion, thus resolving four wedged robots with a single replacement.

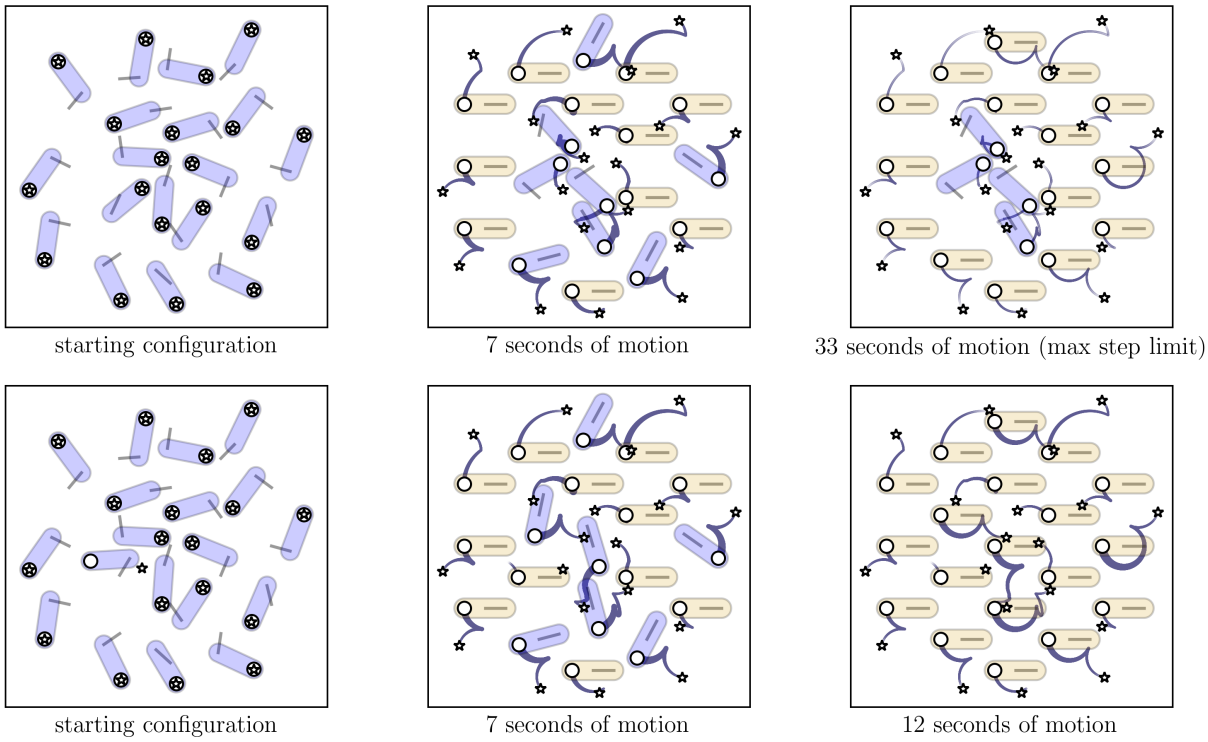

Figure 3.9 – We illustrate a brute force method for deadlock resolution using the GC algorithm, a 19 positioner grid, $\sigma_{\text{cb}} = 3.5$ mm, and $\Delta_\theta = 0.5$ deg. The top three panels show an example sequence of reversely solved motion that results in a 4 positioner deadlock. The bottom three panels show an analogous sequence after a single positioner's initial coordinates have been replaced. The bottom sequence converges in 12 seconds of motion at the loss of a single astronomical target. Arriving at a fully converging grid is necessary to deploy a reverse path generator, and thus our procedure requires an iterative search for viable initial conditions when a deadlock is present. When deadlocks are infrequent, this introduces small computational overhead.

We define an efficiency for the reverse GC and MC algorithms in terms of the required number of replacements to solve a grid. For a grid with total number of positioners n_G requiring source coordinate replacements for a subset of positioners n_R, the efficiency is:

$$\text{efficiency} = \frac{n_G - n_R}{n_G} \tag{3.11}$$

Note that we count n_R as number of robots requiring a source coordinate replacement. If a

single robot is iteratively tried with multiple sets of source coordinates, we count this as a single replacement. This measure of efficiency is the ratio of astronomical targets obtained to astronomical targets assigned. For the example shown in Figure 3.9, the efficiency is $(19-1)/19 \sim 0.95$.

In our trials we generally (but not necessarily) find that the efficiency is higher than the initial convergence of the grid, where we call convergence the ratio of positioners achieving the destination to the total number of positioners in the grid. In the case shown in Figure 3.9, the initial convergence (top panel sequence) is $(19-4)/19 \sim 0.79$. The increased efficiency with respect to convergence is due to the fact that a single replacement will often resolve more than one deadlock. We use efficiency (rather than convergence) to measure algorithmic performance as it is a more relevant statistic in the context of astronomical surveys.

3.4.3 Efficiency vs. Crowding

In a cocktail party setting, navigation becomes more challenging as the free space in the room shrinks. The σ_{cb} parameter is a proxy for either beta arm relative size or collision safety distance, and as σ_{cb} increases, available space for motion in the grid decreases. Here we investigate the path routing performance of the reverse-solve GC and MC algorithms for a range of σ_{cb} values between 1.5 and 3.5 mm to simulate varied levels of crowding.

We use a grid of 547 positioners and set a step size $\Delta_\theta = 0.1$ deg. This step size limits robot arm perturbations (Equation 3.7) to less than 100 microns at each iteration. We run 2000 trials at each σ_{cb} for each algorithm, amounting to 36000 trials in total. Initial coordinate assignments are randomized in all trials. We assign folded destination coordinates $\vec{\boldsymbol{\theta}}^{\text{D}} = (10^{\text{o}}, 170^{\text{o}})$ for all positioners. These destination coordinates leave the positioners with $\pm 10^{\text{o}}$ of free travel in both alpha and beta axes when they arrive at their destination. This choice of parking spot benefits the MC algorithm, in which positioners at rest may be kicked awake when a neighbor encroaches (Equation 3.10), allowing for a larger set of evasive options in these situations. The parameter settings for this experiment are summarized in Table 3.1.

Figure 3.10 shows the trend of trial-averaged efficiency versus σ_{cb} for the MC and GC algorithms. The GC algorithm maintains a mean efficiency greater than 0.998 for $\sigma_{\text{cb}} < 2$ mm, the

Table 3.1 – . Simulation 1 - varied crowding.

Parameter	Values
n robots	547
n trials [a]	36000
l_α (mm)	7.4
l_β (mm)	15
$\vec{\theta}^{\mathrm{I}}$ (deg)	random, right-armed
$\vec{\theta}^{\mathrm{D}}$ (deg)	(10,170)
pitch (mm)	$l_\alpha + l_\beta = 22.4$
Δ_θ (deg)	0.1
max steps	$1000^{\mathrm{o}}/\Delta_\theta$
σ_{cb} (mm)	$\{1.5, 1.75, 2, 2.25, 2.5, 2.75, 3, 3.25, 3.5\}$
greed	0.9
phobia	0.3
algorithm	$\{\mathrm{GC}, \mathrm{MC}\}$

[a]trials split evenly amongst the varied σ_{cb} settings and algorithm type

MC algorithm maintains a mean efficiency is greater than 0.998 for $\sigma_{\mathrm{cb}} < 3$ mm. An efficiency of 0.998 corresponds to a single replacement in a grid of 547 positioners. With either routine only a fraction of a percent of astronomical targets will be lost in the small σ_{cb} regimes.

The MC algorithm outperforms the GC algorithm in terms of efficiency at all σ_{cb} values. For both algorithms, efficiency declines monotonically with σ_{cb}. Under the highest crowding conditions ($\sigma_{\mathrm{cb}} = 3.5$ mm) mean efficiencies of 0.993 and 0.968 are measured for the MC and GC algorithms. In an environment three times more crowded than the SDSS-V FPS design, we are limiting source replacement to less than a percent using the MC algorithm. This result suggests that very crowded RFP arrays may be feasible from a collision avoidance standpoint.

Figure 3.11 shows the minimum observed efficiency as a function of algorithm and σ_{cb} in the set of 36,000 trials. The trends are similar for both algorithms. For $\sigma_{\mathrm{cb}} \leq 2$ mm, minimum efficiency remains above 0.98, beyond $\sigma_{\mathrm{cb}} = 2$ mm, minimum efficiency trends steadily downward. For the largest σ_{cb}, we see minimum efficiencies around 0.92 for the GC algorithm and 0.97 for the MC

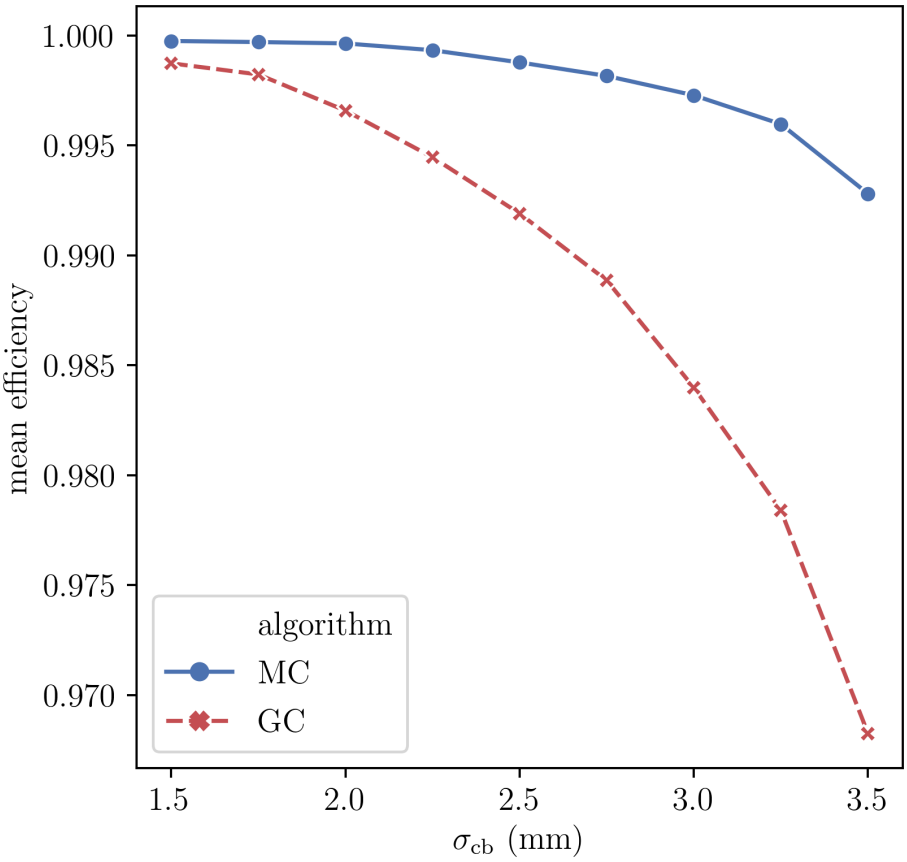

Figure 3.10 – Mean efficiency for MC (blue solid line) and GC (red dashed line) resulting from the suite of trials described in Table 3.1. GC mean efficiency is > 0.998 for $\sigma_{cb} < 2$ mm. MC mean efficiency is > 0.998 for $\sigma_{cb} < 3$ mm. The MC algorithm outperforms the GC algorithm over the full range of σ_{cb}. Both algorithms see monotonic decreases in efficiency as the level of crowding increases. An efficiency of 0.998 corresponds to a single source coordinate replacement in a grid of 547 positioners.

algorithm.

Figure 3.12 presents box plots of measured efficiencies for the MC (upper panel) and GC (lower panel) algorithms across trials. Boxes indicate the innerquartile range, and whiskers capture data within 3/2 the inner quartile range below and above the low and high quartiles. Outliers are plotted as diamonds. Generally the variance of efficiency increases with increasing σ_{cb}. This figure indicates a median target loss on the sub-percent level for the MC algorithm over the full range of

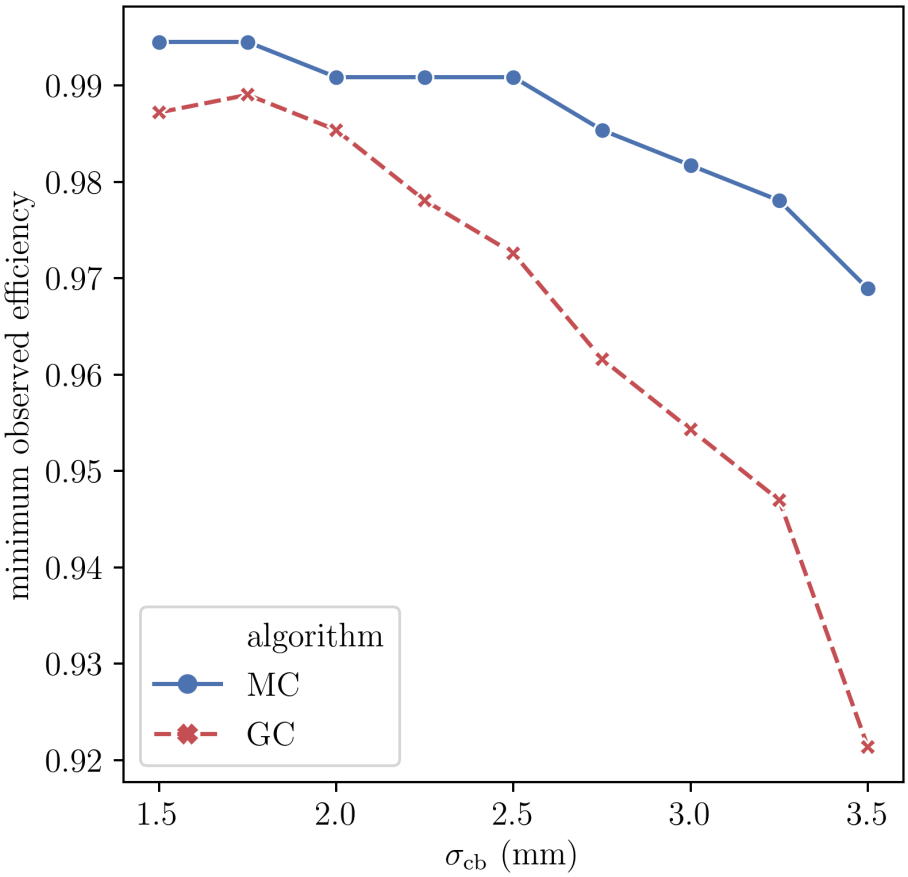

Figure 3.11 – Lowest observed efficiencies for MC (blue solid line) and GC (red dashed line) seen in the suite of 36,000 trials described in Table 3.1. For $\sigma_{cb} \leq 2$ mm, the minimum observed efficiency is > 0.98. For $\sigma_{cb} > 2$ mm, the minimum seen efficiency steadily drops, reaching a minimum around 0.92 for the GC algorithm and 0.97 for the MC algorithm.

σ_{cb} investigated. Sub-percent target loss for the GC algorithm is typical when $\sigma_{cb} < 2.5$ mm.

3.4.4 Reconfiguration Time

Reconfiguration times for RFP arrays are usually measured in seconds. However, when integrated over years of a survey, these seconds add up to significant hours of observational overheads. Here we analyze the reconfiguration times from the simulation suite described in Table 3.1 using SDSS-V positioner velocities. In this section we measure "fold time", which is the time required to

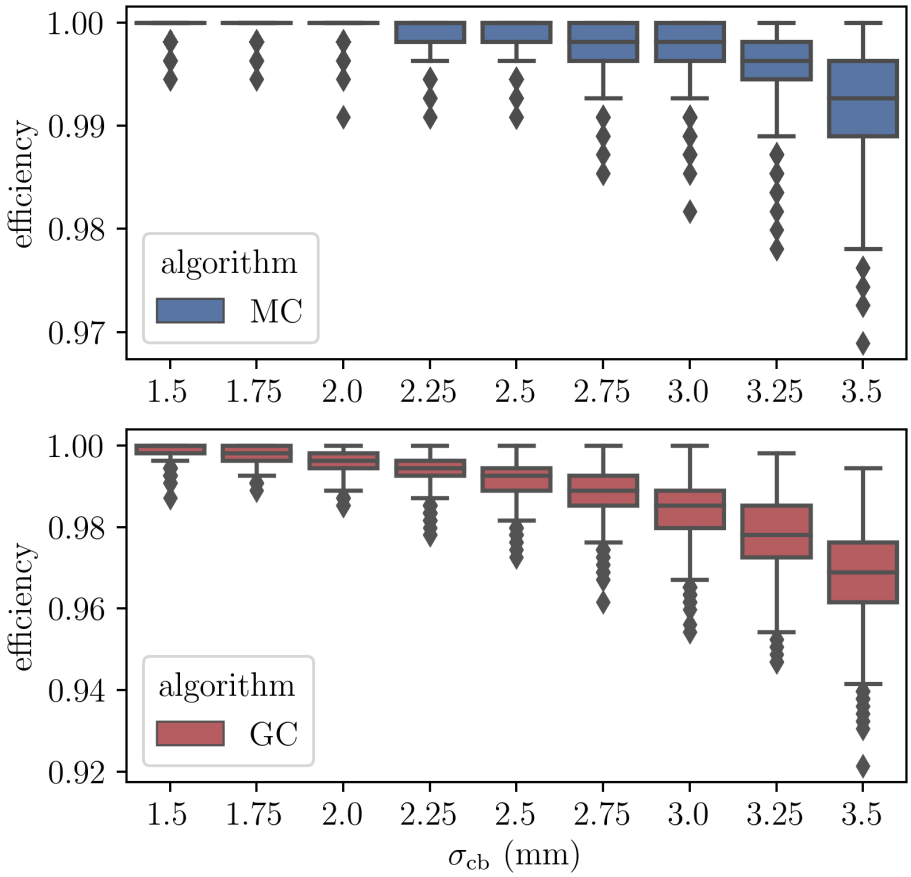

Figure 3.12 – Box plots of the underlying efficiency distributions for the MC (top panel) and GC (bottom panel) algorithms from the suite of trials described in Table 3.1. Boxes capture the innerquartile range, and whiskers capture the data lying within 3/2 of the innerquartile range below and above the low and high quartiles. Points lying outside the whiskers are marked as diamonds. With the MC algorithm, target loss will be limited to a small fraction of a percent over the whole σ_{cb} range. Even in the most crowded regime, the MC algorithm will see a only a small target loss percentage of $\sim$1%. The GC algorithm limits target loss 1% for the lower half of σ_{cb} values investigated.

move between a source (or astronomical target) orientation to a folded state. The total field-to-field reconfiguration time is twice this value, as the positioner array must move first to the folded state before moving to the next desired orientation.

Figure 3.13 shows the mean fold time as a function of σ_{cb} and algorithm. The GC outperforms the MC algorithm by a factor of $\sim$2, depending slightly on σ_{cb}. The longer path lengths observed in

the MC algorithm are due to two effects: (1) the injection of random motion along its path, tuned by the greed parameter, and (2) the additional policy of E_i (energy) minimization, tuned by the phobia parameter. Recall that, as greed approaches 1 and phobia approaches 0, the MC algorithm becomes identical to the GC algorithm. In this sense the fold time curve for the GC algorithm in Figure 3.13 represents a lower bound for the MC algorithm. By varying greed and phobia, one might tune the MC algorithm to produce an optimal balance between efficiency and fold time in the context of an astronomical survey. Here we have fixed greed and phobia to 0.9 and 0.3 to provide a point comparison between the two methods.

Figure 3.14 shows box plots for fold time across $\sigma_{\rm cb}$ and between algorithms. Boxes indicate the innerquartile range, and whiskers capture data within 3/2 the inner quartile range below and above the low and high quartiles. Data falling outside whiskers are indicated with diamonds. For the GC algorithm we see median reconfiguration times less than 30 seconds for SDSS-V positioners across the full range of $\sigma_{\rm cb}$. For the MC algorithm, we expect reconfiguration times closer to 45 seconds for the lower half of $\sigma_{\rm cb}$ values, and reconfiguration times nearing a minute for the upper half of the $\sigma_{\rm cb}$ value range. The GC algorithm generally achieves the SDSS-V benchmark goal of a 30 second RFP reconfiguration time, whereas the MC would require greed and phobia parameter adjustments to reach this benchmark.

3.4.5 Runtime and Efficiency vs. Step Size

Navigating through a moving crowd is more effective when one takes small steps in the right direction, rather than waiting for the opportunity of a big step to present itself. This analogy holds true for the algorithms we've presented. However, a small step comes at the price of an extended runtime.

A fast running routine is desirable for at least two reasons. A fast path generator allows for dynamic decision making throughout a night's observations, as optimal plans are subject to change on short notice. Another benefit of a fast path generator is that it may be incorporated in the optimization stages of survey planning and design. In a large astronomical survey, field assignment for millions of objects is a computationally intensive task, so if path verification is required at

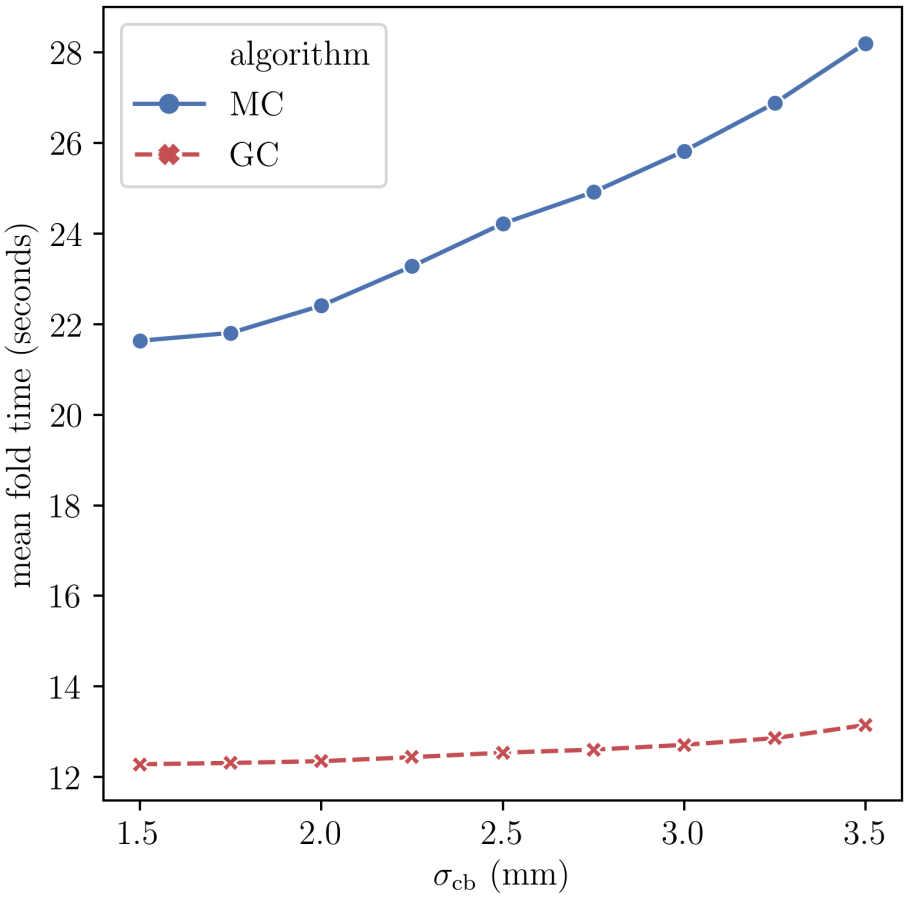

Figure 3.13 – Average time for an SDSS-V robot array to transition between a folded state and a source coordinate (on-target) state, representing half the time of a complete reconfiguration. Results are compiled from the trials described in Table 3.1 for MC (blue solid line) and GC (red dashed line) algorithms. The GC algorithm yields a total reconfiguration time less than 30 seconds. The MC algorithm experiences longer reconfiguration durations due to the injection of stochastic motion along a robot's trajectory. The amount of stochasticity is tunable, and thus the GC fold time curve represents a lower bound for the MC method dependent on parameter tuning.

this stage it must have a low computational overhead. Carrying out path planning during field assignment is desirable as it will inform which specific targets ultimately get observed, providing an opportunity for vetting long before a field is visited by the telescope.

We measure two distinct runtimes in our routines. The first runtime is the source replacement runtime τ_{sr}. This is the computation time accumulated during the source replacement procedure

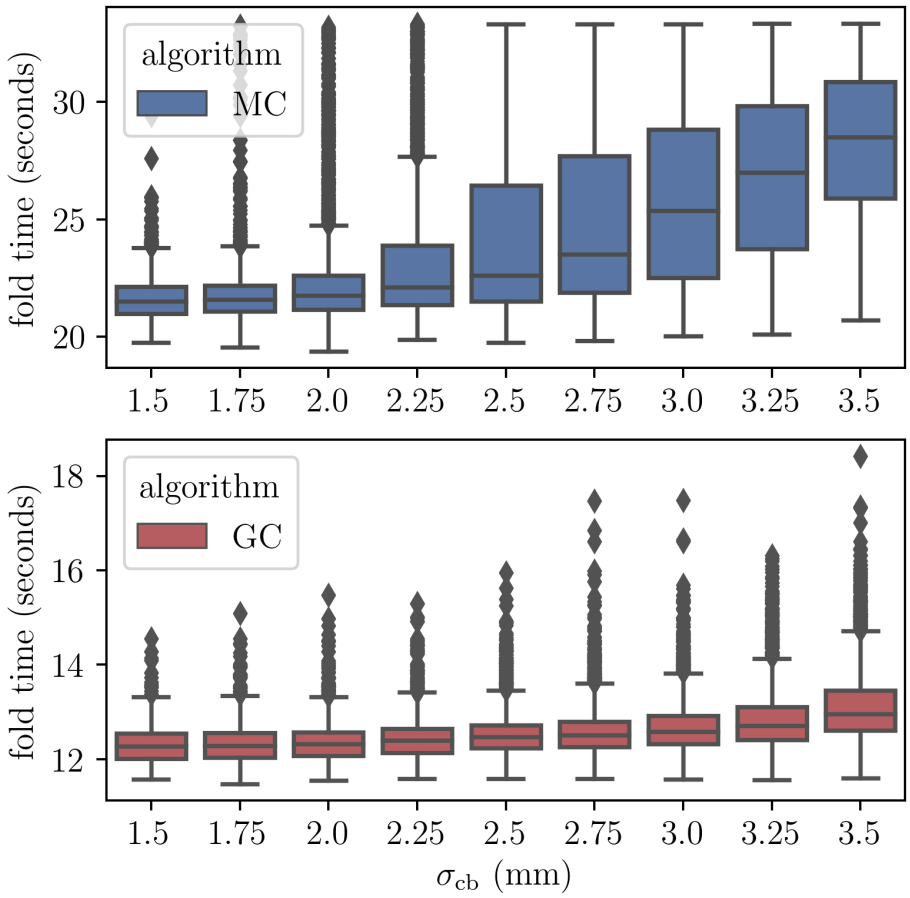

Figure 3.14 – Box plots for the distribution of fold times seen across the σ_{cb} range for the trials described in Table 3.1. Boxes capture the innerquartile range, and whiskers capture the data lying within 3/2 the inner quartile range below and above the low and high quartiles. Data outside whiskers are plotted as diamonds. The MC algorithm yields longer median fold times with a higher level of variance when compared to the GC algorithm.

described in Section 3.4.2. The source replacement procedure requires iterative runs of the path generator to find valid initial coordinates. τ_{sr} is largely an overhead during target assignment, as once initial coordinates have been assigned, and paths shown to converge, they do not need to be recomputed.

The second runtime τ_{pg} is the computational time required to build paths from a set of initial coordinates that are known to converge. Observing conditions during nightly operations may re-

Table 3.2 – . Simulation 2 - vaired crowding and step size.

Parameter	Values
n robots	547
n trials[a]	18000
l_α (mm)	7.4
l_β (mm)	15
$\vec{\boldsymbol{\theta}}^{\mathrm{I}}$ (deg)	random, right-armed
$\vec{\boldsymbol{\theta}}^{\mathrm{D}}$ (deg)	(10,170)
pitch (mm)	$\mathrm{l}_\alpha + \mathrm{l}_\beta = 22.4$ mm
Δ_θ (deg)	$\{0.05, 0.1, 0.25, 0.5, 0.75, 1\}$
max steps	$1000^{\mathrm{o}}/\Delta_\theta$
σ_{cb} (mm)	$\{1.5, 2, 2.5, 3, 3.5\}$
greed	0.9
phobia	0.3
algorithm	$\{\mathrm{GC}, \mathrm{MC}\}$

[a]trials split evenly amongst the varied σ_{cb}, Δ_θ, and algorithm

quire that RFP trajectories remain flexible on short notice. For example, the airmass of observation may require slight adjustments to a precomputed set of initial coordinates. Or perhaps a robot malfunctions and must be taken off-line during the night while remaining in a position that obstructs neighbors. In cases where we envision small adjustments to initial coordinates, we expect the overall runtime of path generation to be much closer to τ_{pg} than τ_{sr}.

For this experiment we vary Δ_θ, σ_{cb}, and algorithm. We run 300 trials at each unique parameter combination, yielding a total of 18000 trials. An analysis of the resulting trends informs a smart decision on step size: a value that produces a reasonable balance between efficiency and runtime. The parameters for this simulation are listed in Table 3.2.

Figure 3.15 shows the effects of Δ_θ on efficiency for both GC and MC algorithms. Efficiency declines as both Δ_θ and σ_{cb} increase. At small σ_{cb} (1.5-2 mm), there is little variation in efficiency, so large step sizes (0.75-1 deg) seem permissible. However, as σ_{cb} increases, smaller step sizes are required to remain near the high end of efficiency. This is especially true for $\sigma_{\mathrm{cb}} = 3.5$ mm, where

efficiency is strongly influenced by step size. The efficiency degradation with increased step size is due to the maximum displacement (MD) factor entering in Equation 3.6, which defends against moves during which robots may undetectably jump through a colliding orientation in a single step.

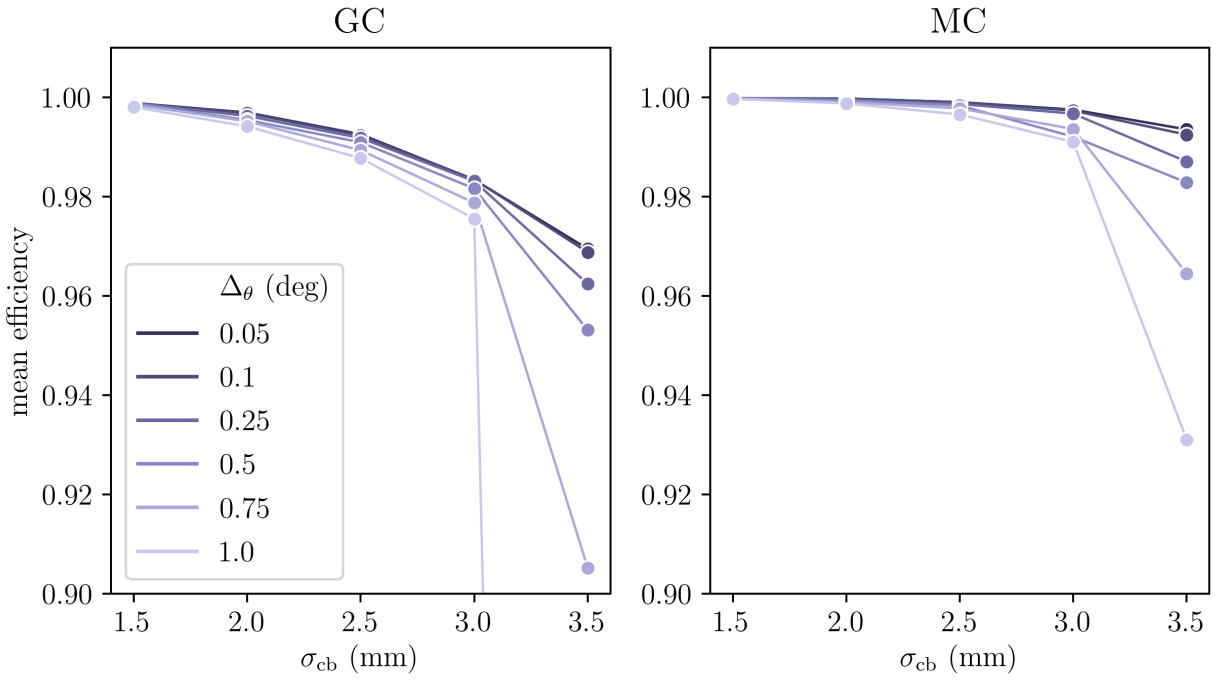

Figure 3.15 – Plots of efficiency for GC (left panel) and MC (right panel) algorithms over a range of crowding (σ_{cb}) and step size (Δ_θ) settings, averaged across trials from the simulation set described in Table 3.2. Efficiency declines as step size is increased. The combination of large step size and high crowding shows drastic reductions in efficiency. In low crowding environments, choice of step size has only a minor effect on overall efficiency. This figure ultimately illustrates the trade off between runtime and efficiency, as larger step sizes are preferable from a program runtime perspective.

Figure 3.16 presents the average observed runtimes across σ_{cb}, Δ_θ, and algorithm. Here we only consider results for which the trial-averaged efficiency is greater than 0.9. The two left hand panels show the average runtime τ_{pg}. Over the full range of Δ_θ, the runtime decreases exponentially, ranging between $\sim 1 - 25$ seconds for the GC algorithm. The MC algorithm runtime requires roughly twice the runtime of the GC algorithm, with a slight dependence on σ_{cb}. The right hand panels of Figure 3.16 show the average runtime τ_{sr}, which includes iterative process of source

coordinate replacement (Section 3.4.2). When including the source replacement procedure, the runtime scales by roughly an order of magnitude over the full range of σ_{cb}. This scaling is largely due to the decrease in overall efficiency as σ_{cb} increases. As σ_{cb} increases, the chance of deadlock increases, and so the required number of iterations of the path generator increase.

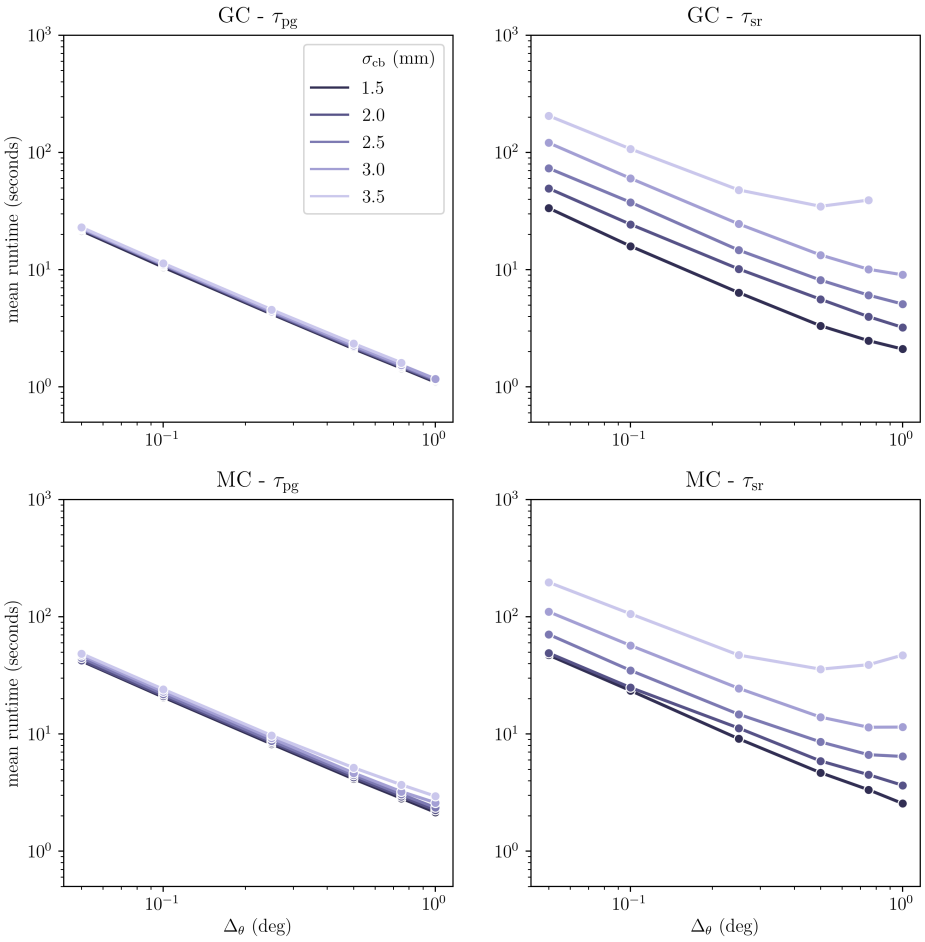

Figure 3.16 – Mean runtimes from the Table 3.2 simulation set. Only results where mean efficiency > 0.9 are included. The left two panels show the mean runtime for a single converging run of the path generator (τ_{pg}). For the GC algorithm, a step size of 1 deg requires $\sim$1 second to compute paths for a grid of 547 positioners, a step size of 0.05 requires $\sim$20 seconds. The MC algorithm requires roughly twice the runtime of the GC algorithm and exhibits a slight dependence on crowding. The right two panels show the cumulative runtime τ_{sr} which includes the iterative procedure of source coordinate replacement. τ_{sr} is strongly influenced by crowding.

Table 3.3 – . Selected Results from Simulation 2

algorithm	$\sigma_{\rm cb}$ (mm)	Δ_θ (deg)	mean $\tau_{\rm pg}$ (sec)[a]	$\tau_{\rm sr}$ (sec)[b]	mean fold time (sec)[c]	mean efficiency
GC	1.50	1.00	1.10	2.10	12.32	0.9980
GC	2.50	0.25	4.34	14.67	12.55	0.9918
GC	3.50	0.10	11.32	107.11	13.17	0.9688
MC	1.50	1.00	2.14	2.55	22.94	0.9997
MC	2.50	0.25	8.74	14.71	24.29	0.9987
MC	3.50	0.10	24.04	105.82	27.90	0.9925

[a]runtime of single path generator pass

[b]runtime of multiple path generator pass with source replacement

[c]half of the expected duration of robot motion during reconfiguration

The trends indicated in Figures 3.16 and 3.15 provide the information we need to select decent Δ_θ settings for each algorithm over a range of $\sigma_{\rm cb}$. Table 3.3 contains a summary of results for each algorithm under some reasonable parameter choices. The table contains runtime, fold time, and efficiency metrics over the full range of $\sigma_{\rm cb}$, providing a concise summary of the performance of the algorithms we have tested over a range of parameter space.

In nightly operations, SDSS-V FPS path computations $\tau_{\rm pg}$ will typically require only few seconds, even when choosing a conservative $\sigma_{\rm cb} = 2.5$ mm. Should a sudden RFP reconfiguration be desired, the overhead due to path planning computations will be negligible when compared to the duration of robot motion. The computational speed of these algorithms provides SDSS-V with a nimble observing system that suffers almost no additional overhead when unscheduled reconfigurations are requested at a moment's notice.

3.4.6 Runtime and Efficiency vs. Grid Size

In this section we provide a brief analysis of how algorithmic performance scales with number of positioners. We use relatively few trials (6000), and choose a mid-range crowding level of $\sigma_{\rm cb} = 2.5$ mm. The complete set of simulation parameters are described in Table 3.4. The results

Table 3.4 – . Simulation 3 - varied grid size.

Parameter	Values
n robots	$\{37, 91, 169, ..., 2269, 2611, 2977\}$
n trials [a]	6000
l_α (mm)	7.4
l_β (mm)	15
$\vec{\boldsymbol{\theta}}^{\mathrm{I}}$ (deg)	random, right-armed
$\vec{\boldsymbol{\theta}}^{\mathrm{D}}$ (deg)	(10,170)
pitch (mm)	$l_\alpha + l_\beta = 22.4$
Δ_θ (deg)	0.1
max steps	$1000^{\mathrm{o}}/\Delta_\theta$
σ_{cb} (mm)	2.5
greed	0.9
phobia	0.3
algorithm	$\{\mathrm{GC}, \mathrm{MC}\}$

[a]trials split evenly amongst the varied grid sizes and algorithm type

here will give a general feel for behavior in grids more massive than the typical 547 robot array we have focused on thus far.

Figure 3.17 plots the mean efficiency against grid size for the simulations described in Table 3.4. The shaded region around each line represents the 95% confidence interval of the mean. For grids larger than the SDSS-V array, the efficiency remains relatively constant. For smaller grids, a direct comparison of efficiency vs grid size should be taken with a grain of salt for two reasons: (1) smaller grids have a larger fraction of positioners without neighbors, and (2) efficiency is computed relative to the total number of positioners in a trial, where smaller grids contain fewer positioners. Despite this, we see that efficiency is not strongly affected by total number of positioners.

Figure 3.18 plots the mean τ_{sr} and τ_{pg} runtimes for each algorithm at various grid sizes for the simulation set described in Table 3.4. For each line in the plot, a 95% confidence interval of the mean is indicated by the shaded region. Runtime τ_{pg} increases linearly with grid size for both MC and GC algorithms, as is typical for distributed control algorithms. Runtime τ_{sr} does not show a

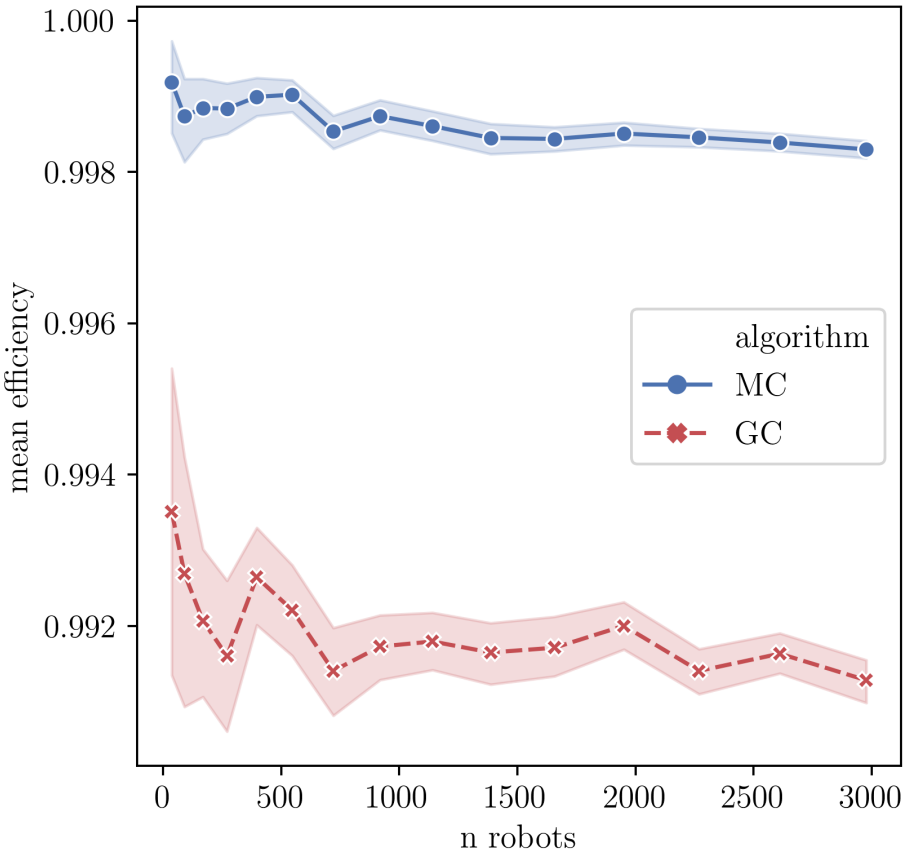

Figure 3.17 – A comparison of mean efficiency between MC and GC algorithms at various grid sizes using the parameters set in Table 3.4. Shaded regions indicate a 95% confidence interval of the mean. Efficiencies for smaller grids are computed from smaller samples of positioners, and thus are more variable than efficiencies measured from large grids. For grids larger than SDSS-V's (> 500 positioners), efficiency is not strongly affected by the total number of positioners in a grid.

tight linear response, as larger grids will experience a higher frequency of deadlock events, and thus require a higher number of source replacement iterations to solve a grid.

3.5 Deployment Considerations

We have made an effort to present generic routines that may be directly applied to many of today's RFP instruments via configurable parameters (pitch, l_α, l_β, σ_{cb}, etc). To remain hardware-agnostic,

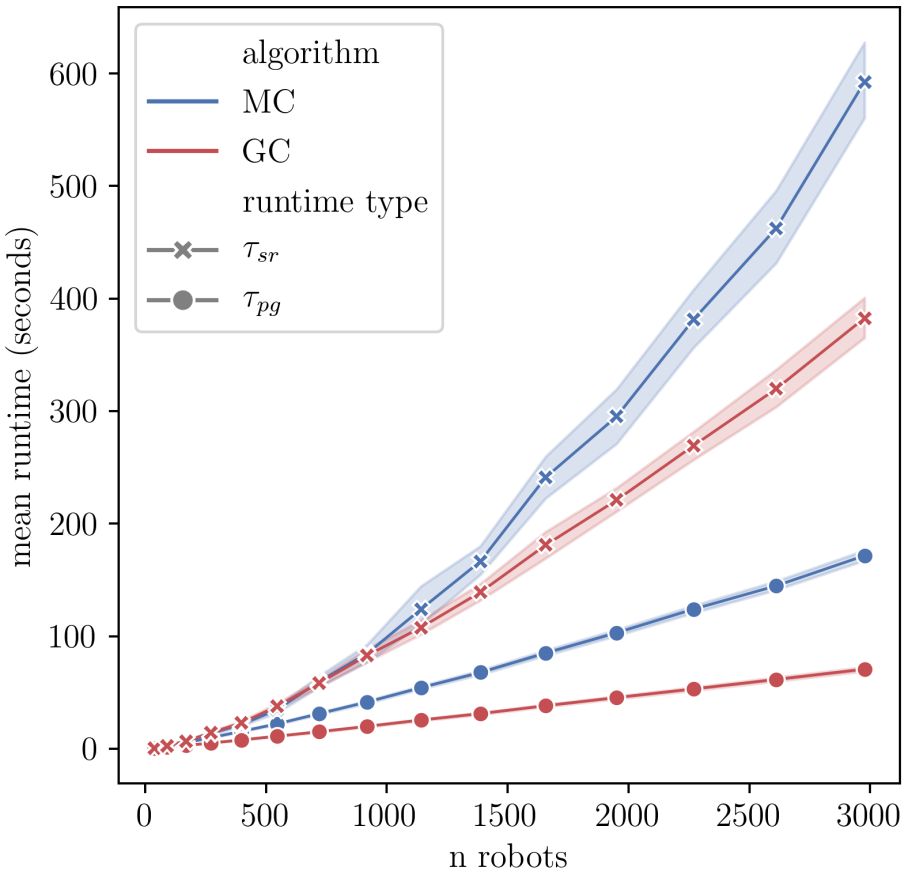

Figure 3.18 – A comparison of mean runtimes between MC and GC algorithms at various grid sizes using the parameters set in Table 3.4. Shaded regions indicate a 95% confidence interval of the mean.

we have inherently assumed grids of "ideal" positioners, where the ideal positioner: (1) possesses infinite acceleration, (2) has sufficient on-board resources to follow an arbitrarily complex path, (3) has no positional uncertainty along a trajectory, and (4) never malfunctions. When deploying the path generator in a realistic setting, points (1)-(4) above need to be considered carefully, and the optimal handling of these constraints may vary from one positioner design to another. This section outlines specific strategies for addressing these issues for SDSS-V positioners, though we suspect they will be relevant for most other positioner designs and interfaces.

First we address points (1) and (2): a path post-processing strategy to account for the accelera-

tion limits and finite on-board memory of an SDSS-V positioner. The raw paths output by `kaiju` intrinsically wiggle: when robot arms encounter each other they switch direction of motion frequently. Applying a running-average filter to the velocity profiles for each axis sufficiently damps these wiggles to adhere to the acceleration limits of the hardware. SDSS-V positioners accept a maximum of 1024 points per alpha or beta axis to define a trajectory, where a point is described by an (angle, time) tuple. The embedded program of the SDSS-V positioner linearly interpolates between the supplied points. We simplify the velocity-smoothed paths using the Ramer-Douglas-Peucker algorithm (Ramer, 1972), which reduces the total number of points required to describe a path. In the regime of small $\sigma_{\rm cb}$, a significant fraction of positioners are free to simply move at constant velocity to their destination without ever encountering a neighbor. In these situations we find that many paths (especially GC paths with no random motion) are specified by only a handful of points. This can be quickly realized from the left panel of Figure 3.5, where more than a few positioners have enough space to fold without interference. As $\sigma_{\rm cb}$ increases, the probability of interactions increases, and the paths necessarily become more complex. We are generally able to represent the most complex paths in less than 250 points after velocity-smoothing and point-simplification. After a simplified path is computed, `kaiju` is used to verify it (with a slightly reduced $\sigma_{\rm cb}$) to ensure that no collisions were created in the post-processing procedure. As a consequence, path smoothing and simplification will require some amount of the overall $\sigma_{\rm cb}$ budget.

To address point (3) we must choose $\sigma_{\rm cb}$ large enough to account for the uncertainty of a robot's position along a path. The dominant source of positional uncertainty is due to slight imperfections in the manufacture and assembly of a robot's gearbox. This manifests as a nonlinear relationship between a positioner's commanded angular velocity and the true angular velocity, where a positioner's true velocity will oscillate about the expected velocity by a small amount in a repeatable way. Kronig et al. (2020a) provide a comprehensive analysis of all the various sources of mechanical error in an SDSS-V positioner.

Collecting points (1)-(3) the selection of $\sigma_{\rm cb}$ must be the summation of three factors:

$$\sigma_{\rm cb} = \sigma_{\rm arm} + \sigma_{\rm smooth} + \sigma_{\epsilon} \tag{3.12}$$

σ_{arm} is the physical half-width of the beta arm (1.5 mm for SDSS-V). σ_{smooth} is an extra buffer required for path smoothing and simplification. We've found that $\sigma_{\text{smooth}} \sim 0.03$ mm is sufficient for ensuring collision-free trajectories after path smoothing at small step sizes ($\Delta\theta \sim 0.1$). σ_ϵ is the maximum lateral uncertainty of the beta arm's absolute position due to mechanical errors. Algorithmic performance increases as σ_{cb} shrinks, so this will encourage finding tight bounds on σ_ϵ for an SDSS-V RFP.

An a priori choice of σ_ϵ can be informed directly from the SDSS-V positioner mechanical requirements where bounds on four independent sources of angular error are specified: nonlinearity, hysteresis, fiber torque, and dynamic control error. When these bounds are constructively summed the maximum permissible angular error is ± 1.50 and ± 1.48 deg for the alpha and beta axes. σ_ϵ is maximized at the fiber-end tip of the beta arm when the positioner is at full extension ($\theta_\beta = 0$). A simple computation for σ_ϵ can be constructed using Equation 3.1. For simplicity, take the positioner's base position to be $\vec{\mathbf{b}} = (0, 0)$. Take $\vec{\boldsymbol{\theta}}_1 = (0, 0)$ deg to be the expected angular coordinates of a robot at full extension, with corresponding Cartesian fiber coordinates $\vec{\mathbf{f}}_1 = (0, 22.4)$ mm. Take $\vec{\boldsymbol{\theta}}_2 = (1.50, 1.48)$ deg to be the actual angular coordinates after the maximum angular uncertainties have been applied. The corresponding Cartesian fiber coordinates are $\vec{\mathbf{f}}_2 = (22.38, 0.97)$ mm. The resulting lateral uncertainty can be estimated as:

$$\sigma_\epsilon = \|\vec{\mathbf{f}}_1 - \vec{\mathbf{f}}_2\| = 0.97\,\text{mm} \tag{3.13}$$

Thus, a setting of $\sigma_{\text{cb}} = 1.5 + 0.03 + 0.97 = 2.5$ mm would be selected based on the summation of toleranced errors from SDSS-V positioner requirements.

Note that the calculation of σ_ϵ by Equation 3.13 represents a "worst case scenario" in which all positioner error tolerances are maximized and summed constructively. Throughout the course of lab testing and survey operations we have found that $\sigma_{\text{cb}} = 2$ mm provides a sufficient safety margin for SDSS-V positioners, and the complete path generation and post-processing procedure has been successfully deployed for SDSS-V positioners for over a year of survey operations.

Finally, we comment on point (4): the case of a malfunctioning robot. Throughout the dura-

tion of a multi-year survey operating with 1000 robots distributed between two hemispheres, it's plausible to assume that a robot may be required to be taken off-line for a period of time while remaining as fixed interfering obstacle within the grid. The anti-collision routine we have presented can model this situation by simply setting the greed parameter to zero for any broken positioner in any orientation. Operational robots will still be required to complete successful fold and unfold sequences, but any off-line robot will remain fixed between subsequent target orientations. In this sense, it will be the duty of neighbors to navigate around a static obstacle. A robot stuck in an unfortunate (e.g. outstretched) orientation will increase the probability of deadlock in its immediate area. In certain orientations, a stationary robot could require additional neighboring robots to be taken off-line. A robot fixed in a folded orientation will have little adverse effect on path generation. In summary, operations may proceed even in the case of stationary robots using the anti-collision algorithm we have presented, although lower efficiencies would be expected. This procedure has also been successfully tested and vetted in the field during SDSS-V survey operations when various malfunctioning robots where required to be taken offline for extended periods of time.

3.6 Discussion

In addition to path routing, `kaiju` is an important component of higher-level algorithms that seek to globally optimize SDSS-V survey planning, design, and overall strategy. Note that `kaiju` possesses no notion of concepts like target priority. In SDSS-V certain targets (e.g. calibration sources) may be more important than others in a field. In this work we have only presented a very simple deadlock resolution strategy that iteratively and randomly tosses away targets until a converging grid is achieved. In practice, target assignment algorithms will preferentially select targets to throwaway only after searching for viable target replacements first. In a grid of 500 heavily overlapping positioners, many opportunities for target swaps between positioners exist, which may serve to eliminate either source coordinate collisions or deadlocked pairs with no loss of original targets. Furthermore, deadlocks may be rectified via focused manipulation of an individual robot's greed and phobia parameters in repeated trials. The options are vast. The targeting optimiza-

tion challenge is arguably at least as complex as the problem of safe path generation, and it's an active area of algorithmic development for SDSS-V that will likely see continuous improvement throughout the survey. In the hierarchy we describe, the selective mitigation of target attrition due to collision avoidance constraints is expected to be delegated to a higher-level piece of software with an awareness of the bigger picture. The fast runtime and high efficiency of `kaiju` make this division of duty computationally feasible, especially in the small $\sigma_{\rm cb}$ regime.

SDSS-V fields span a wide range of target densities, though the majority of fields lie in the densely populated Galactic plane. In dense fields, we plan to use the GC algorithm, which provides maximal reconfiguration speed and minimal runtime. Though the GC algorithm is slightly less efficient, dense fields have a surplus of targets from which to select suitable replacements. For sparser fields, where target replacement opportunities are less abundant, we plan to use the MC algorithm to maximize targeting efficiency. With the options provided between the MC and GC algorithms, we may balance runtime, efficiency, and reconfiguration time to maximize survey productivity over the whole sky. Currently we are achieving overall targeting efficiencies of $>$99.99% and average field-to-field robot reconfiguration times $<$ 90 seconds for SDSS-V.

For projects outside the SDSS-V context, a quicker reconfiguration time may be important. Our reconfiguration process requires that every RFP array transition routes through a common folded state, where the folded state is near the edge of travel for each positioner. In this case, the total distance traveled by a positioner between targets will usually be large when compared to the distance between the subsequent targets. Makarem et al. (2014) modeled direct transitions between random positioner configurations with good results in slightly overlapping RFP workspace regimes. In heavily overlapping RFP regimes, Macktoobian et al. (2019) comment on the challenge of fitting the durations of both path computation and robot reconfiguration within timescales that do not introduce significant operational overheads.

The common state transition we present does provide benefits, as it decouples the dependency of robot trajectory planning from the nightly observing sequence. As all paths are built between a target state and a common state, transitioning between any two target states becomes trivial. This permits all paths to be computed and vetted during the survey design phases well ahead of observa-

tions. For SDSS-V, the runtimes we experience are suitable for on-the-fly path generation, should the need arise. However, for a theoretically large and crowded positioner array, a completely off-line path generator could prove necessary, and thus a common state transition would be mandatory to ensure that program runtime is not a hindrance to observing cadence.

Improvements in reconfiguration time might be found by allowing robot movement to end at a step prior to a completely folded state. In the SDSS-V layout, collision-less motion is guaranteed while all positioners maintain $\theta_\beta \gtrsim 155$ deg, where this minimum value of θ_β is a level of folding that brings the beta arm completely within a radius of half the pitch. The exact condition is given by:

$$\theta_\beta > 180^{\mathrm{o}} - \cos^{-1} \frac{(\frac{1}{2}\mathrm{pitch})^2 - \mathrm{l}_\alpha^2 - (\mathrm{l}_\beta + \sigma_{\mathrm{cb}})^2}{2\mathrm{l}_\alpha \mathrm{l}_\beta}. \tag{3.14}$$

RFP arrays with small overlap zones would benefit most from an earlier exit criterion like Equation 3.14, as beta arms need only to retract a small amount before finding themselves in a guaranteed collision-less environment. Although shortcuts between target transitions for SDSS-V exist, the complete fold/unfold sequence we have presented is sufficiently fast to not rate-limit SDSS-V survey pacing.

It has become increasingly popular to retrofit existing telescopes with robotically filled focal plane arrays. In the case of SDSS-V, positioner density was ultimately limited by the fiber capacity of the existing spectrographs. In proposed future RFP projects with purpose-built spectrographs (e.g MegaMapper Schlegel et al. 2019), the potential multiplexing power may be limited only by the density of positioners in the focal plane. As RFP technology continues to progress, the possibility of ultra-densely packed arrays may be on the horizon. In our analysis, we have shown high efficiencies (>0.99 for MC) in heavily-overlapping and highly-crowded arrays, where as much as 20% of the focal plane space may be occupied by interfering robot arms (right panel, Figure 3.5). The algorithms we present can be used to inform and verify layout choices in future RFP instrument design. Most importantly, our simulations suggest that ultra-densely packed positioner layouts may be operationally feasible.

The success of our collision-avoidance method is mainly attributed to the realization that reverse-solved paths are extremely efficient. We show that even an algorithm based on a simple greedy heuristic obtains an efficient solution to a challenging problem. It may seem suspicious that the directionality should matter at all. However, the reverse-solve strategy resembles a situation that arises in multi-agent pattern formation theory. Multi-agent pattern formation problems are often concerned with deriving control laws that drive agents from random states to lattice-like structures and determining where convergence can be guaranteed (Olfati-Saber, 2006). By adopting a reverse-solve direction for RFP arrays, we frame our problem in the same way, where the initial (target) state is random, and the final (folded) state is a lattice. A lattice configuration only requires that all positioners share the same $(\theta_\alpha, \theta_\beta)$ coordinates. Here we have specifically selected the folded lattice configuration for two reasons. The first reason: as positioners fold they are driving toward a guaranteed collision-free environment (see Equation 3.14), and the chance of interaction decreases with program step. The second reason: throughout the routine θ_α will decrease and θ_β will increase as a positioner moves from a right arm orientation toward a fold. When alpha and beta axes move in opposite directions, the overall motion of the beta arm resembles a thrust rather than a swipe or a swing. Given the elongated shape of a beta arm, a thrust presents a smaller cross section for interaction during motion. We suspect that other existing RFP control codes will improve in efficiency if a reverse solution is employed, especially in heavily overlapping regimes.

The reverse-solve method is obviously beneficial when considering the geometries and kinematics specific to RFP arrays, though a cursory search of the robotics literature at large yields sparse mention of reversely solved paths. In one example, Zhao et al. 2012 find a reverse-path strategy to optimize the routing problem faced in minimally invasive surgeries. We wonder if the concept of path-direction preference is generally extendable to path planning problems in the context of robotic control theory and multi-agent optimization.

The landscape of survey-based astronomy is progressing rapidly, largely due to the continuing development of highly-automated telescope and instrument systems. As the complexity of observing systems continues to increase, overall survey productivity may become limited by our ability to design and implement effective control algorithms. This was realized in SDSS-V, where the

effective utilization of the full suite of SDSS-V positioners was an unsolved problem prior to this work. Ultimately, robotic path routing occupies a small part of a larger picture of overall survey control. Optimization of target assignment, survey scheduling, and feedback from data acquisition are all spaces in which further algorithmic development may have significant effects on the overall productivity of current and future astronomical surveys.

3.7 Conclusion

We have presented a generic, computationally fast, and highly efficient method to determine non-colliding paths for a two armed robotic fiber positioner system, where we measure efficiency in terms of astronomical targets ultimately acquired under collision avoidance constraints. The RFP design we describe has become typical in today's growing number of robotic wide-field multi-object spectroscopic instruments, and so our methods are applicable to a wide range of astronomical surveys and instruments. We have focused our analysis on a layout in which robot arms have heavily overlapping patrol zones, a design currently unique to the SDSS-V and MOONS instruments for which the collision-avoidance problem is especially challenging. We find that efficiency remains high even in environments significantly more crowded than the SDSS-V layout, suggesting the feasibility of ultra-densely packed positioner arrays in future RFP designs.

Chapter 4

FIBER POSITIONING I: LAB CALIBRATION OF THE FPS

4.1 Introduction

The SDSS-V FPS is a complex instrument with thousands of moving parts that are required to operate at high precision both spatially and temporally. Each FPS underwent an extensive lab test and verification phase to ensure that the instrument was fully operational before shipping to the telescope. The specific goals of the lab calibration phase were (1) obtain fiber placements accurate enough to obtain astrophysical light in fibers once at the telescope ($\leq$ 50 μm RMS), and (2) test and tune the `kaiju` path generator (Chapter 3) to ensure that the robot array can seamlessly move from configuration to configuration without colliding.

To achieve this we calibrated each componenet of the FPS for use in `coordio` transforms (Chapter 2). Full-system characterization allows us to accurately predict both where a fiber will land given a positioner's angular coordinates, and where a robot's beta arm is relative to a neighbor for collision-avoidance purposes. Section 4.2 describes the initial calibration of FPS components prior to full instrument assembly. Sections 4.3 and 4.4 describe the characterization of the Lab Test Camera used for full-system calibration and metrology. Sections 4.5, 4.6, 4.7, and 4.8 describe the stepwise characterization of fiducials, GFAs, robots, and science fibers. In Section 4.9 we discuss outcomes and limitations of the lab characterization phase for the SDSS-V FPS units.

4.2 Initial Robot, Fiducial, and GFA Metrology

Metrology, calibration, and verification of individual FPS components (robots, GFAs, fiducials, science fibers) was performed at various stages throughout the FPS instrument build(s). In the earliest stage of the project, SDSS-V robots were designed, prototyped, and built in a partnership between the ASTROBOTS group at EPFL and Micro Precision Systems (MPS) in Switzerland. Building upon prior fiber robot experience from collaborations with DESI and MOONS, EPFL and MPS brought expertise in precision manufacturing, robotic control (Kronig et al., 2020b), and characterization (Kronig et al., 2020a) to SDSS-V's robotic fiber positioners.

Before leaving Switzerland, each robot underwent a rigorous quality assurance and characterization routine. This was performed on an optical bench using a CMOS camera with an ultra-low

distortion lens (Fujinon HF3520-12M; TV distortion 0.01%). A temporary optical fiber was installed into the beta arm of each robot and backlit with an integrating sphere, and the fiber centroid locations were measured by the camera. The camera was calibrated against a precision optical target placed in the plane of the fiber faces to model the camera distortion. The scale of the test bench camera was 22 μm/pixel. Figure 4.1 shows a rendering of the optical test bench setup, which is uses two cameras and simultaneously measured seven robots per camera. Robots were moved $\sim$1000 times during the initial calibration and characterization process, sampling many points over its full range of motion. This SDSS-V robot calibration and verification procedure is summarized in Grossen et al. (2020). Each robot met the SDSS-V FPS requirement: a robot's first (blind) move RMS error is less than 50 μm and this error drops to 5 μm after one or two corrective moves are applied using camera feedback.

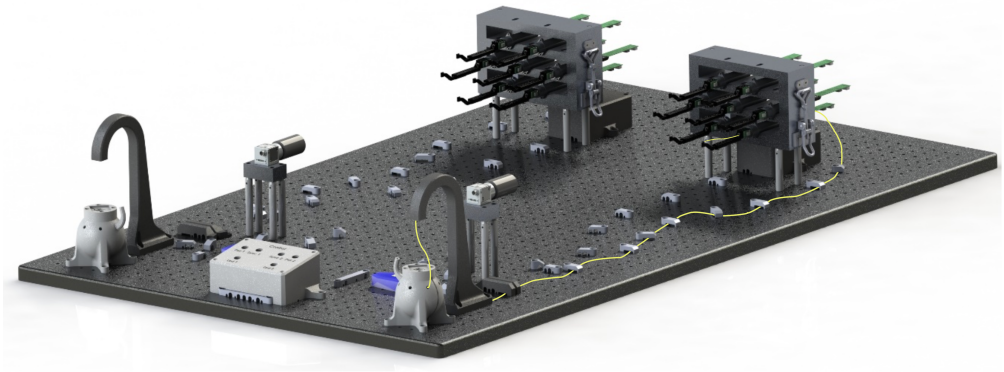

Figure 4.1 – The optical test bench setup for SDSS-V robot characterization and verification prior to robot delivery and integration into the FPS. Temporary fibers were installed in each robot and illuminated using an integrating sphere. Back lit fiber centroids were measured using a distortion calibrated camera. Each camera simultaneously measures 7 robots.

Outcomes from initial test bench calibration are (1) a tailored model for kinematics specific to each robot, and (2) alpha and beta angle zeropoints are measured relative to hard stops and flashed to the on-board memory in robot's firmware. Unfortunately, after removing the robot from the test stand and removing the fiber from the robot, the calibrated kinematic model is no longer valid. Thus, robot calibration must be repeated and updated after science fiber bundles are installed in

the robots and the robots are installed in the FPS. The most important outcome from the test bench calibration is verification that each robot mechanically functions at the required precision, and the bench measured alpha/beta zeropoints will provide a very good starting guess for fitting a new calibration model.

The calibration of robots in the FPS proceeds in an analogous fashion to that of the test bench but at a much larger scale, measuring all 500 robots simultaneously. The general procedure is: move robots around their workspaces, measure the centroid of a back lit fiber on a CCD, convert that centroid from pixels to physical locations in millimeters, and finally fit a kinematic model to each robot. Perhaps the biggest challenge of this task is obtaining an accurate pixel to millimeter transform that sufficiently accounts for any (unknown, but likely present) field distortions. During test bench characterization in Switzerland, a high precision checkerboard target was used for camera calibration. In the case of full-wok calibration, we will employ a grid of fixed fiducial fibers to develop the camera transform.

Sixty fiducial fibers are embedded in and around the SDSS-V robot array to provide static absolute reference points for full-wok imaging and metrology. Twelve of these fiducials are installed into GFA assemblies (two fiducials per GFA) and forty eight fiducials are installed directly into the wok mounting plate. Figure 4.2 plots the locations for all fiducials around the wok, indicating which fiducials are directly associated with GFA assemblies. GFA fiducials were measured relative to guide camera pixels using a CNC machine and a point source microscope. Prior to robot integration, wok fiducials were installed into both the APO and LCO FPS units, and the xy locations of the fiducial fibers were optically measured with a CMM. The maximum expected errors for GFA and wok fiducial measurements were 2 μm and 8 μm respectively. Further detail on the fiducial fiber metrology campaigns is provided by Engelman et al. (2022).

4.3 Lab Test Camera

When the fiducial measurement campaigns were complete, both FPS units were returned to the lab at The Ohio State University (OSU). Robot integration began immediately for the APO FPS. Meanwhile the LCO FPS and was set up in front of the Lab Test Camera (LTC) to provide a head

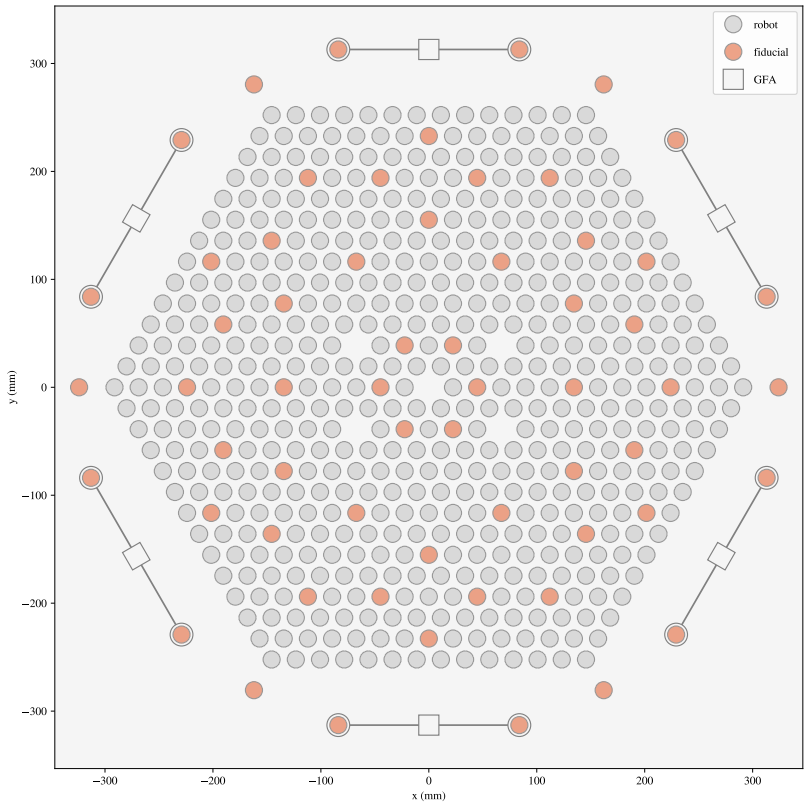

Figure 4.2 – Locations of fiducials, robots, and GFAs in wok coordinates. The twelve fiducials associated with GFAs were not measured with a CMM. The remaining 48 fiducials were measured with a CMM.

start on development of pixel to mm camera transform for later use in full-wok calibration. At this stage the LCO FPS was mostly empty, containing only the forty eight CMM measured wok fiducials and few robots for initial motion testing and calibration strategy development.

The LTC uses a Finger Lakes Instrumentation ML50100 8K x 6K CCD with 6 μm pixels, and it delivers a pixel scale of 110 μm/pixel. The CCD body is mated to a custom lens doublet and 640 nm narrow band filter for background rejection (CHROMA ZET642/20x). Figure 4.3 shows the LTC camera assembly. The LTC is mounted on a vibration isolated optical bench, and it is pointed at the wok which is tipped to horizon in its handling cart. This arrangement is shown in Figure 4.4. A spot diagram for the LTC is shown in the Figure 4.5. In this figure, five spots are shown moving from on axis to 81, 162, 243, and 324 mm off axis. 324 mm is the radii of the outer fiducial ring

on the wok. The LTC was designed to deliver FWHM spot size $\leq$ 3 pixels across the field, but significant coma was expected when measuring far off the optical axis.

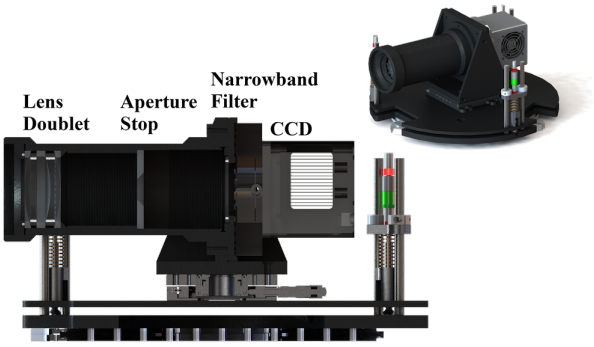

Figure 4.3 – Lab test camera assembly.

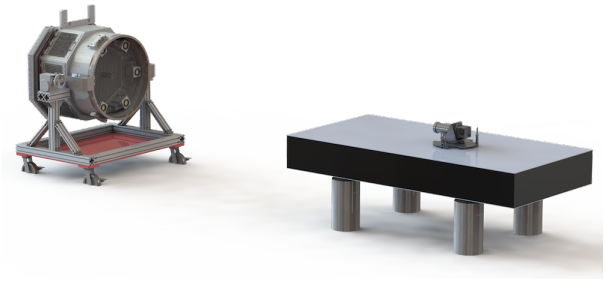

Figure 4.4 – LTC pointed at the FPS in its handling cart.

Alignment between the LTC and the sparsely-populated LCO wok was performed by eyeball. The fiber array was centered as closely as possible on the CCD by iterative nudging of the FPS and the LTC. The wok surface was placed at a distance from the LTC such that the fiducial array completely filled the smaller axis of the chip to maximize the resolution of the imaging system. Visual inspection of PSFs across the field was used to attempt to minimize the obliquity of the camera with respect to the wok surface although the LTC was relatively insensitive to focus.

For LTC imaging, fiducial fibers were back illuminated using a 639 nm LED (ThorLabs LED630E) filled using an integrating sphere mounted to the FPS. Both PSF intensity and image quality were seen to drop at larger field radii. The left hand panel in Figure 4.6 shows four postage-stamp cutouts of PSFs moving from the center of the wok to the edge. Rightward panels show the same centroids clipped at decreasing CCD count levels. Each box in the figure is a 30 x 30 pixel cutout around a fiducial. Fiducial signal varied among fibers at similar radii, and a 1.2 second exposure time was found to avoid saturation in the brightest fiducials in the field. The outermost radius (324 mm) corresponds to the outer ring of fiducials. Roughly 60% of the fiducials and 65% of the robots lie within a radius of 224 mm.

Centroid extractions and measurements were performed using `sep` (Barbary, 2018), a Python implementation of Source Extractor routines (Bertin and Arnouts, 1996). Raw images were column-

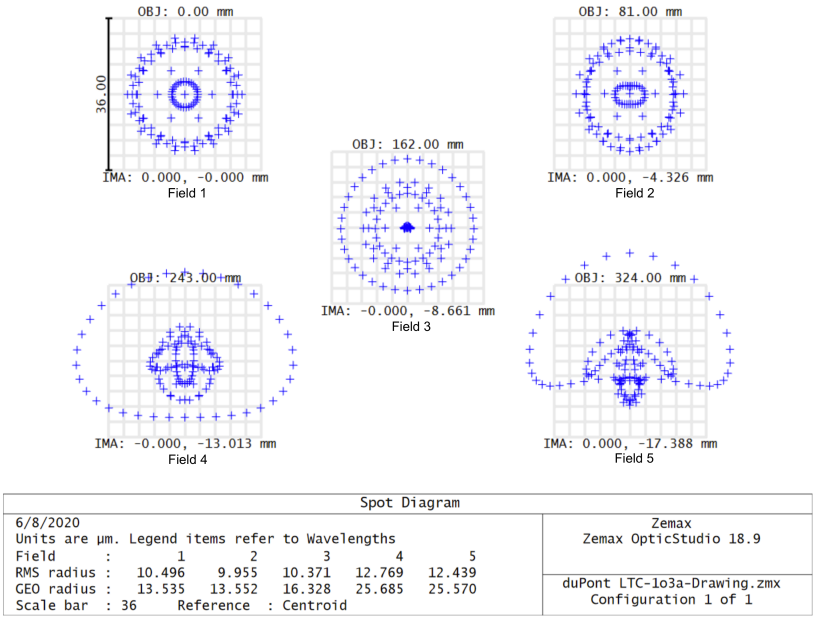

Figure 4.5 – Zemax spot diagram for LTC. Pixel size is 6 μm so each grid displayed in the spot diagram corresponds to a 6 x 6 cutout in pixel space.

wise median subtracted to estimate and remove image bias and background (about 1,000 counts). Any remaining background was estimated and subtracted using a `sep.Background` 2D model. A flat field correction was not attempted. Sources were extracted from the processed frames using `sep.extract` with a detection threshold of 3.5σ where σ is the RMS of the background. Lastly, detections were filtered by size (npix $>$ 100) to remove false detections due to hot pixels, etc. This produced a clean list of bona-fide fiber PSF detections for each frame. Peak counts typically measured between 5,000 and 40,000 above the background, and counts (as visible in the leftmost panel of Figure 4.6) generally decreased with wok radius.

4.4 Lab Test Camera Transform

The LTC transform converts the location of a centroid in pixels from the CCD frame to a location in millimeters in the wok coordinate frame. It is the combination of a similarity transform and a Zhao-Burge polynomial correction, both of which are described in turn. A sufficiently accurate LTC transform will be required for lab calibration of a fully populated FPS system in SDSS-V.

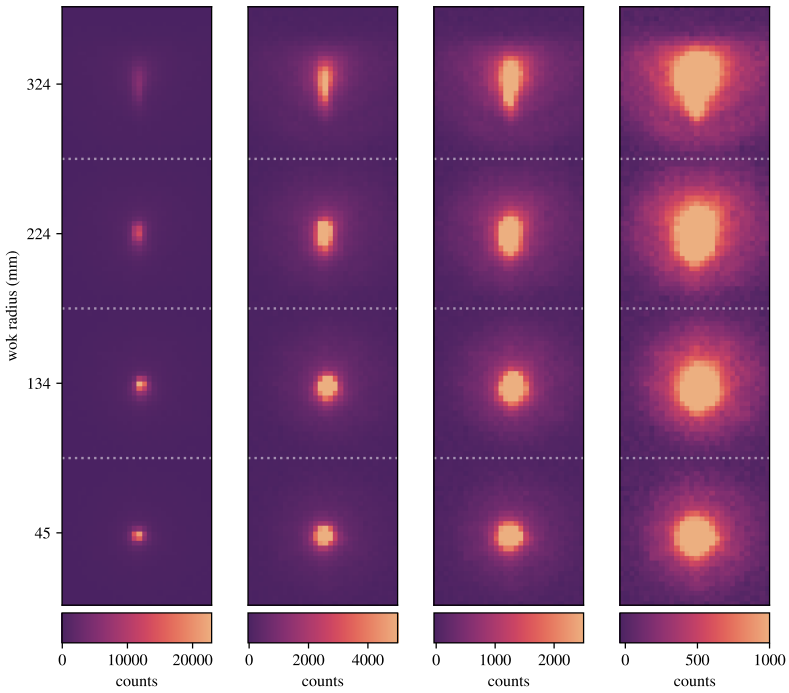

Figure 4.6 – Lab Test Camera PSF examples from four fiducial fibers in the LCO wok at different wok radii. Each box is a 30 x 30 pixel cutout from a background-subtracted LTC image. Boxes are stacked vertically by increasing wok radius. Image strips left to right are the same data with decreasing count thresholds to show different slices of PSF shape. Image quality degrades at wok radius increases, and this qualitatively matches the expected optical performance of the LTC system as shown in Figure 4.5.

The transform will be fit using two sets of 2D points $\{\mathbf{w}_i\}$ and $\{\mathbf{p}_i\}$, which represent CMM xy measurements in millimeters and LTC xy measurements in pixels for each fiducial $i = 1, 2, \ldots, n$.

4.4.1 Similarity Transform

We define a similarity transformation as

$$S(\mathbf{p}, s, \theta, \mathbf{t}) = s \begin{bmatrix} \cos\theta & -\sin\theta \\ \sin\theta & \cos\theta \end{bmatrix} \mathbf{p} + \mathbf{t}, \tag{4.1}$$

were $s \in \mathbb{R}$ is a scaling factor, $\theta \in \mathbb{R}$ is a rotation, $\mathbf{t}$ is an xy translation. We find the best fit similarity transform parameters $\{s, \theta, \mathbf{t}\}$ by solving the minimization problem

$$\min_{s,\theta,\mathbf{t}} \frac{1}{n} \sum_{i=1}^{n} \|\mathbf{w}_i - S(\mathbf{p}_i, s, \theta, \mathbf{t})\|^2. \tag{4.2}$$

A widely-used solution to Equation 4.2 is a least squares method derived by Umeyama (1991), which is implemented in the `skimage.transform` package[1] for Python. We fit a similarity transform to fiducial centroid measurements from an LTC image. Given best fit parameters $\{s^*, \theta^*, \mathbf{t}^*\}$ the xy residual $\{\mathbf{r}_i\}$ for each fiducial is

$$\mathbf{w}'_i = S(\mathbf{p}_i, s^*, \theta^*, \mathbf{t}^*) \tag{4.3}$$

$$\mathbf{r}_i = \mathbf{w}_i - \mathbf{w}'_i \tag{4.4}$$

Figure 4.7 plots residual vector arrows $\{\mathbf{r}_i\}$ as a function of wok position for the forty eight fiducials installed in the sparsely-populated LCO wok. In this view arrow bases mark the expected locations for fiducials $\{\mathbf{w}_i\}$, and arrow heads mark the measured location for fiducials after applying a similarity transform to LTC centroids. Figure 4.8 shows a histogram of the magnitude of the residuals (length of vectors shown in Figure 4.7). A few outer-radius fiducials show relatively large offsets from their known positions, but for nearly all of the robot field the similarity trasform alone will predict a physical wok position to $\sim$0.5 mm. The larger residuals on the right edge of the field might hint at a lens imperfection or misalignment in the LTC camera. The residuals shown in Figure 4.7 are the pattern we will fit using Zhao-Burge polynomials.

[1] https://scikit-image.org/docs/stable/api/skimage.transform.html#skimage.transform.SimilarityTransform

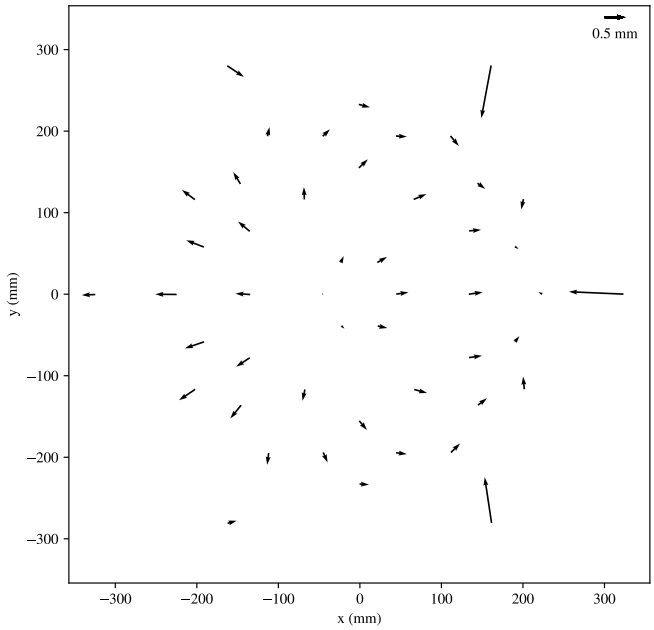

Figure 4.7 – Quiver plot showing fiducial measurement vector residuals after a similarity transform fit is applied to an LTC image of the LCO FPS unit. Arrow tips indicate the predicted locations ($\mathbf{w}_i'$'s), arrow bases indicate the expected locations ($\mathbf{w}_i$'s). Fiducials on the right edge of the field see a stronger distortion, which may indicate LTC lens misalignment.

4.4.2 Zhao-Burge Polynomial Correction

Zernike polynomials are a set of orthogonal scalar functions defined on the unit disk, and these polynomials often arise in the fields of optics and astronomy (and beyond). Zernikes and their gradients are frequently used for modeling distortions and aberrations over a circular region (Noll, 1976). Recent work by Andersen (2018) describes Zernikes, Zernike gradients, and their applications, and provides a pseudocode[2] to compute Zernike gradients in Cartesian coordinates which is often useful. Zhao and Burge (2007) and Zhao and Burge (2008) construct a set of orthogonal vector polynomials built from Zernike gradients which form a nice basis for mapping distortions,

[2] https://opticapublishing.figshare.com/ndownloader/files/10943375

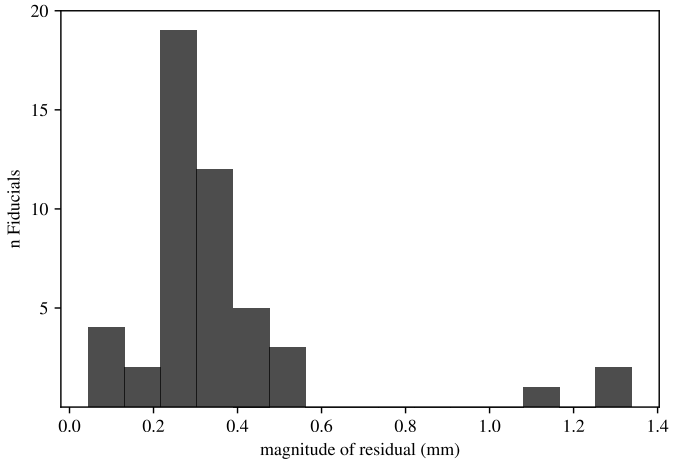

Figure 4.8 – Histogram of residuals from Figure 4.7. Outliers in the histogram correspond to the three outer fiducials along the right hand edge of the field.

such as the one we encounter in Figure 4.7. The DESI Collaboration has implemented Zhao-Burge polynomials in Python[3] and the code is freely available for broad use under their BSD 3-Clause license[4].

As described in their work, the Zhao-Burge 2D vector polynomials are organized into two sets: $\vec{S}$ polynomials and $\vec{T}$ polynomials. These two sets overlap so care must be taken when selecting a basis for modeling distortions. The $\vec{S}$ and $\vec{T}$ vector functions are only defined on the domain of the unit disk, so our xy inputs require a re-normalization. For this we choose to normalize by the outermost fiducial:

$$\mathrm{w}_{MAX} = \max\{\|\mathbf{w}'_1\|, \|\mathbf{w}'_2\|, \ldots, \|\mathbf{w}'_n\|\} \approx 324\,\mathrm{mm} \tag{4.5}$$

$$\mathbf{w}^{\dagger}_i = \frac{\mathbf{w}'_i}{\mathrm{w}_{MAX}}. \tag{4.6}$$

The 2D distortion model built from m Zhao-Burge terms is:

[3] https://github.com/desihub/desimeter/blob/0.6.7/py/desimeter/transform/zhaoburge.py

[4] https://github.com/desihub/desimeter/blob/0.6.7/LICENSE.rst

$$D(\mathbf{w}, \vec{c}) = \sum_{j=1}^{m} c_j \vec{Z}_j(\mathbf{w}/\mathrm{w}_{MAX}), \tag{4.7}$$

where $\vec{Z}_j$ represents a polynomial of either type ($\vec{S}$ or $\vec{T}$), and $\vec{c}$ is a vector of m coefficients. Coefficients $\vec{c}$ are found by least squares approximation: we construct an equation $X\vec{c} = \vec{y}$ with closed form solution $\vec{c} = (X^T X)^{-1} X^T \vec{y}$. Using the unit circle normalized fiducial locations ($\mathbf{w}_i^\dagger$'s) and the measured distortion ($\mathbf{r}_i$'s), this minimization problem is written as

$$\begin{bmatrix} \vec{Z}_1(\mathbf{w}_1^\dagger)\cdot\hat{\mathbf{x}} & \vec{Z}_2(\mathbf{w}_1^\dagger)\cdot\hat{\mathbf{x}} & \dots & \vec{Z}_m(\mathbf{w}_1^\dagger)\cdot\hat{\mathbf{x}} \\ \vec{Z}_1(\mathbf{w}_2^\dagger)\cdot\hat{\mathbf{x}} & \vec{Z}_2(\mathbf{w}_2^\dagger)\cdot\hat{\mathbf{x}} & \dots & \vec{Z}_m(\mathbf{w}_2^\dagger)\cdot\hat{\mathbf{x}} \\ \vdots & \vdots & \vdots & \vdots \\ \vec{Z}_1(\mathbf{w}_n^\dagger)\cdot\hat{\mathbf{x}} & \vec{Z}_2(\mathbf{w}_n^\dagger)\cdot\hat{\mathbf{x}} & \dots & \vec{Z}_m(\mathbf{w}_n^\dagger)\cdot\hat{\mathbf{x}} \\ \vec{Z}_1(\mathbf{w}_1^\dagger)\cdot\hat{\mathbf{y}} & \vec{Z}_2(\mathbf{w}_1^\dagger)\cdot\hat{\mathbf{y}} & \dots & \vec{Z}_m(\mathbf{w}_1^\dagger)\cdot\hat{\mathbf{y}} \\ \vec{Z}_1(\mathbf{w}_2^\dagger)\cdot\hat{\mathbf{y}} & \vec{Z}_2(\mathbf{w}_2^\dagger)\cdot\hat{\mathbf{y}} & \dots & \vec{Z}_m(\mathbf{w}_2^\dagger)\cdot\hat{\mathbf{y}} \\ \vdots & \vdots & \vdots & \vdots \\ \vec{Z}_1(\mathbf{w}_n^\dagger)\cdot\hat{\mathbf{y}} & \vec{Z}_2(\mathbf{w}_n^\dagger)\cdot\hat{\mathbf{y}} & \dots & \vec{Z}_m(\mathbf{w}_n^\dagger)\cdot\hat{\mathbf{y}} \end{bmatrix} \begin{bmatrix} c_1 \\ c_2 \\ \vdots \\ c_m \end{bmatrix} = \begin{bmatrix} \mathbf{r}_1\cdot\hat{\mathbf{x}} \\ \mathbf{r}_2\cdot\hat{\mathbf{x}} \\ \vdots \\ \mathbf{r}_n\cdot\hat{\mathbf{x}} \\ \mathbf{r}_1\cdot\hat{\mathbf{y}} \\ \mathbf{r}_2\cdot\hat{\mathbf{y}} \\ \vdots \\ \mathbf{r}_n\cdot\hat{\mathbf{y}} \end{bmatrix}, \tag{4.8}$$

where $\hat{\mathbf{x}}$ and $\hat{\mathbf{y}}$ are unit vectors that isolate the x and y components of $\mathbf{r}_i$'s and $\vec{Z}_j$'s.

We use leave-one out cross validation (LOOCV) to decide which Zhao-Burge polynomials to include for LTC distortion modeling. LOOCV provides a good way to estimate unbiased errors in modeling, which will help protect against overfitting. The procedure for this is as follows. For each fiducial $i = 1, 2, \dots, n$: (1) fit a model (Equation 4.8) that excludes the i'th row ($\mathbf{w}_i$ and $\mathbf{r}_i$). (2) Use this model (Equation 4.7) to predict the distortion $\mathbf{r'}_i$ from $\mathbf{w}_i$. (3) Record the prediction error for fiducial i as

$$\mathbf{e}_i = \mathbf{r}_i - \mathbf{r}'_i. \tag{4.9}$$

The LOOCV RMS error for a model is

$$\mathrm{e}_{RMS} = \left(\frac{1}{n} \sum_{i=1}^{n} \|\mathbf{e}_i\|^2 \right)^{\frac{1}{2}}. \tag{4.10}$$

Of the models we experimented with during early LTC imaging of the LCO FPS, the Zhao-Burge polynomal basis $\{\vec{S}_2, \vec{S}_3, \vec{S}_4, \vec{S}_5, \vec{S}_6, \vec{S}_7, \vec{S}_8, \vec{S}_{11}, \vec{S}_{20}, \vec{T}_7, \vec{T}_8\}$ produced the lowest observed LOOCV RMS error: $\mathrm{e}_{RMS} \approx 9$ μm. We selected this as the Zhao-Burge basis for LTC modeling. Figure 4.9 plots the Zhao-Burge polynomial correction model alongside the distortion pattern that was used for model training.

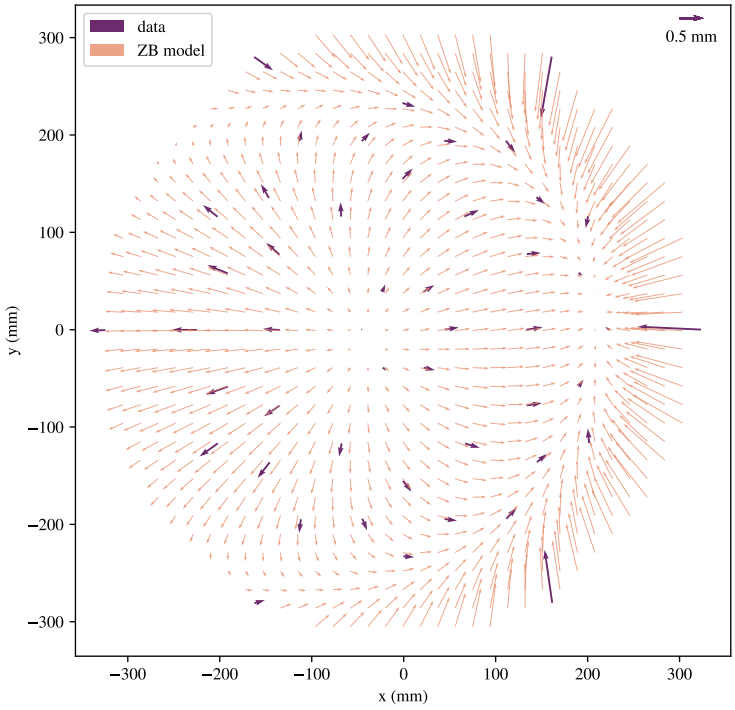

Figure 4.9 – Fiducial distortion data from Figure 4.7 is plotted alongside the best fit model of Zhao-Burge vector polynomials used to explain the distortion for the LCO FPS.

With the similarity and Zhao-Burge transforms defined, the complete LTC transform that maps pixels to wok frame millimeters is written as

$$L(\mathbf{p}) = S(\mathbf{p}, s^*, \theta^*, \mathbf{t}^*) + D(S(\mathbf{p}, s^*, \theta^*, \mathbf{t}^*), \vec{c}^*), \tag{4.11}$$

where model parameters $\{s^*, \theta^*, \mathbf{t}^*, \vec{c}^*\}$ are fit for each LTC image from fiducial spots. Figure 4.10 shows prediction error of fiducial location after a full model is applied to an LTC image. Figure 4.11 plots a histogram of the error magnitudes (length of vectors) shown in Figure 4.10. Each image will produce a unique transform, and we use repeat imaging to understand the stability of our model. For this we compiled fiducial measurement errors from 137 LTC images spanning 7 hours of LTC imaging in the lab. The resulting histogram of errors is shown in Figure 4.12, which shows an RMS prediction error of 8 μm. Recall from Section 4.2 that CMM measurements (which we use to train our transform) are trustworty to $\sim$8 μm, so the LTC transform is operating about as well as one could hope, and the full range of observed measurement errors was acceptable for what we needed to accomplish during the lab calibration stage for the APO and LCO FPS units.

The work presented in this section was based on imaging of the LCO FPS in the OSU lab after the fiducial CMM campaign and prior to robot integration. The fiducial locations were well fit, suggesting that we found a reasonable camera distortion calibration technique. The next section addresses fiducial locations after robot installation, where we saw a degredation in fiducial fitting. This suggests that fiducials moved as work was done around them.

4.5 Fiducial Characterization

After the fiducial CMM campaign, robots and GFAs were installed into the FPS around the previously installed fiducials. When integration was complete the fully-populated FPS was set up in front of the LTC for imaging. The first set of measurements we required were physical locations on the wok (mm) for the newly installed GFA fiducials. During this process we also found the need to re-assign the locations of several fiducials that either (1) most likely moved or (2) were physically replaced due to irreparable fiber breakage.

The APO FPS was the first unit completed. In fact, APO FPS robot integration was done twice. We noted after initial integration that external wires for robot motor control could physically interfere with wires from a neighboring robot. After repeated robot moves, this eventually led to significant wire breakage which resulted in immovable robots. The issue only became evident when operating the instrument at scale (statistics!), as earlier motion tests from smaller sets of

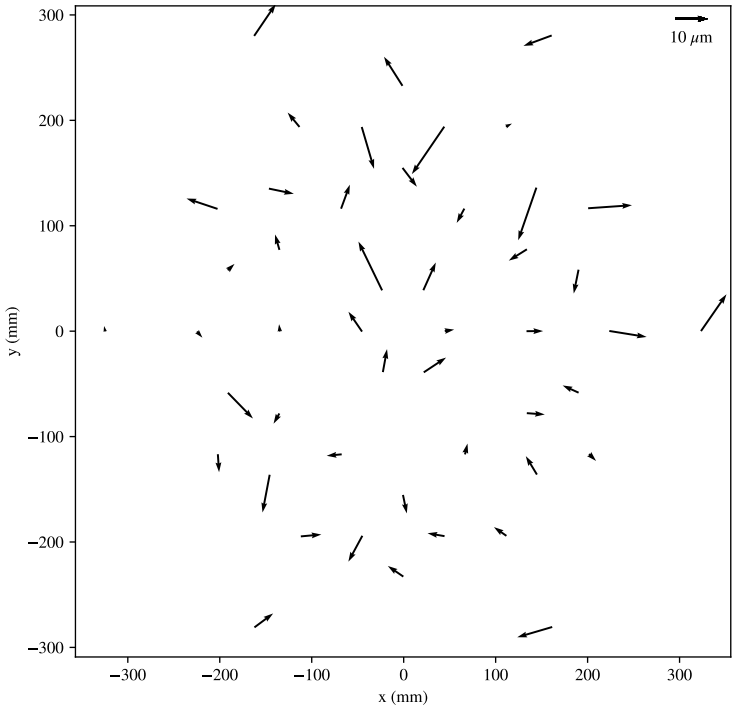

Figure 4.10 – Quiver plot showing fiducial measurement errors after distortion model is applied to a single LTC image for the LCO FPS.

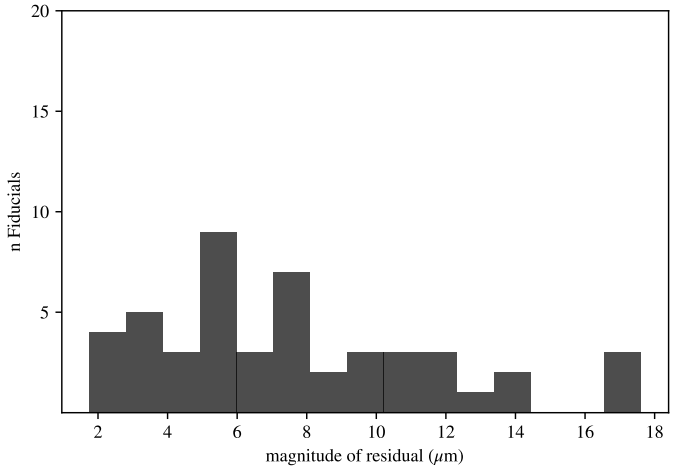

Figure 4.11 – Histogram of fiducial measurement errors after distortion model is applied to a single LTC image for the LCO FPS.

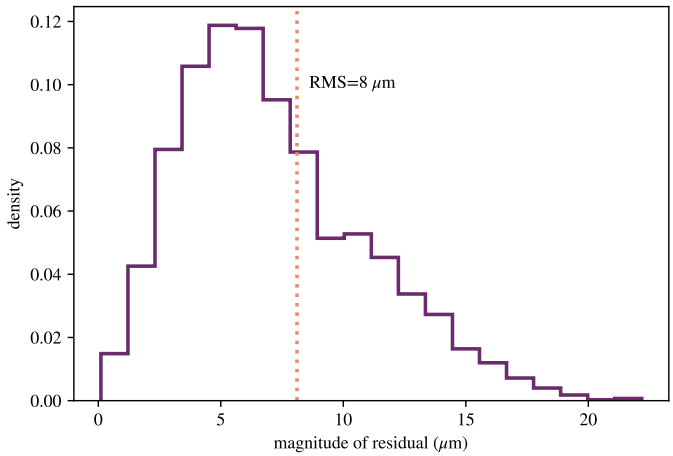

Figure 4.12 – Histogram of fiducial measurement errors after distortion model is applied to 137 LTC images for the LCO FPS.

tightly packed robots never indicated a problem. Fortunately this problem had a straightforward (but arduous) solution: re-solder broken wires and swaddle all wires tightly such that interference with a neighboring robot is physically impossible. This required the removal and remediation of all 500 APO robots, followed by a complete re-installation. Fortunately, LCO robots were remediated prior to FPS integration.

This information is relevant here because the fiducials in the APO wok had probably moved after they were measured with the CMM. The first look at fiducial measurement errors seen by the LTC for the APO FPS are shown as a quiver plot in Figure 4.13 and the histogram in Figure 4.14. The measurement errors were significantly higher than we expected given our results from Section 4.4. Five fiducials in particular with errors > 100 μm appeared as clear outliers. For these five fiducials, the error appears largely as a y displacement in the wok xy frame. This direction happens to align with the two fasteners that hold the fiducial to the wok plate, and at least one fiducial fastener was known to be loosened during the bulk robot removal for the APO FPS, which would cause a fiber displacement along this direction. The forest of fiducials and robots is a dense place and the tools for forestation require steady hands in cramped environments. It's highly likely that most fiducials had been touched or bumped at some point during integration, removal, and

re-integration at a level that we would detect with LTC imaging. In the end we judged that the five fiducials with measurement errors > 100 μm were large enough outliers that we should reset their "official" positions ($\mathbf{w}_i$'s; Section 4.4) based on LTC imaging rather than CMM measurements.

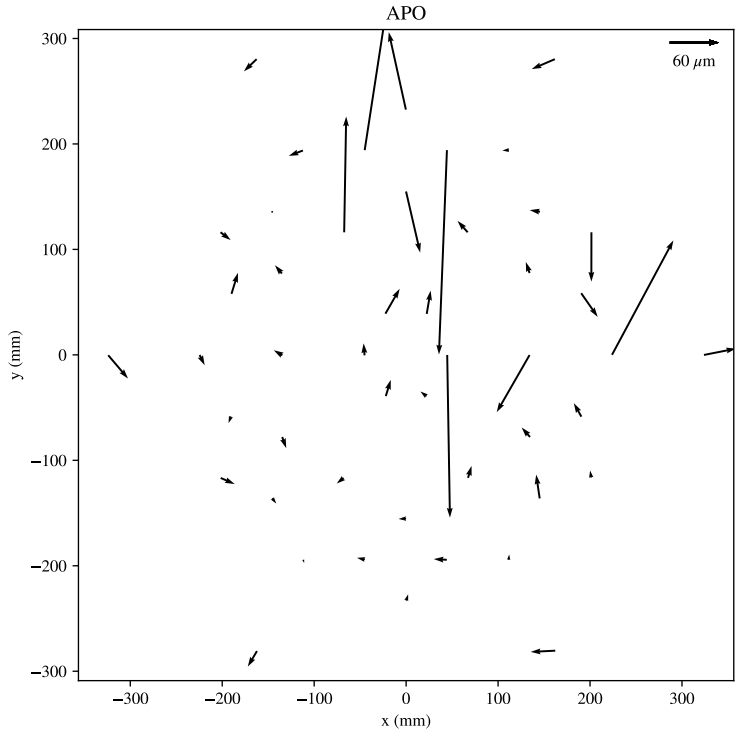

Figure 4.13 – Initial measurement errors for APO fiducials after robot integration. Errors were larger than expected, and five fiducials measured > 100 μm from their expected location.

To characterize the new APO fiducials we fit a distortion model to an LTC image excluding fiducials deemed as outliers. We use that distortion model to infer a new wok location for outlier fiducials and the new GFA fiducials. Figure 4.15 shows the fiduicals used to fit the APO distortion model, and the location of new fiducials that were measured. The final locations for new fiducials were determined by averaging measurements over dozens LTC exposures. After updating locations of fiducials, the LOOCV distortion model error (Equation 4.10) for the APO FPS was $\mathrm{e}_{RMS} \approx 25$ μm, a significant degredation compared to the results seen Section 4.4.

About six months after the APO FPS left the lab for the telescope, the LCO FPS was fully

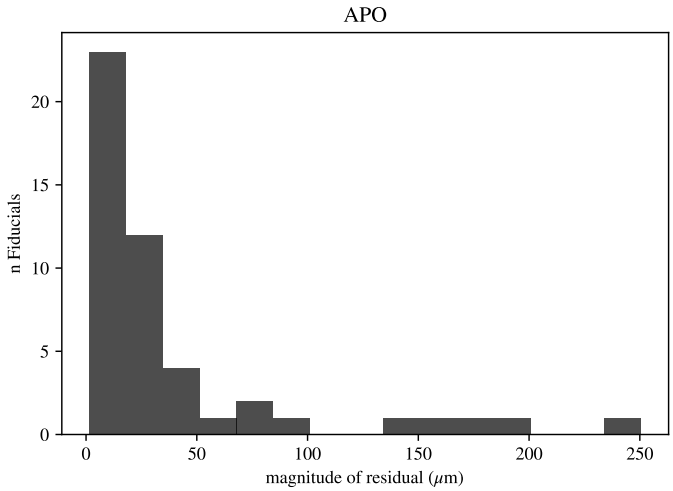

Figure 4.14 – Initial measurement errors for APO fiducials after robot integration. Five fiducials measured > 100 μm from their expected location.

integrated and ready for lab calibration. The calibration results were much more consistent with expectation (we didn't find very large displacements in fiducial locations). This is perhaps due to the increased skill the hardware team had developed over the course of working with the APO unit, and the fact that it was only integrated once. However, the LCO unit suffered from fiducial fiber breakage during robot integration. In truth, the APO unit also experienced fiducial fiber breakage but they were easily fixed with fiber-splice equipment. The fiducial fiber breakages we saw in the LCO wok happened near the fiducial body which made them hard or impossible to mend. In the LCO unit one fiducial was replaced, while two broken fiducials were left in place for the duration of lab calibration.

Figures 4.16 and 4.17 show fiducial measurement errors as a quiver plot and histogram after our first look at the integrated LCO FPS with the LTC. In the first plot the fiducial that was replaced is indicated with a circle and the two broken fiducials are indicated with an x. Clearly these initial measurement errors are much more in line with what we expected from our initial LTC analysis from Section 4.4. New locations for the replaced fiducial and the GFA fiducials were measured in the same way as described for the APO FPS. Figure 4.18 shows where these new fiducials were distributed across the field. The LOOCV distortion model error after fiducial updates was

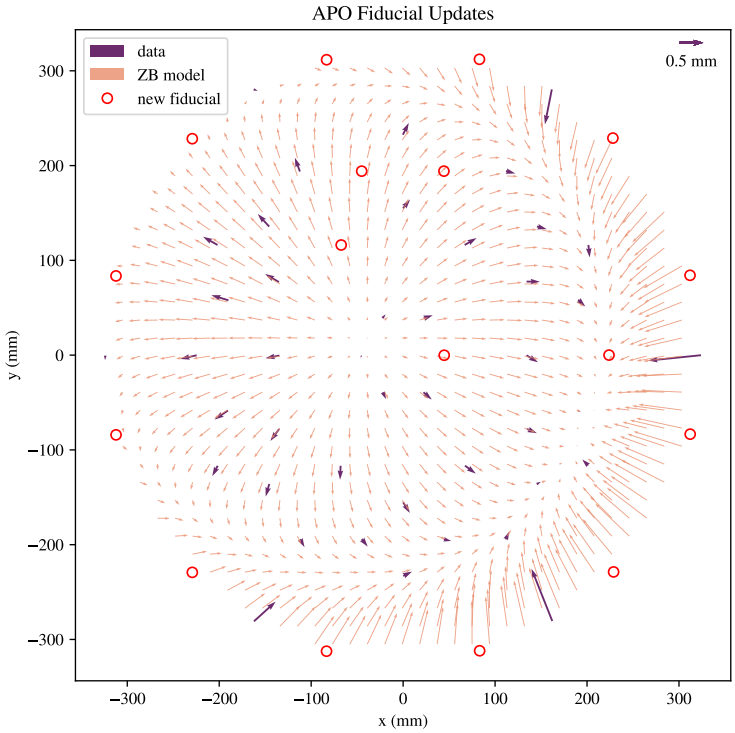

Figure 4.15 – Example of distortion model and the fiducial data used to fit it. Red circles indicate measurements around the field for new fiducials. These were either fiducials that significantly moved or fiducials associated with GFAs.

$e_{RMS} \approx 13$ μm for the LCO FPS.

4.6 GFA Characterization

Using the new fiducial measurements from the proceeding section, we next characterize the location and rotation of the GFA CCD in wok coordinates. Precise knowledge of each GFA CCD's location and rotation within the wok space is a critical component for guiding star or quasar light into science fibers during on-sky calibration and commissioning. The GFA location $\mathbf{w}_{\mathrm{GFA}}$ is the center of the CCD in wok coordinates, and the rotation is specified by the unit vector $\hat{\mathbf{i}}_{\mathrm{GFA}}$ which points along the x-axis of the CCD. Knowledge of these two quantities for each GFA is a prerequisite for computing which pixels guide stars should land on for field acquisition and guiding during science observations.

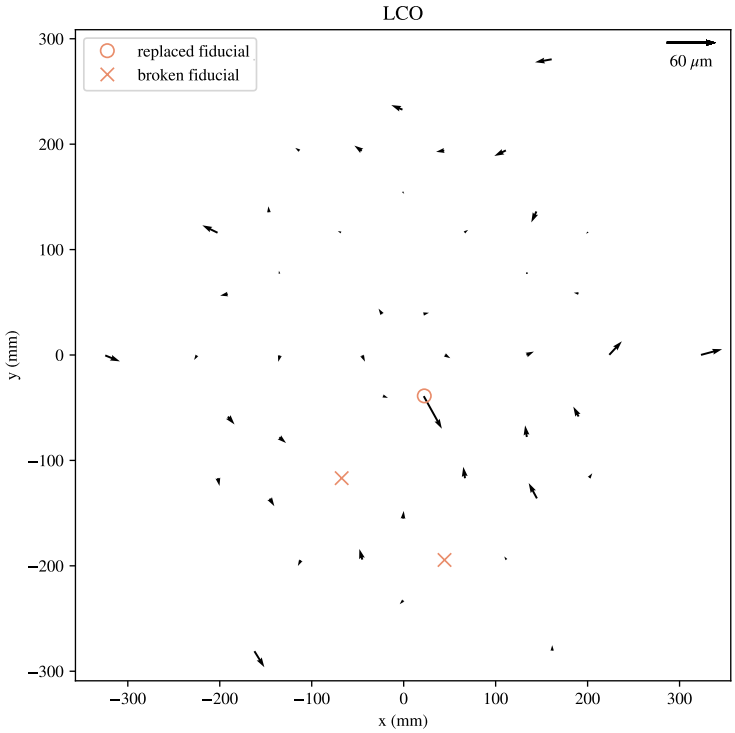

Figure 4.16 – Initial measurement errors for LCO fiducials after robot integration. Errors were smaller than seen with the APO system. One fiducial was replaced (circled), and the two broken fiducials are indicated by X's.

Each GFA assembly has a left and right fiducial. Figure 4.19 shows the relationship of these fiducials with respect to the CCD. Figure 4.20 shows the orientation of GFA units around the wok. This figure provides a visualization of the $\mathbf{w}_{\mathrm{GFA}}$ and $\hat{\mathbf{i}}_{\mathrm{GFA}}$ quantities we want to measure for each GFA.

A product of the initial fiducial metrology campaign (Section 4.2, Engelman et al. (2022)) was the location of the left and right fiducials in CNC coordinates and transform from GFA coordinates ($\mathbf{p}_{\mathrm{GFA}}$, pixels) to CNC coordinates (millimeters). The CNC transform is written like

$$C(\mathbf{p}_{\mathrm{GFA}}) = \begin{bmatrix} c_{xx} & c_{xy} \\ c_{yx} & c_{yy} \end{bmatrix} \mathbf{p}_{\mathrm{GFA}} + \begin{bmatrix} c_x \\ c_y \end{bmatrix}, \tag{4.12}$$

with a unique set of coefficients $\{c_{xx}, c_{xy}, c_{yx}, c_{yy}, c_x, c_y\}$ that Engelman et al. (2022) provided

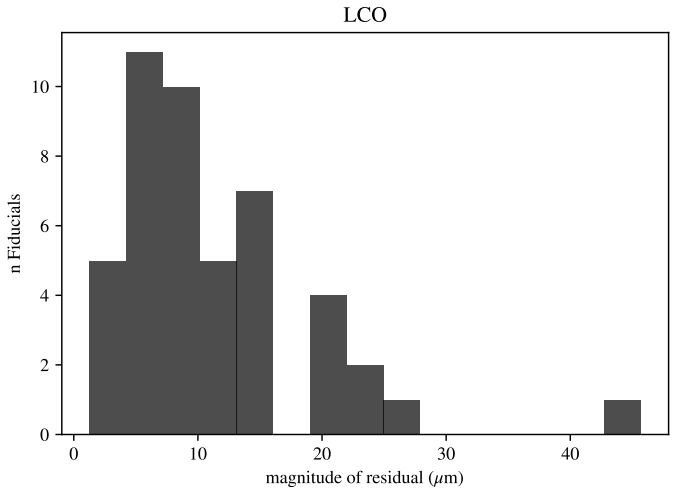

Figure 4.17 – Initial measurement errors for LCO fiducials after robot integration. The outlier at $\sim$40 μm was a replaced fiducial and thus expected to measure poorly.

for each GFA unit.

A transform from the CNC frame to the wok frame is built from two pairs of matched points: the left and right GFA fiducials measured in the CNC frame, and the left and right GFA fiducials measured by the LTC in the wok frame. We fit a similarity transform (Equations 4.1 and 4.2) using these pairs of points to learn the translation $\mathbf{t}^*$, rotation θ^*, and scale s^* that maps CNC coordinates to wok coordinates. Combining these two transforms, the conversion from GFA pixels to wok coordinates is

$$G(\mathbf{p}_{\text{GFA}}) = S(C(\mathbf{p}_{\text{GFA}}), s^*, \theta^*, \mathbf{t}^*). \tag{4.13}$$

With this we can measure $\mathbf{w}_{\text{GFA}}$ and $\hat{\mathbf{i}}_{\text{GFA}}$ using two points from the CCD: the chip center $\mathbf{p}_{\text{o}} = \begin{bmatrix} 1024.5 & 1024.5 \end{bmatrix}^T$ and the midpoint of the chip's right edge $\mathbf{p}_{+x} = \begin{bmatrix} 2048 & 1024.5 \end{bmatrix}^T$ for an unbinned and 1-indexed pixel grid.

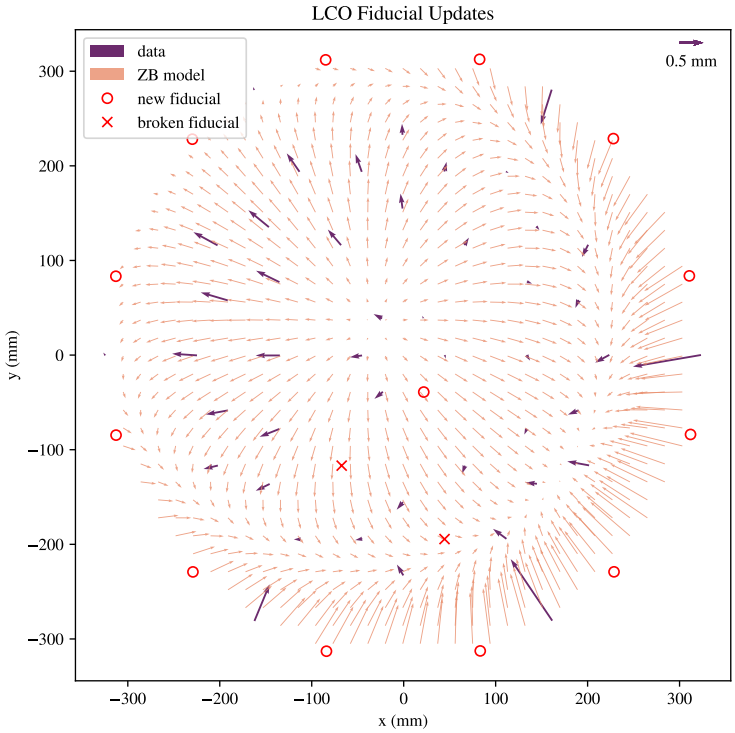

Figure 4.18 – Example of distortion model and the fiducial used data to fit it. The red circles indicates the fiducial that was replaced and the GFA fiducials. The red x's indicate broken fiducials.

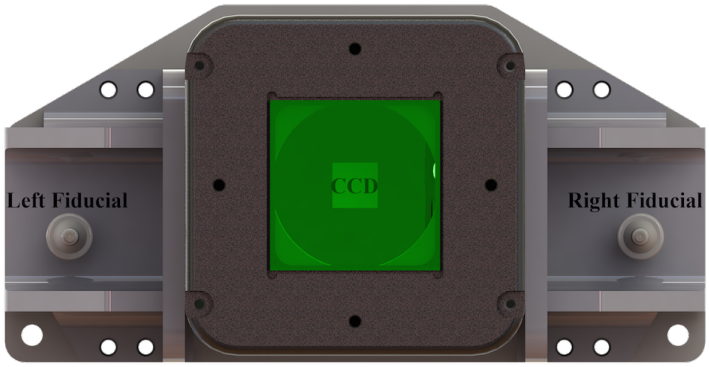

Figure 4.19 – Top down view of a GFA assembly showing relationship of left and right fiducials with respect to the CCD.

$$\mathbf{w}_{\mathrm{GFA}} = G(\mathbf{p}_{\mathrm{o}}) \tag{4.14}$$

$$\hat{\mathbf{i}}_{\mathrm{GFA}} = \frac{G(\mathbf{p}_{+x}) - \mathbf{w}_{\mathrm{GFA}}}{\|G(\mathbf{p}_{+x}) - \mathbf{w}_{\mathrm{GFA}}\|} \tag{4.15}$$

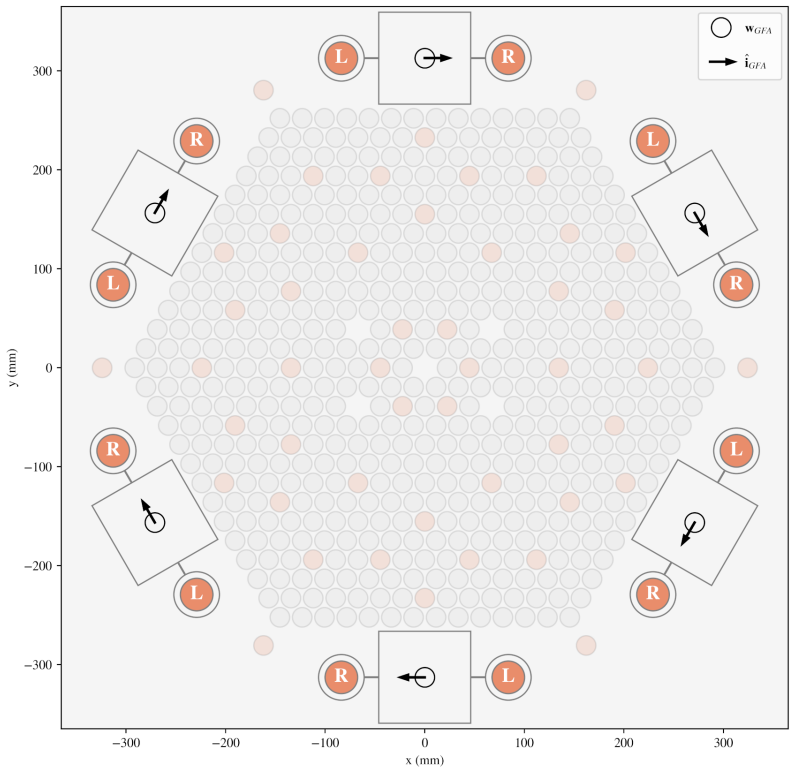

Figure 4.20 – Characterized quantities $\mathbf{w}_{\mathrm{GFA}}$ and $\hat{\mathbf{i}}_{\mathrm{GFA}}$ which define CCD location and rotation. Each GFA has a left and right associated fiducial.

By choosing scale as a free parameter in the procedure above, we are allowing for a perfect fit between CNC and wok coordinates. Any two points can be exactly related to any two other points by a translation, rotation, and scale. However, there is some information in the best fit scale s^* parameter, as it describes how much we had the stretch one system to match another. Reviewing these measurements from both APO and LCO units, the most discrepant scale factor we saw was s^*=1.00123 and nearly all the data fell in the range $0.9995 < s^* < 0.9999$. For context a scale of $s^* = 1.00123$ will create a 200 μm discrepancy in a distance measurement between two GFA fiducials separated by 167 mm. A scale of $s^* = 0.9995$ will create a 70 μm discrepancy. Similarly

to the fiducials installed in the wok, it is possible that GFA fiducials moved minimally during during handling. To a lesser degree, the temperature of the aluminum GFA fixture might also matter. A temperature difference $\Delta T = 5^{\circ}$ C would account for $\sim$20 μm of fiducial distance discrepancies between measurements. More generally, tracking and correcting temperature-dependent trends is important for the FPS units during nightly operations because the aluminum wok expands and contracts as the temperature varies. We measure and adjust for a changing instrument scale using GFA feedback, which is described further in the next chapter.

As a last note, all of these GFA fiducial measurements landed at the edge of the LTC field where our distortion model has the fewest number of points to constrain it. Although the Zhao-Burge polynomials should be well behaved at the domain edges, it's likely our distortion model predicts things less well out there.

In the end total discrepancies for nearly all fiducial to fiducial distances amounted to a fraction of a fiber diameter, and we considered these measurements sufficient for the lab stage of the FPS calibration. Ultimately locations and rotations for GFAs would be updated during on-sky calibration based on Gaia astrometry, but to get any light from astronomical sources down science fibers to begin on sky calibration it is critical that GFA locations are characterized as accurately as possible before going on sky.

4.7 Robot Characterization

Robot characterization requires determining the location and orientation of each robot installed in the wok. To accomplish this we use the LTC to measure a back-illuminated metrology fiber installed into each robot. Metrology fibers are backlit using the same system as fiducial fiber illumination, so metrology fibers and fiducials fibers are always illuminated together. Robot characterization is important for maximizing blind move accuracy when positioning a fiber, but this characterization also creates an accurate model for the full positioner array which is important for (1) path planning and collision avoidance during robot reconfiguration, and (2) science target assignment which requires spatial awareness of robot locations and workspaces across the focal plane. Sayres et al. (2021) describe the challenges of SDSS-V robot reconfiguration due to their

heavily overlapping robot geometries, and Blanton et al. (2022, in prep) describe methods used for target to robot assignment in SDSS-V.

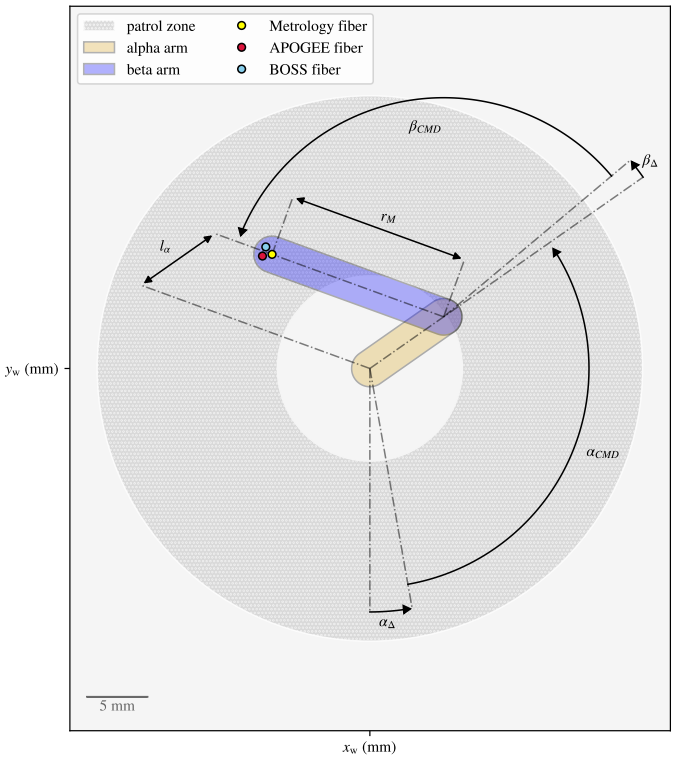

Figure 4.21 – Diagram illustrating kinematics of an SDSS-V robot. The commanded arm angles $\alpha_{\rm CMD}$ and $\beta_{\rm CMD}$ are sent to and executed by the robot. The expected location of the metrology fiber in the wok frame given $\alpha_{\rm CMD}$ and $\beta_{\rm CMD}$ will depend on six fixed parameters that must be fit for each robot. These parameters are the robot's center (x_w, y_w), the alpha/beta angular offsets $(\alpha_\Delta, \beta_\Delta)$, the alpha arm length l_α, and the metrology fiber radius r_M.

A robot is characterized by measuring six parameters:

(x_w, y_w) The the robot's x and y center location in wok coordinates (mm).

$(\alpha_\Delta, \beta_\Delta)$ The angular offsets between the robot's internal α, β angular zeropoints and the "true" α, β zeropoints in the wok frame.

l_α The length of the robot's alpha arm (mm).

r_M The distance between the beta axis of rotation and the metrology fiber (mm).

These six parameters are shown in Figure 4.21 for a robot that has been "commanded" to an alpha angle $\alpha_{\rm CMD}$ and beta angle $\beta_{\rm CMD}$. Given commanded arm angles $(\alpha_{\rm CMD}, \beta_{\rm CMD})$, the kinematic model that describes the location of a metrology fiber in wok coordinates is:

$$R(\alpha_{\text{CMD}}, \beta_{\text{CMD}}, \alpha_\Delta, \beta_\Delta, l_\alpha, r_M, x_w, y_w) = \begin{bmatrix} \cos(\alpha') & \cos(\alpha' + \beta') \\ \sin(\alpha') & \sin(\alpha' + \beta') \end{bmatrix} \begin{bmatrix} l_\alpha \\ r_M \end{bmatrix} + \begin{bmatrix} x_w \\ y_w \end{bmatrix}, \quad (4.16)$$

where we define

$$\alpha' = \alpha_\Delta + \alpha_{\text{CMD}} - \frac{\pi}{2} \quad (4.17)$$

$$\beta' = \beta_\Delta + \beta_{\text{CMD}} \quad (4.18)$$

as the alpha and beta angles measured in the wok frame. Note that $\alpha' = 0$ points the alpha arm in the direction of $\hat{x}$ in wok coordinates, $\beta' = 0$ places the metrology fiber on the outer edge of its patrol zone, and $\beta' = 180^{\text{o}}$ places the metrology fiber on the inner edge of its patrol zone.

Data to fit these parameters were collected by imaging a robot's metrology fiber at $m \approx 50$ random (α_{CMD}, β_{CMD}) configurations. At each configuration: an LTC image was taken, an LTC transform was fit, and the location of the robot's metrology fiber was measured in wok coordinates. The minimization problem to solve for a robot's $\{\alpha_\Delta, \beta_\Delta, l_\alpha, r_M, x_w, y_w\}$ parameters is written as

$$\min_{\alpha_\Delta, \beta_\Delta, l_\alpha, r_M, x_w, y_w} \frac{1}{m} \sum_{i=1}^{m} \| L(\mathbf{p}_i) - R(\alpha^i_{\text{CMD}}, \beta^i_{\text{CMD}}, \alpha_\Delta, \beta_\Delta, l_\alpha, r_M, x_w, y_w) \|^2, \quad (4.19)$$

where $\mathbf{p}_i$ is the metrology fiber centroid on the CCD and $L(\mathbf{p}_i)$ is the LTC transform that converts pixels to millimeters as described in Section 4.4. The minimization problem in Equation 4.19 was solved numerically using Powell's method (Powell, 1964) which is implemented in the `scipy.optimize`[5] package for Python. Powell's method requires an initial guess for each parameter. For this we use the nominal design values for robot location and arm lengths, and we

[5] https://docs.scipy.org/doc/scipy/reference/generated/scipy.optimize.fmin_powell.html

chose $\alpha_\Delta = \beta_\Delta = 0$.

Robot calibration was performed in two stages. In the first stage the beta arm's angular range of motion limited to $\beta_{\mathrm{CMD}} \in [155, 180]$ degrees, with alpha angle motion allowed over the full range of $\alpha_{\mathrm{CMD}} \in [0, 360)$ degrees. This kept all robots near their "folded" configuration where a physical collision between neighboring robots is impossible, and collision-avoidance routines were not necessary. This results in a robot only probing a small fraction (a thin annulus) of its workspace. Figure 4.22 shows the results before (left panel) and after (right panel) stage 1 calibration. Quiver arrows show the xy wok offset between expected position of a metrology fiber (Equation 4.16) and LTC measured position of a metrology fiber (Equation 4.11). The RMS error after stage 1 calibration was 12 μm.

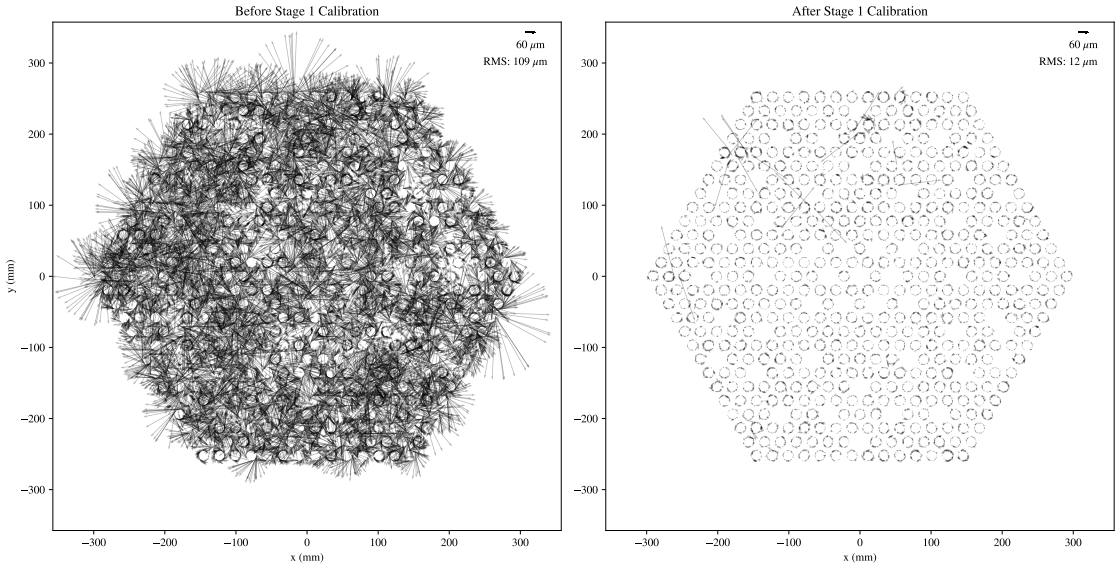

Figure 4.22 – Quiver plot showing fiber positioning error before and after stage 1 calibration. Roughly 50 random configurations were measured to characterize each robot. In stage 1 robot beta arm motion was limited between 155 and 180 degrees to avoid robot collisions. This results in each robot only sampling a thin annulus of the available workspace. This provided a rough calibration as a starting point for stage 2.

After stage 1 calibration, the best fit parameters for each robot were applied in `coordio`

(Sayres et al., 2022) and the robot path generation code `kaiju`[6] (Sayres et al., 2021). In this next stage of calibration the complete range of beta arm motion ($\beta_{\rm CMD} \in [0, 180]$ degrees) was permitted to obtain full-workspace sampling for each the robot. `kaiju` routines were used to compute collision-free paths between subsequent random robot configurations throughout the calibration sequence. This both tested our ability to reconfigure a full array of robots and collected calibration data using the same strategy that we use for moving between science configurations. After the second stage of calibration, the calibrated robot parameters were re-fit and updated in `kaiju`. Figure 4.23 shows fiber positioning errors before and after stage 2 calibration. The RMS fiber positioning error was measured to be 25 μm after stage 2. The increase in RMS with respect to stage 1 calibration is expected as the robots were allowed to sample their full workspaces rather than a thin sliver.

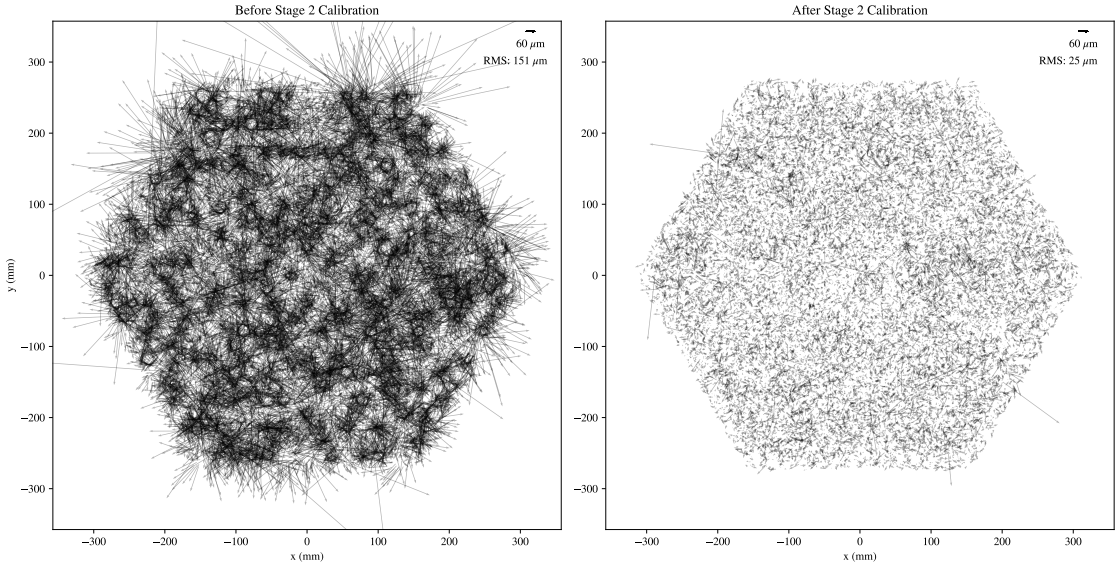

Figure 4.23 – Quiver plot showing fiber positioning error before and after stage 2 calibration. Roughly 50 configurations were measured to characterize each robot. Robots randomly sampled their full workspace using `kaiju` collision avoidance routines to move from configuration to configuration.

The stage 2 calibration results are summarized in Figure 4.24, which shows an empirical CDF

[6] https://github.com/sdss/kaiju

for blind positioning error for each robot in light purple traces, and for all robots as a bold orange trace. After applying stage 2 calibration parameters to each robot, 50% of measurements saw fiber positioning errors ≤ 16 μm and 97% of measurements saw fiber positioning errors ≤ 50 μm. Some additional percentiles for fiber positioning errors are provided in Table 4.1.

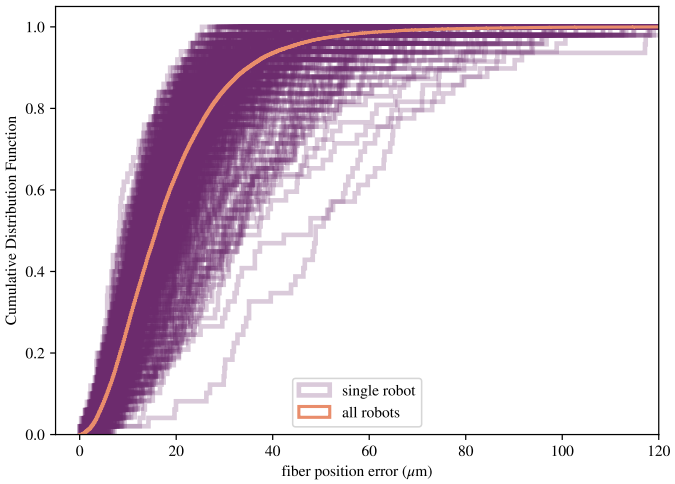

Figure 4.24 – Empirical CDF for blind move fiber positioning error from stage 2 calibrated robots. Data shown here are from ∼50 random moves for 500 robots. Faint traces correspond to an individual robot, while the bold orange trace summarizes all robots.

Figure 4.24 also indicates a hand-full of outliers: some robots see significantly larger fiber position errors than the rest of the population. These outliers could be due to either measurement errors (eg, faint or false metrology fiber detections) or unpredictable robot motion. The occasional large error vectors seen in the right hand panels of Figures 4.22 and 4.23 are likely measurement errors, but they don't explain the consistently worse behavior observed in some robots seen in Figure 4.24. We found (with the APO FPS) that throughout the course of early survey operations robots with the highest lab calibration errors began to increasingly throw internal motion faults until ultimately we were forced to disable them. It's likely that poor lab calibration results indicate a compromised unit that will eventually stop working. This was taken into account when deciding which robots to replace in the lab during LCO FPS calibration. Despite a few under-performing robots, we were happy with the robot lab calibration results which showed robots generally performing at the SDSS-V blind move specification (≤ 50 μm) while successfully avoiding each other during reconfigurations.

Table 4.1 – . Percentiles for blind move fiber positioning error after stage 2 lab calibration.

Percentile	error (μm)
50	16
90	35
95	43
97	50
99	68

4.8 Science Fiber Characterization

Each robot carries three fibers: a metrology fiber, a BOSS fiber, and an APOGEE fiber. During survey operations, we will measure and adjust locations of metrology fibers using camera feedback for each field configuration. Ultimately care about positioning a science fiber. Accurate science fiber positioning requires knowledge of where a science fiber is relative to the metrology fiber. We specify all fiber locations in the (non-rotating) beta arm frame (mm). The origin of the beta arm frame is the center of beta rotation and the +x axis passes through the metrology fiber's center. A picture of this coordinate system is shown in Figure 4.25. The location of the metrology fiber in this coordinate system is already known: it is measured in the robot characterization stage described in the previous section. This section describes our strategy to measure science fibers relative to the known metrology fiber location.

Immediately after robots were received, fiber bundles called "robotails" were installed into the beta arm of each robot. At the beta arm interface, a robotail consists of three 120 μm diameter fibers (metrology, APOGEE, BOSS) packed inside a single ferrule. The three fibers form an equilateral triangle. Fiber to fiber spacing is fairly well constrained within the ferrule, but the rotation of the fiber triad with respect to the beta arm is hard to control during manufacturing and assembly. Figure 4.26 shows a microscope image of a robotail ferrule installed in a robot's beta arm. In this example image the fiber triangle is rotated slightly clockwise with respect to the beta frame's x axis. To learn exactly where science fibers land in the beta frame, we have back lit them and

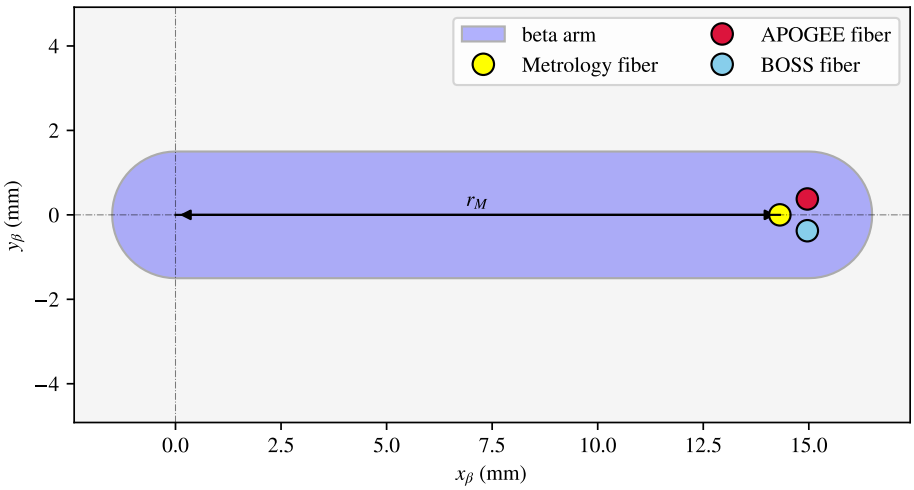

Figure 4.25 – The non-rotating beta arm coordinate system in which fiber locations are specified. The frame origin is located at the center of beta arm rotation. By construction, the metrology fiber location lands on the beta frame +x axis and r_M (the metrology fiber radius) is measured during robot characterization. The locations for APOGEE and BOSS fibers are measured and defined in this coordinate system.

measured their locations using the LTC.

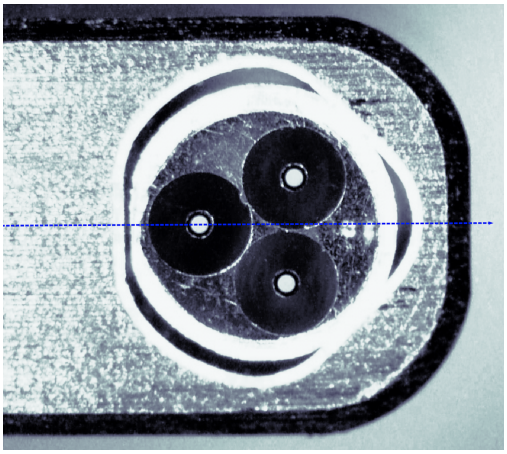

Figure 4.26 – Microscope image of the three fiber ferrule installed in a beta arm. The x axis of the beta frame is shown as a dashed line passing through the center of the metrology fiber. This image provides an example of a slight clockwise rotation of the fiber triad with respect to the beta arm coordinate system.

Science fibers were back lit from where they exit the FPS. BOSS fibers terminate in the BOSS slithead and APOGEE fibers terminate in the the "gang connector" port at the bottom of the instrument. Both of these are indicated in Figure 4.27. BOSS fibers were illuminated with a white light

LED strip and diffuser mounted in front of the BOSS slithead. APOGEE fibers were illuminated with an integrating sphere installed in the gang connector port. The integrating sphere was filled with the same red LED light (639 nm) that is used to illuminate metrology and fiducial fibers. The left side of Figure 4.27 shows the LED strip illuminating the BOSS fibers, the right side of the image shows the integrating sphere installed in the APOGEE gang connector port. Illumination intensity for BOSS and APOGEE backlighting systems was tuned to match the intensity seen from the fiducial and metrology backlighting system. Qualitatively, the PSFs from BOSS, APOGEE, and metrology/fiducial fibers all appeared similar during LTC measurement.

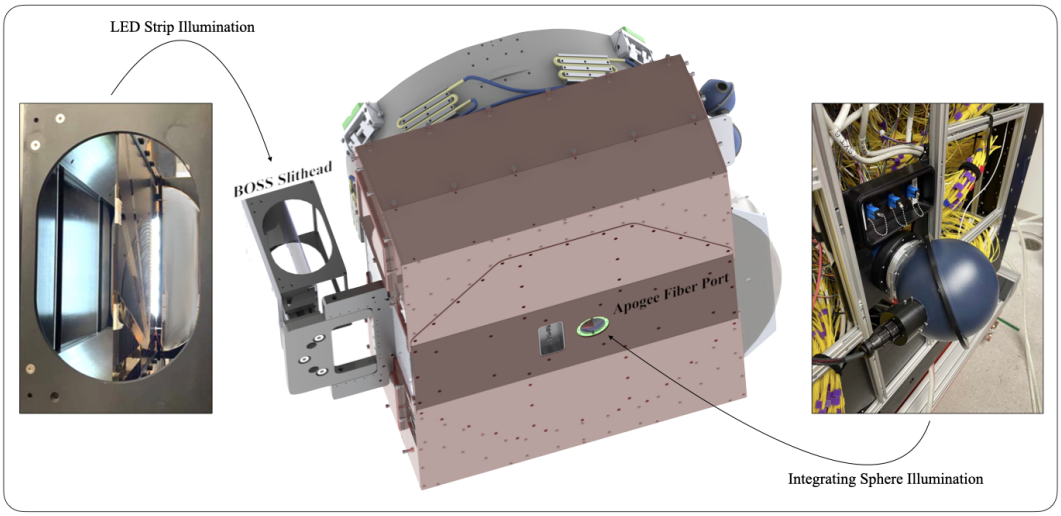

Figure 4.27 – View of FPS showing where science fibers exit the instrument. APOGEE fibers exit through a gang connector port on the underside of the instrument. BOSS fibers exit through the slithead. Both the slithead and gang connector port were illuminated for science fiber measurements in the lab.

Robots were moved to 40 random configurations to collect data for science fiber measurement. At each random configuration we took three sets of LTC images while the robots remain in fixed positions:

- **Set 1** Five LTC images with fiducial and metrology fibers illuminated.
- **Set 2** Five LTC images with only APOGEE fibers illuminated.
- **Set 3** Five LTC images with only BOSS fibers illuminated.

Using Set 1, 2, and 3 at each configuration j we measure:

- $\bar{\mathbf{w}}_{ij}^{M}$ The location of the metrology fiber in wok coordinates for robot i (an average over Set 1). In each image, the LTC transform (Equation 4.11) is fit from fiducial spots to provide wok coordinate estimation.
- $(\bar{\alpha'}_{ij}, \bar{\beta'}_{ij})$ The *measured* alpha and beta arm angles (Equations 4.17 and 4.18) for robot i (an average over Set 1).
- $\bar{L}_j$ The *mean* LTC transform, an average of similarity and Zhao-Burge parameters/coefficients from Set 1.[7]
- $\bar{\mathbf{p}}_{ij}^{A}$ The location of the APOGEE fiber in LTC pixels for robot i (an average over Set 2).
- $\bar{\mathbf{p}}_{ij}^{B}$ The location of the BOSS fiber in LTC pixels for robot i (an average over Set 3).

At each configuration j we compute the metrology to science fiber offset in wok coordinates (APOGEE and BOSS) for robot i

$$\mathbf{dw}_{ij}^{A|B} = \bar{\mathbf{w}}_{ij}^{M} - \bar{L}_j(\bar{\mathbf{p}}_{ij}^{A|B}). \tag{4.20}$$

The LTC transform $\bar{L}_j$ must be estimated and applied to (rather than fit from) science fiber measurement images because they lack the fiducial spots necessary for building a transform. Ideally science fibers, metrology fibers, and fiducial fibers would all be measured in the same image. In practice this was difficult due to the very close spacing between science and metrology fibers. Metrology and fiducial fibers are routed to the same illumination system, so we were unable to illuminate fiducial fibers without also illuminating metrology fibers (which land very close to science fibers). PSFs between metrology fibers and science fibers were clearly resolved over most of the LTC field but would bleed together at the field edges where the image quality degrades. This led to variable results when applying automatic centroid extraction routines to images in which all fibers were illuminated together, so we adopted a measurement strategy that only illuminated a single fiber on each robot at a time.

[7] We utilize this average transform for science fiber spots because fiducial spots are not illuminated during science fiber back illumination.

The procedure described above requires the measurement of a robot's alpha and beta angles. Framing the problem specifically: given the wok coordinate for robot's metrology fiber ($\mathbf{w}$), what are the robot's alpha and beta angles (α', β')? Inverse kinematic problems like this are of general interest in robotic control. There is no solution to this problem if $\mathbf{w}$ lands outside the robot's fiber patrol zone, there is one solution if $\mathbf{w}$ lands exactly on a patrol zone's outer or inner edge ($\beta' = 0$ or $\beta' = 180^{\rm o}$), and there are two solutions for $\mathbf{w}$ within the patrol zone. These two solutions correspond to "left armed" robots and "right armed" robots. In FPS operations we limit $0 \leq \beta' \leq 180^{\rm o}$ which means we need only consider the right armed robot solution. An algorithm (2RIK) providing the inverse kinematic solution for 2D robot arms is available online[8]. Here we show the mathematical steps of 2RIK algorithm applied SDSS-V robots governed by Equation 4.16, and we assume that the metrology fiber location $\mathbf{w}$ lies within the fiber patrol zone:

$$\mathbf{t} = \mathbf{w} - \begin{bmatrix} x_w \\ y_w \end{bmatrix} \tag{4.21}$$

$$c_2 = \frac{\|\mathbf{t}\|^2 - l_\alpha^2 - r_M^2}{2 l_\alpha r_M} \tag{4.22}$$

$$\theta = \arctan 2(\mathrm{t}_y, \mathrm{t}_x) \tag{4.23}$$

$$\beta' = \arccos(c_2) \tag{4.24}$$

$$\alpha' = \theta - \arctan 2(r_M \sin(\beta'), l_\alpha + r_M \cos(\beta'))). \tag{4.25}$$

The metrology to science fiber offset vector (Equation 4.20) is rotated from wok coordinates into the beta arm coordinate system using the measured alpha/beta angles for each robot i from configuration j

$$\mathbf{db}_{ij}^{A|B} = \begin{bmatrix} \cos(\bar{\alpha}'_{ij} + \bar{\beta}'_{ij}) & \sin(\bar{\alpha}'_{ij} + \bar{\beta}'_{ij}) \\ -\sin(\bar{\alpha}'_{ij} + \bar{\beta}'_{ij}) & \cos(\bar{\alpha}'_{ij} + \beta') \end{bmatrix} \mathbf{dw}_{ij}^{A|B}. \tag{4.26}$$

[8] https://motion.cs.illinois.edu/RoboticSystems/InverseKinematics.html

The left hand panel in Figure 4.28 shows APOGEE and BOSS fiber offsets measured in the beta arm frame from every configuration ($\mathbf{db}_{ij}$'s) for the 298 robots that carry both types of science fiber. The right hand panel shows the same data after averaging over all 40 configurations:

$$\langle \mathbf{db} \rangle_i^{A|B} = \frac{1}{40} \sum_{j=1}^{40} \mathbf{db}_{ij}^{A|B}. \tag{4.27}$$

It is clear from the left hand panel that BOSS fiber location measurements show very high variance with respect to the tightly-clustered APOGEE fiber measurements. This variance was found to be largely explained by an LTC scale difference when comparing BOSS and APOGEE/metrology fiber measurements.

This relative scale effect is shown in Figure 4.29. For this figure, we separately consider the mean wok location of the metrology fiber and the mean wok location of BOSS fiber. These mean positions were simple averages across all 40 configurations. Because robots were moved randomly around their workspaces, the mean location for any robot's fiber should roughly correspond to the robot's center. The arrows in this figure represent the difference between a robot's center according to BOSS or metrology fiber estimates. The radial component of the quiver pattern shown in Figure 4.29 was least-squares fit with a scale factor $s^* = 1.0007$. The results of this fit are shown in Figure 4.30. We apply this scale factor as a correction to Equation 4.20 for BOSS fiber measurements:

$$\mathbf{dw}_{ij}^B = \bar{\mathbf{w}}_{ij}^M - s^* \bar{L}_j(\bar{\mathbf{p}}_{ij}^B). \tag{4.28}$$

Figure 4.31 repeats the visualization shown in in Figure 4.28 using the modified LTC scale for BOSS fibers in Equation 4.28. With this image scale correction the variance in BOSS dxy fiber measurement is greatly reduced, and the spatial distribution of BOSS fiber measurements more closely resembles a translated and rotated version of the APOGEE fiber distribution. This is what we expect given the tri-fiber ferrule design when the rotation of the fiber triplet is not well constrained during fiber integration into the beta arm. Although greatly improved, BOSS fiber measurement scatter remains noticeably larger than APOGEE fiber measurements and so we

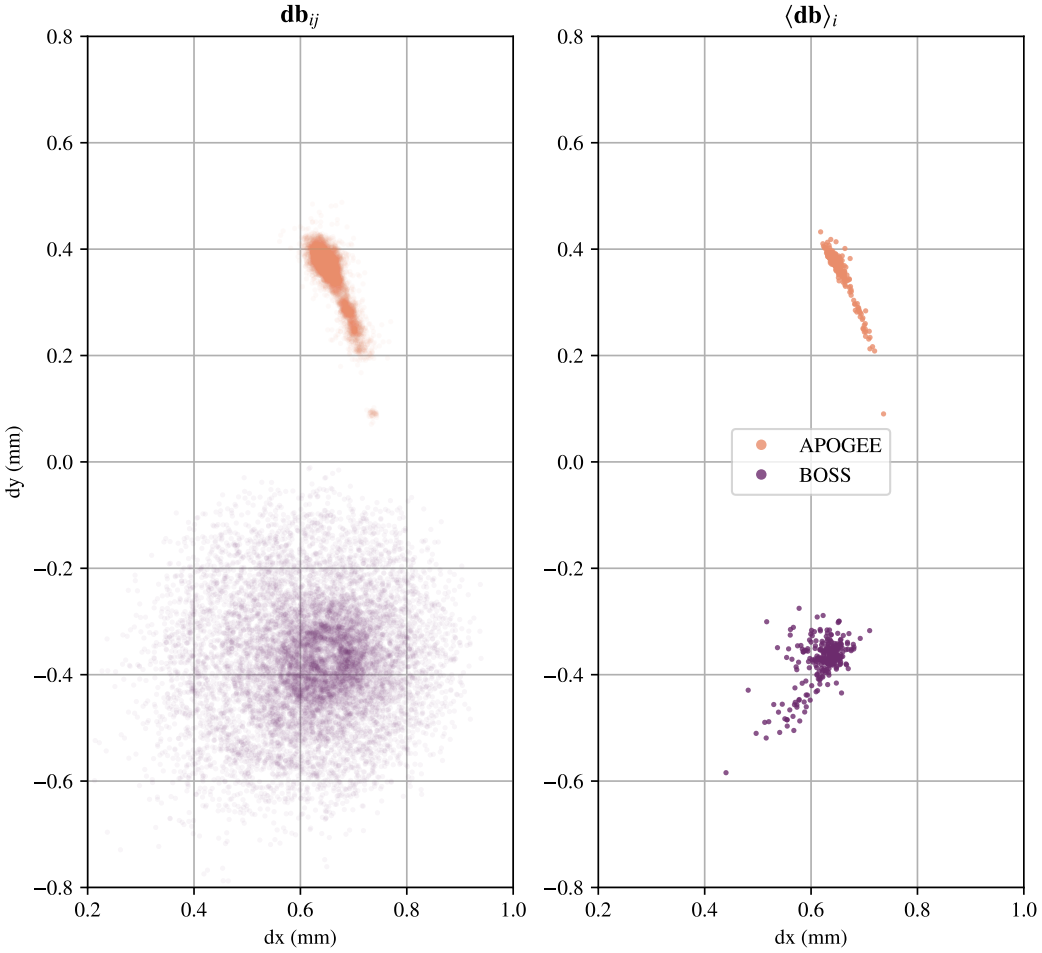

Figure 4.28 – Measured locations of science fiber offset relative to metrology fibers in the beta arm coordinate system for the 298 robots with both APOGEE and BOSS fibers. APOGEE fibers plotted in orange, BOSS fibers are plotted in purple. The left panel includes measurements from each robot in each configuration. The right panel shows the offset for each robot after averaging over all 40 configurations. BOSS fiber measurements show high variance relative to APOGEE fiber measurements.

attribute a higher uncertainty to BOSS fiber position measurements.

Fiber offset measurements are translated by the metrology fiber location to set science fiber locations ($\mathbf{b}^{A|B}$) in the beta arm coordinate system (Figure 4.25). For each robot i

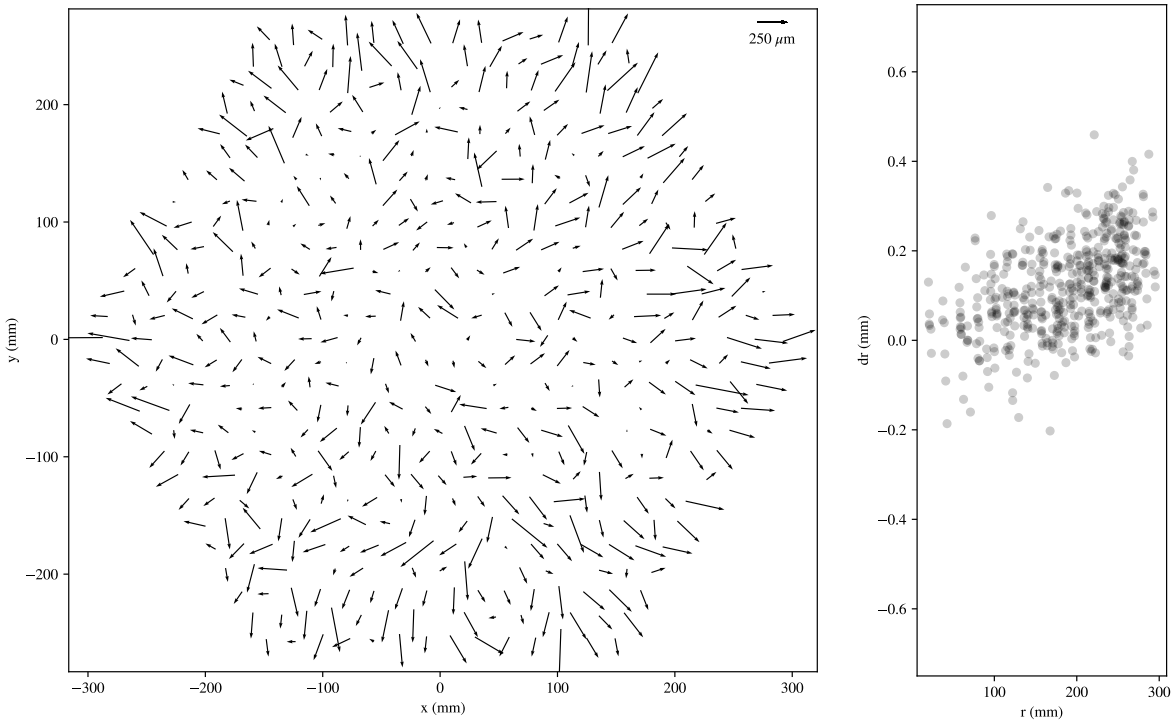

Figure 4.29 – Left panel: quiver plot indicating a scale difference between metrology fiber measurements and BOSS fiber measurements. Right panel: the radial error component plotted as a function of wok radius.

$$\mathbf{b}_i^{A|B} = \begin{bmatrix} r_M^i \\ 0 \end{bmatrix} + \langle \mathbf{db} \rangle_i^{A|B}. \tag{4.29}$$

With science fiber locations characterized we can write down the forward kinematic equations that describe the location of a science fiber in wok coordinates ($\mathbf{w}$) given alpha and beta angles (α', β')

$$\mathbf{w} = \begin{bmatrix} \cos(\alpha') & \cos(\alpha' + \beta') \\ \sin(\alpha') & \sin(\alpha' + \beta') \end{bmatrix} \begin{bmatrix} l_\alpha \\ l_\beta \end{bmatrix} + \begin{bmatrix} x_w \\ y_w \end{bmatrix}, \tag{4.30}$$

where

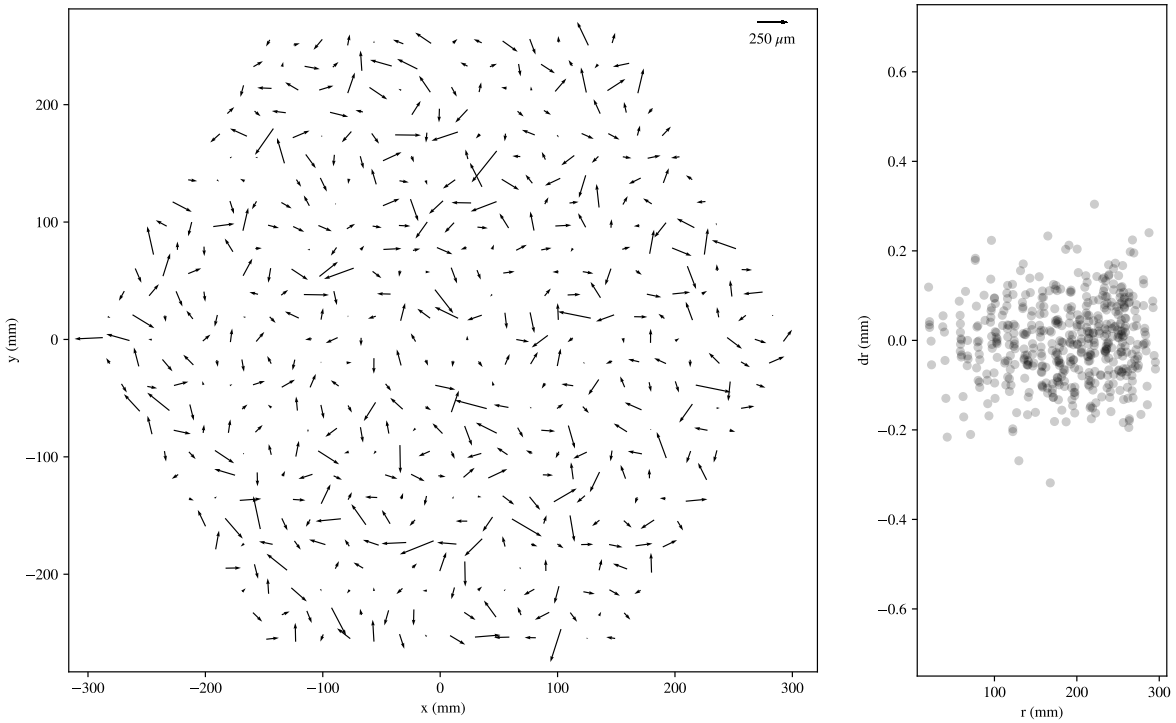

Figure 4.30 – Same as Figure 4.29 but after fitting and applying a scale factor to BOSS fiber measurement errors. The radial stretching observed in the original pattern has been removed.

$$l_\beta = \|\mathbf{b}\| \tag{4.31}$$

$$\theta_\beta = \arctan 2(\mathrm{b}_y, \mathrm{b}_x) \tag{4.32}$$

$$\alpha' = \alpha_\Delta + \alpha_{\mathrm{CMD}} - \frac{\pi}{2} \tag{4.33}$$

$$\beta' = \beta_\Delta + \beta_{\mathrm{CMD}} + \theta_\beta \tag{4.34}$$

A satisfactory explanation for the discrepancy between BOSS and APOGEE fiber measurements was never found. The LTC uses a narrow band filter, so a chromatic distortion cannot explain the observed differences between the white light illuminated BOSS fibers and the red light illuminated APOGEE/metrology fibers. Both APOGEE and metrology fibers were illuminated

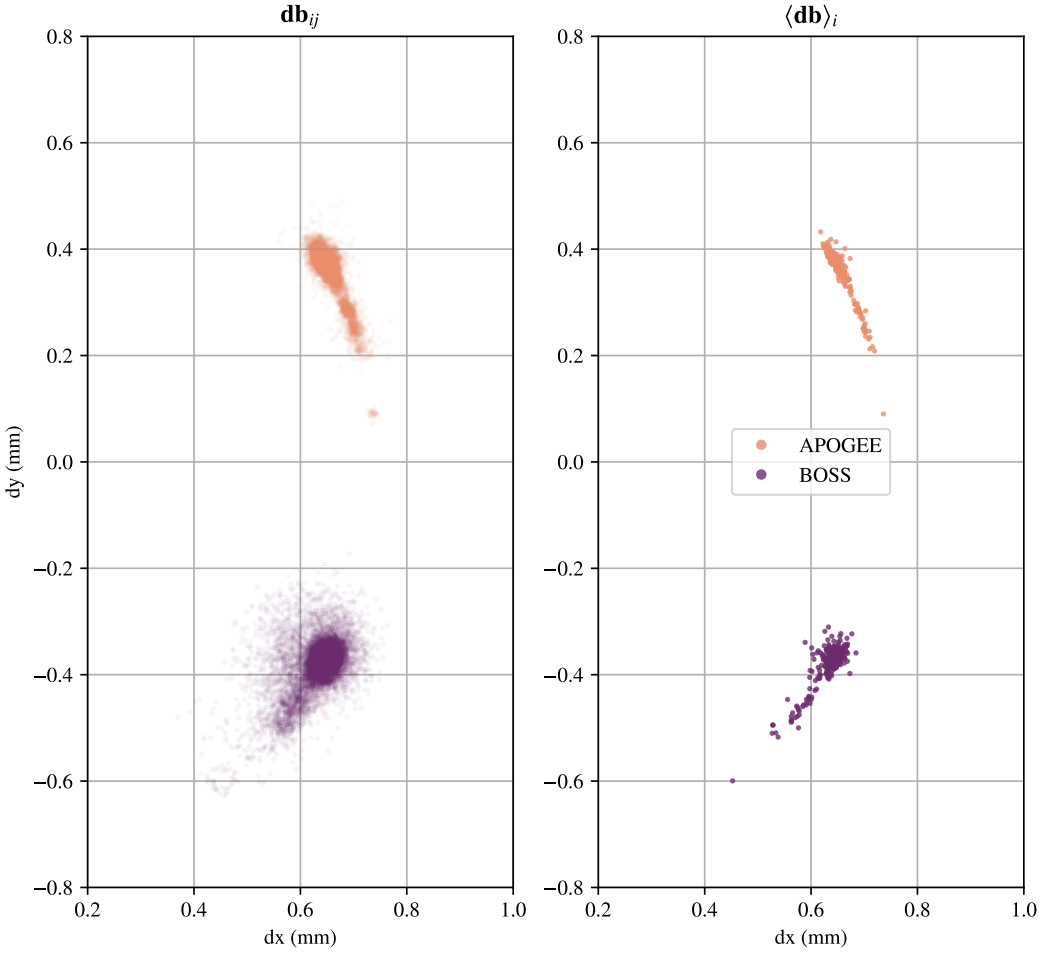

Figure 4.31 – Same as Figure 4.28 after BOSS fiber locations were adjusted by a scale correction factor. Variance in BOSS fiber measurements is greatly reduced, though it still remains higher than seen in APOGEE fiber measurements.

with integration spheres, while BOSS fibers were not. Perhaps the mechanism of light injection led to a (mostly scale) discrepancy between the two types of science fiber measurements.

For the APO FPS (the first unit completed), this discrepancy was not realized until the instrument was on sky for science commissioning. At this time we observed good throughput from APOGEE fibers and very poor throughput in BOSS fibers, and this was eventually recognized as the result from poor BOSS fiber location estimation during lab calibration. The BOSS fiber position errors were eventually corrected at APO using on-sky calibration sequences which are de-

scribed in later sections of this work. Months later during lab characterization of the LCO FPS, we anticipated this issue and collected significantly more science fiber measurement data to analyze and correct the differences between APOGEE and BOSS fibers. At the time of this writing LCO on-sky commissioning is ongoing, but initial BOSS fiber positions for the the LCO FPS appear more accurate when compared to our initial starting point for APO.

4.9 Discussion

The lab calibration stage for both APO and LCO FPS units was a crucial period for the project. Nearly all components of the instrument systems had been tested and exercised independently, but this was the first time the instrument was used in a way resembling normal telescope operations. This time period was very fast paced with pressure to get the instruments to the telescopes and on sky as soon as possible, and the lab calibration stage lasted less than two weeks for each instrument. Throughout the lab calibration campaign, continuous modifications were made to the instrument: poorly functioning robots were discovered and replaced, power and communication issues were discovered and resolved, fiducial fibers were repaired, etc. Most of these issues only manifested after the full array of 500 robots were in place and exercised over dozens of reconfigurations. Problems at the $\sim$1% level are rarely detected during piecewise component testing, but they show up with high frequency when using the full array. This full scale shakedown period was important to accomplish prior to shipping the instrument, as problems could be diagnosed and remedied much more efficiently in a lab setting.

In addition to hardware and electronic issues, software challenges arose and were addressed during the lab testing periods for both FPS units. Control and analysis software saw rapid development, debugging, and optimization. Robust strategies to automatically match centroids on a CCD to a specific fiducial or robot fiber were developed and tested. Procedures to configure robots and recover from motion errors were designed and implemented. Parameters for robot path generation and execution were explored and optimized. Real time monitoring of instrument metrology and GUI displays were implemented. Throughout the lab calibration stage for FPS units, flight SDSS-V control software was used and improved. Like the mechanical issues, this often required fixes

to bugs that only emerged when attempting to simultaneously operate a system composed of 500 common-networked robots.

Beyond general hardware and software fixes, the primary outcomes from FPS lab characterization were (1) ensuring that the instrument could successfully and consistently reconfigure robots, and (2) the calibrated quantities for fiducials, GFAs, robots, and science fibers (Sections 4.5-4.8) were measured "accurately enough" to take the instrument on sky. The definition of good enough is somewhat vague. For on-sky work to be successful we needed to get light down at least a handful of science fibers simultaneously as a starting point for on-sky calibration routines. If the uncertainty in relative location of GFAs to robots/fibers was greater than few arcseconds on sky we would risk an extremely lengthy and tedious fishing campaign to successfully latch even a single star in a single fiber. Along this line of reasoning the better we could characterize the instrument in the lab, the less time we would need to spend during on-sky commissioning before proceeding to general survey operations. The lab calibration results indicated that we had pinned critical measurements to less than a fiber width (120 μm), and this was expected to be sufficient to proceed with on-sky instrument calibration.

Most of our measurement uncertainty fell on BOSS fiber positions. We suspect that if we had been able to back illuminate BOSS fibers using the same system that was used for metrology and APOGEE fibers, the lab measurements would have been greatly improved. If this was anticipated prior to FPS assembly, a different BOSS illumination system might have been designed. This would have required lab calibration to happen before the BOSS slithead assembly was installed in the instrument, and would have necessitated changes in the sequencing of the instrument build. More science fiber data was collected for the LCO FPS than the APO FPS during lab testing, and this allowed us to model a correction for the LCO unit.

Fiber face microscopy was an extra resource available for measuring science fiber locations. After robotails were installed into each robot, they were imaged with a microscope for quality assurance purposes (see Figure 4.26). These images generally provided good measurements for centroids of all three fibers, however mapping these centroids to locations in the beta arm frame proved challenging. The fiber microscopy station was not designed nor calibrated to produce pre-

cision measurements of this type. The magnification, illumination, and robot beta arm orientation/alignment varied significantly from image to image, and the origin of the beta arm frame was very hard to estimate from microscopy imaging alone. For the 298 robots that carried an APOGEE science fiber, we were able to build a transform from the microscopy image to the beta arm frame when paired with LTC measurements of the metrology and APOGEE fibers. This allowed us to estimate the BOSS fiber location in the beta arm frame for a subset of robots. For the remaining 302 robots we were not able to leverage fiber microscopy imaging to estimate BOSS fiber locations. This was done as a stop gap measure during FPS commissioning at APO when BOSS fiber locations were discovered to be poorly measured (Figure 4.28), and after this procedure throughput was seen to improve for most BOSS fibers on sky. BOSS fiber locations for the LCO unit were more carefully characterized in the lab, and fiber face microscopy was not deemed necessary.

The movement seen in fiducials after CMM measurements was concerning, especially the larger fiducial displacements seen in the APO FPS. In the lab and on the telescope, the fiducials provide the means to measure fiber locations across the instrument. To achieve the fiber positioning performance we want, our measurements need to be very accurate. A CMM fiducial measurement campaign after the instrument was completely assembled would have led to better initial fiducial metrology, rather than measuring fiducials first and constructing the instrument around them. Post-assembly CMM measurements would have had the added benefit of measuring the locations for GFA fiducials after their installation into the wok, rather than estimating their locations based on LTC imaging. For a number of reasons this was impractical and would have required significant deviation from the project's schedule and budget to accomplish. The motivations for measuring fiducials first were (1) a fiducial-only populated FPS would fit within the envelope of the CMM we had identified for the task and the completely assembled instrument would not. (2) The fiducial-only populated instruments were much lighter and easier to move and manipulate, and (3) the fiducial-only populated units were much lower risk items to ship between the lab and the CMM vendor. Minimizing the shipping and handling for the complete FPS was a priority.

Lastly, the optical distortion pattern observed by the LTC was more complex than anticipated. Based on the optical design of the LTC lens doublet, we expected a purely radial distortion pattern.

If more time were available for lab experimentation, imaging the wok testing different relative locations or camera rotations between the LTC and FPS might have helped us better map LTC distortions, and this might also have informed an optimal location on the chip to place the back illuminated fiber field. When compared to other similar instruments, the lab characterization phase for the FPS was somewhat minimal. For example, lab calibration for the 4MOST instrument (Winkler et al., 2022) included a complete optomechanical mock up of their telescope, and also utilized a high spatial frequency metrology target to map optical distortions seen by their fiber metrology cameras at the fiber plane. Gear like this would have certainty aided lab calibration outcomes for our instrument. To improve upon lab calibration results, we move to on-sky calibration techniques. By our estimation the results we obtained during lab calibration phase indicated that is was reasonable to attempt on-sky work.

Chapter 5

FIBER POSITIONING II: ALIGNING FIBERS TO ASTROPHYSICAL SOURCES

5.1 Introduction

After the lab characterization phase, each fully-assembled FPS was shipped to the site (APO or LCO) and installed on the telescope to begin on-sky calibration and instrument commissioning. The FPS at APO saw first light in December 2021, and the FPS at LCO saw first light in August 2022. SDSS-V's goal for robotic fiber position accuracy is to consistently place an astrophysical sources within 16.5 μm of a science fiber's center. The derivation of this fiber position tolerance is covered in Section 5.2. A series of on-telescope calibration steps were performed to tune and improve fiber positioning. A key tool used for fiber positioning is the Fiber View Camera, which is described in Section 5.3. This instrument works in an analogous fashion to the Lab Test Camera (Section 4.3), but suffers from a more complicated and time dependent distortion field. On-sky fiber positioning was improved using "telescope dither" sequences, which are described in Section 5.4. These sequences allow us to measure and correct systematic errors in fiber placement and telescope pointing, both of which contribute to total fiber position error. Finally in Section 5.5 we provide an assessment of current fiber position accuracy using absolute photometric results from standard star observations reduced using the BOSS spectroscopic pipeline. A general discussion follows in Section 5.6 of outcomes and next steps.

For the on-sky work presented in Section 5.4 we will usually focus on data and results from APO. Although the FPS at LCO is fully operational and collecting data, we haven't yet implemented an extensive set of corrections built from on-sky commissioning results. We currently estimate that most fibers are achieving the 16.5 μm goal at APO, and all fibers are positioned such that the PSF center is within the fiber aperture (≤ 60 μm). We expect to continue improving fiber position error for each FPS over time.

5.2 On-sky Fiber Positioning Requirements

When positioning a science fiber, we attempt to minimize the displacement between fiber's center and the point spread function (PSF) of an observed object on the focal plane. We will generally refer to this displacement as a "fiber offset". A fiber offset of zero would collect the maximum

amount of flux available, assuming the telescope is well collimated, focused, and guiding. Maximizing flux collection is a clear objective for a survey that wants to move fast, as signal to noise thresholds will be reached in the quickest way possible. In practice a perfect alignment between a fiber and an astronomical source will never be achieved, and so we must consider tolerances or acceptable errors in fiber positioning in the context of SDSS-V's science requirements.

The amount of flux captured from a fiber will decrease as either fiber offset or seeing increases. At a given fiber offset, the amount of flux lost will depend on the size of the fiber, the seeing conditions, and the telescope's plate scale. Figure 5.1 provides a visual representation of these effects for the telescopes at APO and LCO. Both APO and LCO fibers have a diameter of 120 μm, which correspond to $\sim$2 and $\sim$1.3 arcseconds on sky. The white circles in Figure 5.1 represent a fiber aperture, and the color contours show a PSF under 0.8 arcsecond seeing (top panels) and 1.5 arcsecond seeing (bottom panels). We use a Gaussian to represent a PSF, and the seeing is described as the full width at half maximum (FWHM) of the Gaussian. In all panels in Figure 5.1 the PSF is displaced from the fiber center by 20 μm. The differing plate scales at APO and LCO mean that under the same seeing conditions the PSF will fill a different amount of the fiber aperture at the two sites. Although the PSF shape will have some field dependence throughout the focal plane, we will generally adopt symmetric Gaussian PSFs of identical widths throughout the focal plane for this work.

Our PSF model is a 2D symmetric Gaussian profile

$$F_{\mathrm{PSF}}(x, y, dx, dy, \sigma, f_o) = \frac{f_o}{2\pi\sigma^2} \exp\left(-\frac{1}{2}\left[\left(\frac{x-dx}{\sigma}\right)^2 + \left(\frac{y-dy}{\sigma}\right)^2\right]\right), \tag{5.1}$$

where σ is related to the seeing by the familiar relation

$$\mathrm{FWHM} = 2.355\sigma, \tag{5.2}$$

and dx and dy describe the fiber offset vector. f_o represents the total flux of the source. The total flux captured (TFC) can be calculated by integrating F_{PSF} over the fiber's aperture. Choosing polar coordinates for integration with dx, dy, and σ in units of microns, this can be written as

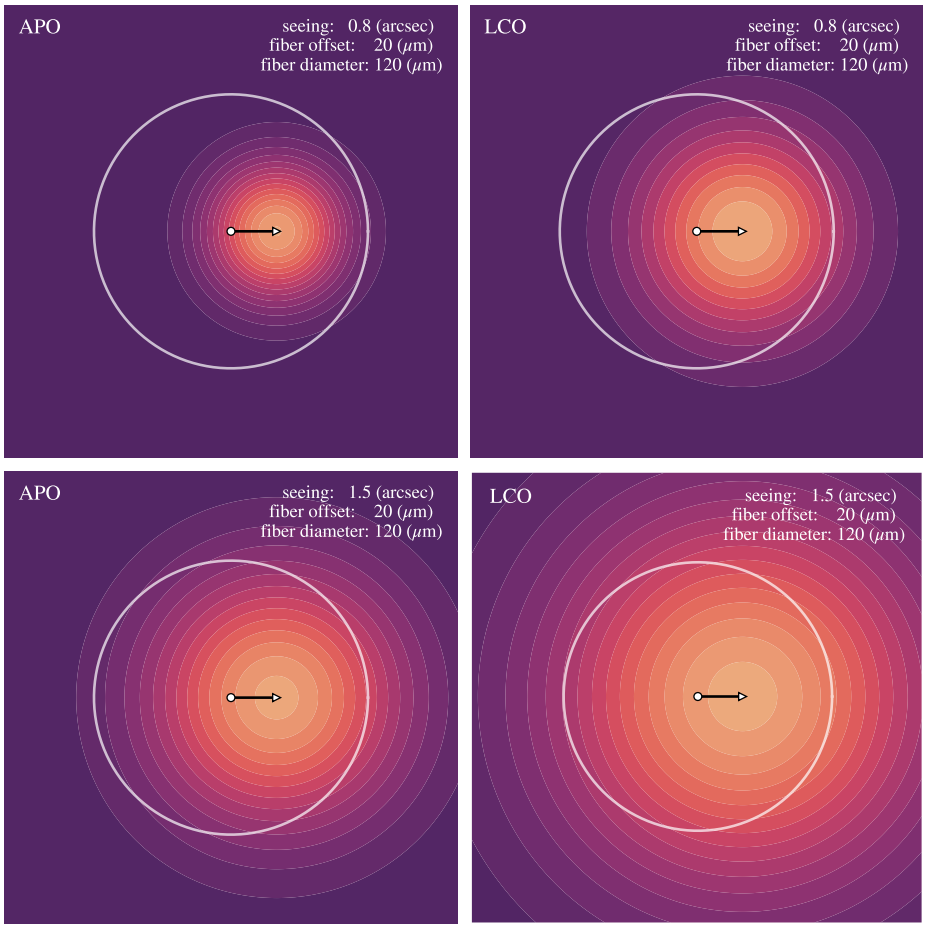

Figure 5.1 – Comparisons between fiber size and seeing at both APO and LCO. The white circles represent the 120 μm fiber. PSFs are modeled as 2D Gaussians, and seeing is the FHWM of the Gaussian PSF. In all panels the fiber offset between the fiber center and PSF is 20 μm and indicated by the arrow.

$$F_{\mathrm{TFC}}(dx, dy, \sigma, f_o) = \int_0^{2\pi} \int_0^{60} F_{\mathrm{PSF}}(r\cos\theta, r\sin\theta, dx, dy, \sigma, f_o) r\, dr\, d\theta, \tag{5.3}$$

and thus the total flux lost (TFL) is

$$F_{TFL}(dx, dy, \sigma, f_o) = f_o - F_{\mathrm{TFC}}(dx, dy, \sigma, f_o). \tag{5.4}$$

Figure 5.2 plots the total flux loss computed by Equation 5.4 for LCO and APO over a wide

range of seeing and fiber offset values, where fiber offset is $\sqrt{dx^2 + dy^2}$. f_o is set to 1 for these plots. APO is less sensitive to both seeing and fiber offset as fibers fill a larger area on sky with respect to LCO.

Relative flux loss (RFL) will be a more useful metric for tolerancing fiber offsets. Relative flux loss describes the fraction of flux lost relative to the amount of flux available given the seeing conditions. This is given by

$$F_{\mathrm{RFL}}(dx, dy, \sigma) = 1 - \frac{F_{\mathrm{TFC}}(dx, dy, \sigma, f_o \mid f_o = 1)}{F_{\mathrm{TFC}}(dx, dx, \sigma, f_o \mid dx = dy = 0, f_o = 1)}, \tag{5.5}$$

and plotted in Figure 5.3 over a wide range of fiber offsets and seeing values for APO and LCO.

Among SDSS-V's array of science programs, the BHM reverberation mapping project places the tightest constraints on fiber positioning errors. This program aims to limit spectrophotometric variability to $\sim$5% for repeat observations of quasars. This constraint can be directly translated into a bound on fiber offset as a function of seeing:

$$F_{\mathrm{RFL}}(dx, dy, \sigma) \leq 0.05. \tag{5.6}$$

Figure 5.4 plots this inequality. Shaded regions below the respective APO and LCO curves indicate where the inequality is satisfied. The maximum permitted fiber offset that satisfies Equation 5.6 across all seeing conditions is 16.5μm. This limit defines our fiber positioning error budget in SDSS-V operations.

5.3 Fiber View Camera

5.3.1 Optical Design and Ray Trace Distortion Analysis

The Fiber View Camera (FVC) performs a task at the telescope similar to LTC's role in the lab. The FVC measures centroids from back illuminated metrology and fiducial fibers to estimate their absolute position in the focal plane. The FVC delivers an image scale of 120 μm/pixel. We use FVC feedback to iteratively correct a robot's orientation during array reconfiguration to position

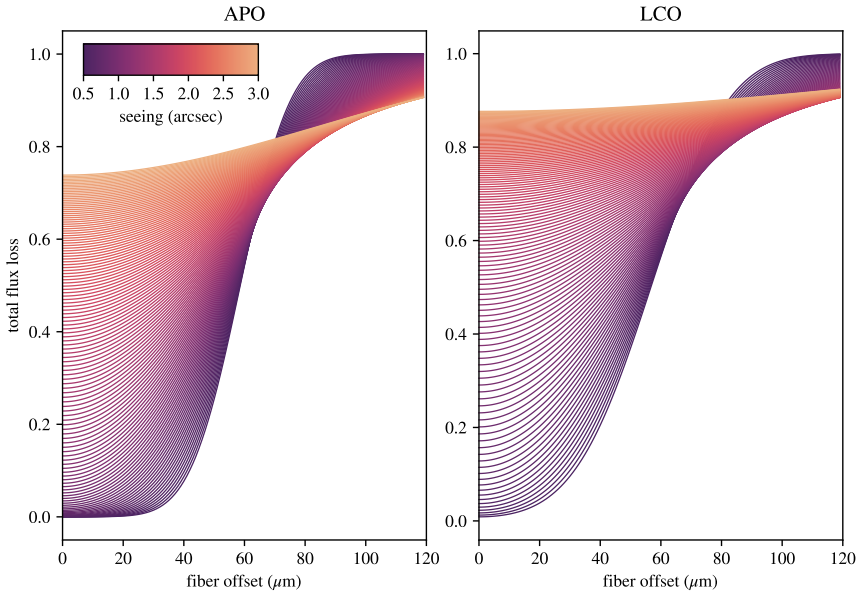

Figure 5.2 – Total flux loss over a range of fiber offset and seeing values for APO and LCO. Curves are generated from Equation 5.4.

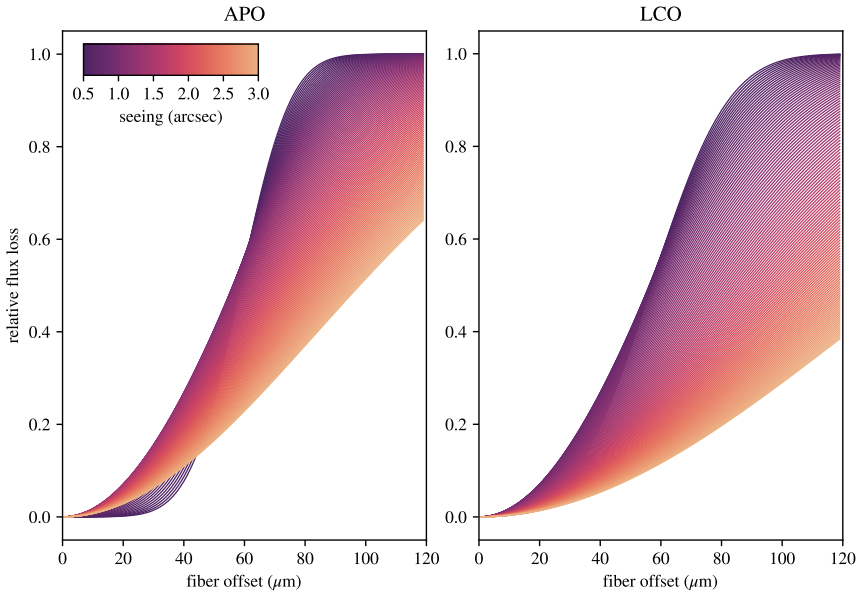

Figure 5.3 – Relative flux loss over a range of fiber offset and seeing values for APO and LCO. Curves are generated from Equation 5.5.

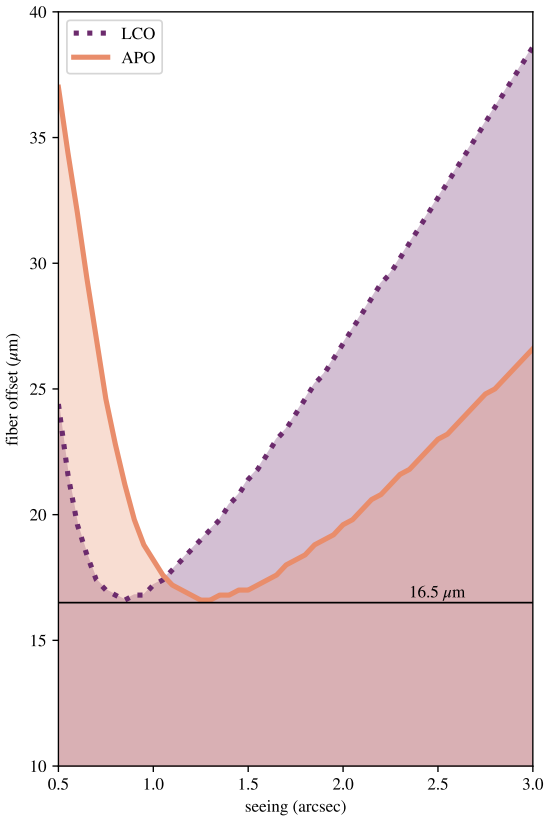

Figure 5.4 – Shaded regions for APO and LCO where flux variation is $\leq 5\%$, representing the acceptable limits for BHM spectrophotometry. Fiber offsets $\leq 16.5\mu$m will always satisfy the inequality in Equation 5.6 and inform tolerancing for fiber positioning errors in SDSS-V. The differing shape between the two curves is due to the different plate scales at each telescope.

science fibers at higher accuracy than a typical blind robot move would accomplish. The FVC uses the same CCD, narrowband filter, and fiducial/metrology fiber back illumintion system as described in Section 4.3, but the optical path from FPS to the CCD is significantly more complicated than the lab imaging system. At both APO and LCO, the FVC is mounted to a custom lens barrel, and uses a pickoff mirror to stare at a small patch of the telescope's primary mirror. At both telescopes, light rays from illuminated fibers pass through a Gascoigne corrector, reflect off the telescope's secondary and primary mirrors before entering the FVC lens tube. Figure 5.5 shows the FVC optical path at both APO and LCO telescopes. Details of the FVC optomechanical design are described in Jurgenson et al. (2020).

FVC optical distortions are important to understand for accurately measuring and placing fibers. Zemax models for both the APO and LCO FVC systems were used to perform ray tracing from the FPS fiber tips to the FVC CCD to simulate distortions and test models for distortion

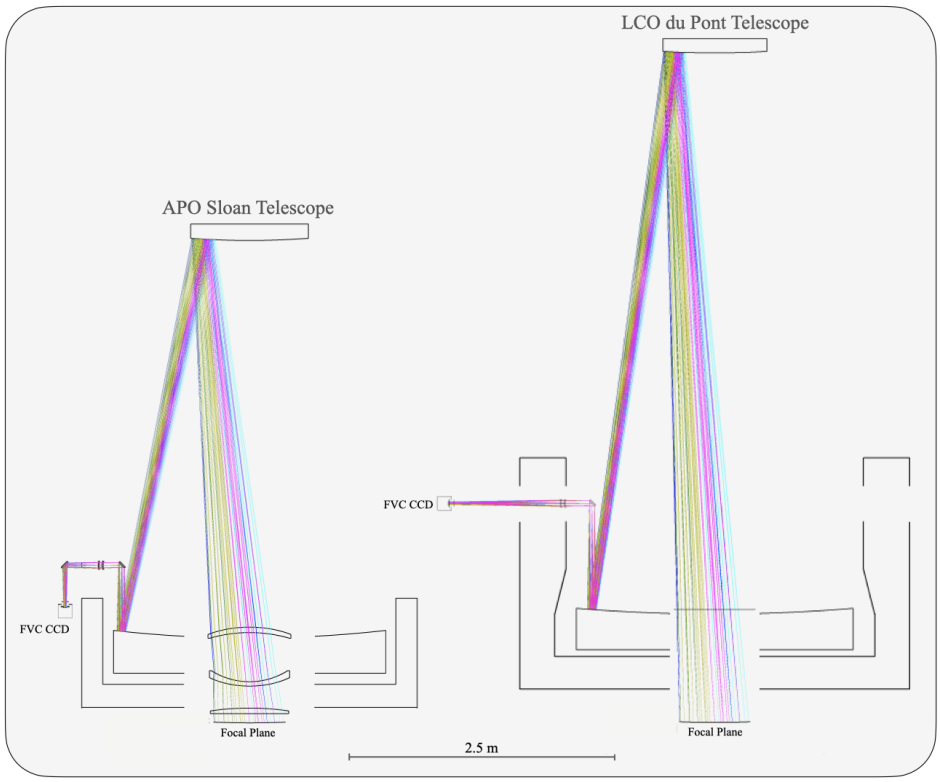

Figure 5.5 – FVC optical path for both APO (left) and LCO (right).

fitting. Zemax's ZOS-API was used to script ray traces for ∼30,000 spatially uniform points across the wok within or equal to the outer fiducial radius. The fiducial locations were explicitly included in the simulated ray trace data. The fiducial data (60 points) were then used to fit a similarity and Zhao-Burge transform (Section 4.4) to predict wok location from a CCD measurement. We report errors by testing the model against the ∼23,000 simulated points across the hexagonal field that the robots patrol.

The Zemax-derived field distortion for the LCO FVC is shown in Figure 5.6. Rays are traced from the xy wok surface in mm to the CCD surface in pixels. The left hand panel shows the residuals after fitting applying a pixel to mm similarity transform, the right hand panel shows the residuals after fitting and applying an additional Zhao-Burge polynomial correction (same procedure as Section 4.4). Only data from the fiducial locations (open circles in left panel) were used for fitting, and the remainder of the field was used to test the model. For this model, we used the

same basis of Zhao-Burge polynomials as was used in the lab (Section 4.4). The model residuals for the LCO FVC were 2 μm RMS, with a maximum error of 5 μm.

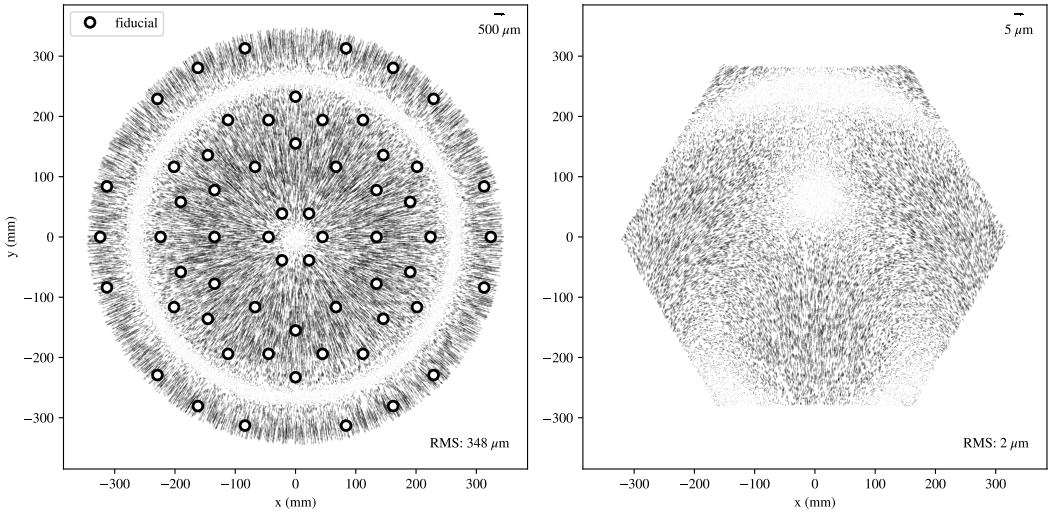

Figure 5.6 – LCO FVC simulated optical distortion derived from Zemax ray traces. Left panel: distortion field residuals after similarity transform fit. Right panel: residuals after applying Zhao-Burge polynomial fit over the positioner field. The distortion model was fit from the 60 points at the fiducial locations in wok coordinates.

Ray trace analysis of the APO FVC system revealed a tricky distortion pattern to model. Figure 5.7 shows the model fitting results (analogous to Figure 5.6 for LCO). For APO, we tested and included additional Zhao-Burge terms that minimized test error. The extra Zhao-Burge polynomials included in the APO FVC transform model were $\{\vec{S}_9, \vec{S}_{12}, \vec{S}_{17}, \vec{S}_{24}, \vec{T}_{13}\}$. Our model resulted with an RMS test error of 15 μm across the positioner field. The RMS error is skewed high by the large errors seen near the top of the field in Figure 5.7. The median error was 7 μm, the 80th percentile error was 13 μm, and the maximum error was 50 μm. At LCO and APO, these ray trace simulations informed the basis functions for FVC pixel to world transforms we would at the telescopes.

At both telescopes, the FPS is mounted to an instrument rotator at Cassegrain focus, thus we can rotate the fiber field with respect to the FVC CCD. The Sloan Foundation Telescope at APO is an alt-az design, so the orientation of the FPS with respect to the FVC will depend on telescope

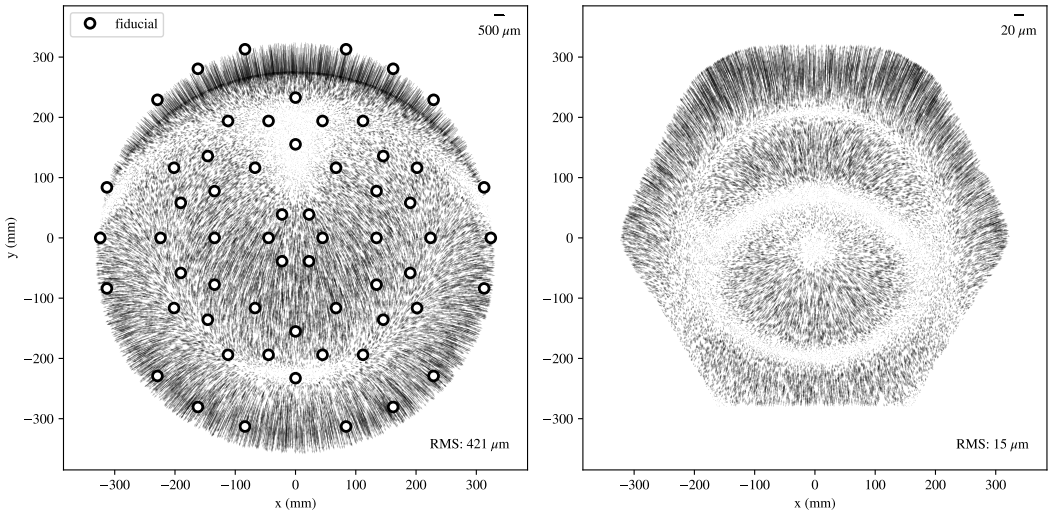

Figure 5.7 – Same as Figure 5.6, but showing APO Zemax simulations.

pointing and desired field position angle. The du Pont telescope at LCO is an equatorial design, so the rotation of the FPS with respect to the FVC will generally stay within a 30 degree rotator range. This corresponds to the range of position angles for which SDSS-V science fields are designed. For calibration purposes we will use the full range of rotator motion available at LCO, which is roughly 300 degrees.

5.3.2 Delivered Image Quality

Figure 5.8 shows a full field FVC image of back illuminated metrology and science fibers from both APO (left) and LCO (right). In this figure the image scale has been adjusted to show extra contrast. FVC images are processed and centroids are extracted using the same procedure as described in Section 4.3. Figure 5.9 shows a random selection of 100 centroids identified in background subtracted FVC images at APO (left panel) and LCO (right panel). Each centroid is plotted as a 10 x 10 pixel cutout, stacked into a 10 x 10 grid with no particular grid ordering. The delivered spot size at APO is smaller than LCO, suggesting a better focused system. However at both telescopes the PSF shape and intensity varies across the field.

To investigate field dependence of the PSF we compile data from several random robot con-

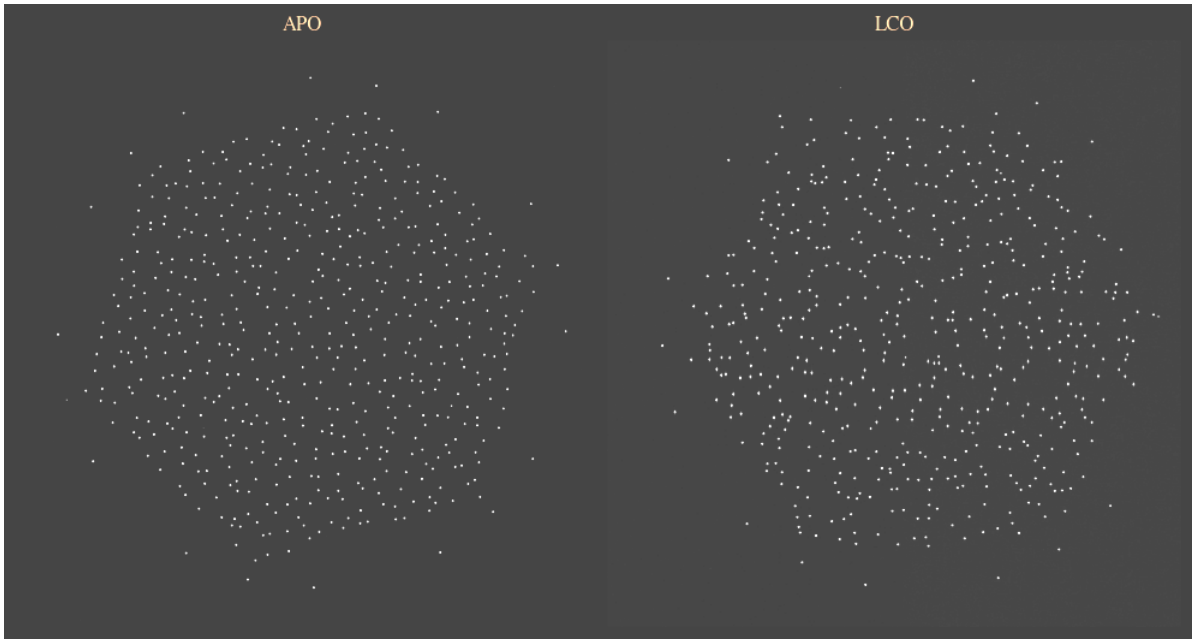

Figure 5.8 – FVC images of back illuminated metrology and science fibers. APO is shown on the left, LCO is shown on the right. The image scale has been modified to increase contrast in both images.

figurations imaged at dozens of instrument rotator angles. This provides a dense sampling across the FVC FOV. We use second moment analysis of extracted centroids as a metric for PSF spread. Specifically we choose to look at the variance in the x (σ_x^2) and y (σ_y^2) CCD directions across the FVC FOV. Figure 5.10 shows histograms for these values at APO (top panel) and LCO (bottom panel). At both telescopes σ_x^2 varies slightly, but σ_y^2 shows a population of PSFs that are very elongated along the CCD's y axis. Spots at APO are generally rounder than spots at LCO. Figures 5.11 and 5.12 plot the same data spatially across the FVC FOV. At both APO and LCO, the PSF y-elongation is concentrated in a band across the middle CCD roughly aligned with the CCD's x axis. The PSF y-elongation effect is larger at LCO than at APO.

The FVC was designed to deliver uniform diffraction limited PSFs across the field, so this PSF non-uniformity was not anticipated. In fact this effect went unnoticed at APO until well into commissioning where we detected a central band of low fiber throughput, and this band happened to always align with the FVC's CCD axes. This strongly hinted at where we should begin to

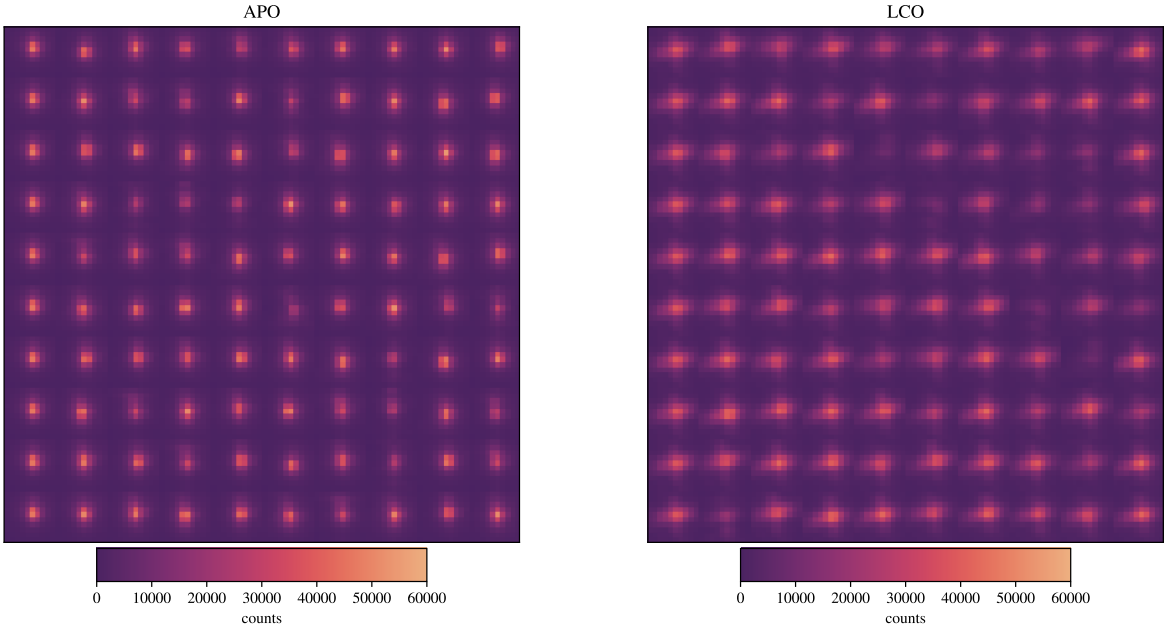

Figure 5.9 – A random selection of 100 centroids from across the FVC field arranged into a randomly ordered grid. APO centroids are shown in the left panel, LCO centroids are shown in the right panel. Each centroid is a 10 x 10 pixel cutout from the original image.

investigate. The most probable explanation for PSF y-elongation is that it is due to diffraction off one or more thin wires. Both telescopes are installed with a mid-baffle which is supported by several thin wires that bisect the FVC FOV along the CCD's x axis. Figure 5.13 shows baffle locations with respect to the FVC's optical path for both telescopes.

Related to baffling, the LCO FOV is partially vignetted along the right edge. This can be noticed in Figure 5.12, where the outer ring of fiducials is not detected for x pixels $>$ 6500. This effect was anticipated from the optical model. Figure 5.14 provides a more obvious view of vignetting and diffraction at LCO. The left image is a raw FVC image taken with the dome lights on and the FPS unmounted, imaging the illuminated dome floor. The right image was taken with the dome lights on, FPS mounted, and the fiber back illumination intensity cranked to maximum power. The dome illumination in the right image provides contrast for physical elements lying in the optical path from the focal plane to the CCD, and reveals ghost reflections. In both views the baffle partially vignettes the right side of the FVC image. The full area of the fiber positioner field

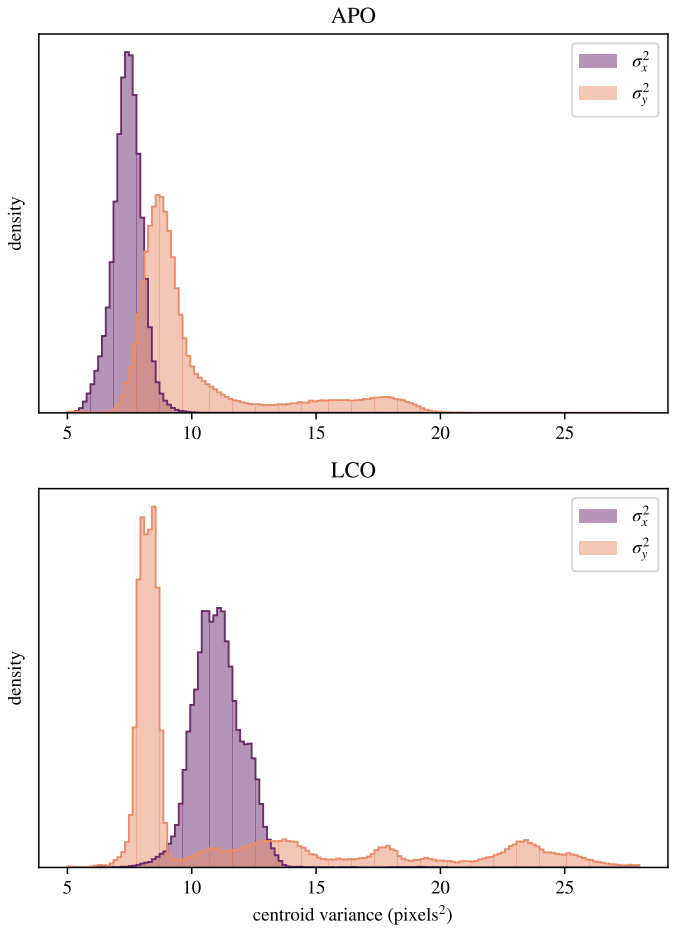

Figure 5.10 – Histogram showing PSF widths in x and y directions across the FVC FOV. PSF widths are characterized by the variance along each axis. APO results are shown on the top panel, LCO results on the bottom panel.

is visible, but outer ring fiducials are lost. Baffle support wires are seen bisecting the FVC image and spatially coinciding with observed PSF y-elongation.

5.3.3 Static Distortion Correction: 2D Fourier Model

Here we present our strategy to empirically measure and fit the optical distortion field seen by the FVC. In the absence of a distortion field, we would expect the spot from a robot's metrology fiber to trace a perfect circle around the CCD as a function of instrument rotator angle. For each metrology fiber, we can measure the deviation from circularity as a function of CCD position and use this to empirically construct a mean distortion pattern across the field. Rather than being limited to the fiducial fibers, this strategy uses spots from 500 metrology fibers in each FVC image which yields

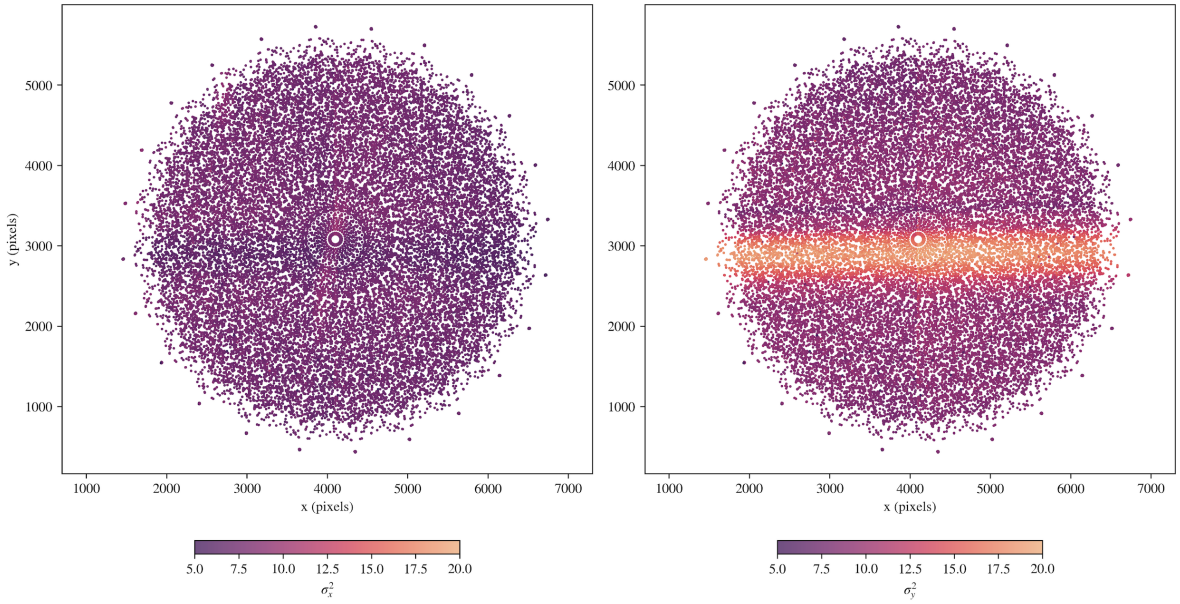

Figure 5.11 – PSF width as a function of FVC field position for APO. Left hand panel plots PSF variance in CCD x direction, Right hand panel plots variance in CCD y direction.

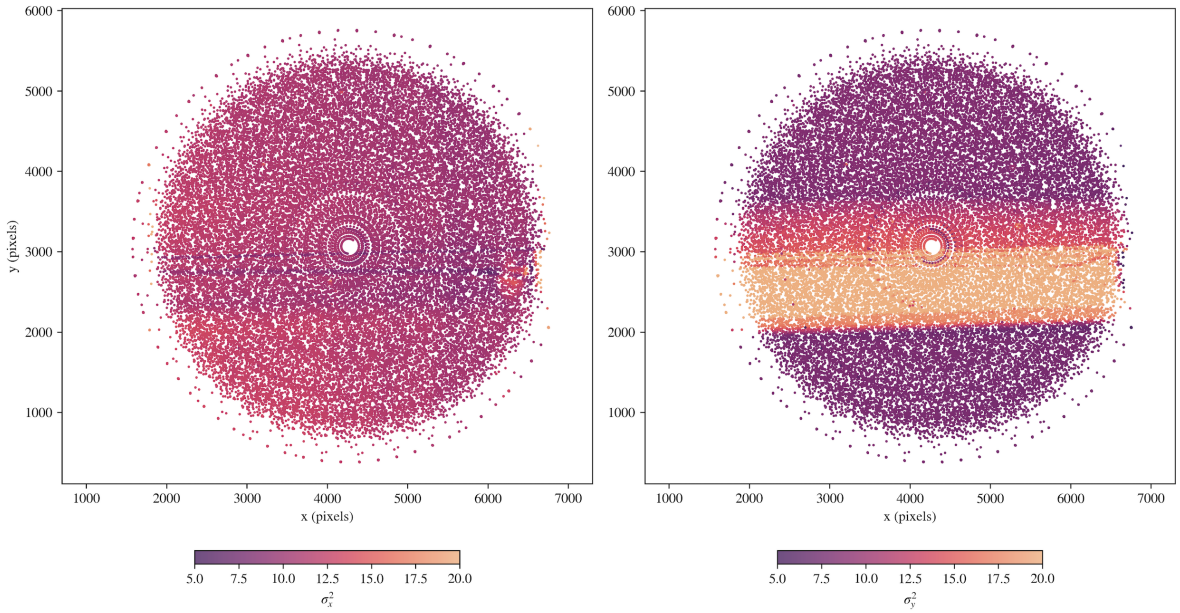

Figure 5.12 – PSF width as a function of FVC field position for LCO. Left hand panel plots PSF variance in CCD x direction, Right hand panel plots variance in CCD y direction.

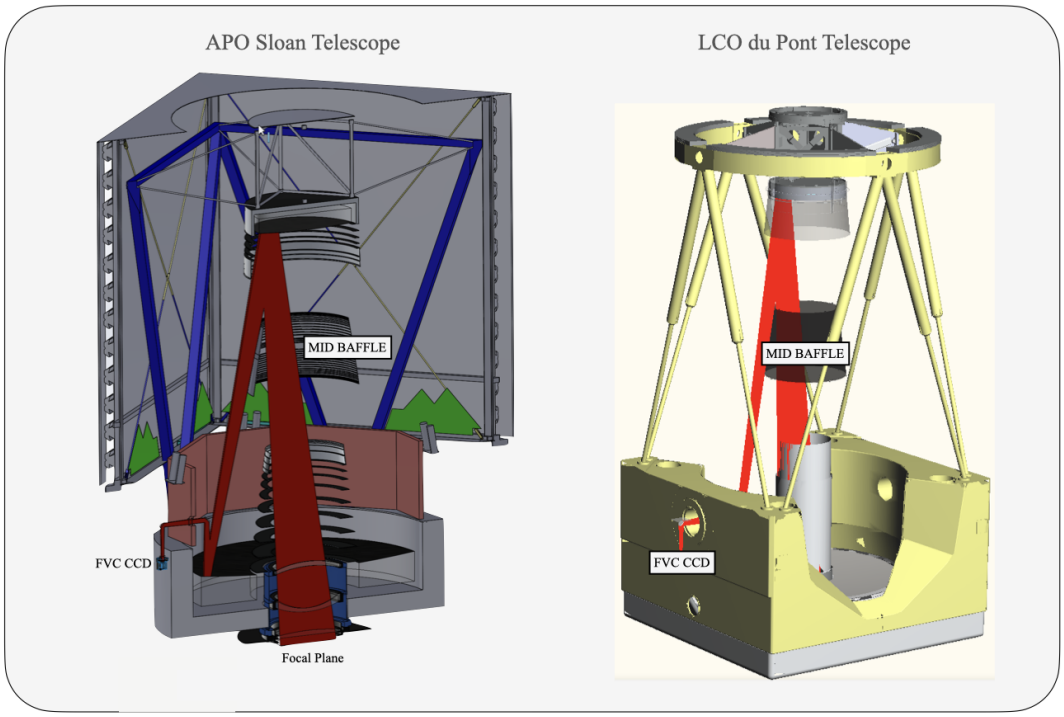

Figure 5.13 – FVC optical path for APO (left) and LCO (right) including telescope baffles. Mid baffle support wires are not shown, though in reality they bisect the FVC FOV.

a dense sampling across the CCD.

For this we use the same data presented in the previous section which showed a field dependence on PSF shape. The data collection steps are specifically: (1) arrange the robots in a random configuration, (2) move the instrument rotator in $\sim$ 15 degree increments over its full range, (3) take several FVC images at each rotator position of backlit metrology fibers. Steps 1-3 were repeated twice at APO and three times at LCO. Throughout each rotator scan the robot configuration remains stationary. The data were collected with the telescope pointed at zenith.

In each image j from robot configuration k, fiducials are identified and fit with a similarity transform (Equation 4.1) to estimate s^*_{jk}, θ^*_{jk}, and $\mathbf{t}^*_{jk}$. We omit the Zhao-Burge correction for this analysis, as we aim to capture field distortions rather than fit them out at this stage. In each FVC image, we apply the similarity transform to each metrology fiber location $\mathbf{p}_{ijk}$ on the CCD to estimate the wok coordinates $\mathbf{w}_{ijk}$ for each robot i, and we compute the average wok location for

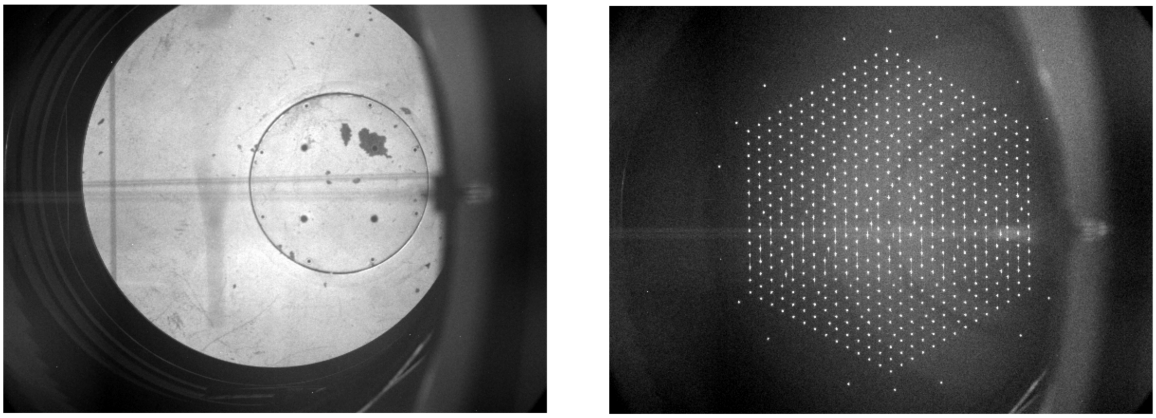

Figure 5.14 – Two FVC images from LCO with dome lights on, illuminating features in and around the telescope. Left image shows a picture of the dome floor (FPS was not mounted). In the right image the FPS was mounted and back illumination power was maximized (saturating the CCD). In both views telescope baffling affects the right side of the FVC FOV. Baffle support wires bisect the field. Ghost reflections are also present.

each metrology fiber over each configuration j as

$$\langle \mathbf{w} \rangle_{ik} = \frac{1}{n} \sum_{j=0}^{n} \mathbf{w}_{ijk}, \tag{5.7}$$

where n is the number of images obtained over a single rotator scan. Given the mean wok location over a rotator scan, we compute the wok frame deviation for each robot in each FVC image within a rotator scan

$$\mathbf{dw}_{ijk} = \mathbf{w}_{ijk} - \langle \mathbf{w} \rangle_{ik}. \tag{5.8}$$

The wok frame rotates with respect to the CCD frame throughout a rotator scan, but we seek to measure the fixed distortion pattern in the CCD frame. As a final step we rotate and scale the $\mathbf{dw}_{ikj}$ deviation vector back into the CCD frame using the best fit rotation and scale parameters from each image

$$\mathbf{dp}_{ijk} = \frac{1}{s^*_{jk}} \begin{bmatrix} \cos\theta^*_{jk} & \sin\theta^*_{jk} \\ -\sin\theta^*_{jk} & \cos\theta^*_{jk} \end{bmatrix} \mathbf{dw}_{ijk}. \tag{5.9}$$

The calculations above are applied to ∼228,000 metrology fiber measurements taken at APO and ∼165,000 metrology fiber measurements taken at LCO. Figure 5.15 plots these data in the CCD coordinate system. Quiver arrows represent $\mathbf{dp}_{ijk}$ vectors, and arrow bases are located at the metrology fiber centroid location $\mathbf{p}_{ijk}$ on the FVC CCD. APO data are plotted on the left panel, and LCO data are plotted on the right panel. For each pattern we calculate an RMS for the measured deviations as

$$\mathrm{RMS} = \sqrt{\mathrm{mean}(\{\|\mathbf{dp}_{\mathrm{ijk}}\|^2\})}, \tag{5.10}$$

which has units of pixels. This RMS may be scaled to microns using the FVC scale of 120 μm/pixel.

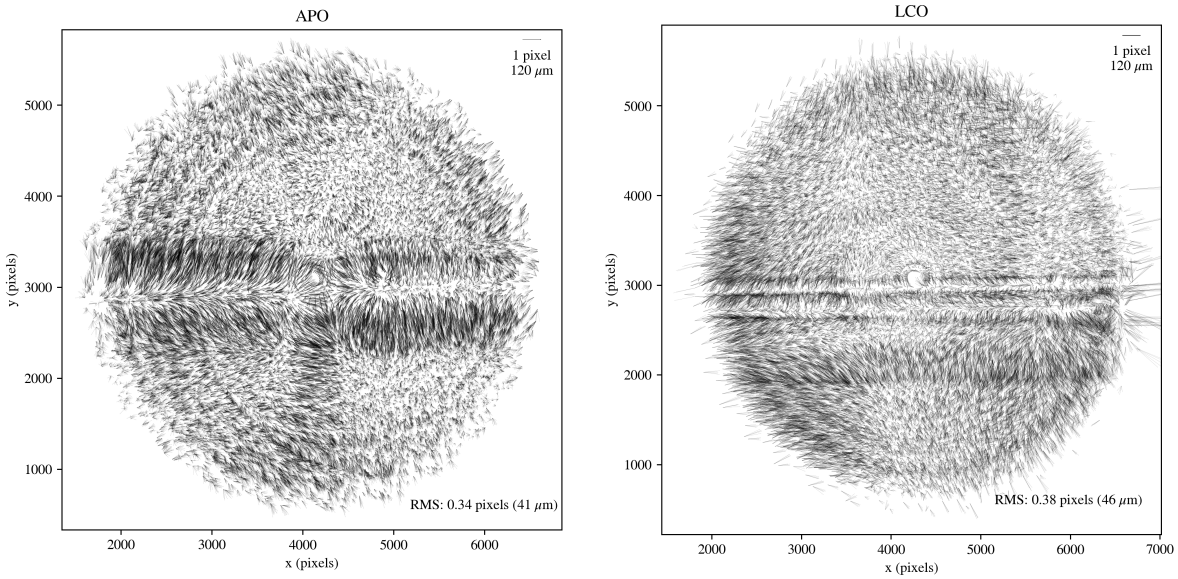

Figure 5.15 – Empirical FVC distortion pattern generated by FVC imaging of metrology fibers at different instrument rotator angles.

At both telescopes we see a strong distortion associated with the PSF y-elongation bands shown

in Figures 5.11 and 5.12. Generally, centroids measured in the lower half of this band are biased upward on the chip, and centroids measured in the upper half of this band are biased downward on the chip. There are additional high-frequency spatially correlated distortions seen around the field in both APO and LCO.

These mean distortion patterns are different in appearance and lower in magnitude than what was expected from the ray trace analysis shown in Figures 5.6 and 5.7. The empirically measured distortion RMS values are < 50 μm, where RMS values derived from ray trace analyses were $\sim$ 400 μm. Note that our rotator scan strategy to measuring this distortion field is largely insensitive to a purely radial distortion (the expected distortion at LCO appears largely radial). Zhao-Burge polynomials will be used in a later stage of FVC distortion mapping to account for this.

We fit a 2D Fourier model to the spatial patterns shown in Figure 5.15, and apply this model to every FVC image at APO and LCO in pixel space to subtract off the mean measured distortion. Our model parameters are:

- $\mathbf{p} = (x, y)$ location of centroid in FVC pixels
- i integer wave number in x direction
- j integer wave number in y direction
- m maximum bound on spatial frequencies where $i^2 + j^2 \leq \mathrm{m}^2$
- ℓ half the Fourier series interval length in pixels.

Our model definition is:

$$
\begin{aligned}
f(x, y, \vec{c}) = &\sum_{i=0}^{\mathrm{m}} \sum_{j=0}^{\lfloor\sqrt{\mathrm{m}^2 - i^2}\rfloor} \cos\left(\frac{i\pi x}{\ell}\right) \cos\left(\frac{j\pi y}{\ell}\right) d_{ij} \\
&+ \sum_{j=1}^{\mathrm{m}} \sum_{i=0}^{\lfloor\sqrt{\mathrm{m}^2 - j^2}\rfloor} \cos\left(\frac{i\pi x}{\ell}\right) \sin\left(\frac{j\pi y}{\ell}\right) e_{ij} \\
&+ \sum_{i=1}^{\mathrm{m}} \sum_{j=0}^{\lfloor\sqrt{\mathrm{m}^2 - i^2}\rfloor} \sin\left(\frac{i\pi x}{\ell}\right) \cos\left(\frac{j\pi y}{\ell}\right) f_{ij} \\
&+ \sum_{i=1}^{\mathrm{m}-1} \sum_{j=1}^{\lfloor\sqrt{\mathrm{m}^2 - i^2}\rfloor} \sin\left(\frac{i\pi x}{\ell}\right) \sin\left(\frac{j\pi y}{\ell}\right) g_{ij}, \qquad (5.11)
\end{aligned}
$$

where coefficients $\vec{c} = \{d_{ij}, e_{ij}, f_{ij}, g_{ij}\}$ will be solved for by constructing an ordinary least squares problem $X\vec{c} = \vec{y}$. For this model, we choose $\mathrm{m} = 32$ and $\ell = 5000$ pixels. Expanding the sums in Equation 5.11 leads to a linear model of 3209 terms. We randomly sort our data into an 80% training and 20% testing set, resulting in a design matrix X shape of 181962×3209 for APO and 131968×3209 for LCO. We fit the x and y distortion components separately by solving the least squares problems

$$X\vec{c}_x = \vec{dx} \tag{5.12}$$

$$X\vec{c}_y = \vec{dy}, \tag{5.13}$$

where $\vec{dx}$ and $\vec{dy}$ are the x and y components from each $\mathbf{dp}$ vector included in the training set. After solving for the best fit x and y coefficients ($\vec{c}_x$ and $\vec{c}_y$), this FVC pixel correction model is:

$$P(\mathbf{p}) = \begin{bmatrix} f(\mathbf{p}\cdot\hat{\mathbf{x}}, \mathbf{p}\cdot\hat{\mathbf{y}}, \vec{c}_x) \\ f(\mathbf{p}\cdot\hat{\mathbf{x}}, \mathbf{p}\cdot\hat{\mathbf{y}}, \vec{c}_y) \end{bmatrix} \tag{5.14}$$

We apply this Fourier model to the APO and LCO datasets. The residuals after fitting are shown in Figure 5.16. The test errors are 0.14 and 0.19 pixels RMS for APO and LCO, reducing the measurement error by roughly a factor of two. The Fourier model clearly captures the large scale distortions seen across the field, especially in the y-elongation band. Additionally it accurately predicts much of the higher spatial order distortions seen in the original data. At LCO clear stripes of higher residuals remain, and these stripes are spatially correlated with the nearly in focus baffle support wires shown in Figure 5.14. For fibers landing in these thin stripes in the LCO FOV we will expect less accurate fiber positioning performance. At this time we are hesitant to apply a higher order fit, and instead wait to see if these stripes at LCO show poorer performance on sky before acting further.

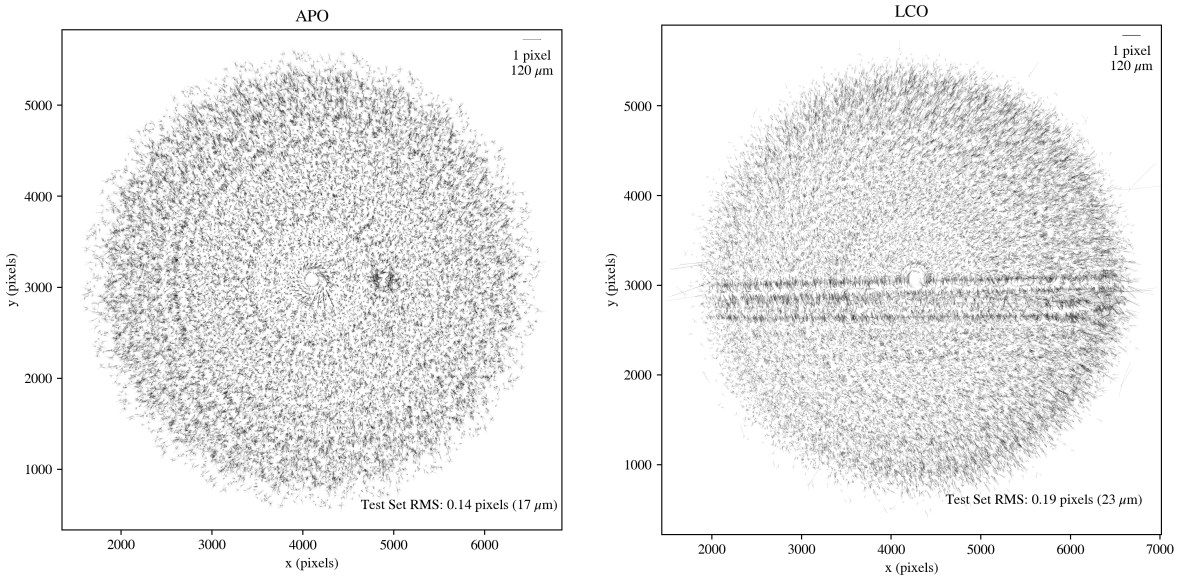

Figure 5.16 – Residuals after fitting a 2D Fourier model to the distortion patterns shown in Figure 5.15.

5.3.4 Dynamic Distortion Correction and Measurement Repeatability

In this section we describe an additional "dynamic" distortion model which is fit from fiducial fiber spots in each FVC image. This model is applied on top of the static-model pixel adjustment (Equation 5.14) that is applied to every FVC measurement. This dynamic adjustment significantly reduces the variance in metrology fiber measurement. The strategy is identical to the method described in Section 4.4. In each FVC image fiducial spots are identified and fit with a similarity transform and the similarity transform residuals are further fit with a Zhao-Burge (ZB) polynomial correction. The only difference between this dynamic distortion model and the LTC transform is that we choose an extended ZB basis of 33 polynomial terms: $\vec{S}_{\{2-28\}}$ and $\vec{T}_{\{4,7,8,11,12,13\}}$. Combining Equations 4.11 and 5.14 yields the FVC transform[1]

$$F_1(\mathbf{p}) = L(P(\mathbf{p})). \tag{5.15}$$

[1]The FVC transform will receive an additional static term derived from on-sky measurements. The adjusted FVC transform is described later in Section 5.4.7 Equation 5.23.

To investigate the image to image variance in FVC measurement we again use the data set described in the previous two sections. At each rotator angle and robot configuration pair we compute the average metrology fiber location for robot i over a set of $n = 5$ repeat images. We subtract the mean value from each FVC measurement to construct an error vector. Each exposure is 5 seconds long, and time between subsequent exposures is ∼20 seconds. We show three piecewise flavors of this error vector, where each flavor represents an increasing layer of modeling. The first flavor shows the measured displacement of a metrology fiber centroid on the CCD

$$\mathbf{ep}_{in} = 120 \left[P(\mathbf{p}_{in}) - \frac{1}{5} \sum_{n=1}^{5} P(\mathbf{p}_{in}) \right], \tag{5.16}$$

where the factor of 120 scales the units from pixels to microns of motion in the focal plane. The second set of error vectors are the residuals after a similarity transform is applied to metrology fiber centroids in each frame

$$\mathbf{es}_{in} = S(P(\mathbf{p}_{in}), s^*, \theta^*, \mathbf{t}^*) - \frac{1}{5} \sum_{n=1}^{5} S(P(\mathbf{p}_{in}), s^*, \theta^*, \mathbf{t}^*), \tag{5.17}$$

where similarity transform parameters $s^*, \theta^*, \mathbf{t}^*$ are fit from fiducial spots for each image. The final error flavor results from a similarity transform and 33 ZB term vector polynomial model fit to the fiducial spots in each FVC image

$$\mathbf{ez}_{in} = F_1(\mathbf{p}_{in}) - \frac{1}{5} \sum_{n=1}^{5} F_1(\mathbf{p}_{in}). \tag{5.18}$$

Figures 5.17 and 5.18 show the error flavor sequence from Equations 5.16-5.18 for three repeated images at APO and LCO. Three subsequent exposures ($n = 1, 2, 3$) are shown along columns from left to right, and the error vector flavors $\mathbf{ep}_{in}$, $\mathbf{es}_{in}$, and $\mathbf{ez}_{in}$ are plotted along panel rows from top to bottom. At both sites the distortion pattern is seen to change shape significantly from image to image. We attribute this shifting pattern to changing dome seeing conditions between images. The density of fiducials across the field provide a means to de-warp these distortion patterns for each image.

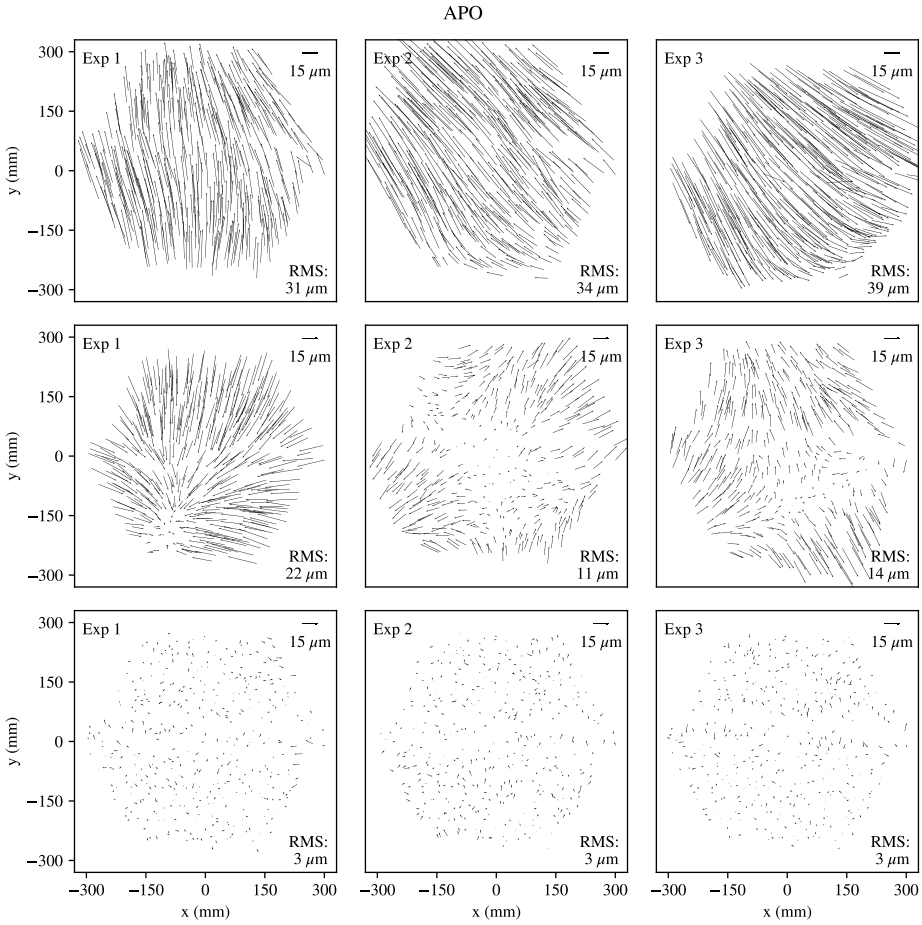

Figure 5.17 – Image to image centroid motion for metrology fiber measurements by the FVC at APO. Columns left to right plot data obtained from three subsequent FVC images. Quiver arrows represent the deviation from the mean measured location for metrology fibers over a set of five FVC images. The top row shows error relative to the mean pixel for each metrology fiber (scaled to micrometers). The middle row shows residuals after applying a similarity transform fit to fiducials in each image. The bottom rows shows residuals after applying a similarity transform + Zhao-Burge polynomial fit to fiducials in each image. The distortion pattern is seen to vary significantly from image to image. We attribute this variation to dome seeing conditions.

Figure 5.19 plots a histogram of error magnitudes ($\|\mathbf{ez}_{in}\|$, Equation 5.18), after repeating 5 image sequences for 2-3 robot configurations over dozens of rotator angles. Table 5.1 provides percentile statistics that describe these FVC measurement error distributions. The variance in FVC measurement is slightly higher at LCO, but at both sites we expect measurement repeatability to

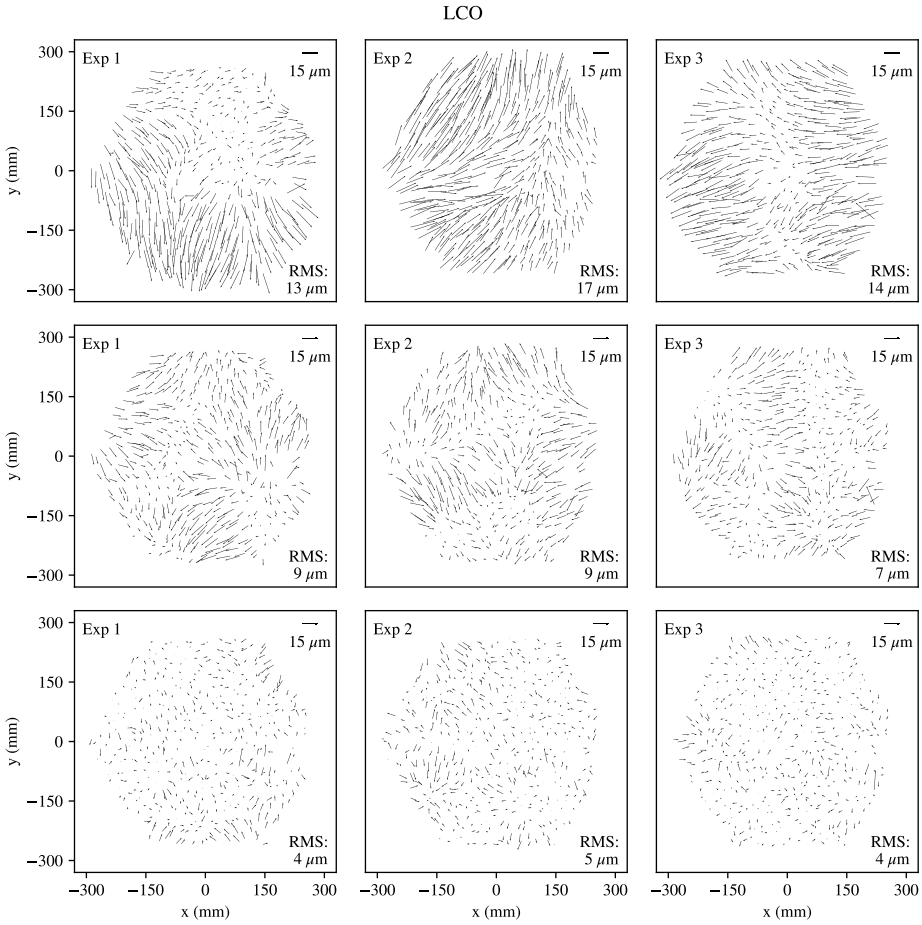

Figure 5.18 – Same as Figure 5.17, but applied to sequential FVC measurements from LCO.

$\sim$10 μm or better in the focal plane with RMS errors around 4 μm.

5.3.5 FVC Loop: Robotic Fiber Positioning Feedback

Sections 5.3.3 and 5.3.4 describe the construction and repeatability of the FVC transform (Equation 5.15) that maps FVC pixels to millimeters in the wok frame. With this transform defined, we will use the FVC to measure and correct the absolute orientation of robots during field reconfiguration, a procedure we call the FVC loop.

The FVC loop requires the assignment of a science fiber (APOGEE or BOSS) for each robot to a target wok coordinate $\mathbf{w}_T^S$. The coordinate assignment must be reachable by the intended robot

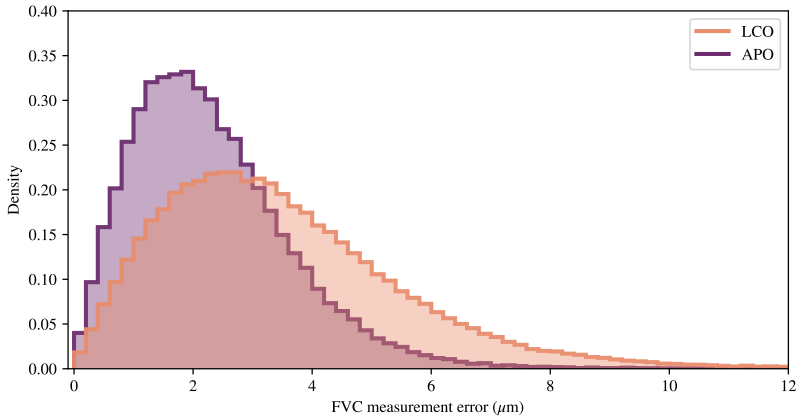

Figure 5.19 – Histogram of FVC metrology fiber measurement errors after fitting fiducials in each image with a similarity + ZB model. The histogram is generated using repeat images taken from dozens of rotator angles and robot configurations at APO and LCO.

(within the robot's annular workspace), and the set of all coordinate assignments must not create a situation in which robot arms are collided with one another. Science fiber targets are selected from astronomical catalogs and converted into wok coordinates via the coordinate systems and transform stack described in Sayres et al. (2022). In addition to a valid set of target assignments, the FVC loop requires the calibrated quantities derived in Sections 4.7 and 4.8: robot centers, angular arm offsets, alpha arm lengths, and beta frame fiber locations.

The FVC loop steps are for each robot (1) calculate the target (α_T, β_T) angular coordinates such that the desired science fiber lands on $\mathbf{w}_T^S$ and command the robot to move there. (2) After the blind move, use the FVC to measure the error in robot arm orientation $(\mathrm{d}\alpha, \mathrm{d}\beta)$, and command a corrective move $(\alpha_T + \mathrm{d}\alpha, \beta_T + \mathrm{d}\beta)$. (3) Use the FVC to measure the final location of the science fiber in wok coordinates $\mathbf{w}_F^S$. The FVC cannot directly measure the location of a science fiber, a science fiber's location is computed based on a measurement of the metrology fiber and a robot's calibrated quantities. At stages (2) and (3) of this procedure we record the metrology fiber position error (ϵ_1 and ϵ_2) to monitor FVC loop convergence. The inputs and outputs for the FVC loop are shown in Table 5.2, and a detailed algorithm for this procedure is provided in Section A.2.

The performance of the FVC loop at both APO and LCO is shown in the cumulative distri-

Table 5.1 – . Percentiles for FVC single exposure measurement error of metrology fibers. Errors are reported relative to the mean position from a five image sequence during which robots and instrument rotator remain fixed. Statistics are compiled from dozens of sequences taken at varied instrument rotator angles and robot configurations.

Percentile	APO error (μm)	LCO error (μm)
50	2	3
90	4	6
95	5	7
97	5	7
99	6	11

butions of Figure 5.20. At each site 500 FVC loops were performed, corresponding to ∼250,000 fiber placements. The purple curves plot the ϵ_1 (blind move) error and the orange curves plot ϵ_2 (FVC corrected) metrology fiber position error. Dashed lines indicate LCO data, and solid lines indicate APO data. Percentiles for ϵ_2 errors at APO and LCO are provided in Table 5.3.

We compare the ϵ_2 values to the 16.5 μm fiber position error bound derived in Section 5.2. From these FVC measurements 97.5% and 96.5% of fiber placements meet this criteria at APO and LCO respectively. Additional iterations of FVC correction may be explored in the future as a method to further reduce fiber positioning errors during reconfiguration, although decisions like these need to be balanced against overall survey efficiency and the time cost of performing extra iterations or image averaging. Currently we record FVC measured fiber position errors for each science configuration, and allow data pipeline teams to decide whether and when to exclude certain fibers from a specific analysis.

5.4 On-Sky Calibration

5.4.1 Section Overview

This section covers the many stages of on-sky FPS operations from target selection to data analysis in the context of instrument commissioning. The purpose of commissioning observations is to

Table 5.2 – . Inputs and outputs of FVC loop procedure.

Inputs	
W_T^S	500×2 array of science target xy wok coordinates for each robot
B	500×2 array of calibrated xy beta arm coordinates for each robot's APOGEE or BOSS fiber.
C	500×2 array of calibrated xy robot centers in wok coordinates.
$\vec{r}^M$	500×1 array of calibrated metrology fiber radii for each robot.
$\vec{l_\alpha}$	500×1 array of calibrated alpha arm lengths for each robot.
$\vec{\alpha}_\Delta$	500×1 array of calibrated alpha angle offsets for each robot.
$\vec{\beta}_\Delta$	500×1 array of calibrated beta angle offsets for each robot.
Outputs	
ϵ_1	500×1 array of metrology fiber position errors after blind move for each robot as measured by the FVC.
ϵ_2	500×1 array of metrology fiber position errors after corrective move for each robot as measured by the FVC.
W_F^S	500×2 array of final measured xy wok coordinates for robot science fibers after FVC feedback correction.

Table 5.3 – . Percentiles for ϵ_2 errors from 500 FVC loops ($\sim$250,000 metrology fiber placements) at APO and LCO.

Percentile	APO ϵ_2 (μm)	LCO ϵ_2 (μm)
50	5	5
90	10	12
95	12	15
97	15	18
98	18	22
99	31	33

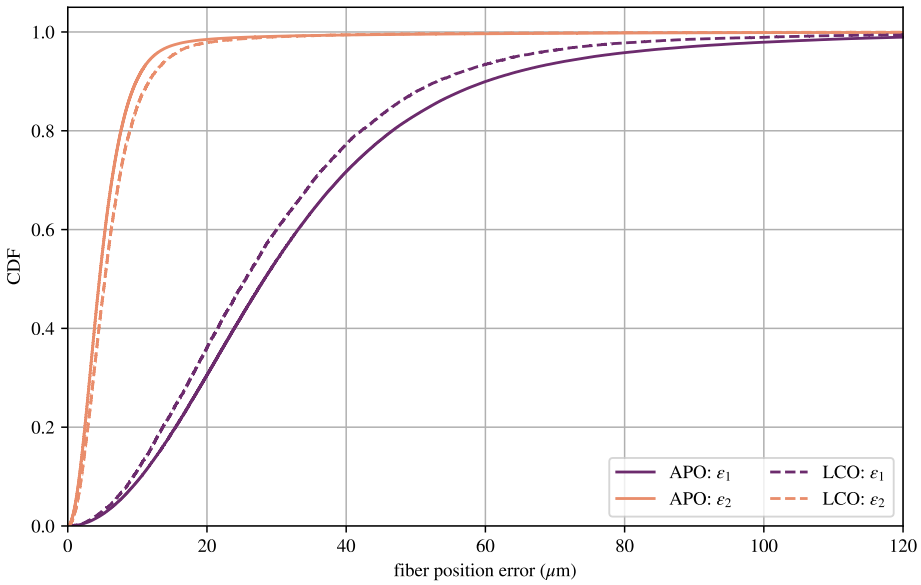

Figure 5.20 – Cumulative distribution of fiber positioning errors measured by the FVC at APO and LCO. Curves are built from 500 FVC loops taken from each telescope. Purple curves correspond to ϵ_1 (blind move metrology fiber placement error) and orange curves correspond to ϵ_2 (fiber placement error after FVC correction). Dashed lines represent data from LCO, solid lines represent data from APO.

measure and maximize science fiber throughput. For this task, we construct a commissioning-specific "survey" of bright stars, and we use the spectrographs to measure broad band photometry for each fiber in each exposure. These measurements provide an estimate of the relative flux loss (Equation 5.5) for each fiber over many different array configurations. Analysis of flux-in-fiber measurements allows us to detect and correct systematic errors in fiber positioning and GFA locations.

Commissioning-specific target selection is described in Section 5.4.2, and Section 5.4.3 summarizes how spectroscopic fields are acquired and guided using the GFA cameras. Telescope dither sequences are a special observing mode used for commissioning and on-sky calibration. These are described in Section 5.4.4 along with quick data reduction routines that provide flux-in-fiber measurements.

The first on-sky calibration step taken was an update to GFA locations in the wok. This was per-

formed by comparing `coordio` predictions against Gaia-measured astrometry for many sources in each chip, then translating and rotating each chip to minimize the `coordio` predictive error. This analysis step is described in Section 5.4.5. The next step involved a search for a telescope pointing offset that maximized flux captured over the full array. It was found that a small field rotation brought starlight into most fibers, and this process is described in Section 5.4.6. Finally, analysis of telescope dither sequences (Section 5.4.7) yielded two additional corrections: a global field distortion correction, and a science fiber location correction.

For the analysis in this section, we usually work in the the fundamental coordinate system of the instrument: wok coordinates. When converting a coordinate from sky (RA/Dec ICRS) to wok (xy mm) we need to specify the following parameters: field center (RA/Dec of telescope pointing), position angle of observation, wavelength of observation, focal plane scale factor, telescope site information (latitude, longitude, altitude, humidity, pressure, temperature), and time of observation. Additionally a coordinate epoch is required if propagating proper motions is desired. The `coordio` package (Chapter 2) was developed to handle transformations like this and its inverse (converting wok coordinates to ICRS coordinates).

With `coordio` we can seamlessly convert to any coordinate system provided in the stack. This is an important tool when searching for correlated errors in fiber positioning. Errors might look uncorrelated in one coordinate system, and systematic in another. Take Figure 5.15 as an example of this. This figure plots a distortion pattern that is constant in the CCD frame of the FVC but varies in wok coordinates as a function of rotator angle. We choose the FVC CCD frame to measure, fit, and correct this distortion.

5.4.2 Commissioning Target Selection

Commissioning-specific targets were drawn from the Gaia DR2 catalog (Gaia Collaboration et al., 2018) which provides all sky coverage and (importantly for our purposes) very precise astrometry. The selection criteria for commissioning targets were simply (1) Gaia G magnitudes between 11 and 15 and (2) no neighboring sources within a ten arcsecond radius. Relatively bright stars were selected to minimize exposure times during commissioning activities. Target candidates are

filtered into "designs". A design is defined by a field center (RA, Dec), a position angle, and a set of target to science fiber assignments. The SDSS-V code `robostrategy`[2] (Blanton et al. in prep) performs the fiber assignments, drawing from the pool of target selection candidates. This code seeks to maximize the number of targets per design while simultaneously accounting for the physical robot collision constraints inherent in the SDSS-V fiber positioner array. Additionally `robostrategy` allocates sky fibers for use in data reduction. Designs are loaded into an operations database at APO or LCO, making them available for observation.

An RA/Dec grid of field centers for commissioning designs was chosen to span the sky such that a commissioning field is observable at any time of night on any day of the year at low airmass. For each predefined field center, several designs consisting of different sets of targets are available for observation. Commissioning designs were specifically constructed as APOGEE-only or BOSS-only designs. BOSS designs accommodate up to 500 targets, and APOGEE designs accommodate up to 298 targets. The number of successfully assigned targets (after `robostrategy` optimizations) per design is largely a function of Galactic latitude. In sparse fields many robots remain unassigned due to lack of bright star availability. In and around the Galactic plane the vast majority of robots in a design will receive targets.

5.4.3 Field Acquisition and Guiding

The observation of a design is initiated through the operations software product `jaeger`[3]. When a telescope user asks `jaeger` to load a specific design, the following operations happen (in parallel where possible):

- Design information is pulled from the operations database.
- The telescope is slewed to the design's field center and position angle and set tracking.
- Robot trajectories are computed and executed to send all positioners to their desired locations.
- The FVC loop is applied to fine tune robot positioning.

[2] https://github.com/sdss/robostrategy

[3] https://github.com/sdss/jaeger

- When the telescope reaches the field, the guider is enabled.

The operations software product `cherno`[4] manages the telescope guide loop during science integrations. By default, `cherno` utilizes an offline installation of `astrometry.net` (Lang et al., 2010) to provide a WCS solution for every exposure for each GFA camera. This on-site installation of `astrometry.net` uses the Gaia-based 5200 series index files, and it only uses the index files that correspond to the GFA field of view to speed up performance. During the guide loop all six GFAs are exposed synchronously with a default exposure time of 5 seconds. The limiting magnitude for the GFA cameras is $\sim$ 19, and at APO `astrometry.net` very rarely (if ever) fails to find a WCS solution. At LCO the GFA FOV is significantly reduced, and it is possible for one or two cameras to fail to solve when observing very sparse fields. In these situations `cherno` modes can be switched to guide on pre-selected guide stars drawn from the Gaia catalogs. A major benefit of the `astrometry.net` guider is its ability to robustly solve in very crowded fields. Additionally `cherno` provides the option to guide the telescope at a fixed offset in RA, Dec, and/or rotator angle. The ability to stability guide at an offset position from the designated field center will be utilized to measure and correct fiber placements on-sky.

The metric that `cherno` attempts to minimize is guide RMS (grms), which is defined as

$$\mathrm{grms} = \left(\frac{1}{6} \sum_{i=1}^{6} \| \mathbf{w}^i_{GFA} - \widehat{\mathbf{w}}^i_{GFA} \|^2 \right)^{\frac{1}{2}}, \tag{5.19}$$

where $\mathbf{w}^i_{GFA}$ is the chip center in wok coordinates for GFA i determined from fiducial fiber imaging in Section 4.6, and $\widehat{\mathbf{w}}^i_{GFA}$ is the `coordio` calculated chip center given the desired field center and the `astrometry.net` WCS solution for the central pixel in GFA i. `cherno` minimizes grms by solving for the similarity transform that best maps $\{\widehat{\mathbf{w}}^i_{GFA}\}$ to $\{\mathbf{w}^i_{GFA}\}$. In this scheme each GFA carries an equal weight in the fit. The best fit translation is converted to an RA/Dec telescope offset and the best fit rotation is converted to an instrument rotator offset. These translation and rotation offsets are sent to the telescope after each GFA exposure and are controlled

[4] https://github.com/sdss/cherno

by a PID loop. The best fit scale parameter is continuously recorded to monitor telescope plate scale variation.

The telescope plate scale drifts throughout the night, and this effect is generally (but not perfectly) correlated with temperature. If not accounted for, scale variation can result in significant loss of flux, and this is especially problematic for fibers on the periphery of the field. Previous SDSS surveys "guided" the telescope's plate scale by actively modifying the back focal distance of the plug plate during science integrations. The ability to guide in scale was mandatory during plug plate operations because plates were manufactured months in advance of observations with poor knowledge of what the actual scale might be at time observation. With the robotic positioner array, we can configure the robots according to near-realtime telescope scale information. This is managed by `jaeger` querying `cherno` for the telescope plate scale at the time of robot reconfiguration. Potential scale errors are further mitigated by the fact that science exposures in SDSS-V are 15 minutes, and detrimental scale variations typically occur over $\sim$1 hour timescales. Despite this, we are always "chasing" scale with our current observing strategy. At LCO the ability to dynamically adjust telescope scale has been lost in SDSS-V because the hardware that modulated back focal distance was incompatible with the FPS. At APO we retain the option to dynamically adjust telescope scale, though we don't currently utilize it in an effort to keep observing strategies, procedures, and code consistent between the two sites.

Once the `cherno` guide loop is activated, the guider-measured field center is driven toward the desired field center, and convergence is reached in a few guide iterations. We consider $\mathrm{grms} < 60$ μm an acceptable value for starting a spectrograph exposure. This limit translates to ~ 1 arcsecond on-sky at APO and ~ 0.7 arcseconds on-sky at LCO. At these grms values (less than a fiber radius), target stars should be within the aperture of their designated fiber. As the guide loop continues during the science exposure, stars should become more and more centered in fibers. The default spectrograph exposure time for bright star commissioning designs is 300 seconds. BOSS exposures are used in BOSS-only designs, and APOGEE exposures are used in APOGEE-only designs.

5.4.4 Telescope Dither Sequences and Quick Data Reduction

Much of the analysis presented later in this section is largely based on "telescope dither" sequences. For a dither sequence robots are configured once for a specific design, and that configuration is observed with $\sim$12 back to back science exposures. For each science exposure `cherno` deliberately guides the telescope at a different slightly offset field center. Telescope dither offsets are chosen randomly in RA and Dec within a 1.6 arcsecond radius of the design's intended field center. Effort is made to observe dither sequences in the second half of the night when the telescope has thermalized to mitigate potential scale variation. Dither sequences were obtained under stable atmospheric conditions to minimize seeing and transparency variation from exposure to exposure. A typical 12 point dither sequence requires slightly over an hour of on-sky time to complete.

After each spectrograph exposure, the raw data are automatically processed by quick reduction pipelines on the mountain. These pipelines provide a means for fast observational feedback of data quality by producing and analyzing sky-subtracted spectral extractions for each fiber. The quick reduction pipelines have been slightly modified from SDSS-IV for use with the SDSS-V FPS. For FPS commissioning purposes we are generally only concerned with total fiber throughput. To facilitate this, quick reduction pipeline features have been added to estimate fiber photometry in common bandpasses. For BOSS spectra, an average flux in both the SDSS g' and i' bandpasses is reported for each fiber in each exposure. For APOGEE spectra, H band flux is reported. Units of flux are reported in e^-/sec for both spectrographs. Comparing instrumental flux or magnitude to the known magnitudes of commissioning targets will allow us to determine flux loss due to fiber positioning errors.

5.4.5 GFA Relative Orientation Tuning

Each GFA is characterized by two quantities: $\mathbf{w}_{GFA}$, and $\hat{\mathbf{i}}_{GFA}$. The former is the location of the chip center in wok coordinates, and the latter is the unit vector indicating the CCD x axis direction in wok coordinates. These quantities were measured in lab using GFA-associated fiducial fibers (Section 4.6) and are shown in Figure 4.20. In this section we use `coordio` and Gaia astrometry

to update the relative positions and rotations of each GFA.

Here we elect to show results from LCO as an example of our method. GFA data were compiled from observations of $\sim$ 17 different designs over a span of nights. For each centroid in each GFA frame, the WCS solution was used to query Gaia DR2 for the nearest neighboring source with phot_g_mean_mag $<$ 18, providing a match between a centroid on a chip and a source_id from Gaia. This yielded $\sim$1,500 unique Gaia sources distributed across GFAs in this particular dataset.

Each GFA-measured centroid i is converted to wok coordinates $\mathbf{w}_i^M$ using a `coordio` transformation based on $\mathbf{w}_{GFA}$, and $\hat{\mathbf{i}}_{GFA}$ for each CCD. Astrometry from each matching Gaia source_id i is propagated to wok coordinates $\mathbf{w}_i^P$ by `coordio` routines using the time of observation and design-specific parameters.

During the guide loop, all six GFAs are exposed simultaneously (with identical exposure times) and organized into "bundles" of six images that represent the same moment in time. To remove time-variable (guiding) errors explainable by telescope pointing, instrument rotation, or scale we fit and apply a similarity transform that best maps measured coordinates $\{\mathbf{w}_i^M\}$ to predicted coordinates $\{\mathbf{w}_i^P\}$ independently for each guide bundle. We call our similarity transform adjusted coordinates $\{\widehat{\mathbf{w}}_i^M\}$. Figure 5.21 plots the $\{\widehat{\mathbf{w}}_i^M - \mathbf{w}_i^P\}$ for each GFA across all exposures and designs in our data set. Clearly GFA 3 and 6 show significant rotational error, some GFAs have detectable amount of translational error.

Finally, each of the 6 patterns in Figure 5.21 are fit with a similarity transform to inform the modification of $\mathbf{w}_{GFA}$, and $\hat{\mathbf{i}}_{GFA}$ for each GFA. The results for each GFA's fit are shown in Table 5.4.

Using the results from Table 5.4, new values for GFA calibration are determined by

$$\mathbf{w}'_{GFA} = \mathbf{w}_{GFA} + \begin{bmatrix} \mathrm{xt} \\ \mathrm{yt} \end{bmatrix} \tag{5.20}$$

$$\hat{\mathbf{i}}'_{GFA} = \begin{bmatrix} \cos\theta & -\sin\theta \\ \sin\theta & \cos\theta \end{bmatrix} \hat{\mathbf{i}}_{GFA}, \tag{5.21}$$

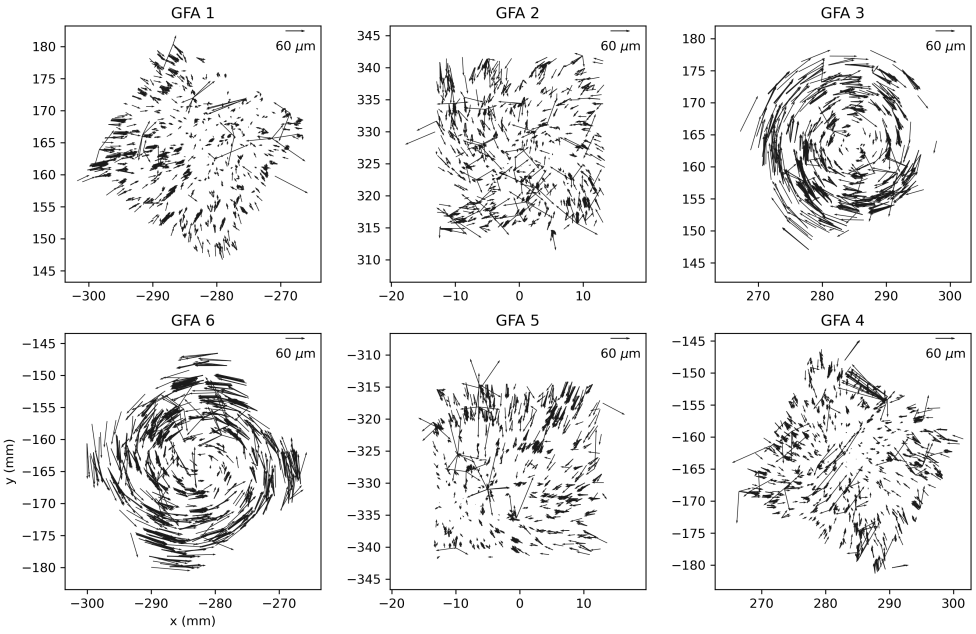

Figure 5.21 – Quiver plot of errors between GFA-measured star locations and `coordio`-predicted star locations after telescope pointing, rotation, and scale errors are removed.

and Figure 5.22 plots the residuals after the characterization updates above are applied to each GFA. After this on-sky characterization of GFA units, grms values were seen to drop during active guiding due to the improvement of relative positions and orientations of GFAs with respect to one another.

5.4.6 Initial Fiber to Sky Alignment

Finally, we describe the process of putting astronomical light down science fibers, and the telescope dither methods and analysis used to improve fiber positioning. Figure 5.23 shows the first exposure of the first commissioning design observed at APO. The figure is an image of the raw 2D APOGEE spectra, where fiber traces are stacked horizontally (with the wavelength dispersion direction along the x axis). Vertical stripes in the data are spectral sky features. The bright horizontal stripes apparent in the image correspond to fibers that are receiving flux from an astronomical

Table 5.4 – . Best fit similarity transform parameters that explain on-sky measurement errors for each GFA at LCO.

GFA	xt (x translation, mm)	yt (y translation, mm)	θ (rotation, deg)
1	0.011	0.005	-0.003
2	-0.001	-0.003	0.073
3	0.008	0.016	-0.350
4	0.000	0.004	0.047
5	-0.011	-0.014	-0.031
6	0.006	-0.003	0.327

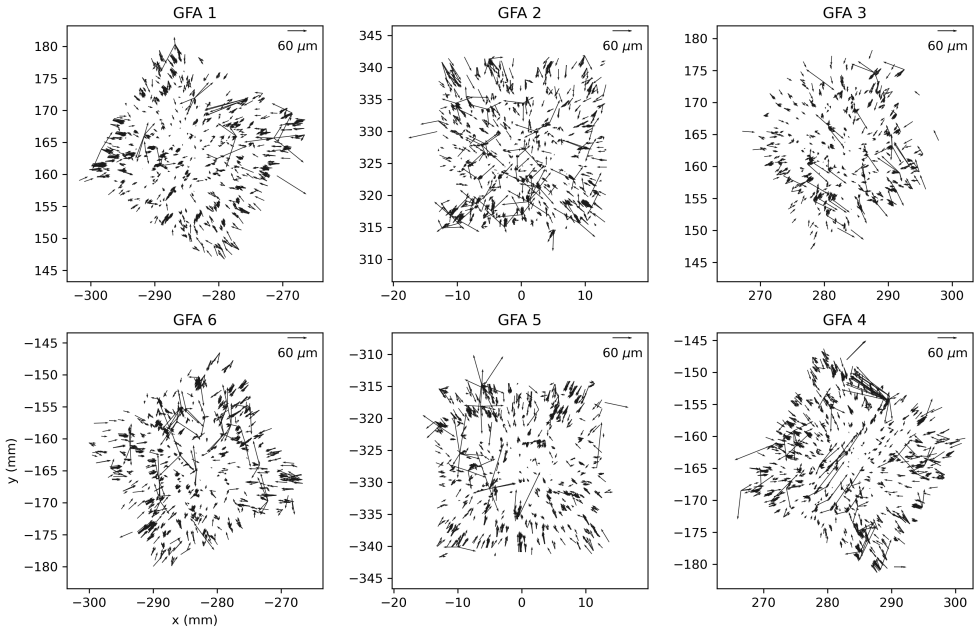

Figure 5.22 – Same as Figure 5.21 after GFA characterization has been corrected by the values in Table 5.4.

source. In this exposure, roughly 20 of the 200 assigned fibers saw flux significantly above the sky background. A 10% success may sound small, but in actuality it was a huge relief. Twenty fibers with decent flux suggested that the remainder of the fibers could not be far off. We were not

completely lost in space, and had a baseline for beginning improvements.

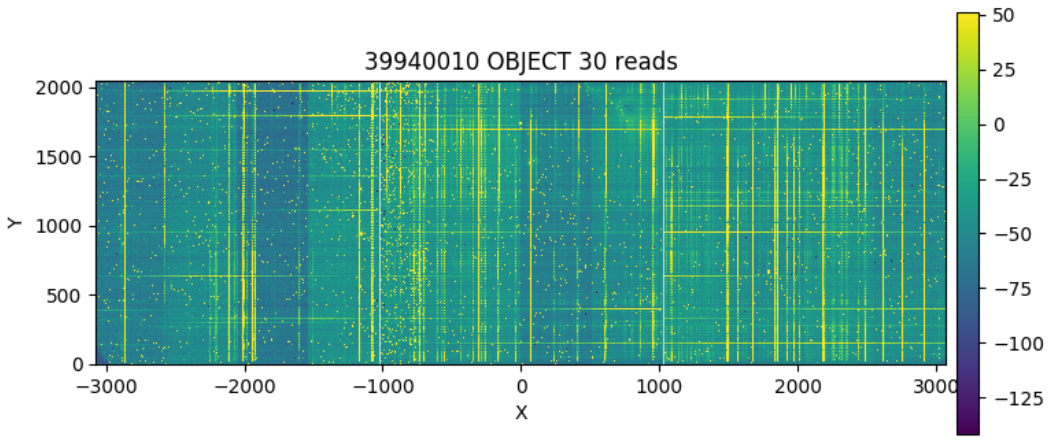

Figure 5.23 – First light exposure of the APOGEE spectrograph on a commissioning design bright star field. Vertical bands are sky spectral features. Horizontal bands indicate fibers receiving flux. After spectral extraction, roughly 20 fibers were seen to have bona fide signal in this exposure.

The next stage of nightly commissioning operations consisted of several nights of human directed hunting. Science exposures were taken while guiding designs at offset field centers and rotation in hopes of finding flux in more fibers. This was generally done as a grid searches with $\sim$1 arcsecond increments in RA and Dec, and 150 arcsecond increments in rotation. The raw spectral traces (eg, Figure 5.23) were used to provide feedback between exposures on whether or not more or less fibers were receiving flux, informing whether or not to continue moving the telescope along a certain direction. It was witnessed that some fibers lost flux and other fibers gained flux as the telescope was dithered around, again suggesting that we were near but not quite at alignment. Eventually we latched on a rotator offset of 420 arcseconds that suddenly lit up nearly all fibers at once. The raw APOGEE spectra for this frame is shown in Figure 5.24. The RA and Dec offset for this image were zero, so the main pointing error was realized as a pure rotation at APO. Figure 5.25 plots the relationship between instrument-measured H band magnitude and expected H band magnitude for targets in this exposure. The linear relationship is clear but with large scatter ($\sim$2-3 magnitudes). This scatter in flux measurement indicates significant errors in fiber positioning remain.

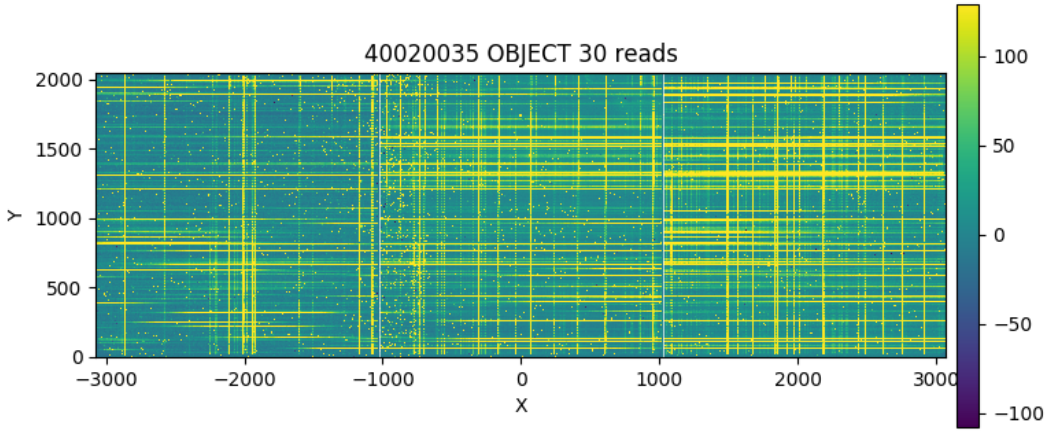

Figure 5.24 – Raw APOGEE spectra for a commissioning field offset by 420 arcseconds in instrument rotation. Nearly all assigned fibers are receiving flux.

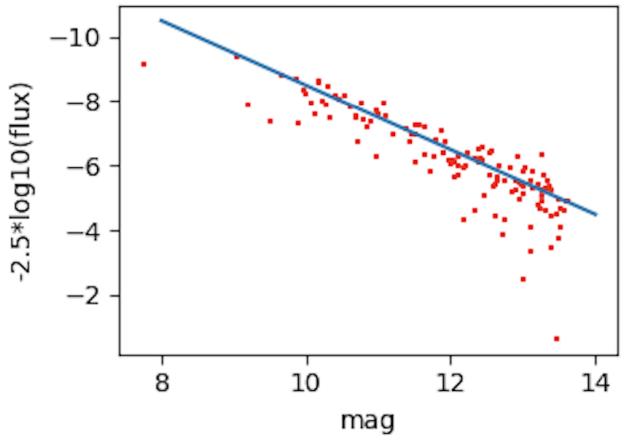

Figure 5.25 – Measured (instrumental) H band magnitude (y axis) vs expected (2MASS) H band magnitude (x axis) for APOGEE spectra extracted from raw data shown in Figure 5.24.

5.4.7 Improving Fiber Positioning: Telescope Dither Analysis

After the rough pointing correction was discovered, telescope dither sequence analysis was used to further improve fiber positioning. The dither analysis strategy was developed by the DESI instrument team (Abareshi et al. 2022, Schlafly et al. in prep), and the DESI dither analysis code (and consultation) was kindly shared with us (Schafly & Schlegel private communication). After a period of early on-sky experimentation we arrived at a dither observation and analysis strategy inspired by DESI techniques using an independent analysis code.

Before a dither sequence, the array is configured for observing a specific design. During a dither sequence the telescope is randomly offset within a ∼1.6 arcsecond pointing radius of the design's field center, and a spectrograph exposure is taken at each offset pointing. This provides a flux measurement at several different fiber locations relative to the spectroscopic target. For analysis we convert each on-sky telescope offset to a dx and dy displacement in wok coordinates. Figure 5.26 plots measurements from four different dither sequences taken over a few nights for the same BOSS fiber. Each point is color scaled according to the flux measured by the spectrograph, and each point is plotted spatially according to the telescope offset. If the fiber were well centered on a target, dx=dy=0 would maximize the flux. For this particular fiber it is generally clear that flux is maximized at an off-center location, indicating an error in fiber placement.

Measurements from each dither sequences are analyzed to estimate the location of the star relative to the fiber using the fiber-integrated flux model introduced in Section 5.2. Specifically, F_{TFC} (Equation 5.3) describes the model that predicts the flux measured in an SDSS-V fiber given a 2D symmetric Gaussian PSF source parametrized by f_o (total flux of source), σ (standard deviation of Gaussian PSF), dx (x offset from fiber to star), and dy (y offset from fiber to star). Dither sequence observations directly sample this function, and we use this as a forward model to fit each of the input parameters numerically using Powell's method (implemented in Python's `scipy.optimize`). The optimization problem for each fiber is written as

$$\min_{\mu_x,\mu_y,\sigma,f_o} \sum_{i=1}^{n} \|F_{\mathrm{TFC}}(\mu_x - dx_i, \mu_y - dy_i, \sigma, f_o) - f_i\|^2 \tag{5.22}$$

for a sequence of n telescope dithers. dx_i and dy_i are the telescope-dither offsets in wok coordinates, and f_i is the flux measured at each dither offset. μ_x and μ_y indicate the xy offset from the fiber's desired location (dx=dy=0) to the star's dither-measured location in wok coordinates. σ and f_o are free parameters that allow for varying seeing conditions and total brightness of the star.

Figure 5.27 plots the results of this optimization procedure for the data shown in Figure 5.26. The raw data from the previous figure are plotted over the best fit model for each dither sequence. The best fit model parameters are listed in the lower left corner of each panel. The dashed cross

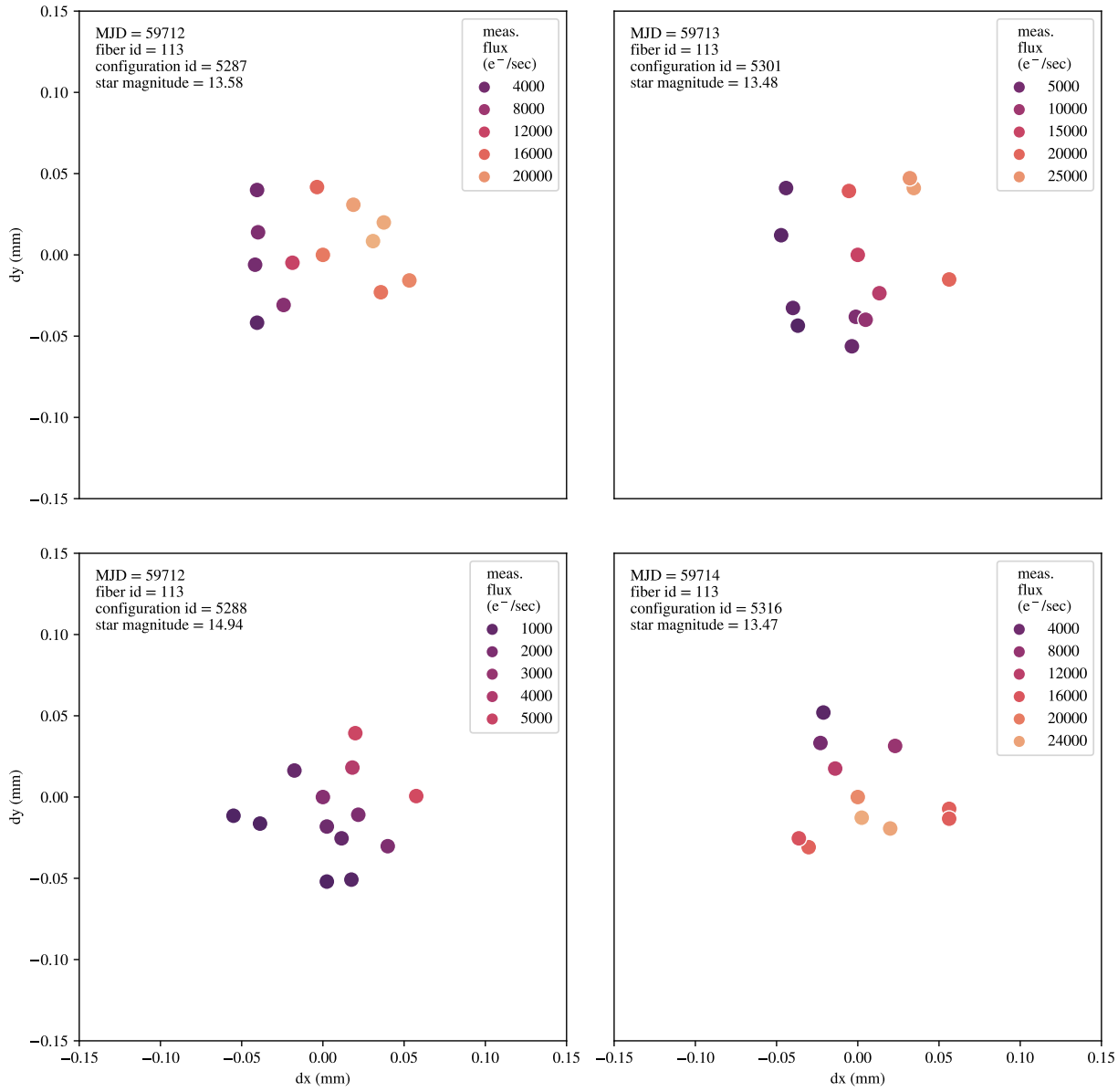

Figure 5.26 – Examples of dither data for the same BOSS fiber across four different designs spanning three nights. Each panel plots ∼12 fiber flux measurements (SDSS i' band) taken at different random telescope-dithered locations. Telescope RA and Dec offsets are converted to a displacement in mm on the wok, and dx=dy=0 represents an undithered exposure. The color scale of the individual points indicate the flux measured in each spectrograph exposure.

shows the estimated location of the star (μ_x, μ_y). We use this method to measure the xy fiber positioning error for each fiber in each dither sequence.

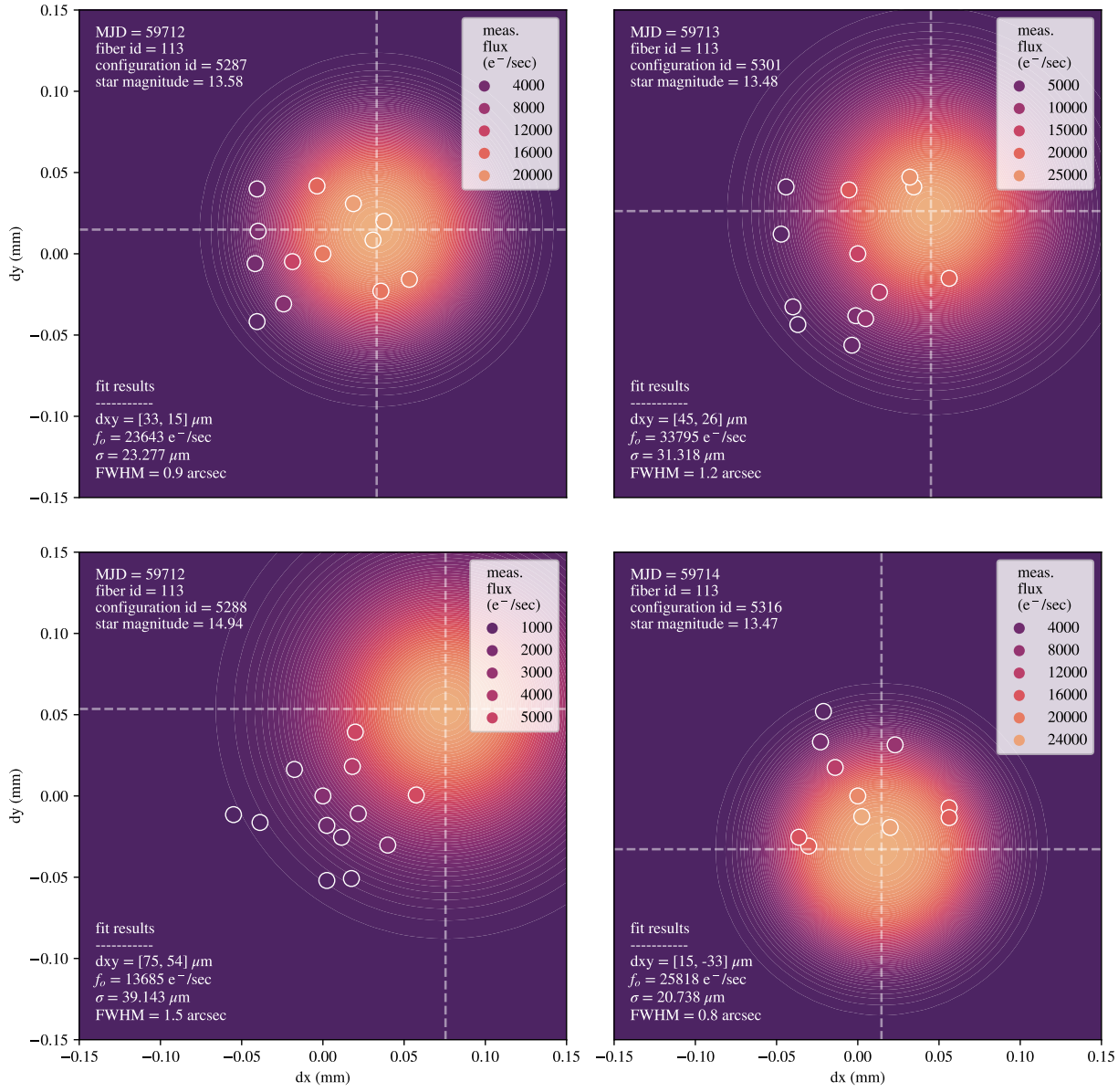

Figure 5.27 – Results of a fiber-integrated PSF fits to dither data shown in Figure 5.26. Measured flux values are plotted on top of the best fit model for each panel. The best fit model provides an estimate of dxy fiber offset for each fiber from a ∼12 point telescope dither sequence.

The processed result of a dither sequence is a measurement that estimates the xy positioning

error for every assigned fiber in the observed design. We obtain multiple measurements for each science fiber by performing many dither sequences using different designs because not every fiber is guaranteed to be assigned a target in every design. Combining measurements from multiple designs will also ensure that each fiber will sample several different stars around its workspace. In the analysis that follows we will focus on a set of BOSS dithers obtained at APO, although dither observations were also conducted on APOGEE fields during commissioning. APOGEE and BOSS dither observations have been collected for LCO, but have not yet provided consistent results (more comments on this are provided in Section 5.6).

We analyze BOSS data from twenty dither sequences observed using ten unique designs at APO. Data were collected over a period of seven nights. Observations of four designs were repeated 3 or 4 times over the span of nights, while the remaining six designs were observed only once. This produced an average of 16 independent measurements per BOSS fiber for 493 active fibers (several robots were offline and thus received no fiber measurement data). In total our data set consisted of $\sim$8000 on-sky measurements of fiber position errors.

The left panel in Figure 5.28 shows the dither-derived fiber position errors as a function of wok location and direction. The right panel collapses the spatial data into a single histogram of fiber position errors. The RMS fiber position error is measured to be 33 μm. Spatially correlated errors across the positioner field are present in the quiver plot. We hypothesize that this field distortion component is due to uncertainties in absolute fiducial locations which were indicated during lab calibration of the APO FPS unit[5]. Errors in fiducial locations cause errors in the FVC transform which would manifest as something resembling a smooth distortion across the field. Regardless of the true source of this observed spatially-correlated bias in fiber positioning, we choose to correct it by adding an additional static Zhao-Burge correction term to the FVC transform. For this we fit a ZB model to the spatial error pattern shown in Figure 5.28 using the same 33 term ZB polynomial basis for the FVC transform discussed in Section 5.3.4. This best fit ZB distortion model is shown in Figure 5.29 and is characterized by a set of static coefficients $\vec{c}^{+}$. The FVC transform in Equation

[5]See Section 4.5

5.15 is modified by the addition of this static ZB correction term[6]

$$F_2(\mathbf{p}) = F_1(\mathbf{p}) + D(F_1(\mathbf{p}), \vec{c}^{+}). \tag{5.23}$$

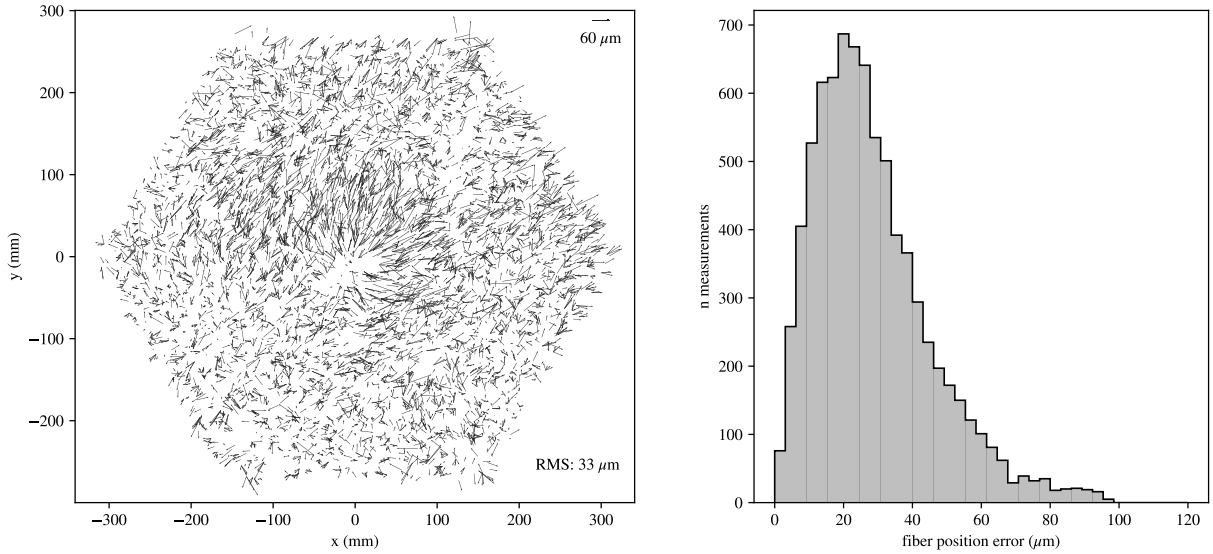

Figure 5.28 – Left panel: xy fiber postioning errors compiled from ∼20 BOSS dither sequences at APO plotted in wok coordinates. Right panel: histogram of fiber positioning error magnitudes. The RMS fiber position error is 33 μm.

Figure 5.30 displays the dither-derived fiber position errors after removing the modeled field distortion component. The RMS error is reduced from 33 μm to 26 μm, and the obvious spatial correlation in fiber position errors across the field appears significantly reduced. The next systematic error component we seek to measure and remove in these data is related to the the physical location of the science fiber within the beta arm of the robot.

Science fiber locations were initially characterized during lab calibration (Section 4.8), and BOSS fiber measurements for the APO FPS unit were seen to have much higher variance when compared to APOGEE fiber measurements. A scale factor correction improved BOSS fiber estimation for the LCO unit, but the BOSS dither data presented here were taken before any attempt

[6]ZB models of the form $D(\mathbf{w}, \vec{c})$ are described in Section 4.4.2

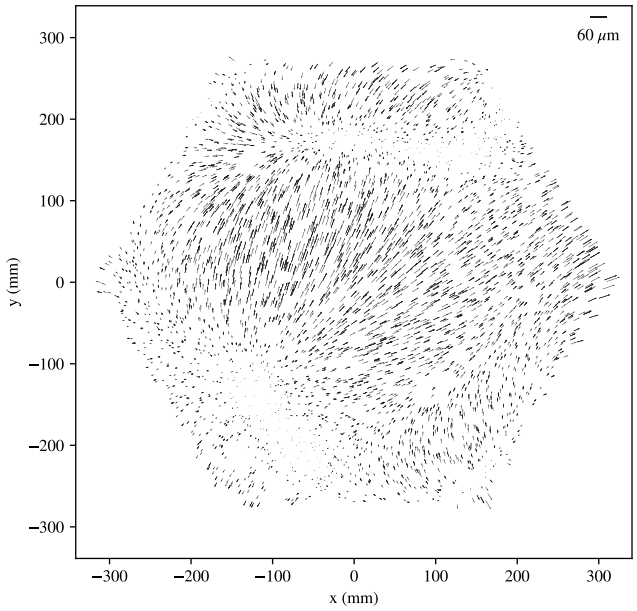

Figure 5.29 – Zhao-Burge polynomial model correction fit to the error vectors in the left panel of Figure 5.28. This wok coordinate distortion correction is implemented in the FVC transform.

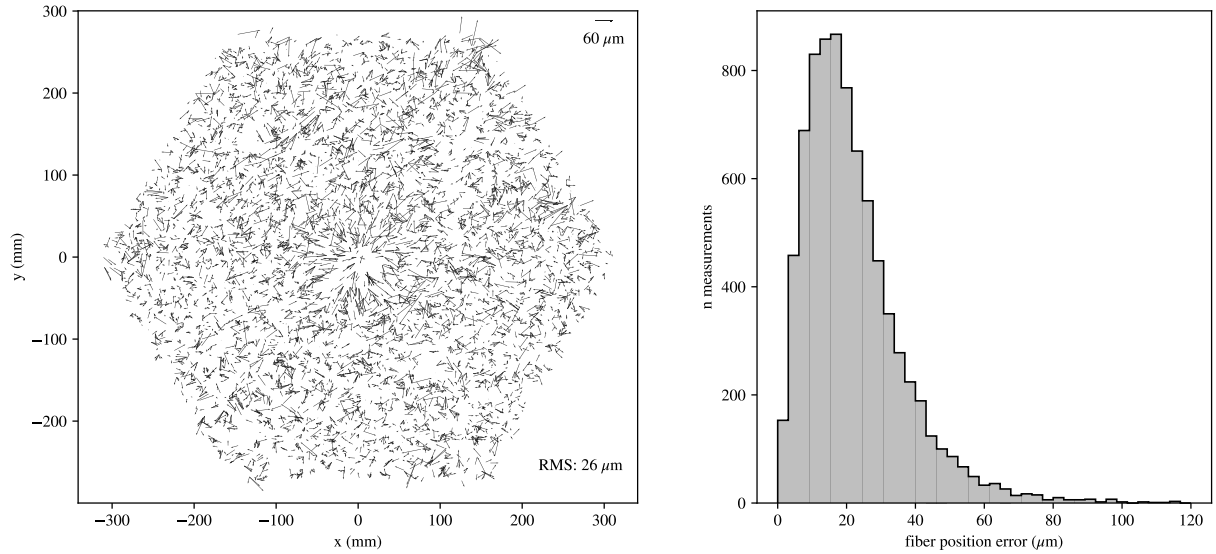

Figure 5.30 – Left panel: xy fiber postioning errors compiled from ∼20 BOSS dither sequences at APO after the ZB correction model in Figure 5.29 is applied. Right panel: histogram of fiber positioning error magnitude. The RMS fiber position error is reduced to 26 μm and the previous spatially correlated error has been generally removed.

at fiber location correction was made, and so provide a good example of improving science fiber locations on sky.

Ultimately the FVC determines where a fiber gets placed for an observation, and the FVC loop specifically measures and corrects the position of a metrology fiber (not a science fiber). The FVC correction will minimize effects of most errors related to robot kinematics because after the FVC loop is completed the metrology fiber should end up extremely close to its desired location (assuming an accurate FVC transform). For a science fiber to land at its intended position, the assumed location of the science fiber relative to the metrology fiber has to be accurately known.

We measure the metrology-to-science fiber error by rotating every error vector shown in Figure 5.30 from the wok coordinate system into beta arm coordinate frame. For each robot i in each design j this amounts to a coordinate rotation of $\theta = \alpha'_{ij} + \beta ij'$ (Equation 4.26). Figure 5.31 displays the result of this coordinate system rotation applied to four BOSS fibers selected for their relatively large fiber position errors. Open orange circles show fiber-to-star offsets measured in the wok coordinate system, filled purple circles show the same data after rotation into the beta arm coordinate system. We observe that fiber-to-star offsets tend to cluster in the latter coordinate system, indicating a systematic error in metrology-to-science fiber characterization. For each robot we calculate the median xy fiber position error in the beta arm frame, and add this value to the initial calibrated locations of BOSS science fibers.

Figure 5.32 plots the distribution of fiber position errors after applying the wok frame static distortion model and adjusting the characterized location for each BOSS fiber. The RMS error has been further reduced to 21 μm, and Table 5.5 lists percentiles for fiber position error in both microns and arcseconds on sky. The distribution of fiber positioning errors as measured by dither observations suggest that 60% of science fibers are reaching or exceeding the 16.5 μm fiber positioning goal outlined in Section 5.2, and effectively all fibers should be capturing the majority of the available flux from astrophysical sources.

5.5 Spectrophotometric Results from the BOSS Pipeline

We assess the FPS spectrophotometric performance at APO using BOSS pipeline reductions from version `v6_0_9` of `idlspec2D` (Bolton et al. 2012, Dawson et al. 2012, Morrison et al. in prep) to verify that progress seen on-sky using bright star commissioning fields is reflected in the SDSS-

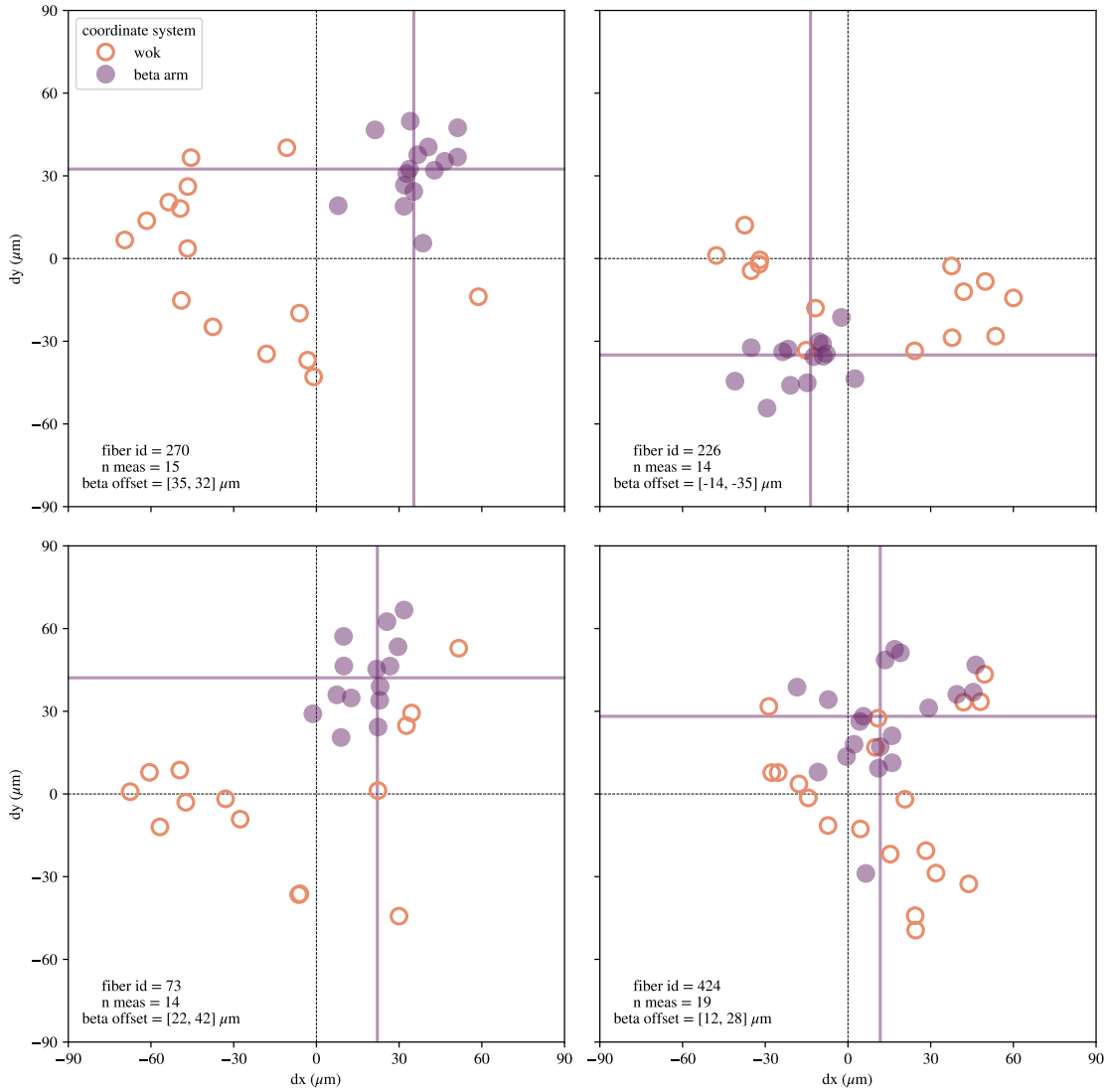

Figure 5.31 – Examples of four BOSS fibers with relatively large fiber position errors. Each point represents an error derived from a single dither sequence. Open orange circles indicate error vectors measured in wok coordinates. Filled purple circles plot the same errors rotated into the beta arm frame where measurements are seen to cluster. The solid purple cross indicates the median beta arm error in each cluster.

V survey science fields. For this we specifically consider FPS observations of the Black Hole Mapper's Reverberation Mapping (RM), AQMES, and SPIDERS fields (Almeida et al., 2023), largely because these programs use an increased amount of standard star calibrators in comparison

Table 5.5 – . Percentiles for BOSS fiber position errors from telescope dither sequences at APO after correcting for a general distortion in wok coordinates (Figure 5.29) and corrections for each BOSS fiber in the beta arm frame (Figure 5.31).

Percentile	fiber position error (μm)	(arcsec)
50	14	0.2
60	17	0.3
75	22	0.4
90	32	0.5
95	40	0.7
99	60	1.0

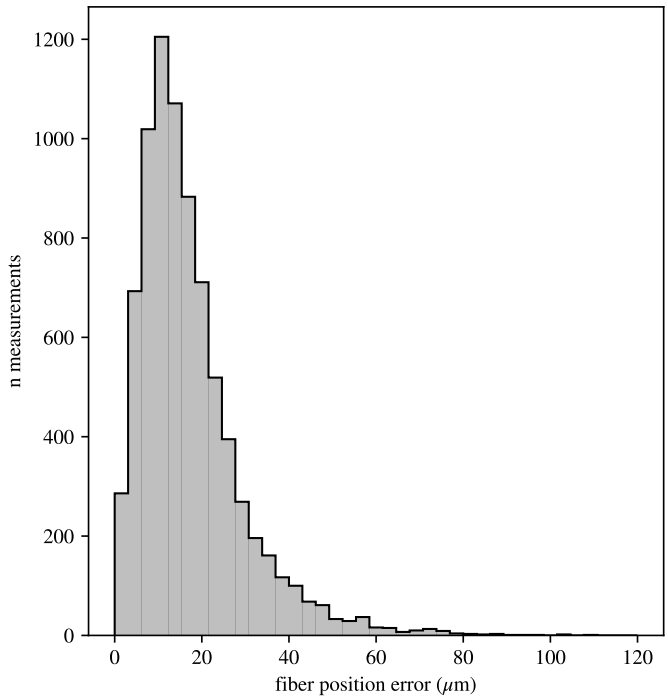

Figure 5.32 – Histogram of fiber position errors after applying the global Zhao-Burge distortion correction (Figure 5.29) and beta arm offset corrections (Figure 5.31). The RMS fiber position error is 21 μm. Percentiles for this error distribution are shown in Table 5.5.

to other SDSS-V programs. In these fields roughly 70 of 500 fibers are allocated to standard stars. In pipeline processing, the spatial sampling of standards across the field is used to fit and remove smooth systematic flux variation across the focal plane, calibrating effects such as field-dependent image quality variation. Overall the heightened number of standards and the attention to absolute

flux calibration for these specific fields make them a valuable diagnostic for assessing throughput variability from data obtained with the robotic fiber positioners.

For this analysis we query BOSS spectroscopic reductions from RM, AQMES, and SPIDERS fields for standard standard star observations between MJDs 59708 and 59958. This yields 194 exposures distributed among 63 unique science fields. This selection consists of ∼4700 standard star measurements. Figure 5.33 shows the relationship between BOSS pipeline expected ($r_{\rm expect}$) and spectroscopically measured ($r_{\rm meas}$) r band flux for these standard star observations. The over-plotted orange line indicates the 1:1 correspondence between measured and expected flux, and the scatter about this line shows the photometric variance present in this sample of BOSS standard star observations. We expect that a large component of this variance is due to errors in robotic fiber positioning.

For these data, we translate the photometric errors to a percentage

$$\text{error} = \frac{|r_{\rm expect} - r_{\rm meas}|}{r_{\rm expect}} \times 100, \tag{5.24}$$

and show the cumulative distribution of photometric errors in Figure 5.34. The orange trace in this figure represents data taken before MJD 59733, and the purple trace shows data taken from that date forward. On MJD 59733 the results from the on-sky calibration methods described in Section 5.4.7 were implemented in survey operations, and a clear improvement in fiber throughput is apparent as a result of our recalibration strategy. The mean photometric error improved from 14.5% to 10.2%, and the median photometric error improved from 10.5% to 6.5%. Overall the distribution of BOSS standard star flux error is consistent with our dither-derived distribution of fiber position error (Table 5.5) based on a Gaussian PSF of width that varies with seeing conditions.

The 5% spectrophotometric requirement for RM science is in touch, but not yet achieved. Most observations will experience spectrophotometric errors of 6-7% or better, and only 2% of standard star observations see flux errors $> 50\%$. This suggests that the PSF core is within the fiber aperture for almost every fiber, and very well centered for half of the fibers. The main FPS calibration effort moving forward is to continue improving fiber placement with a focus on the population of

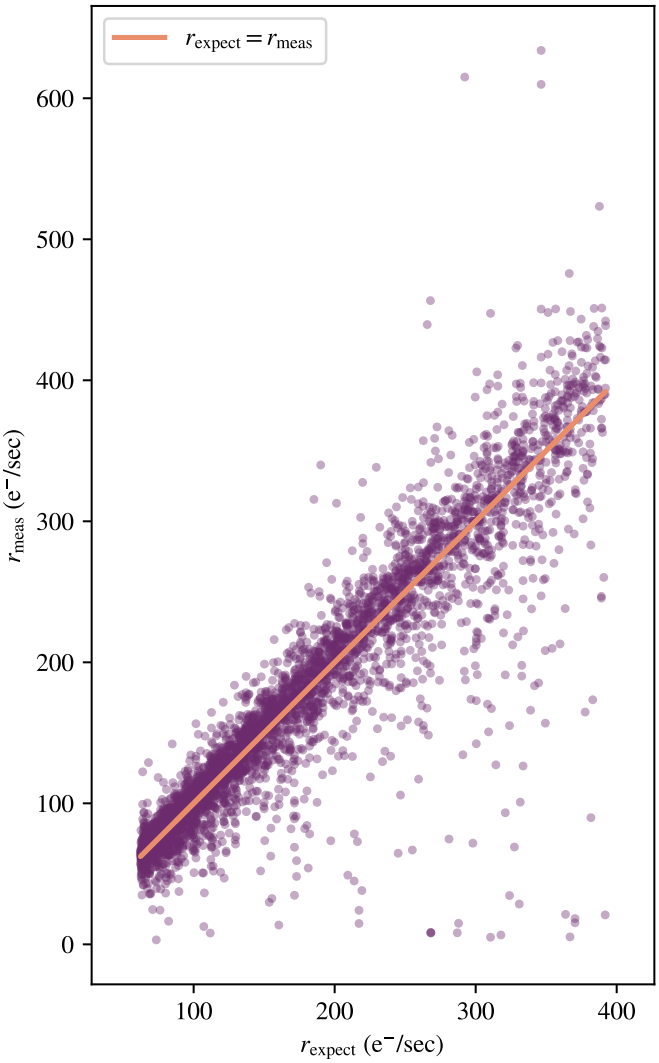

Figure 5.33 – Comparison between expected and measured r band flux for fully reduced standard stars from BOSS RM, AQMES and SPIDERS fields between MJDs 59708 and 59958.

obviously de-centered fibers.

5.6 Discussion and Future Improvement

The majority of fiber position analysis has focused on BOSS fibers at APO. We have focused here for a few reasons: (1) BOSS RM programs put the tightest tolerance on fiber position errors, (2) the FPS carries significantly more BOSS fibers than APOGEE, providing a means for denser sampling across the focal plane, and (3) BOSS fiber positions for the APO FPS were measured significantly

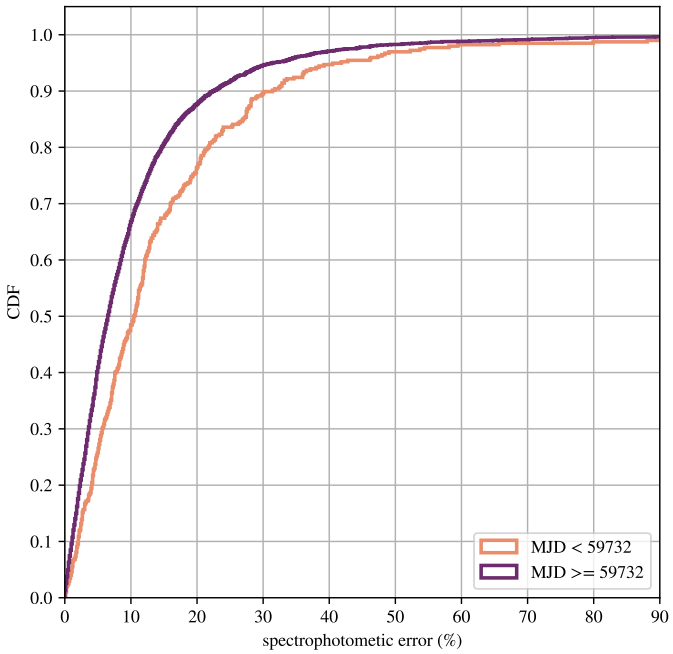

Figure 5.34 – Cumulative distribution for r band spectrophotometric error measured in BOSS standard stars before (orange trace) and after (purple trace) dither-derived fiber positioning corrections were implemented. Constructed from the data shown in Figure 5.33.

less accurately in the lab than APOGEE fiber positions. This was immediately confirmed on sky when BOSS throughput variability was significantly higher than APOGEE throughput variability. As of yet we have made no update to APOGEE fiber positions largely because current throughput is meeting science requirements. This suggests that lab calibration of APOGEE fibers was a general success. APOGEE throughput has benefited from the distortion correction made to the FVC (Equation 5.23) based on telescope dither campaigns and analysis. We expect both APOGEE and BOSS fiber positioning can be further improved at APO and LCO.

So far we have not mentioned any on-sky calibration results from LCO, and we offer some brief discussion points on this topic here. Initial throughput for both APOGEE and BOSS fibers at LCO was significantly improved with respect to where we started on-sky work at APO. Much of this "headstart" was a result of our previous experience characterizing the first instrument in the lab and on sky. Specifically of note, BOSS fiber positions appear much more accurate based on reduced throughput variation when compared to our initial experience at APO. Obtaining full spectroscopic reductions from both APOGEE and BOSS pipelines has been a challenge due to various unforeseen problems with both hardware and software at LCO. Many of these issues are

now resolved and science verification has begun. Several sets of dither observations have been taken at LCO, but as of February 2023 the results do not seem wholly consistent and no fiber position corrections have been attempted. We hope that an improved analysis routines will reduce the measurement scatter at both LCO and APO providing a means for further improvement for robotic fiber positioning.

Our main tools for deducing and correcting fiber position errors are FVC measurements and dither analysis measurements, and both of these come with an associated measurement uncertainty. Techniques for reducing measurement scatter in each of these tools is a continuing area of research and development.

The FVC pixel scale is 120 μm/pixel and the goal for fiber placement error is $\sim$10 μm or roughly 1/10 of a pixel. To accurately measure and adjust fiber positions during the FVC loop we would like centroid measurement uncertainties that are comfortably below this limit, ideally the ballpark of 1/20 of a pixel. High precision centroid methods typically require an accurate model of the PSF. Unfortunately, as shown in Figures 5.9, 5.11, and 5.12 our PSFs are non-round and significantly vary in shape across the field. We expect that PSF quality and spatial variation could be improved if telescope baffle support wires that bisect the FVC FOV were removed. These are assumed to produce the observed PSF elongation band across the middle of the CCD due to diffraction. Additionally applying effort to precisely focusing the FVC may further improve PSFs, only a small amount of effort was spent focusing the FVC during on-site instrument commissioning.

Averaging over multiple FVC exposures is another option for reducing FVC measurement scatter, although this comes at the cost of decreased observing cadence. SDSS-V survey requirements state that a maximum of 5 minutes for field-to-field reconfiguration is allowable to achieve survey goals within the duration of the project. At this time a full field reconfiguration takes 5-6 minutes to complete, and a portion of this time is used for the FVC loop. The FVC currently uses $\sim$20 seconds to expose and process a single frame, and three exposures are required in the FVC loop. Averaging each FVC measurement over three exposures would add a 2 minute overhead to each SDSS-V field visited, and averaging over five exposures would add a 4 minute overhead, etc. Adding additional time to field reconfiguration sequence is not a long-term sustainable solution unless that time can

be saved elsewhere in the process[7].

We expect that the variance seen in dither analysis results (eg Figure 5.31) can be improved by moving to a more sophisticated flux model. Feedback from guider exposures can be used to better constrain and adjust for many of the time-varying parameters that will affect flux measurement throughout a dither sequence including: telescope pointing and stability, atmospheric transparency, telescope plate scale, and seeing. Additionally, modifying our PSF model to incorporate the known radial dependence on PSF shape is also under active investigation. We have already begun to test some of these modifications in our dither analysis and modeling code, and are optimistic for future results.

Continuing to improve fiber positioning is not just a priority for BOSS RM fields. It is important for every science program in the SDSS-V. Although no other programs specify a spectrophotometric requirement, they do require photons! With fractional losses of flux due to fiber position errors, repeated exposures become necessary for achieving signal to noise thresholds. Repeating exposures is a major loss of survey efficiency and could result in a significant downscope in the SDSS-V survey plan if fiber positioning does not continue to improve. In this sense the work is not done, but we're off to a good start. Science quality data is now flowing from the FPS instruments at APO and LCO, and our major task now is to make it flow faster and more efficiently.

[7] Active progress is being pursued here by pipeline teams investigating necessity of certain spectrograph calibration frames that are currently being taken at each field. If calibrations were removed this would draw total reconfiguration time into the 4 minute range.

Chapter 6

CONCLUSIONS

SDSS-V builds on a heritage of evolution and cooperation between instrument, infrastructure, science, and data teams to obtain and deliver a wide and diverse set of data products to the astronomical community. Operationally, SDSS has seen major changes with the inclusion of the FPS instruments, and various teams continue to tackle the many challenges inherent in organizing, optimizing, and deploying a successful SDSS survey operating in a completely new mode. The work presented here details several major operational challenges and solutions related to SDSS-V's adoption of a robotic fiber positioner for multi-object wide field spectroscopy.

SDSS has just completed its eighteenth data release (Almeida et al., 2023) which contains targeting information for the SDSS-V survey. Normal survey operations at APO are now underway, and normal survey operations at LCO are rapidly approaching after a period of instrument commissioning and science verification. SDSS-V is one of the first few robotically-positioned MOS surveys in operation today.

Several other robotic MOS instruments and surveys of comparable scale and scope to SDSS-V are nearing deployment. Many of these contemporary projects are facing challenges analogous to those presented in this work, and cross-project solutions are already emerging. This is clearly evident from the SDSS-V perspective where advice from the DESI team directly informed and improved our on-sky calibration strategy. Another example of a shared solution in this space is the adoption of SDSS-V's `kaiju` path planning methods for the MOONS instrument, which uses a robot design and layout that is similar to the SDSS-V FPS (Beard et al., 2022).

Looking ahead, this work can directly inform next generation of robotic MOS designs and operations. This decade will see a massive increase in available photometric data from surveys like Gaia and LSST. Spectroscopic followup for any meaningful fraction of available sources from these surveys will require MOS instruments with an order of magnitude more fibers on larger telescopes packed into tighter arrangements. Software frameworks like `coordio` and `kaiju` can be used to explore the ranges of feasible robot designs and layouts in terms of both targeting and operational efficiency. Lessons and techniques learned from instrument metrology and calibration efforts both in-lab and on-sky from today's robotic arrays will provide critical inputs for the next generation of robotic MOS instrument design.

BIBLIOGRAPHY

Abareshi, B., Aguilar, J., Ahlen, S., Alam, S., Alexander, D. M., Alfarsy, R., Allen, L., Allende Prieto, C., Alves, O., Ameel, J., Armengaud, E., Asorey, J., Aviles, A., Bailey, S., Balaguera-Antolínez, A., Ballester, O., Baltay, C., Bault, A., Beltran, S. F., Benavides, B., BenZvi, S., Berti, A., Besuner, R., Beutler, F., Bianchi, D., Blake, C., Blanc, P., Blum, R., Bolton, A., Bose, S., Bramall, D., Brieden, S., Brodzeller, A., Brooks, D., Brownewell, C., Buckley-Geer, E., Cahn, R. N., Cai, Z., Canning, R., Carnero Rosell, A., Carton, P., Casas, R., Castander, F. J., Cervantes-Cota, J. L., Chabanier, S., Chaussidon, E., Chuang, C., Circosta, C., Cole, S., Cooper, A. P., da Costa, L., Cousinou, M. C., Cuceu, A., Davis, T. M., Dawson, K., de la Cruz-Noriega, R., de la Macorra, A., de Mattia, A., Della Costa, J., Demmer, P., Derwent, M., Dey, A., Dey, B., Dhungana, G., Ding, Z., Dobson, C., Doel, P., Donald-McCann, J., Donaldson, J., Douglass, K., Duan, Y., Dunlop, P., Edelstein, J., Eftekharzadeh, S., Eisenstein, D. J., Enriquez-Vargas, M., Escoffier, S., Evatt, M., Fagrelius, P., Fan, X., Fanning, K., Fawcett, V. A., Ferraro, S., Ereza, J., Flaugher, B., Font-Ribera, A., Forero-Romero, J. E., Frenk, C. S., Fromenteau, S., Gänsicke, B. T., Garcia-Quintero, C., Garrison, L., Gaztañaga, E., Gerardi, F., Gil-Marín, H., Gontcho, S. G. A., Gonzalez-Morales, A. X., Gonzalez-de-Rivera, G., Gonzalez-Perez, V., Gordon, C., Graur, O., Green, D., Grove, C., Gruen, D., Gutierrez, G., Guy, J., Hahn, C., Harris, S., Herrera, D., Herrera-Alcantar, H. K., Honscheid, K., Howlett, C., Huterer, D., Iršič, V., Ishak, M., Jelinsky, P., Jiang, L., Jimenez, J., Jing, Y. P., Joyce, R., Jullo, E., Juneau, S., Karaçaylı, N. G., Karamanis, M., Karcher, A., Karim, T., Kehoe, R., Kent, S., Kirkby, D., Kisner, T., Kitaura, F., Koposov, S. E., Kovács, A., Kremin, A., Krolewski, A., L'Huillier, B., Lahav, O., Lambert, A., Lamman, C., Lan, T.-W., Landriau, M., Lane, S., Lang, D., Lange, J. U., Lasker, J., Le Guillou, L., Leauthaud, A., Le Van Suu, A., Levi, M. E., Li, T. S., Magneville, C., Manera, M., Manser, C. J., Marshall, B., McCollam, W., McDonald, P., Meisner, A. M., Mezcua, J.

M.-F. M., Miller, T., Miquel, R., Montero-Camacho, P., Moon, J., Martini, J. P., Meneses-Rizo, J., Moustakas, J., Mueller, E., Muñoz-Gutiérrez, A., Myers, A. D., Nadathur, S., Najita, J., Napolitano, L., Neilsen, E., Newman, J. A., Nie, J. D., Ning, Y., Niz, G., Norberg, P., Noriega, H. E., O'Brien, T., Obuljen, A., Palanque-Delabrouille, N., Palmese, A., Zhiwei, P., Pappalardo, D., Peng, X., Percival, W. J., Perruchot, S., Pogge, R., Poppett, C., Porredon, A., Prada, F., Prochaska, J., Pucha, R., Pérez-Fernández, A., Pérez-Ráfols, I., Rabinowitz, D., Raichoor, A., Ramirez-Solano, S., Ramírez-Pérez, C., Ravoux, C., Reil, K., Rezaie, M., Rocher, A., Rockosi, C., Roe, N. A., Roodman, A., Ross, A. J., Rossi, G., Ruggeri, R., Ruhlmann-Kleider, V., Sabiu, C. G., Safonova, S., Said, K., Saintonge, A., Salas Catonga, J., Samushia, L., Sanchez, E., Saulder, C., Schaan, E., Schlafly, E., Schlegel, D., Schmoll, J., Scholte, D., Schubnell, M., Secroun, A., Seo, H., Serrano, S., Sharples, R. M., Sholl, M. J., Silber, J. H., Silva, D. R., Sirk, M., Siudek, M., Smith, A., Sprayberry, D., Staten, R., Stupak, B., Tan, T., Tarlé, G., Sien Tie, S., Tojeiro, R., Ureña-López, L. A., Valdes, F., Valenzuela, O., Valluri, M., Vargas-Magaña, M., Verde, L., Walther, M., Wang, B., Wang, M. S., Weaver, B. A., Weaverdyck, C., Wechsler, R., Wilson, M. J., Yang, J., Yu, Y., Yuan, S., Yèche, C., Zhang, H., Zhang, K., Zhao, C., Zhou, R., Zhou, Z., Zou, H., Zou, J., Zou, S., and Zu, Y. (2022). Overview of the Instrumentation for the Dark Energy Spectroscopic Instrument. *arXiv e-prints*, page arXiv:2205.10939.

Almeida, A., Anderson, S. F., Argudo-Fernández, M., Badenes, C., Barger, K., Barrera-Ballesteros, J. K., Bender, C. F., Benitez, E., Besser, F., Bizyaev, D., Blanton, M. R., Bochanski, J., Bovy, J., Brandt, W. N., Brownstein, J. R., Buchner, J., Bulbul, E., Burchett, J. N., Díaz, M. C., Carlberg, J. K., Casey, A. R., Chandra, V., Cherinka, B., Chiappini, C., Coker, A. A., Comparat, J., Conroy, C., Contardo, G., Cortes, A., Covey, K., Crane, J. D., Cunha, K., Dabbieri, C., Davidson, J. W., Davis, M. C., De Lee, N., Delgado, J. E. M., Demasi, S., Di Mille, F., Donor, J., Dow, P., Dwelly, T., Eracleous, M., Eriksen, J., Fan, X., Farr, E., Frederick, S., Fries, L., Frinchaboy, P., Gaensicke, B. T., Ge, J., Ávila, C. G., Grabowski, K., Grier, C., Guiglion, G., Gupta, P., Hall, P., Hawkins, K., Hayes, C. R., Hermes, J. J., Hernández-García, L., Hogg, D. W., Holtzman, J. A., Ibarra-Medel, H. J., Ji, A., Jofre, P., Johnson, J. A., Jones, A. M., Kinemuchi, K., Kluge, M.,

Koekemoer, A., Kollmeier, J. A., Kounkel, M., Krishnarao, D., Krumpe, M., Lacerna, I., Lago, P. J. A., Laporte, C., Liu, A., Liu, C., Liu, X., Lopes, A. R., Macktoobian, M., Malanushenko, V., Maoz, D., Masseron, T., Masters, K. L., Matijevic, G., McBride, A., Medan, I., Merloni, A., Morrison, S., Myers, N., Mészáros, S., Negrete, C. A., Nidever, D. L., Nitschelm, C., Oravetz, A., Oravetz, D., Pan, K., Peng, Y., Pinsonneault, M. H., Pogge, R., Qiu, D., Queiroz, A. B. d. A., Ramirez, S. V., Rix, H.-W., Rosso, D. F., Runnoe, J., Salvato, M., Sanchez, S. F., Santana, F. A., Saydjari, A., Sayres, C., Schlaufman, K. C., Schneider, D. P., Schwope, A., Serna, J., Shen, Y., Sobeck, J., Song, Y.-Y., Souto, D., Spoo, T., Stassun, K. G., Steinmetz, M., Straumit, I., Stringfellow, G., Sánchez-Gallego, J., Taghizadeh-Popp, M., Tayar, J., Thakar, A., Tissera, P. B., Tkachenko, A., Toledo, H. H., Trakhtenbrot, B., Trincado, J. G. F., Troup, N., Trump, J. R., Tuttle, S., Ulloa, N., Vazquez-Mata, J. A., Alfaro, P. V., Villanova, S., Wachter, S., Weijmans, A.-M., Wheeler, A., Wilson, J., Wojno, L., Wolf, J., Xue, X.-X., Ybarra, J. E., Zari, E., and Zasowski, G. (2023). The eighteenth data release of the sloan digital sky surveys: Targeting and first spectra from sdss-v.

Andersen, T. B. (2018). Efficient and robust recurrence relations for the zernike circle polynomials and their derivatives in cartesian coordinates. *Opt. Express*, 26(15):18878–18896.

Arslan, G., Marden, J. R., and Shamma, J. S. (2007). Autonomous vehicle-target assignment: a game theoretical formulation. *ASME JOURNAL OF DYNAMIC SYSTEMS, MEASUREMENT AND CONTROL*, page 2007.

Barbary, K. (2018). SEP: Source Extraction and Photometry. Astrophysics Source Code Library, record ascl:1811.004.

Barkhouser, R. H., Smee, S. A., Hammond, R. P., Harding, A. C., Gray, A. C., Ramirez, S., Wachter, S., Kollmeier, J., Downey, J., Eriksen, J. E., and Wilson, J. C. (2022). Design of the new SDSS 2.5m telescope wide field corrector for SDSS-V. In Marshall, H. K., Spyromilio, J., and Usuda, T., editors, *Ground-based and Airborne Telescopes IX*, volume 12182, page 121823O. International Society for Optics and Photonics, SPIE.

Beard, S., Willemse, B., Watson, S., Atkinson, D., Cheetham, P. G., Franzetti, P., and Nix, J. (2022). MOONS fibre positioner control and path planning software. In Ibsen, J. and Chiozzi, G., editors, *Software and Cyberinfrastructure for Astronomy VII*, volume 12189, page 121890V. International Society for Optics and Photonics, SPIE.

Bellm, E. C., Kulkarni, S. R., Graham, M. J., Dekany, R., Smith, R. M., Riddle, R., Masci, F. J., Helou, G., Prince, T. A., Adams, S. M., Barbarino, C., Barlow, T., Bauer, J., Beck, R., Belicki, J., Biswas, R., Blagorodnova, N., Bodewits, D., Bolin, B., Brinnel, V., Brooke, T., Bue, B., Bulla, M., Burruss, R., Cenko, S. B., Chang, C.-K., Connolly, A., Coughlin, M., Cromer, J., Cunningham, V., De, K., Delacroix, A., Desai, V., Duev, D. A., Eadie, G., Farnham, T. L., Feeney, M., Feindt, U., Flynn, D., Franckowiak, A., Frederick, S., Fremling, C., Gal-Yam, A., Gezari, S., Giomi, M., Goldstein, D. A., Golkhou, V. Z., Goobar, A., Groom, S., Hacopians, E., Hale, D., Henning, J., Ho, A. Y. Q., Hover, D., Howell, J., Hung, T., Huppenkothen, D., Imel, D., Ip, W.-H., Ivezić, Ž., Jackson, E., Jones, L., Juric, M., Kasliwal, M. M., Kaspi, S., Kaye, S., Kelley, M. S. P., Kowalski, M., Kramer, E., Kupfer, T., Landry, W., Laher, R. R., Lee, C.-D., Lin, H. W., Lin, Z.-Y., Lunnan, R., Giomi, M., Mahabal, A., Mao, P., Miller, A. A., Monkewitz, S., Murphy, P., Ngeow, C.-C., Nordin, J., Nugent, P., Ofek, E., Patterson, M. T., Penprase, B., Porter, M., Rauch, L., Rebbapragada, U., Reiley, D., Rigault, M., Rodriguez, H., van Roestel, J., Rusholme, B., van Santen, J., Schulze, S., Shupe, D. L., Singer, L. P., Soumagnac, M. T., Stein, R., Surace, J., Sollerman, J., Szkody, P., Taddia, F., Terek, S., Van Sistine, A., van Velzen, S., Vestrand, W. T., Walters, R., Ward, C., Ye, Q.-Z., Yu, P.-C., Yan, L., and Zolkower, J. (2019). The Zwicky Transient Facility: System Overview, Performance, and First Results. PASP, 131(995):018002.

Bertin, E. and Arnouts, S. (1996). SExtractor: Software for source extraction. A&AS, 117:393–404.

Blanton, M. R., Bershady, M. A., Abolfathi, B., Albareti, F. D., Allende Prieto, C., Almeida, A., Alonso-García, J., Anders, F., Anderson, S. F., Andrews, B., Aquino-Ortíz, E., Aragón-Salamanca, A., Argudo-Fernández, M., Armengaud, E., Aubourg, E., Avila-Reese, V., Badenes,

C., Bailey, S., Barger, K. A., Barrera-Ballesteros, J., Bartosz, C., Bates, D., Baumgarten, F., Bautista, J., Beaton, R., Beers, T. C., Belfiore, F., Bender, C. F., Berlind, A. A., Bernardi, M., Beutler, F., Bird, J. C., Bizyaev, D., Blanc, G. A., Blomqvist, M., Bolton, A. S., Boquien, M., Borissova, J., van den Bosch, R., Bovy, J., Brandt, W. N., Brinkmann, J., Brownstein, J. R., Bundy, K., Burgasser, A. J., Burtin, E., Busca, N. G., Cappellari, M., Delgado Carigi, M. L., Carlberg, J. K., Carnero Rosell, A., Carrera, R., Chanover, N. J., Cherinka, B., Cheung, E., Gómez Maqueo Chew, Y., Chiappini, C., Choi, P. D., Chojnowski, D., Chuang, C.-H., Chung, H., Cirolini, R. F., Clerc, N., Cohen, R. E., Comparat, J., da Costa, L., Cousinou, M.-C., Covey, K., Crane, J. D., Croft, R. A. C., Cruz-Gonzalez, I., Garrido Cuadra, D., Cunha, K., Damke, G. J., Darling, J., Davies, R., Dawson, K., de la Macorra, A., Dell'Agli, F., De Lee, N., Delubac, T., Di Mille, F., Diamond-Stanic, A., Cano-Díaz, M., Donor, J., Downes, J. J., Drory, N., du Mas des Bourboux, H., Duckworth, C. J., Dwelly, T., Dyer, J., Ebelke, G., Eigenbrot, A. D., Eisenstein, D. J., Emsellem, E., Eracleous, M., Escoffier, S., Evans, M. L., Fan, X., Fernández-Alvar, E., Fernandez-Trincado, J. G., Feuillet, D. K., Finoguenov, A., Fleming, S. W., Font-Ribera, A., Fredrickson, A., Freischlad, G., Frinchaboy, P. M., Fuentes, C. E., Galbany, L., Garcia-Dias, R., García-Hernández, D. A., Gaulme, P., Geisler, D., Gelfand, J. D., Gil-Marín, H., Gillespie, B. A., Goddard, D., Gonzalez-Perez, V., Grabowski, K., Green, P. J., Grier, C. J., Gunn, J. E., Guo, H., Guy, J., Hagen, A., Hahn, C., Hall, M., Harding, P., Hasselquist, S., Hawley, S. L., Hearty, F., Gonzalez Hernández, J. I., Ho, S., Hogg, D. W., Holley-Bockelmann, K., Holtzman, J. A., Holzer, P. H., Huehnerhoff, J., Hutchinson, T. A., Hwang, H. S., Ibarra-Medel, H. J., da Silva Ilha, G., Ivans, I. I., Ivory, K., Jackson, K., Jensen, T. W., Johnson, J. A., Jones, A., Jönsson, H., Jullo, E., Kamble, V., Kinemuchi, K., Kirkby, D., Kitaura, F.-S., Klaene, M., Knapp, G. R., Kneib, J.-P., Kollmeier, J. A., Lacerna, I., Lane, R. R., Lang, D., Law, D. R., Lazarz, D., Lee, Y., Le Goff, J.-M., Liang, F.-H., Li, C., Li, H., Lian, J., Lima, M., Lin, L., Lin, Y.-T., Bertran de Lis, S., Liu, C., de Icaza Lizaola, M. A. C., Long, D., Lucatello, S., Lundgren, B., MacDonald, N. K., Deconto Machado, A., MacLeod, C. L., Mahadevan, S., Geimba Maia, M. A., Maiolino, R., Majewski, S. R., Malanushenko, E., Malanushenko, V., Manchado, A., Mao, S., Maraston, C., Marques-Chaves, R., Masseron, T., Masters, K. L., McBride, C. K.,

McDermid, R. M., McGrath, B., McGreer, I. D., Medina Peña, N., Melendez, M., Merloni, A., Merrifield, M. R., Meszaros, S., Meza, A., Minchev, I., Minniti, D., Miyaji, T., More, S., Mulchaey, J., Müller-Sánchez, F., Muna, D., Munoz, R. R., Myers, A. D., Nair, P., Nandra, K., Correa do Nascimento, J., Negrete, A., Ness, M., Newman, J. A., Nichol, R. C., Nidever, D. L., Nitschelm, C., Ntelis, P., O'Connell, J. E., Oelkers, R. J., Oravetz, A., Oravetz, D., Pace, Z., Padilla, N., Palanque-Delabrouille, N., Alonso Palicio, P., Pan, K., Parejko, J. K., Parikh, T., Pâris, I., Park, C., Patten, A. Y., Peirani, S., Pellejero-Ibanez, M., Penny, S., Percival, W. J., Perez-Fournon, I., Petitjean, P., Pieri, M. M., Pinsonneault, M., Pisani, A., Poleski, R., Prada, F., Prakash, A., Queiroz, A. B. d. A., Raddick, M. J., Raichoor, A., Barboza Rembold, S. r., Richstein, H., Riffel, R. A., Riffel, R., Rix, H.-W., Robin, A. C., Rockosi, C. M., Rodríguez-Torres, S., Roman-Lopes, A., Román-Zúñiga, C., Rosado, M., Ross, A. J., Rossi, G., Ruan, J., Ruggeri, R., Rykoff, E. S., Salazar-Albornoz, S., Salvato, M., Sánchez, A. G., Aguado, D. S., Sánchez-Gallego, J. R., Santana, F. A., Santiago, B. X., Sayres, C., Schiavon, R. P., da Silva Schimoia, J., Schlafly, E. F., Schlegel, D. J., Schneider, D. P., Schultheis, M., Schuster, W. J., Schwope, A., Seo, H.-J., Shao, Z., Shen, S., Shetrone, M., Shull, M., Simon, J. D., Skinner, D., Skrutskie, M. F., Slosar, A., Smith, V. V., Sobeck, J. S., Sobreira, F., Somers, G., Souto, D., Stark, D. V., Stassun, K., Stauffer, F., Steinmetz, M., Storchi-Bergmann, T., Streblyanska, A., Stringfellow, G. S., Suárez, G., Sun, J., Suzuki, N., Szigeti, L., Taghizadeh-Popp, M., Tang, B., Tao, C., Tayar, J., Tembe, M., Teske, J., Thakar, A. R., Thomas, D., Thompson, B. A., Tinker, J. L., Tissera, P., Tojeiro, R., Hernandez Toledo, H., de la Torre, S., Tremonti, C., Troup, N. W., Valenzuela, O., Martinez Valpuesta, I., Vargas-González, J., Vargas-Magaña, M., Vazquez, J. A., Villanova, S., Vivek, M., Vogt, N., Wake, D., Walterbos, R., Wang, Y., Weaver, B. A., Weijmans, A.-M., Weinberg, D. H., Westfall, K. B., Whelan, D. G., Wild, V., Wilson, J., Wood-Vasey, W. M., Wylezalek, D., Xiao, T., Yan, R., Yang, M., Ybarra, J. E., Yèche, C., Zakamska, N., Zamora, O., Zarrouk, P., Zasowski, G., Zhang, K., Zhao, G.-B., Zheng, Z., Zheng, Z., Zhou, X., Zhou, Z.-M., Zhu, G. B., Zoccali, M., and Zou, H. (2017). Sloan Digital Sky Survey IV: Mapping the Milky Way, Nearby Galaxies, and the Distant Universe. AJ, 154(1):28.

Bolton, A. S., Schlegel, D. J., Éric Aubourg, Bailey, S., Bhardwaj, V., Brownstein, J. R., Burles, S., Chen, Y.-M., Dawson, K., Eisenstein, D. J., Gunn, J. E., Knapp, G. R., Loomis, C. P., Lupton, R. H., Maraston, C., Muna, D., Myers, A. D., Olmstead, M. D., Padmanabhan, N., Pâris, I., Percival, W. J., Petitjean, P., Rockosi, C. M., Ross, N. P., Schneider, D. P., Shu, Y., Strauss, M. A., Thomas, D., Tremonti, C. A., Wake, D. A., Weaver, B. A., and Wood-Vasey, W. M. (2012). Spectral classification and redshift measurement for the sdss-iii baryon oscillation spectroscopic survey. *The Astronomical Journal*, 144(5):144.

Bowen, I. S. and Vaughan, Jr., A. H. (1973). The optical design of the 40-in. telescope and of the Irénée DuPont telescope at Las Campanas Observatory, Chile. Appl. Opt., 12:1430–1434.

Bundy, K., Bershady, M. A., Law, D. R., Yan, R., Drory, N., MacDonald, N., Wake, D. A., Cherinka, B., Sánchez-Gallego, J. R., Weijmans, A.-M., Thomas, D., Tremonti, C., Masters, K., Coccato, L., Diamond-Stanic, A. M., Aragón-Salamanca, A., Avila-Reese, V., Badenes, C., Falcón-Barroso, J., Belfiore, F., Bizyaev, D., Blanc, G. A., Bland-Hawthorn, J., Blanton, M. R., Brownstein, J. R., Byler, N., Cappellari, M., Conroy, C., Dutton, A. A., Emsellem, E., Etherington, J., Frinchaboy, P. M., Fu, H., Gunn, J. E., Harding, P., Johnston, E. J., Kauffmann, G., Kinemuchi, K., Klaene, M. A., Knapen, J. H., Leauthaud, A., Li, C., Lin, L., Maiolino, R., Malanushenko, V., Malanushenko, E., Mao, S., Maraston, C., McDermid, R. M., Merrifield, M. R., Nichol, R. C., Oravetz, D., Pan, K., Parejko, J. K., Sanchez, S. F., Schlegel, D., Simmons, A., Steele, O., Steinmetz, M., Thanjavur, K., Thompson, B. A., Tinker, J. L., van den Bosch, R. C. E., Westfall, K. B., Wilkinson, D., Wright, S., Xiao, T., and Zhang, K. (2015). Overview of the SDSS-IV MaNGA Survey: Mapping nearby Galaxies at Apache Point Observatory. ApJ, 798(1):7.

Bundy, K., Westfall, K., MacDonald, N., Kupke, R., Savage, M., Poppett, C., Alabi, A., Becker, G., Burchett, J., Capak, P., Coil, A., Cooper, M., Cowley, D., Deich, W., Dillon, D., Edelstein, J., Guhathakurta, P., Hennawi, J., Kassis, M., Lee, K. G., Masters, D., Miller, T., Newman, J., O'Meara, J., Prochaska, J. X., Rau, M., Rhodes, J., Rich, R. M., Rockosi, C., Romanowsky, A., Schafer, C., Schlegel, D., Shapley, A., Siana, B., Ting, Y. S., Weisz, D., White, M., Williams,

B., Wilson, G., Wilson, M., and Yan, R. (2019). FOBOS: A Next-Generation Spectroscopic Facility. In *Bulletin of the American Astronomical Society*, volume 51, page 198.

Camponogara, E., Jia, D., Krogh, B. H., and Talukdar, S. (2002). Distributed model predictive control. *IEEE Control Systems Magazine*, 22(1):44–52.

Cao, Y., Yu, W., Ren, W., and Chen, G. (2012). An overview of recent progress in the study of distributed multi-agent coordination. *IEEE Transactions on Industrial Informatics*, 9.

Cirasuolo, M., Afonso, J., Bender, R., Bonifacio, P., Evans, C., Kaper, L., Oliva, E., and Vanzi, L. (2011). MOONS: The Multi-Object Optical and Near-infrared Spectrograph. *The Messenger*, 145:11–13.

Cui, X.-Q., Zhao, Y.-H., Chu, Y.-Q., Li, G.-P., Li, Q., Zhang, L.-P., Su, H.-J., Yao, Z.-Q., Wang, Y.-N., Xing, X.-Z., Li, X.-N., Zhu, Y.-T., Wang, G., Gu, B.-Z., Luo, A. L., Xu, X.-Q., Zhang, Z.-C., Liu, G.-R., Zhang, H.-T., Yang, D.-H., Cao, S.-Y., Chen, H.-Y., Chen, J.-J., Chen, K.-X., Chen, Y., Chu, J.-R., Feng, L., Gong, X.-F., Hou, Y.-H., Hu, H.-Z., Hu, N.-S., Hu, Z.-W., Jia, L., Jiang, F.-H., Jiang, X., Jiang, Z.-B., Jin, G., Li, A.-H., Li, Y., Li, Y.-P., Liu, G.-Q., Liu, Z.-G., Lu, W.-Z., Mao, Y.-D., Men, L., Qi, Y.-J., Qi, Z.-X., Shi, H.-M., Tang, Z.-H., Tao, Q.-S., Wang, D.-Q., Wang, D., Wang, G.-M., Wang, H., Wang, J.-N., Wang, J., Wang, J.-L., Wang, J.-P., Wang, L., Wang, S.-Q., Wang, Y., Wang, Y.-F., Xu, L.-Z., Xu, Y., Yang, S.-H., Yu, Y., Yuan, H., Yuan, X.-Y., Zhai, C., Zhang, J., Zhang, Y.-X., Zhang, Y., Zhao, M., Zhou, F., Zhou, G.-H., Zhu, J., and Zou, S.-C. (2012). The Large Sky Area Multi-Object Fiber Spectroscopic Telescope (LAMOST). *Research in Astronomy and Astrophysics*, 12(9):1197–1242.

Dalton, G., Trager, S. C., Abrams, D. C., Carter, D., Bonifacio, P., Aguerri, J. A. L., MacIntosh, M., Evans, C., Lewis, I., Navarro, R., Agocs, T., Dee, K., Rousset, S., Tosh, I., Middleton, K., Pragt, J., Terrett, D., Brock, M., Benn, C., Verheijen, M., Cano Infantes, D., Bevil, C., Steele, I., Mottram, C., Bates, S., Gribbin, F. J., Rey, J., Rodriguez, L. F., Delgado, J. M., Guinouard, I., Walton, N., Irwin, M. J., Jagourel, P., Stuik, R., Gerlofsma, G., Roelfsma, R., Skillen, I., Ridings, A., Balcells, M., Daban, J.-B., Gouvret, C., Venema, L., and Girard, P. (2012). WEAVE: the

next generation wide-field spectroscopy facility for the William Herschel Telescope. In McLean, I. S., Ramsay, S. K., and Takami, H., editors, *Ground-based and Airborne Instrumentation for Astronomy IV*, volume 8446 of *Society of Photo-Optical Instrumentation Engineers (SPIE) Conference Series*, page 84460P.

Dawson, K. S., Schlegel, D. J., Ahn, C. P., Anderson, S. F., Éric Aubourg, Bailey, S., Barkhouser, R. H., Bautista, J. E., Beifiori, A., Berlind, A. A., Bhardwaj, V., Bizyaev, D., Blake, C. H., Blanton, M. R., Blomqvist, M., Bolton, A. S., Borde, A., Bovy, J., Brandt, W. N., Brewington, H., Brinkmann, J., Brown, P. J., Brownstein, J. R., Bundy, K., Busca, N. G., Carithers, W., Carnero, A. R., Carr, M. A., Chen, Y., Comparat, J., Connolly, N., Cope, F., Croft, R. A. C., Cuesta, A. J., da Costa, L. N., Davenport, J. R. A., Delubac, T., de Putter, R., Dhital, S., Ealet, A., Ebelke, G. L., Eisenstein, D. J., Escoffier, S., Fan, X., Ak, N. F., Finley, H., Font-Ribera, A., Génova-Santos, R., Gunn, J. E., Guo, H., Haggard, D., Hall, P. B., Hamilton, J.-C., Harris, B., Harris, D. W., Ho, S., Hogg, D. W., Holder, D., Honscheid, K., Huehnerhoff, J., Jordan, B., Jordan, W. P., Kauffmann, G., Kazin, E. A., Kirkby, D., Klaene, M. A., Kneib, J.-P., Goff, J.-M. L., Lee, K.-G., Long, D. C., Loomis, C. P., Lundgren, B., Lupton, R. H., Maia, M. A. G., Makler, M., Malanushenko, E., Malanushenko, V., Mandelbaum, R., Manera, M., Maraston, C., Margala, D., Masters, K. L., McBride, C. K., McDonald, P., McGreer, I. D., McMahon, R. G., Mena, O., Miralda-Escudé, J., Montero-Dorta, A. D., Montesano, F., Muna, D., Myers, A. D., Naugle, T., Nichol, R. C., Noterdaeme, P., Nuza, S. E., Olmstead, M. D., Oravetz, A., Oravetz, D. J., Owen, R., Padmanabhan, N., Palanque-Delabrouille, N., Pan, K., Parejko, J. K., Pâris, I., Percival, W. J., Pérez-Fournon, I., Pérez-Ràfols, I., Petitjean, P., Pfaffenberger, R., Pforr, J., Pieri, M. M., Prada, F., Price-Whelan, A. M., Raddick, M. J., Rebolo, R., Rich, J., Richards, G. T., Rockosi, C. M., Roe, N. A., Ross, A. J., Ross, N. P., Rossi, G., Rubiño-Martin, J. A., Samushia, L., Sánchez, A. G., Sayres, C., Schmidt, S. J., Schneider, D. P., Scóccola, C. G., Seo, H.-J., Shelden, A., Sheldon, E., Shen, Y., Shu, Y., Slosar, A., Smee, S. A., Snedden, S. A., Stauffer, F., Steele, O., Strauss, M. A., Streblyanska, A., Suzuki, N., Swanson, M. E. C., Tal, T., Tanaka, M., Thomas, D., Tinker, J. L., Tojeiro, R., Tremonti, C. A., Magaña, M. V., Verde, L.,

Viel, M., Wake, D. A., Watson, M., Weaver, B. A., Weinberg, D. H., Weiner, B. J., West, A. A., White, M., Wood-Vasey, W. M., Yeche, C., Zehavi, I., Zhao, G.-B., and Zheng, Z. (2012). The baryon oscillation spectroscopic survey of sdss-iii. *The Astronomical Journal*, 145(1):10.

de Jong, R. S., Agertz, O., Berbel, A. A., Aird, J., Alexander, D. A., Amarsi, A., Anders, F., Andrae, R., Ansarinejad, B., Ansorge, W., Antilogus, P., Anwand-Heerwart, H., Arentsen, A., Arnadottir, A., Asplund, M., Auger, M., Azais, N., Baade, D., Baker, G., Baker, S., Balbinot, E., Baldry, I. K., Banerji, M., Barden, S., Barklem, P., Barthélémy-Mazot, E., Battistini, C., Bauer, S., Bell, C. P. M., Bellido-Tirado, O., Bellstedt, S., Belokurov, V., Bensby, T., Bergemann, M., Bestenlehner, J. M., Bielby, R., Bilicki, M., Blake, C., Bland-Hawthorn, J., Boeche, C., Boland, W., Boller, T., Bongard, S., Bongiorno, A., Bonifacio, P., Boudon, D., Brooks, D., Brown, M. J. I., Brown, R., Brüggen, M., Brynnel, J., Brzeski, J., Buchert, T., Buschkamp, P., Caffau, E., Caillier, P., Carrick, J., Casagrande, L., Case, S., Casey, A., Cesarini, I., Cescutti, G., Chapuis, D., Chiappini, C., Childress, M., Christlieb, N., Church, R., Cioni, M. R. L., Cluver, M., Colless, M., Collett, T., Comparat, J., Cooper, A., Couch, W., Courbin, F., Croom, S., Croton, D., Daguisé, E., Dalton, G., Davies, L. J. M., Davis, T., de Laverny, P., Deason, A., Dionies, F., Disseau, K., Doel, P., Döscher, D., Driver, S. P., Dwelly, T., Eckert, D., Edge, A., Edvardsson, B., Youssoufi, D. E., Elhaddad, A., Enke, H., Erfanianfar, G., Farrell, T., Fechner, T., Feiz, C., Feltzing, S., Ferreras, I., Feuerstein, D., Feuillet, D., Finoguenov, A., Ford, D., Fotopoulou, S., Fouesneau, M., Frenk, C., Frey, S., Gaessler, W., Geier, S., Gentile Fusillo, N., Gerhard, O., Giannantonio, T., Giannone, D., Gibson, B., Gillingham, P., González-Fernández, C., Gonzalez-Solares, E., Gottloeber, S., Gould, A., Grebel, E. K., Gueguen, A., Guiglion, G., Haehnelt, M., Hahn, T., Hansen, C. J., Hartman, H., Hauptner, K., Hawkins, K., Haynes, D., Haynes, R., Heiter, U., Helmi, A., Aguayo, C. H., Hewett, P., Hinton, S., Hobbs, D., Hoenig, S., Hofman, D., Hook, I., Hopgood, J., Hopkins, A., Hourihane, A., Howes, L., Howlett, C., Huet, T., Irwin, M., Iwert, O., Jablonka, P., Jahn, T., Jahnke, K., Jarno, A., Jin, S., Jofre, P., Johl, D., Jones, D., Jönsson, H., Jordan, C., Karovicova, I., Khalatyan, A., Kelz, A., Kennicutt, R., King, D., Kitaura, F., Klar, J., Klauser, U., Kneib, J. P., Koch, A., Koposov, S., Kordopatis, G., Korn, A.,

Kosmalski, J., Kotak, R., Kovalev, M., Kreckel, K., Kripak, Y., Krumpe, M., Kuijken, K., Kunder, A., Kushniruk, I., Lam, M. I., Lamer, G., Laurent, F., Lawrence, J., Lehmitz, M., Lemasle, B., Lewis, J., Li, B., Lidman, C., Lind, K., Liske, J., Lizon, J. L., Loveday, J., Ludwig, H. G., McDermid, R. M., Maguire, K., Mainieri, V., Mali, S., Mandel, H., Mandel, K., Mannering, L., Martell, S., Martinez Delgado, D., Matijevic, G., McGregor, H., McMahon, R., McMillan, P., Mena, O., Merloni, A., Meyer, M. J., Michel, C., Micheva, G., Migniau, J. E., Minchev, I., Monari, G., Muller, R., Murphy, D., Muthukrishna, D., Nandra, K., Navarro, R., Ness, M., Nichani, V., Nichol, R., Nicklas, H., Niederhofer, F., Norberg, P., Obreschkow, D., Oliver, S., Owers, M., Pai, N., Pankratow, S., Parkinson, D., Paschke, J., Paterson, R., Pecontal, A., Parry, I., Phillips, D., Pillepich, A., Pinard, L., Pirard, J., Piskunov, N., Plank, V., Plüschke, D., Pons, E., Popesso, P., Power, C., Pragt, J., Pramskiy, A., Pryer, D., Quattri, M., Queiroz, A. B. d. A., Quirrenbach, A., Rahurkar, S., Raichoor, A., Ramstedt, S., Rau, A., Recio-Blanco, A., Reiss, R., Renaud, F., Revaz, Y., Rhode, P., Richard, J., Richter, A. D., Rix, H. W., Robotham, A. S. G., Roelfsema, R., Romaniello, M., Rosario, D., Rothmaier, F., Roukema, B., Ruchti, G., Rupprecht, G., Rybizki, J., Ryde, N., Saar, A., Sadler, E., Sahlén, M., Salvato, M., Sassolas, B., Saunders, W., Saviauk, A., Sbordone, L., Schmidt, T., Schnurr, O., Scholz, R. D., Schwope, A., Seifert, W., Shanks, T., Sheinis, A., Sivov, T., Skúladóttir, Á., Smartt, S., Smedley, S., Smith, G., Smith, R., Sorce, J., Spitler, L., Starkenburg, E., Steinmetz, M., Stilz, I., Storm, J., Sullivan, M., Sutherland, W., Swann, E., Tamone, A., Taylor, E. N., Teillon, J., Tempel, E., ter Horst, R., Thi, W. F., Tolstoy, E., Trager, S., Traven, G., Tremblay, P. E., Tresse, L., Valentini, M., van de Weygaert, R., van den Ancker, M., Veljanoski, J., Venkatesan, S., Wagner, L., Wagner, K., Walcher, C. J., Waller, L., Walton, N., Wang, L., Winkler, R., Wisotzki, L., Worley, C. C., Worseck, G., Xiang, M., Xu, W., Yong, D., Zhao, C., Zheng, J., Zscheyge, F., and Zucker, D. (2019). 4MOST: Project overview and information for the First Call for Proposals. *The Messenger*, 175:3–11.

DESI Collaboration, Aghamousa, A., Aguilar, J., Ahlen, S., Alam, S., Allen, L. E., Allende Prieto, C., Annis, J., Bailey, S., Balland, C., Ballester, O., Baltay, C., Beaufore, L., Bebek, C., Beers, T. C., Bell, E. F., Bernal, J. L., Besuner, R., Beutler, F., Blake, C., Bleuler, H., Blomqvist, M.,

Blum, R., Bolton, A. S., Briceno, C., Brooks, D., Brownstein, J. R., Buckley-Geer, E., Burden, A., Burtin, E., Busca, N. G., Cahn, R. N., Cai, Y.-C., Cardiel-Sas, L., Carlberg, R. G., Carton, P.-H., Casas, R., Castander, F. J., Cervantes-Cota, J. L., Claybaugh, T. M., Close, M., Coker, C. T., Cole, S., Comparat, J., Cooper, A. P., Cousinou, M. C., Crocce, M., Cuby, J.-G., Cunningham, D. P., Davis, T. M., Dawson, K. S., de la Macorra, A., De Vicente, J., Delubac, T., Derwent, M., Dey, A., Dhungana, G., Ding, Z., Doel, P., Duan, Y. T., Ealet, A., Edelstein, J., Eftekharzadeh, S., Eisenstein, D. J., Elliott, A., Escoffier, S., Evatt, M., Fagrelius, P., Fan, X., Fanning, K., Farahi, A., Farihi, J., Favole, G., Feng, Y., Fernandez, E., Findlay, J. R., Finkbeiner, D. P., Fitzpatrick, M. J., Flaugher, B., Flender, S., Font-Ribera, A., Forero-Romero, J. E., Fosalba, P., Frenk, C. S., Fumagalli, M., Gaensicke, B. T., Gallo, G., Garcia-Bellido, J., Gaztanaga, E., Pietro Gentile Fusillo, N., Gerard, T., Gershkovich, I., Giannantonio, T., Gillet, D., Gonzalez-de-Rivera, G., Gonzalez-Perez, V., Gott, S., Graur, O., Gutierrez, G., Guy, J., Habib, S., Heetderks, H., Heetderks, I., Heitmann, K., Hellwing, W. A., Herrera, D. A., Ho, S., Holland, S., Honscheid, K., Huff, E., Hutchinson, T. A., Huterer, D., Hwang, H. S., Illa Laguna, J. M., Ishikawa, Y., Jacobs, D., Jeffrey, N., Jelinsky, P., Jennings, E., Jiang, L., Jimenez, J., Johnson, J., Joyce, R., Jullo, E., Juneau, S., Kama, S., Karcher, A., Karkar, S., Kehoe, R., Kennamer, N., Kent, S., Kilbinger, M., Kim, A. G., Kirkby, D., Kisner, T., Kitanidis, E., Kneib, J.-P., Koposov, S., Kovacs, E., Koyama, K., Kremin, A., Kron, R., Kronig, L., Kueter-Young, A., Lacey, C. G., Lafever, R., Lahav, O., Lambert, A., Lampton, M., Landriau, M., Lang, D., Lauer, T. R., Le Goff, J.-M., Le Guillou, L., Le Van Suu, A., Lee, J. H., Lee, S.-J., Leitner, D., Lesser, M., Levi, M. E., L'Huillier, B., Li, B., Liang, M., Lin, H., Linder, E., Loebman, S. R., Lukić, Z., Ma, J., MacCrann, N., Magneville, C., Makarem, L., Manera, M., Manser, C. J., Marshall, R., Martini, P., Massey, R., Matheson, T., McCauley, J., McDonald, P., McGreer, I. D., Meisner, A., Metcalfe, N., Miller, T. N., Miquel, R., Moustakas, J., Myers, A., Naik, M., Newman, J. A., Nichol, R. C., Nicola, A., Nicolati da Costa, L., Nie, J., Niz, G., Norberg, P., Nord, B., Norman, D., Nugent, P., O'Brien, T., Oh, M., Olsen, K. A. G., Padilla, C., Padmanabhan, H., Padmanabhan, N., Palanque-Delabrouille, N., Palmese, A., Pappalardo, D., Pâris, I., Park, C., Patej, A., Peacock, J. A., Peiris, H. V., Peng, X., Percival, W. J., Perruchot, S., Pieri, M. M.,

Pogge, R., Pollack, J. E., Poppett, C., Prada, F., Prakash, A., Probst, R. G., Rabinowitz, D., Raichoor, A., Ree, C. H., Refregier, A., Regal, X., Reid, B., Reil, K., Rezaie, M., Rockosi, C. M., Roe, N., Ronayette, S., Roodman, A., Ross, A. J., Ross, N. P., Rossi, G., Rozo, E., Ruhlmann-Kleider, V., Rykoff, E. S., Sabiu, C., Samushia, L., Sanchez, E., Sanchez, J., Schlegel, D. J., Schneider, M., Schubnell, M., Secroun, A., Seljak, U., Seo, H.-J., Serrano, S., Shafieloo, A., Shan, H., Sharples, R., Sholl, M. J., Shourt, W. V., Silber, J. H., Silva, D. R., Sirk, M. M., Slosar, A., Smith, A., Smoot, G. F., Som, D., Song, Y.-S., Sprayberry, D., Staten, R., Stefanik, A., Tarle, G., Sien Tie, S., Tinker, J. L., Tojeiro, R., Valdes, F., Valenzuela, O., Valluri, M., Vargas-Magana, M., Verde, L., Walker, A. R., Wang, J., Wang, Y., Weaver, B. A., Weaverdyck, C., Wechsler, R. H., Weinberg, D. H., White, M., Yang, Q., Yeche, C., Zhang, T., Zhao, G.-B., Zheng, Y., Zhou, X., Zhou, Z., Zhu, Y., Zou, H., and Zu, Y. (2016). The DESI Experiment Part I: Science,Targeting, and Survey Design. *arXiv e-prints*, page arXiv:1611.00036.

Eisenstein, D. J., Weinberg, D. H., Agol, E., Aihara, H., Allende Prieto, C., Anderson, S. F., Arns, J. A., Aubourg, É., Bailey, S., Balbinot, E., Barkhouser, R., Beers, T. C., Berlind, A. A., Bickerton, S. J., Bizyaev, D., Blanton, M. R., Bochanski, J. J., Bolton, A. S., Bosman, C. T., Bovy, J., Brandt, W. N., Breslauer, B., Brewington, H. J., Brinkmann, J., Brown, P. J., Brownstein, J. R., Burger, D., Busca, N. G., Campbell, H., Cargile, P. A., Carithers, W. C., Carlberg, J. K., Carr, M. A., Chang, L., Chen, Y., Chiappini, C., Comparat, J., Connolly, N., Cortes, M., Croft, R. A. C., Cunha, K., da Costa, L. N., Davenport, J. R. A., Dawson, K., De Lee, N., Porto de Mello, G. F., de Simoni, F. o., Dean, J., Dhital, S., Ealet, A., Ebelke, G. L., Edmondson, E. M., Eiting, J. M., Escoffier, S., Esposito, M., Evans, M. L., Fan, X., Femenía Castellá, B., Dutra Ferreira, L., Fitzgerald, G., Fleming, S. W., Font-Ribera, A., Ford, E. B., Frinchaboy, P. M., García Pérez, A. E., Gaudi, B. S., Ge, J., Ghezzi, L., Gillespie, B. A., Gilmore, G., Girardi, L., Gott, J. R., Gould, A., Grebel, E. K., Gunn, J. E., Hamilton, J.-C., Harding, P., Harris, D. W., Hawley, S. L., Hearty, F. R., Hennawi, J. F., González Hernández, J. I., Ho, S., Hogg, D. W., Holtzman, J. A., Honscheid, K., Inada, N., Ivans, I. I., Jiang, L., Jiang, P., Johnson, J. A., Jordan, C., Jordan, W. P., Kauffmann, G., Kazin, E., Kirkby, D., Klaene, M. A., Knapp, G. R., Kneib,

J.-P., Kochanek, C. S., Koesterke, L., Kollmeier, J. A., Kron, R. G., Lampeitl, H., Lang, D., Lawler, J. E., Le Goff, J.-M., Lee, B. L., Lee, Y. S., Leisenring, J. M., Lin, Y.-T., Liu, J., Long, D. C., Loomis, C. P., Lucatello, S., Lundgren, B., Lupton, R. H., Ma, B., Ma, Z., MacDonald, N., Mack, C., Mahadevan, S., Maia, M. A. G., Majewski, S. R., Makler, M., Malanushenko, E., Malanushenko, V., Mand elbaum, R., Maraston, C., Margala, D., Maseman, P., Masters, K. L., McBride, C. K., McDonald, P., McGreer, I. D., McMahon, R. G., Mena Requejo, O., Ménard, B., Miralda-Escudé, J., Morrison, H. L., Mullally, F., Muna, D., Murayama, H., Myers, A. D., Naugle, T., Neto, A. F., Nguyen, D. C., Nichol, R. C., Nidever, D. L., O'Connell, R. W., Ogando, R. L. C., Olmstead, M. D., Oravetz, D. J., Padmanabhan, N., Paegert, M., Palanque-Delabrouille, N., Pan, K., Pandey, P., Parejko, J. K., Pâris, I., Pellegrini, P., Pepper, J., Percival, W. J., Petitjean, P., Pfaffenberger, R., Pforr, J., Phleps, S., Pichon, C., Pieri, M. M., Prada, F., Price-Whelan, A. M., Raddick, M. J., Ramos, B. H. F., Reid, I. N., Reyle, C., Rich, J., Richards, G. T., Rieke, G. H., Rieke, M. J., Rix, H.-W., Robin, A. C., Rocha-Pinto, H. J., Rockosi, C. M., Roe, N. A., Rollinde, E., Ross, A. J., Ross, N. P., Rossetto, B., Sánchez, A. G., Santiago, B., Sayres, C., Schiavon, R., Schlegel, D. J., Schlesinger, K. J., Schmidt, S. J., Schneider, D. P., Sellgren, K., Shelden, A., Sheldon, E., Shetrone, M., Shu, Y., Silverman, J. D., Simmerer, J., Simmons, A. E., Sivarani, T., Skrutskie, M. F., Slosar, A., Smee, S., Smith, V. V., Snedden, S. A., Stassun, K. G., Steele, O., Steinmetz, M., Stockett, M. H., Stollberg, T., Strauss, M. A., Szalay, A. S., Tanaka, M., Thakar, A. R., Thomas, D., Tinker, J. L., Tofflemire, B. M., Tojeiro, R., Tremonti, C. A., Vargas Magaña, M., Verde, L., Vogt, N. P., Wake, D. A., Wan, X., Wang, J., Weaver, B. A., White, M., White, S. D. M., Wilson, J. C., Wisniewski, J. P., Wood-Vasey, W. M., Yanny, B., Yasuda, N., Yèche, C., York, D. G., Young, E., Zasowski, G., Zehavi, I., and Zhao, B. (2011). SDSS-III: Massive Spectroscopic Surveys of the Distant Universe, the Milky Way, and Extra-Solar Planetary Systems. AJ, 142(3):72.

Ellis, R. and Dawson, K. (2019). SpecTel: A 10-12 meter class Spectroscopic Survey Telescope. In *Bulletin of the American Astronomical Society*, volume 51, page 45.

Emenheiser, J., Chapman, A., Pósfai, M., Crutchfield, J. P., Mesbahi, M., and D'Souza, R. M.

(2016). Patterns of patterns of synchronization: Noise induced attractor switching in rings of coupled nonlinear oscillators. *Chaos: An Interdisciplinary Journal of Nonlinear Science*, 26(9):094816.

Engelman, M., O'Brien, T. P., Pogge, R. W., Derwent, M., Sayres, C., Pappalardo, D., Brandon, C., Shover, J., Ramírez, S., and Wachter, S. (2022). SDSS-V focal plane system high-precision metrology. In Evans, C. J., Bryant, J. J., and Motohara, K., editors, *Ground-based and Airborne Instrumentation for Astronomy IX*, volume 12184, page 121847J. International Society for Optics and Photonics, SPIE.

Gaia Collaboration, Brown, A. G. A., Vallenari, A., Prusti, T., de Bruijne, J. H. J., Babusiaux, C., Bailer-Jones, C. A. L., Biermann, M., Evans, D. W., Eyer, L., Jansen, F., Jordi, C., Klioner, S. A., Lammers, U., Lindegren, L., Luri, X., Mignard, F., Panem, C., Pourbaix, D., Randich, S., Sartoretti, P., Siddiqui, H. I., Soubiran, C., van Leeuwen, F., Walton, N. A., Arenou, F., Bastian, U., Cropper, M., Drimmel, R., Katz, D., Lattanzi, M. G., Bakker, J., Cacciari, C., Castañeda, J., Chaoul, L., Cheek, N., De Angeli, F., Fabricius, C., Guerra, R., Holl, B., Masana, E., Messineo, R., Mowlavi, N., Nienartowicz, K., Panuzzo, P., Portell, J., Riello, M., Seabroke, G. M., Tanga, P., Thévenin, F., Gracia-Abril, G., Comoretto, G., Garcia-Reinaldos, M., Teyssier, D., Altmann, M., Andrae, R., Audard, M., Bellas-Velidis, I., Benson, K., Berthier, J., Blomme, R., Burgess, P., Busso, G., Carry, B., Cellino, A., Clementini, G., Clotet, M., Creevey, O., Davidson, M., De Ridder, J., Delchambre, L., Dell'Oro, A., Ducourant, C., Fernández-Hernández, J., Fouesneau, M., Frémat, Y., Galluccio, L., García-Torres, M., González-Núñez, J., González-Vidal, J. J., Gosset, E., Guy, L. P., Halbwachs, J. L., Hambly, N. C., Harrison, D. L., Hernández, J., Hestroffer, D., Hodgkin, S. T., Hutton, A., Jasniewicz, G., Jean-Antoine-Piccolo, A., Jordan, S., Korn, A. J., Krone-Martins, A., Lanzafame, A. C., Lebzelter, T., Löffler, W., Manteiga, M., Marrese, P. M., Martín-Fleitas, J. M., Moitinho, A., Mora, A., Muinonen, K., Osinde, J., Pancino, E., Pauwels, T., Petit, J. M., Recio-Blanco, A., Richards, P. J., Rimoldini, L., Robin, A. C., Sarro, L. M., Siopis, C., Smith, M., Sozzetti, A., Süveges, M., Torra, J., van Reeven, W., Abbas, U., Abreu Aramburu, A., Accart, S., Aerts, C., Altavilla, G., Álvarez, M. A., Alvarez, R., Alves,

J., Anderson, R. I., Andrei, A. H., Anglada Varela, E., Antiche, E., Antoja, T., Arcay, B., Astraatmadja, T. L., Bach, N., Baker, S. G., Balaguer-Núñez, L., Balm, P., Barache, C., Barata, C., Barbato, D., Barblan, F., Barklem, P. S., Barrado, D., Barros, M., Barstow, M. A., Bartholomé Muñoz, S., Bassilana, J. L., Becciani, U., Bellazzini, M., Berihuete, A., Bertone, S., Bianchi, L., Bienaymé, O., Blanco-Cuaresma, S., Boch, T., Boeche, C., Bombrun, A., Borrachero, R., Bossini, D., Bouquillon, S., Bourda, G., Bragaglia, A., Bramante, L., Breddels, M. A., Bressan, A., Brouillet, N., Brüsemeister, T., Brugaletta, E., Bucciarelli, B., Burlacu, A., Busonero, D., Butkevich, A. G., Buzzi, R., Caffau, E., Cancelliere, R., Cannizzaro, G., Cantat-Gaudin, T., Carballo, R., Carlucci, T., Carrasco, J. M., Casamiquela, L., Castellani, M., Castro-Ginard, A., Charlot, P., Chemin, L., Chiavassa, A., Cocozza, G., Costigan, G., Cowell, S., Crifo, F., Crosta, M., Crowley, C., Cuypers, J., Dafonte, C., Damerdji, Y., Dapergolas, A., David, P., David, M., de Laverny, P., De Luise, F., De March, R., de Martino, D., de Souza, R., de Torres, A., Debosscher, J., del Pozo, E., Delbo, M., Delgado, A., Delgado, H. E., Di Matteo, P., Diakite, S., Diener, C., Distefano, E., Dolding, C., Drazinos, P., Durán, J., Edvardsson, B., Enke, H., Eriksson, K., Esquej, P., Eynard Bontemps, G., Fabre, C., Fabrizio, M., Faigler, S., Falcão, A. J., Farràs Casas, M., Federici, L., Fedorets, G., Fernique, P., Figueras, F., Filippi, F., Findeisen, K., Fonti, A., Fraile, E., Fraser, M., Frézouls, B., Gai, M., Galleti, S., Garabato, D., García-Sedano, F., Garofalo, A., Garralda, N., Gavel, A., Gavras, P., Gerssen, J., Geyer, R., Giacobbe, P., Gilmore, G., Girona, S., Giuffrida, G., Glass, F., Gomes, M., Granvik, M., Gueguen, A., Guerrier, A., Guiraud, J., Gutiérrez-Sánchez, R., Haigron, R., Hatzidimitriou, D., Hauser, M., Haywood, M., Heiter, U., Helmi, A., Heu, J., Hilger, T., Hobbs, D., Hofmann, W., Holland, G., Huckle, H. E., Hypki, A., Icardi, V., Janßen, K., Jevardat de Fombelle, G., Jonker, P. G., Juhász, Á. L., Julbe, F., Karampelas, A., Kewley, A., Klar, J., Kochoska, A., Kohley, R., Kolenberg, K., Kontizas, M., Kontizas, E., Koposov, S. E., Kordopatis, G., Kostrzewa-Rutkowska, Z., Koubsky, P., Lambert, S., Lanza, A. F., Lasne, Y., Lavigne, J. B., Le Fustec, Y., Le Poncin-Lafitte, C., Lebreton, Y., Leccia, S., Leclerc, N., Lecoeur-Taibi, I., Lenhardt, H., Leroux, F., Liao, S., Licata, E., Lindstrøm, H. E. P., Lister, T. A., Livanou, E., Lobel, A., López, M., Managau, S., Mann, R. G., Mantelet, G., Marchal, O., Marchant, J. M., Marconi, M., Marinoni, S., Marschalkó, G., Marshall, D. J.,

Martino, M., Marton, G., Mary, N., Massari, D., Matijevič, G., Mazeh, T., McMillan, P. J., Messina, S., Michalik, D., Millar, N. R., Molina, D., Molinaro, R., Molnár, L., Montegriffo, P., Mor, R., Morbidelli, R., Morel, T., Morris, D., Mulone, A. F., Muraveva, T., Musella, I., Nelemans, G., Nicastro, L., Noval, L., O'Mullane, W., Ordénovic, C., Ordóñez-Blanco, D., Osborne, P., Pagani, C., Pagano, I., Pailler, F., Palacin, H., Palaversa, L., Panahi, A., Pawlak, M., Piersimoni, A. M., Pineau, F. X., Plachy, E., Plum, G., Poggio, E., Poujoulet, E., Prša, A., Pulone, L., Racero, E., Ragaini, S., Rambaux, N., Ramos-Lerate, M., Regibo, S., Reylé, C., Riclet, F., Ripepi, V., Riva, A., Rivard, A., Rixon, G., Roegiers, T., Roelens, M., Romero-Gómez, M., Rowell, N., Royer, F., Ruiz-Dern, L., Sadowski, G., Sagristà Sellés, T., Sahlmann, J., Salgado, J., Salguero, E., Sanna, N., Santana-Ros, T., Sarasso, M., Savietto, H., Schultheis, M., Sciacca, E., Segol, M., Segovia, J. C., Ségransan, D., Shih, I. C., Siltala, L., Silva, A. F., Smart, R. L., Smith, K. W., Solano, E., Solitro, F., Sordo, R., Soria Nieto, S., Souchay, J., Spagna, A., Spoto, F., Stampa, U., Steele, I. A., Steidelmüller, H., Stephenson, C. A., Stoev, H., Suess, F. F., Surdej, J., Szabados, L., Szegedi-Elek, E., Tapiador, D., Taris, F., Tauran, G., Taylor, M. B., Teixeira, R., Terrett, D., Teyssandier, P., Thuillot, W., Titarenko, A., Torra Clotet, F., Turon, C., Ulla, A., Utrilla, E., Uzzi, S., Vaillant, M., Valentini, G., Valette, V., van Elteren, A., Van Hemelryck, E., van Leeuwen, M., Vaschetto, M., Vecchiato, A., Veljanoski, J., Viala, Y., Vicente, D., Vogt, S., von Essen, C., Voss, H., Votruba, V., Voutsinas, S., Walmsley, G., Weiler, M., Wertz, O., Wevers, T., Wyrzykowski, Ł., Yoldas, A., Žerjal, M., Ziaeepour, H., Zorec, J., Zschocke, S., Zucker, S., Zurbach, C., and Zwitter, T. (2018). Gaia Data Release 2. Summary of the contents and survey properties. A&A, 616:A1.

Gaia Collaboration, Prusti, T., de Bruijne, J. H. J., Brown, A. G. A., Vallenari, A., Babusiaux, C., Bailer-Jones, C. A. L., Bastian, U., Biermann, M., Evans, D. W., Eyer, L., Jansen, F., Jordi, C., Klioner, S. A., Lammers, U., Lindegren, L., Luri, X., Mignard, F., Milligan, D. J., Panem, C., Poinsignon, V., Pourbaix, D., Randich, S., Sarri, G., Sartoretti, P., Siddiqui, H. I., Soubiran, C., Valette, V., van Leeuwen, F., Walton, N. A., Aerts, C., Arenou, F., Cropper, M., Drimmel, R., Høg, E., Katz, D., Lattanzi, M. G., O'Mullane, W., Grebel, E. K., Holland, A. D., Huc,

C., Passot, X., Bramante, L., Cacciari, C., Castañeda, J., Chaoul, L., Cheek, N., De Angeli, F., Fabricius, C., Guerra, R., Hernández, J., Jean-Antoine-Piccolo, A., Masana, E., Messineo, R., Mowlavi, N., Nienartowicz, K., Ordóñez-Blanco, D., Panuzzo, P., Portell, J., Richards, P. J., Riello, M., Seabroke, G. M., Tanga, P., Thévenin, F., Torra, J., Els, S. G., Gracia-Abril, G., Comoretto, G., Garcia-Reinaldos, M., Lock, T., Mercier, E., Altmann, M., Andrae, R., Astraatmadja, T. L., Bellas-Velidis, I., Benson, K., Berthier, J., Blomme, R., Busso, G., Carry, B., Cellino, A., Clementini, G., Cowell, S., Creevey, O., Cuypers, J., Davidson, M., De Ridder, J., de Torres, A., Delchambre, L., Dell'Oro, A., Ducourant, C., Frémat, Y., García-Torres, M., Gosset, E., Halbwachs, J. L., Hambly, N. C., Harrison, D. L., Hauser, M., Hestroffer, D., Hodgkin, S. T., Huckle, H. E., Hutton, A., Jasniewicz, G., Jordan, S., Kontizas, M., Korn, A. J., Lanzafame, A. C., Manteiga, M., Moitinho, A., Muinonen, K., Osinde, J., Pancino, E., Pauwels, T., Petit, J. M., Recio-Blanco, A., Robin, A. C., Sarro, L. M., Siopis, C., Smith, M., Smith, K. W., Sozzetti, A., Thuillot, W., van Reeven, W., Viala, Y., Abbas, U., Abreu Aramburu, A., Accart, S., Aguado, J. J., Allan, P. M., Allasia, W., Altavilla, G., Álvarez, M. A., Alves, J., Anderson, R. I., Andrei, A. H., Anglada Varela, E., Antiche, E., Antoja, T., Antón, S., Arcay, B., Atzei, A., Ayache, L., Bach, N., Baker, S. G., Balaguer-Núñez, L., Barache, C., Barata, C., Barbier, A., Barblan, F., Baroni, M., Barrado y Navascués, D., Barros, M., Barstow, M. A., Becciani, U., Bellazzini, M., Bellei, G., Bello García, A., Belokurov, V., Bendjoya, P., Berihuete, A., Bianchi, L., Bienaymé, O., Billebaud, F., Blagorodnova, N., Blanco-Cuaresma, S., Boch, T., Bombrun, A., Borrachero, R., Bouquillon, S., Bourda, G., Bouy, H., Bragaglia, A., Breddels, M. A., Brouillet, N., Brüsemeister, T., Bucciarelli, B., Budnik, F., Burgess, P., Burgon, R., Burlacu, A., Busonero, D., Buzzi, R., Caffau, E., Cambras, J., Campbell, H., Cancelliere, R., Cantat-Gaudin, T., Carlucci, T., Carrasco, J. M., Castellani, M., Charlot, P., Charnas, J., Charvet, P., Chassat, F., Chiavassa, A., Clotet, M., Cocozza, G., Collins, R. S., Collins, P., Costigan, G., Crifo, F., Cross, N. J. G., Crosta, M., Crowley, C., Dafonte, C., Damerdji, Y., Dapergolas, A., David, P., David, M., De Cat, P., de Felice, F., de Laverny, P., De Luise, F., De March, R., de Martino, D., de Souza, R., Debosscher, J., del Pozo, E., Delbo, M., Delgado, A., Delgado, H. E., di Marco, F., Di Matteo, P., Diakite, S., Distefano, E., Dolding, C., Dos Anjos, S., Drazinos, P., Durán, J.,

Dzigan, Y., Ecale, E., Edvardsson, B., Enke, H., Erdmann, M., Escolar, D., Espina, M., Evans, N. W., Eynard Bontemps, G., Fabre, C., Fabrizio, M., Faigler, S., Falcão, A. J., Farràs Casas, M., Faye, F., Federici, L., Fedorets, G., Fernández-Hernández, J., Fernique, P., Fienga, A., Figueras, F., Filippi, F., Findeisen, K., Fonti, A., Fouesneau, M., Fraile, E., Fraser, M., Fuchs, J., Furnell, R., Gai, M., Galleti, S., Galluccio, L., Garabato, D., García-Sedano, F., Garé, P., Garofalo, A., Garralda, N., Gavras, P., Gerssen, J., Geyer, R., Gilmore, G., Girona, S., Giuffrida, G., Gomes, M., González-Marcos, A., González-Núñez, J., González-Vidal, J. J., Granvik, M., Guerrier, A., Guillout, P., Guiraud, J., Gúrpide, A., Gutiérrez-Sánchez, R., Guy, L. P., Haigron, R., Hatzidimitriou, D., Haywood, M., Heiter, U., Helmi, A., Hobbs, D., Hofmann, W., Holl, B., Holland , G., Hunt, J. A. S., Hypki, A., Icardi, V., Irwin, M., Jevardat de Fombelle, G., Jofré, P., Jonker, P. G., Jorissen, A., Julbe, F., Karampelas, A., Kochoska, A., Kohley, R., Kolenberg, K., Kontizas, E., Koposov, S. E., Kordopatis, G., Koubsky, P., Kowalczyk, A., Krone-Martins, A., Kudryashova, M., Kull, I., Bachchan, R. K., Lacoste-Seris, F., Lanza, A. F., Lavigne, J. B., Le Poncin-Lafitte, C., Lebreton, Y., Lebzelter, T., Leccia, S., Leclerc, N., Lecoeur-Taibi, I., Lemaitre, V., Lenhardt, H., Leroux, F., Liao, S., Licata, E., Lindstrøm, H. E. P., Lister, T. A., Livanou, E., Lobel, A., Löffler, W., López, M., Lopez-Lozano, A., Lorenz, D., Loureiro, T., MacDonald, I., Magalhães Fernandes, T., Managau, S., Mann, R. G., Mantelet, G., Marchal, O., Marchant, J. M., Marconi, M., Marie, J., Marinoni, S., Marrese, P. M., Marschalkó, G., Marshall, D. J., Martín-Fleitas, J. M., Martino, M., Mary, N., Matijevič, G., Mazeh, T., McMillan, P. J., Messina, S., Mestre, A., Michalik, D., Millar, N. R., Miranda, B. M. H., Molina, D., Molinaro, R., Molinaro, M., Molnár, L., Moniez, M., Montegriffo, P., Monteiro, D., Mor, R., Mora, A., Morbidelli, R., Morel, T., Morgenthaler, S., Morley, T., Morris, D., Mulone, A. F., Muraveva, T., Musella, I., Narbonne, J., Nelemans, G., Nicastro, L., Noval, L., Ordénovic, C., Ordieres-Meré, J., Osborne, P., Pagani, C., Pagano, I., Pailler, F., Palacin, H., Palaversa, L., Parsons, P., Paulsen, T., Pecoraro, M., Pedrosa, R., Pentikäinen, H., Pereira, J., Pichon, B., Piersimoni, A. M., Pineau, F. X., Plachy, E., Plum, G., Poujoulet, E., Prša, A., Pulone, L., Ragaini, S., Rago, S., Rambaux, N., Ramos-Lerate, M., Ranalli, P., Rauw, G., Read, A., Regibo, S., Renk, F., Reylé, C., Ribeiro, R. A., Rimoldini, L., Ripepi, V., Riva, A., Rixon, G., Roelens, M., Romero-Gómez, M., Row-

ell, N., Royer, F., Rudolph, A., Ruiz-Dern, L., Sadowski, G., Sagristà Sellés, T., Sahlmann, J., Salgado, J., Salguero, E., Sarasso, M., Savietto, H., Schnorhk, A., Schultheis, M., Sciacca, E., Segol, M., Segovia, J. C., Segransan, D., Serpell, E., Shih, I. C., Smareglia, R., Smart, R. L., Smith, C., Solano, E., Solitro, F., Sordo, R., Soria Nieto, S., Souchay, J., Spagna, A., Spoto, F., Stampa, U., Steele, I. A., Steidelmüller, H., Stephenson, C. A., Stoev, H., Suess, F. F., Süveges, M., Surdej, J., Szabados, L., Szegedi-Elek, E., Tapiador, D., Taris, F., Tauran, G., Taylor, M. B., Teixeira, R., Terrett, D., Tingley, B., Trager, S. C., Turon, C., Ulla, A., Utrilla, E., Valentini, G., van Elteren, A., Van Hemelryck, E., van Leeuwen, M., Varadi, M., Vecchiato, A., Veljanoski, J., Via, T., Vicente, D., Vogt, S., Voss, H., Votruba, V., Voutsinas, S., Walmsley, G., Weiler, M., Weingrill, K., Werner, D., Wevers, T., Whitehead, G., Wyrzykowski, Ł., Yoldas, A., Žerjal, M., Zucker, S., Zurbach, C., Zwitter, T., Alecu, A., Allen, M., Allende Prieto, C., Amorim, A., Anglada-Escudé, G., Arsenijevic, V., Azaz, S., Balm, P., Beck, M., Bernstein, H. H., Bigot, L., Bijaoui, A., Blasco, C., Bonfigli, M., Bono, G., Boudreault, S., Bressan, A., Brown, S., Brunet, P. M., Bunclark, P., Buonanno, R., Butkevich, A. G., Carret, C., Carrion, C., Chemin, L., Chéreau, F., Corcione, L., Darmigny, E., de Boer, K. S., de Teodoro, P., de Zeeuw, P. T., Delle Luche, C., Domingues, C. D., Dubath, P., Fodor, F., Frézouls, B., Fries, A., Fustes, D., Fyfe, D., Gallardo, E., Gallegos, J., Gardiol, D., Gebran, M., Gomboc, A., Gómez, A., Grux, E., Gueguen, A., Heyrovsky, A., Hoar, J., Iannicola, G., Isasi Parache, Y., Janotto, A. M., Joliet, E., Jonckheere, A., Keil, R., Kim, D. W., Klagyivik, P., Klar, J., Knude, J., Kochukhov, O., Kolka, I., Kos, J., Kutka, A., Lainey, V., LeBouquin, D., Liu, C., Loreggia, D., Makarov, V. V., Marseille, M. G., Martayan, C., Martinez-Rubi, O., Massart, B., Meynadier, F., Mignot, S., Munari, U., Nguyen, A. T., Nordlander, T., Ocvirk, P., O'Flaherty, K. S., Olias Sanz, A., Ortiz, P., Osorio, J., Oszkiewicz, D., Ouzounis, A., Palmer, M., Park, P., Pasquato, E., Peltzer, C., Peralta, J., Péturaud, F., Pieniluoma, T., Pigozzi, E., Poels, J., Prat, G., Prod'homme, T., Raison, F., Rebordao, J. M., Risquez, D., Rocca-Volmerange, B., Rosen, S., Ruiz-Fuertes, M. I., Russo, F., Sembay, S., Serraller Vizcaino, I., Short, A., Siebert, A., Silva, H., Sinachopoulos, D., Slezak, E., Soffel, M., Sosnowska, D., Straižys, V., ter Linden, M., Terrell, D., Theil, S., Tiede, C., Troisi, L., Tsalmantza, P., Tur, D., Vaccari, M., Vachier, F., Valles, P., Van Hamme, W., Veltz,

L., Virtanen, J., Wallut, J. M., Wichmann, R., Wilkinson, M. I., Ziaeepour, H., and Zschocke, S. (2016). The Gaia mission. A&A, 595:A1.

Ge, J., Lee, B., Lee, N. D., Wan, X., Groot, J., Zhao, B., Varosi, F., Hanna, K., Mahadevan, S., Hearty, F., Chang, L., Liu, J., van Eyken, J., Wang, J., Pais, R., Chen, Z., Shelden, A., and Costello, E. (2009). A new generation multi-object Doppler instrument for the SDSS-III Multi-object APO Radial Velocity Exoplanet Large-area Survey. In Shaklan, S. B., editor, *Techniques and Instrumentation for Detection of Exoplanets IV*, volume 7440, pages 187 – 196. International Society for Optics and Photonics, SPIE.

Gray, A. C., Barkhouser, R. H., Smee, S. A., Hammond, R. P., Harding, A., Ramírez, S., Wachter, S., Kollmeier, J., Bizyaev, D., Eriksen, J., Gatlin, D., Grabowski, K., Kinemuchi, K., Long, D., Malanushenko, V., Mrozek, F., Naugle, T., Oravetz, A., Oravetz, D., Pan, K., Wagner, R., and Wilson, J. (2022). On-sky performance of the SDSS-V wide field corrector. In Evans, C. J., Bryant, J. J., and Motohara, K., editors, *Ground-based and Airborne Instrumentation for Astronomy IX*, volume 12184, page 1218462. International Society for Optics and Photonics, SPIE.

Grossen, L., Kronig, L., Araujo, R., Caseiro, S., Sayres, C., Sánchez-Gallego, J., Bouri, M., and Kneib, J.-P. (2020). Test results of the sdss-v fiber micro-positioners. In Evans, C. J., Bryant, J. J., and Motohara, K., editors, *Ground-based and Airborne Instrumentation for Astronomy VIII*, volume 11447, page 114478P. International Society for Optics and Photonics, SPIE.

Gunn, J. E., Carr, M., Rockosi, C., Sekiguchi, M., Berry, K., Elms, B., de Haas, E., Ivezić, Ž., Knapp, G., Lupton, R., Pauls, G., Simcoe, R., Hirsch, R., Sanford, D., Wang, S., York, D., Harris, F., Annis, J., Bartozek, L., Boroski, W., Bakken, J., Haldeman, M., Kent, S., Holm, S., Holmgren, D., Petravick, D., Prosapio, A., Rechenmacher, R., Doi, M., Fukugita, M., Shimasaku, K., Okada, N., Hull, C., Siegmund, W., Mannery, E., Blouke, M., Heidtman, D., Schneider, D., Lucinio, R., and Brinkman, J. (1998). The sloan digital sky survey photometric camera. *The Astronomical Journal*, 116(6):3040–3081.

Gunn, J. E., Siegmund, W. A., Mannery, E. J., Owen, R. E., Hull, C. L., Leger, R. F., Carey, L. N., Knapp, G. R., York, D. G., Boroski, W. N., Kent, S. M., Lupton, R. H., Rockosi, C. M., Evans, M. L., Waddell, P., Anderson, J. E., Annis, J., Barentine, J. C., Bartoszek, L. M., Bastian, S., Bracker, S. B., Brewington, H. J., Briegel, C. I., Brinkmann, J., Brown, Y. J., Carr, M. A., Czarapata, P. C., Drennan, C. C., Dombeck, T., Federwitz, G. R., Gillespie, B. A., Gonzales, C., Hansen, S. U., Harvanek, M., Hayes, J., Jordan, W., Kinney, E., Klaene, M., Kleinman, S. J., Kron, R. G., Kresinski, J., Lee, G., Limmongkol, S., Lindenmeyer, C. W., Long, D. C., Loomis, C. L., McGehee, P. M., Mantsch, P. M., Neilsen, Jr., E. H., Neswold, R. M., Newman, P. R., Nitta, A., Peoples, Jr., J., Pier, J. R., Prieto, P. S., Prosapio, A., Rivetta, C., Schneider, D. P., Snedden, S., and Wang, S.-i. (2006). The 2.5 m Telescope of the Sloan Digital Sky Survey. AJ, 131:2332–2359.

Hall, P., Balogh, M., Barmby, P., Blakeslee, J., Bovy, J., Bradley, C., Bridges, T., Cami, J., Chapman, S., Chateauneuf, F., Cowan, N., Cote, P., Damjanov, I., Drout, M., Eadie, G., Ellison, A., Ferrarese, L., Fraser, W., Gaensler, B., Gallagher, S., Haggard, D., Henault-Brunet, V., Herwig, F., Hill, A., Hlavacek-Larrondo, J., Hudson, M., Johnson, M., Khatu, V., Laporte, C., McConnachie, A., McNamara, B., Mohammad, F., Muzzin, A., Neilson, H., Nemec, J., O'dea, C., Parker, L., Patton, D., Percival, W., Rogerson, J., Ruan, J. J., Sakara, C., Sawicki, M., Simons, D., Sivakoff, G., Szeto, K., Tesfamariam, S., Thanjavur, K., Thibeault, S., Thomas, G., Van Waerbeke, L., Venn, K., Webb, T., Willis, J., and Woo, J. (2019). The Maunakea Spectroscopic Explorer. In *Canadian Long Range Plan for Astronomy and Astrophysics White Papers*, volume 2020, page 30.

Hörler, P., Kronig, L., Kneib, J.-P., Bouri, M., Bleuler, H., and von Moos, D. (2018). High density fiber postitioner system for massive spectroscopic surveys. MNRAS, 481(3):3070–3082.

Ivezić, Ž., Kahn, S. M., Tyson, J. A., Abel, B., Acosta, E., Allsman, R., Alonso, D., AlSayyad, Y., Anderson, S. F., Andrew, J., and et al. (2019). LSST: From Science Drivers to Reference Design and Anticipated Data Products. ApJ, 873:111.

Jha, S., Bianco, F., Brandt, W. N., Galaz, G., Gawiser, E., Gizis, J., Hložek, R., Kaviraj, S., Newman, J. A., Verma, A., and Wood-Vasey, W. M. (2019). Next Generation LSST Science. In *Bulletin of the American Astronomical Society*, volume 51, page 268.

Jurgenson, C., Engelman, M., Pogge, R., O'Brien, T., Pappalardo, D., Clawson, N., Derwent, M., Brandon, C., Mason, J., Brady, J., and Shover, J. (2020). SDSS-V focal plane robot positioning metrology. In *Society of Photo-Optical Instrumentation Engineers (SPIE) Conference Series*, volume 11447 of *Society of Photo-Optical Instrumentation Engineers (SPIE) Conference Series*, page 114478O.

Kollmeier, J. A., Zasowski, G., Rix, H.-W., Johns, M., Anderson, S. F., Drory, N., Johnson, J. A., Pogge, R. W., Bird, J. C., Blanc, G. A., Brownstein, J. R., Crane, J. D., De Lee, N. M., Klaene, M. A., Kreckel, K., MacDonald, N., Merloni, A., Ness, M. K., O'Brien, T., Sanchez-Gallego, J. R., Sayres, C. C., Shen, Y., Thakar, A. R., Tkachenko, A., Aerts, C., Blanton, M. R., Eisenstein, D. J., Holtzman, J. A., Maoz, D., Nandra, K., Rockosi, C., Weinberg, D. H., Bovy, J., Casey, A. R., Chaname, J., Clerc, N., Conroy, C., Eracleous, M., Gänsicke, B. T., Hekker, S., Horne, K., Kauffmann, J., McQuinn, K. B. W., Pellegrini, E. W., Schinnerer, E., Schlafly, E. F., Schwope, A. D., Seibert, M., Teske, J. K., and van Saders, J. L. (2017). SDSS-V: Pioneering Panoptic Spectroscopy. *arXiv e-prints*, page arXiv:1711.03234.

Kronig, L., Hörler, P., Caseiro, S., Grossen, L., Araujo, R., Kneib, J.-P., and Bouri, M. (2020a). Optical test procedure for characterization and calibration of robotic fiber positioners for multi-object spectrographs. *Journal of Astronomical Telescopes, Instruments, and Systems*, 6:1.

Kronig, L., Hörler, P., Caseiro, S., Grossen, L., Araujo, R., Kneib, J.-P., and Bouri, M. (2020b). Precision control of miniature scara robots for multi-object spectrographs. *International Journal of Optomechatronics*, 14(1):53–77.

Lang, D., Hogg, D. W., Mierle, K., Blanton, M., and Roweis, S. (2010). Astrometry.net: Blind Astrometric Calibration of Arbitrary Astronomical Images. AJ, 139(5):1782–1800.

Lumelsky, V. J. and Harinarayan, K. R. (1997). Decentralized motion planning for multiple mobile robots: The cocktail party model. *Autonomous Robots*, 4(1):121–135.

Luo, A. L., Zhang, H.-T., Zhao, Y.-H., Zhao, G., Cui, X.-Q., Li, G.-P., Chu, Y.-Q., Shi, J.-R., Wang, G., Zhang, J.-N., Bai, Z.-R., Chen, X.-Y., Wang, F.-F., Guo, Y.-X., Chen, J.-J., Du, B., Kong, X., Lei, Y.-J., Li, Y.-B., Song, Y.-H., Wu, Y., Zhang, Y.-X., Zhou, X.-L., Zuo, F., Du, P., He, L., Hou, W., Dong, Y.-Q., Li, J., Li, G.-W., Li, S., Song, J., Tian, Y., Wang, M.-X., Wu, K.-F., Yang, H.-Q., Yuan, H.-L., Cao, S.-Y., Chen, H.-Y., Chen, K.-X., Chen, Y., Chu, J.-R., Feng, L., Gong, X.-F., Gu, B.-Z., Hou, Y.-H., Huo, Z.-Y., Hu, H.-Z., Hu, N.-S., Hu, Z.-W., Jia, L., Jiang, F.-H., Jiang, X., Jiang, Z.-B., Jin, G., Li, A.-H., Li, Q., Li, X.-N., Li, Y., Li, Y.-P., Liu, G.-R., Liu, G.-Q., Liu, Z.-G., Lu, Q.-S., Lu, W.-Z., Luo, Y., Mao, Y.-D., Men, L., Ni, J.-J., Qi, Y.-J., Qi, Z.-X., Shi, H.-M., Su, D.-Q., Sun, S.-W., Su, H.-J., Tang, Z.-H., Tao, Q.-S., Tu, L.-P., Wang, D.-Q., Wang, D., Wang, G.-M., Wang, H., Wang, J.-N., Wang, J., Wang, J.-L., Wang, J.-P., Wang, L., Wang, S.-G., Wang, S.-Q., Wang, Y.-N., Wang, Y., Wang, Y.-F., Wei, M.-Z., Xue, X.-X., Xing, X.-Z., Xu, L.-Z., Xu, X.-Q., Xu, Y., Yang, D.-H., Yang, S.-H., Yao, Z.-Q., Yu, Y., Yuan, H., Zhai, C., Zhang, E.-P., Zhang, J., Zhang, L.-P., Zhang, W., Zhang, Y., Zhang, Z.-C., Zhao, M., Zhou, F., Zhu, Y.-T., Zhu, J., and Zou, S.-C. (2012). Data release of the LAMOST pilot survey. *Research in Astronomy and Astrophysics*, 12(9):1243–1246.

Luo, A. L., Zhao, Y.-H., Zhao, G., Deng, L.-C., Liu, X.-W., Jing, Y.-P., Wang, G., Zhang, H.-T., Shi, J.-R., Cui, X.-Q., Chu, Y.-Q., Li, G.-P., Bai, Z.-R., Wu, Y., Cai, Y., Cao, S.-Y., Cao, Z.-H., Carlin, J. L., Chen, H.-Y., Chen, J.-J., Chen, K.-X., Chen, L., Chen, X.-L., Chen, X.-Y., Chen, Y., Christlieb, N., Chu, J.-R., Cui, C.-Z., Dong, Y.-Q., Du, B., Fan, D.-W., Feng, L., Fu, J.-N., Gao, P., Gong, X.-F., Gu, B.-Z., Guo, Y.-X., Han, Z.-W., He, B.-L., Hou, J.-L., Hou, Y.-H., Hou, W., Hu, H.-Z., Hu, N.-S., Hu, Z.-W., Huo, Z.-Y., Jia, L., Jiang, F.-H., Jiang, X., Jiang, Z.-B., Jin, G., Kong, X., Kong, X., Lei, Y.-J., Li, A.-H., Li, C.-H., Li, G.-W., Li, H.-N., Li, J., Li, Q., Li, S., Li, S.-S., Li, X.-N., Li, Y., Li, Y.-B., Li, Y.-P., Liang, Y., Lin, C.-C., Liu, C., Liu, G.-R., Liu, G.-Q., Liu, Z.-G., Lu, W.-Z., Luo, Y., Mao, Y.-D., Newberg, H., Ni, J.-J., Qi, Z.-X., Qi, Y.-J., Shen, S.-Y., Shi, H.-M., Song, J., Song, Y.-H., Su, D.-Q., Su, H.-J., Tang, Z.-H., Tao, Q.-S.,

Tian, Y., Wang, D., Wang, D.-Q., Wang, F.-F., Wang, G.-M., Wang, H., Wang, H.-C., Wang, J., Wang, J.-N., Wang, J.-L., Wang, J.-P., Wang, J.-X., Wang, L., Wang, M.-X., Wang, S.-G., Wang, S.-Q., Wang, X., Wang, Y.-N., Wang, Y., Wang, Y.-F., Wang, Y.-F., Wei, P., Wei, M.-Z., Wu, H., Wu, K.-F., Wu, X.-B., Wu, Y.-Z., Xing, X.-Z., Xu, L.-Z., Xu, X.-Q., Xu, Y., Yan, T.-S., Yang, D.-H., Yang, H.-F., Yang, H.-Q., Yang, M., Yao, Z.-Q., Yu, Y., Yuan, H., Yuan, H.-B., Yuan, H.-L., Yuan, W.-M., Zhai, C., Zhang, E.-P., Zhang, H.-W., Zhang, J.-N., Zhang, L.-P., Zhang, W., Zhang, Y., Zhang, Y.-X., Zhang, Z.-C., Zhao, M., Zhou, F., Zhou, X., Zhu, J., Zhu, Y.-T., Zou, S.-C., and Zuo, F. (2015). The first data release (DR1) of the LAMOST regular survey. *Research in Astronomy and Astrophysics*, 15(8):1095.

Macktoobian, M., Gillet, D., and Kneib, J.-P. (2019). Complete coordination of robotic fiber positioners for massive spectroscopic surveys. *Journal of Astronomical Telescopes, Instruments, and Systems*, 5(4):1 – 12.

Majewski, S. R., Schiavon, R. P., Frinchaboy, P. M., Allende Prieto, C., Barkhouser, R., Bizyaev, D., Blank, B., Brunner, S., Burton, A., Carrera, R., Chojnowski, S. D., Cunha, K., Epstein, C., Fitzgerald, G., García Pérez, A. E., Hearty, F. R., Henderson, C., Holtzman, J. A., Johnson, J. A., Lam, C. R., Lawler, J. E., Maseman, P., Mészáros, S., Nelson, M., Nguyen, D. C., Nidever, D. L., Pinsonneault, M., Shetrone, M., Smee, S., Smith, V. V., Stolberg, T., Skrutskie, M. F., Walker, E., Wilson, J. C., Zasowski, G., Anders, F., Basu, S., Beland, S., Blanton, M. R., Bovy, J., Brownstein, J. R., Carlberg, J., Chaplin, W., Chiappini, C., Eisenstein, D. J., Elsworth, Y., Feuillet, D., Fleming, S. W., Galbraith-Frew, J., García, R. A., García-Hernández, D. A., Gillespie, B. A., Girardi, L., Gunn, J. E., Hasselquist, S., Hayden, M. R., Hekker, S., Ivans, I., Kinemuchi, K., Klaene, M., Mahadevan, S., Mathur, S., Mosser, B., Muna, D., Munn, J. A., Nichol, R. C., O'Connell, R. W., Parejko, J. K., Robin, A. C., Rocha-Pinto, H., Schultheis, M., Serenelli, A. M., Shane, N., Silva Aguirre, V., Sobeck, J. S., Thompson, B., Troup, N. W., Weinberg, D. H., and Zamora, O. (2017). The Apache Point Observatory Galactic Evolution Experiment (APOGEE). AJ, 154(3):94.

Makarem, L., Kneib, J.-P., Gillet, D., Bleuler, H., Bouri, M., Jenni, L., Prada, F., and Sanchez, J.

(2014). Collision avoidance in next-generation fiber positioner robotic systems for large survey spectrographs. A&A, 566:A84.

National Research Council (2015). Optimizing the U.S. Ground-Based Optical and Infared Astronomy System. In *The National Academies Press*.

Noll, R. J. (1976). Zernike polynomials and atmospheric turbulence∗. *J. Opt. Soc. Am.*, 66(3):207–211.

Olfati-Saber, R. (2006). Flocking for multi-agent dynamic systems: Algorithms and theory. *Automatic Control, IEEE Transactions on*, 51:401 – 420.

Pogge, R. W., Derwent, M. A., O'Brien, T. P., Jurgenson, C. A., Pappalardo, D., Engelman, M., Brandon, C., Brady, J., Clawson, N., Shover, J., Mason, J., Kneib, J.-P., Araujo, R., Bouri, M., Kronig, L., Grossen, L., Gillet, D., Macktoobian, M., Tuttle, S. E., Farr, E., Sánchez-Gallego, J., and Sayres, C. (2020). A robotic Focal Plane System (FPS) for the Sloan Digital Sky Survey V. In *Society of Photo-Optical Instrumentation Engineers (SPIE) Conference Series*, volume 11447 of *Society of Photo-Optical Instrumentation Engineers (SPIE) Conference Series*, page 1144781.

Powell, M. J. D. (1964). An efficient method for finding the minimum of a function of several variables without calculating derivatives. *The Computer Journal*, 7(2):155–162.

Predehl, P., Andritschke, R., Böhringer, H., Bornemann, W., Bräuninger, H., Brunner, H., Brusa, M., Burkert, W., Burwitz, V., Cappelluti, N., Churazov, E., Dennerl, K., Eder, J., Elbs, J., Freyberg, M., Friedrich, P., Fürmetz, M., Gaida, R., Hälker, O., Hartner, G., Hasinger, G., Hermann, S., Huber, H., Kendziorra, E., von Kienlin, A., Kink, W., Kreykenbohm, I., Lamer, G., Lapchov, I., Lehmann, K., Meidinger, N., Mican, B., Mohr, J., Mühlegger, M., Müller, S., Nandra, K., Pavlinsky, M., Pfeffermann, E., Reiprich, T., Robrade, J., Rohé, C., Santangelo, A., Schächner, G., Schanz, T., Schmid, C., Schmitt, J., Schreib, R., Schrey, F., Schwope, A., Steinmetz, M., Strüder, L., Sunyaev, R., Tenzer, C., Tiedemann, L., Vongehr, M., and Wilms, J.

(2010). eROSITA on SRG. In Proc. SPIE, volume 7732 of *Society of Photo-Optical Instrumentation Engineers (SPIE) Conference Series*, page 77320U.

Ramer, U. (1972). An iterative procedure for the polygonal approximation of plane curves. *Computer Graphics and Image Processing*, 1(3):244 – 256.

Ricker, G. R., Winn, J. N., Vanderspek, R., Latham, D. W., Bakos, G. Á., Bean, J. L., Berta-Thompson, Z. K., Brown, T. M., Buchhave, L., Butler, N. R., Butler, R. P., Chaplin, W. J., Charbonneau, D., Christensen-Dalsgaard, J., Clampin, M., Deming, D., Doty, J., De Lee, N., Dressing, C., Dunham, E. W., Endl, M., Fressin, F., Ge, J., Henning, T., Holman, M. J., Howard, A. W., Ida, S., Jenkins, J., Jernigan, G., Johnson, J. A., Kaltenegger, L., Kawai, N., Kjeldsen, H., Laughlin, G., Levine, A. M., Lin, D., Lissauer, J. J., MacQueen, P., Marcy, G., McCullough, P. R., Morton, T. D., Narita, N., Paegert, M., Palle, E., Pepe, F., Pepper, J., Quirrenbach, A., Rinehart, S. A., Sasselov, D., Sato, B., Seager, S., Sozzetti, A., Stassun, K. G., Sullivan, P., Szentgyorgyi, A., Torres, G., Udry, S., and Villasenor, J. (2014). Transiting Exoplanet Survey Satellite (TESS). In Proc. SPIE, volume 9143 of *Society of Photo-Optical Instrumentation Engineers (SPIE) Conference Series*, page 914320.

Rossi, F., Bandyopadhyay, S., Wolf, M., and Pavone, M. (2018). Review of multi-agent algorithms for collective behavior: a structural taxonomy. *ArXiv*, abs/1803.05464.

Sayres, C., Sánchez-Gallego, J. R., Blanton, M. R., Araujo, R., Bouri, M., Grossen, L., Kneib, J.-P., Kollmeier, J. A., Kronig, L., Pogge, R. W., and Tuttle, S. (2021). SDSS-V Algorithms: Fast, Collision-free Trajectory Planning for Heavily Overlapping Robotic Fiber Positioners. *AJ*, 161(2):92.

Sayres, C., Sánchez-Gallego, J. R., Blanton, M. R., Engelman, M., Finkbeiner, D. P., Hogg, D. W., Holtzman, J. A., Jurgenson, C., Pogge, R. W., Ramírez, S., Saydjari, A. K., Schlafly, E. F., and Tuttle, S. (2022). SDSS-V robotic focal plane system: overview of coordinate systems and transforms. In Evans, C. J., Bryant, J. J., and Motohara, K., editors, *Ground-based and Air-*

borne Instrumentation for Astronomy IX, volume 12184, page 121847K. International Society for Optics and Photonics, SPIE.

Schlegel, D. J., Kollmeier, J. A., Aldering, G., Bailey, S., Baltay, C., Bebek, C., BenZvi, S., Besuner, R., Blanc, G., Bolton, A. S., Bouri, M., Brooks, D., Buckley-Geer, E., Cai, Z., Crane, J., Dey, A., Doel, P., Fan, X., Ferraro, S., Font-Ribera, A., Gutierrez, G., Guy, J., Heetderks, H., Huterer, D., Infante, L., Jelinsky, P., Johns, M., Karagiannis, D., Kent, S. M., Kim, A. G., Kneib, J.-P., Kronig, L., Konidaris, N., Lahav, O., Lampton, M. L., Lang, D., Leauthaud, A., Liguori, M., Linder, E. V., Magneville, C., Martini, P., Mateo, M., McDonald, P., Miller, C. J., Moustakas, J., Myers, A. D., Mulchaey, J., Newman, J. A., Nugent, P. E., Palanque-Delabrouille, N., Padmanabhan, N., Piro, A. L., Poppett, C., Prochaska, J. X., Pullen, A. R., Rabinowitz, D., Ramirez, S., Rix, H.-W., Ross, A. J., Samushia, L., Schaan, E., Schubnell, M., Seljak, U., Seo, H.-J., Shectman, S. A., Silber, J., Simon, J. D., Slepian, Z., Soares-Santos, M., Tarle, G., Thompson, I., Valluri, M., Wechsler, R. H., White, M., Wilson, M. J., Yeche, C., and Zaritsky, D. (2019). Astro2020 apc white paper: The megamapper: a z ¿ 2 spectroscopic instrument for the study of inflation and dark energy.

Shen, Y., Brandt, W. N., Dawson, K. S., Hall, P. B., McGreer, I. D., Anderson, S. F., Chen, Y., Denney, K. D., Eftekharzadeh, S., Fan, X., Gao, Y., Green, P. J., Greene, J. E., Ho, L. C., Horne, K., Jiang, L., Kelly, B. C., Kinemuchi, K., Kochanek, C. S., Pâris, I., Peters, C. M., Peterson, B. M., Petitjean, P., Ponder, K., Richards, G. T., Schneider, D. P., Seth, A., Smith, R. N., Strauss, M. A., Tao, C., Trump, J. R., Wood-Vasey, W. M., Zu, Y., Eisenstein, D. J., Pan, K., Bizyaev, D., Malanushenko, V., Malanushenko, E., and Oravetz, D. (2015). The Sloan Digital Sky Survey Reverberation Mapping Project: Technical Overview. ApJS, 216(1):4.

Smee, S. A., Gunn, J. E., Uomoto, A., Roe, N., Schlegel, D., Rockosi, C. M., Carr, M. A., Leger, F., Dawson, K. S., Olmstead, M. D., Brinkmann, J., Owen, R., Barkhouser, R. H., Honscheid, K., Harding, P., Long, D., Lupton, R. H., Loomis, C., Anderson, L., Annis, J., Bernardi, M., Bhardwaj, V., Bizyaev, D., Bolton, A. S., Brewington, H., Briggs, J. W., Burles, S., Burns, J. G., Castander, F. J., Connolly, A., Davenport, J. R. A., Ebelke, G., Epps, H., Feldman, P. D., Fried-

man, S. D., Frieman, J., Heckman, T., Hull, C. L., Knapp, G. R., Lawrence, D. M., Loveday, J., Mannery, E. J., Malanushenko, E., Malanushenko, V., Merrelli, A. J., Muna, D., Newman, P. R., Nichol, R. C., Oravetz, D., Pan, K., Pope, A. C., Ricketts, P. G., Shelden, A., Sandford, D., Siegmund, W., Simmons, A., Smith, D. S., Snedden, S., Schneider, D. P., SubbaRao, M., Tremonti, C., Waddell, P., and York, D. G. (2013). The Multi-object, Fiber-fed Spectrographs for the Sloan Digital Sky Survey and the Baryon Oscillation Spectroscopic Survey. *AJ*, 146:32.

Sugai, H., Tamura, N., Karoji, H., Shimono, A., Takato, N., Kimura, M., Ohyama, Y., Ueda, A., Aghazarian, H., de Arruda, M. V., Barkhouser, R. H., Bennett, C. L., Bickerton, S., Bozier, A., Braun, D. F., Bui, K., Capocasale, C. M., Carr, M. A., Castilho, B., Chang, Y.-C., Chen, H.-Y., Chou, R. C. Y., Dawson, O. R., Dekany, R. G., Ek, E. M., Ellis, R. S., English, R. J., Ferrand, D., Ferreira, D., Fisher, C. D., Golebiowski, M., Gunn, J. E., Hart, M., Heckman, T. M., Ho, P. T. P., Hope, S., Hovland, L. E., Hsu, S.-F., Hu, Y.-S., Huang, P. J., Jaquet, M., Karr, J. E., Kempenaar, J. G., King, M. E., le Fèvre, O., Mignant, D. L., Ling, H.-H., Loomis, C., Lupton, R. H., Madec, F., Mao, P., Souza Marrara, L., Ménard, B., Morantz, C., Murayama, H., Murray, G. J., Cesar de Oliveira, A., Mendes de Oliveira, C., Souza de Oliveira, L., Orndorff, J. D., de Paiva Vilaça, R., Partos, E. J., Pascal, S. r., Pegot-Ogier, T., Reiley, D. J., Riddle, R., Santos, L., dos Santos, J. B., Schwochert, M. A., Seiffert, M. D., Smee, S. A., Smith, R. M., Steinkraus, R. E., Sodré, L., Spergel, D. N., Surace, C., Tresse, L., Vidal, C., Vives, S., Wang, S.-Y., Wen, C.-Y., Wu, A. C., Wyse, R., and Yan, C.-H. (2015). Prime Focus Spectrograph for the Subaru telescope: massively multiplexed optical and near-infrared fiber spectrograph. *Journal of Astronomical Telescopes, Instruments, and Systems*, 1:035001.

Sánchez-Gallego, J. R., Sayres, C., Donor, J., Toro, A. A., Araujo, R., Kronig, L., Grossen, L., Pogge, R., Wachter, S., Ramírez, S., and Brownstein, J. (2020). Multi-object spectroscopic operations with the Sloan Digital Sky Survey V. In Adler, D. S., Seaman, R. L., and Benn, C. R., editors, *Observatory Operations: Strategies, Processes, and Systems VIII*, volume 11449, pages 83 – 96. International Society for Optics and Photonics, SPIE.

Tao, D., Makarem, L., Bouri, M., Kneib, J.-P., and Gillet, D. (2018). Priority coordination of fiber

positioners in multi-objects spectrographs. In Proc. SPIE, volume 10702 of *Society of Photo-Optical Instrumentation Engineers (SPIE) Conference Series*, page 107028K.

The Dark Energy Survey Collaboration (2005). The Dark Energy Survey. *arXiv e-prints*, pages astro–ph/0510346.

Umeyama, S. (1991). Least-squares estimation of transformation parameters between two point patterns. *IEEE Transactions on Pattern Analysis and Machine Intelligence*, 13(4):376–380.

Wilson, J. C., Hearty, F. R., Skrutskie, M. F., Majewski, S. R., Holtzman, J. A., Eisenstein, D., Gunn, J., Blank, B., Henderson, C., Smee, S., Nelson, M., Nidever, D., Arns, J., Barkhouser, R., Barr, J., Beland, S., Bershady, M. A., Blanton, M. R., Brunner, S., Burton, A., Carey, L., Carr, M., Colque, J. P., Crane, J., Damke, G. J., Davidson, J. W., J., Dean, J., Di Mille, F., Don, K. W., Ebelke, G., Evans, M., Fitzgerald, G., Gillespie, B., Hall, M., Harding, A., Harding, P., Hammond, R., Hancock, D., Harrison, C., Hope, S., Horne, T., Karakla, J., Lam, C., Leger, F., MacDonald, N., Maseman, P., Matsunari, J., Melton, S., Mitcheltree, T., O'Brien, T., O'Connell, R. W., Patten, A., Richardson, W., Rieke, G., Rieke, M., Roman-Lopes, A., Schiavon, R. P., Sobeck, J. S., Stolberg, T., Stoll, R., Tembe, M., Trujillo, J. D., Uomoto, A., Vernieri, M., Walker, E., Weinberg, D. H., Young, E., Anthony-Brumfield, B., Bizyaev, D., Breslauer, B., De Lee, N., Downey, J., Halverson, S., Huehnerhoff, J., Klaene, M., Leon, E., Long, D., Mahadevan, S., Malanushenko, E., Nguyen, D. C., Owen, R., Sánchez-Gallego, J. R., Sayres, C., Shane, N., Shectman, S. A., Shetrone, M., Skinner, D., Stauffer, F., and Zhao, B. (2019). The Apache Point Observatory Galactic Evolution Experiment (APOGEE) Spectrographs. PASP, 131(999):055001.

Wilson, J. C., Jr., J. W. D., Bender, C., Dow, P., Nelson, M., Walters, L., Irving, D., Farr, E., Tuttle, S., Nidever, D., DeLee, N., Holtzman, J., Majewski, S., Fox, J., Harkins, D., Green, L., Ericksen, J., Wagner, R., Derwent, M., Jurgenson, C., Pogge, R., Wachter, S., Ramirez, S., and Kollmeier, J. (2022). External upgrades to improve the RV precision of the APOGEE Spectrographs. In Evans, C. J., Bryant, J. J., and Motohara, K., editors, *Ground-based and Airborne Instrumen-*

tation for Astronomy IX, volume 12184, page 121847H. International Society for Optics and Photonics, SPIE.

Winkler, R., Liebner, T., Sobiella, D., Alvarez, C. R., Fechner, T., Bittner, W., Feuerstein, D., Leseberg, B., Hahn, T., Rektorschrek, L., Lemke, U., Sablowski, D., Pramskiy, A., Rothmaier, F., Stilz, I., Lehmitz, M., Smedley, S., Onel, H., and Frey, S. (2022). 4MOST metrology system lab calibration and performance. In Navarro, R. and Geyl, R., editors, *Advances in Optical and Mechanical Technologies for Telescopes and Instrumentation V*, volume 12188, page 121882A. International Society for Optics and Photonics, SPIE.

Yan, H., Li, H., Wang, S., Zong, W., Yuan, H., Xiang, M., Huang, Y., Xie, J., Dong, S., Yuan, H., Bi, S., Chu, Y., Cui, X., Deng, L., Fu, J., Han, Z., Hou, J., Li, G., Liu, C., Liu, J., Liu, X., Luo, A., Shi, J., Wu, X., Zhang, H., Zhao, G., and Zhao, Y. (2022). Overview of the lamost survey in the first decade. *The Innovation*, 3(2):100224.

York, D. G., Adelman, J., John E. Anderson, J., Anderson, S. F., Annis, J., Bahcall, N. A., Bakken, J. A., Barkhouser, R., Bastian, S., Berman, E., Boroski, W. N., Bracker, S., Briegel, C., Briggs, J. W., Brinkmann, J., Brunner, R., Burles, S., Carey, L., Carr, M. A., Castander, F. J., Chen, B., Colestock, P. L., Connolly, A. J., Crocker, J. H., Csabai, I., Czarapata, P. C., Davis, J. E., Doi, M., Dombeck, T., Eisenstein, D., Ellman, N., Elms, B. R., Evans, M. L., Fan, X., Federwitz, G. R., Fiscelli, L., Friedman, S., Frieman, J. A., Fukugita, M., Gillespie, B., Gunn, J. E., Gurbani, V. K., de Haas, E., Haldeman, M., Harris, F. H., Hayes, J., Heckman, T. M., Hennessy, G. S., Hindsley, R. B., Holm, S., Holmgren, D. J., hao Huang, C., Hull, C., Husby, D., Ichikawa, S.-I., Ichikawa, T., Ivezić, Ž., Kent, S., Kim, R. S. J., Kinney, E., Klaene, M., Kleinman, A. N., Kleinman, S., Knapp, G. R., Korienek, J., Kron, R. G., Kunszt, P. Z., Lamb, D. Q., Lee, B., Leger, R. F., Limmongkol, S., Lindenmeyer, C., Long, D. C., Loomis, C., Loveday, J., Lucinio, R., Lupton, R. H., MacKinnon, B., Mannery, E. J., Mantsch, P. M., Margon, B., McGehee, P., McKay, T. A., Meiksin, A., Merelli, A., Monet, D. G., Munn, J. A., Narayanan, V. K., Nash, T., Neilsen, E., Neswold, R., Newberg, H. J., Nichol, R. C., Nicinski, T., Nonino, M., Okada, N., Okamura, S., Ostriker, J. P., Owen, R., Pauls, A. G., Peoples, J., Peterson, R. L., Petravick, D.,

Pier, J. R., Pope, A., Pordes, R., Prosapio, A., Rechenmacher, R., Quinn, T. R., Richards, G. T., Richmond, M. W., Rivetta, C. H., Rockosi, C. M., Ruthmansdorfer, K., Sandford, D., Schlegel, D. J., Schneider, D. P., Sekiguchi, M., Sergey, G., Shimasaku, K., Siegmund, W. A., Smee, S., Smith, J. A., Snedden, S., Stone, R., Stoughton, C., Strauss, M. A., Stubbs, C., SubbaRao, M., Szalay, A. S., Szapudi, I., Szokoly, G. P., Thakar, A. R., Tremonti, C., Tucker, D. L., Uomoto, A., Berk, D. V., Vogeley, M. S., Waddell, P., i Wang, S., Watanabe, M., Weinberg, D. H., Yanny, B., and Yasuda, N. (2000). The sloan digital sky survey: Technical summary. *The Astronomical Journal*, 120(3):1579–1587.

Zhao, C. and Burge, J. H. (2007). Orthonormal vector polynomials in a unit circle, part i: basis set derived from gradients of zernike polynomials. *Opt. Express*, 15(26):18014–18024.

Zhao, C. and Burge, J. H. (2008). Orthonormal vector polynomials in a unit circle, part ii : completing the basis set. *Opt. Express*, 16(9):6586–6591.

Zhao, Y. J., Zhang, Y. D., and Tu, F. (2012). Reverse path planning for flexible needle in 2d soft tissue with obstacles. In *Frontiers of Manufacturing and Design Science II*, volume 121 of *Applied Mechanics and Materials*, pages 4132–4137. Trans Tech Publications Ltd.

Appendix A

ALGORITHMS

A.1 KAIJU Algorithm

A pseudocode implementation of the anti-collision algorithm to generate a reverse path for an RFP array follows below, favoring clarity over computational efficiency. The routine assumes that a few functions are defined. **dot(v1, v2)** and **norm(v1)** return the dot product and Euclidean norm for input vectors **v1, v2**. **rand()** returns a uniform random value between 0 and 1. **shuffle(array)** randomizes the order of elements in the input array. Vector subtraction and scalar multiplication is defined in the normal linear algebra sense.

```
# ------------------
# runtime parameters
# ------------------

# note that setting greed=1 and phobia=0 results in the GC algorithm

alphaArmLen ← length of alpha arm, l_α
betaArmLen ← length of beta arm, l_β
collisionBuffer ← buffer that describes the collision envelope, σ_cb
dTheta ← maximum angular step size for a positioner axis perturbation, Δ_θ
maxIter ← maximum iterations to perform
greed ← desired greed setting between 0 and 1
phobia ← desired phobia setting between 0 and 1
maxDispl ← (alphaArmLen + betaArmLen)*sin(2*dTheta) # Equation 7

# build the list of axis perturbations from dTheta
perturbArray ← []
foreach dAlpha in [-dTheta, 0, dTheta]:
  foreach dBeta in [-dTheta, 0, dTheta]:
    perturbArray.append([dAlpha, dBeta])


# ---------------------
# structure definitions
# ---------------------

struct Robot:
  # holds relevant coordinates and neighbors for a given positioner
  x ← x coordinate of positioner base position, x_b
  y ← y coordinate of positioner base position, y_b
  alphaCurr ← current alpha angle, θ_α^C
```

```
32    betaCurr ← current beta angle, θ⃗_β^C
33    alphaDest ← 10 # alpha angle destination, θ⃗_α^D
34    betaDest ← 170 # beta angle destination, θ⃗_β^D
35    neighbors ← list of Robot instances with whom I risk collision (Equation 4)
36
37  struct Vector3:
38    # simply, a 3-vector
39    x ← x coordinate
40    y ← y coordinate
41    z ← 0 # work in the z=0 focal plane
42
43  struct LineSegment:
44    # a container representing a line segment between two Vector3's v0 and v1
45    v0 ← an instance of Vector3
46    v1 ← an instance of Vector3
47
48
49  # --------------------
50  # function definitions
51  # --------------------
52
53  function dist3D_Line_to_Line(L1, L2):
54    # Almost verbatim from Dan Sunday's algorithm: http://geomalgorithms.com/a07-_distance.html
55    # this computes D_ij used Equations 3, 6, and 9.
56    parameters: L1, L2 each a LineSegment
57    output: the minimum distance between L1 and L2.
58
59    SMALL_NUM ← 0.00000001 # anything that avoids division overflow
60    u ← L1.v1 - L1.v0
61    v ← L2.v1 - L2.v0
62    w ← L1.v0 - L2.v0
63    a ← dot(u,u)        # always >= 0
64    b ← dot(u,v)
65    c ← dot(v,v)        # always >= 0
66    d ← dot(u,w)
67    e ← dot(v,w)
68    D ← a*c - b*b       # always >= 0
69
70    # compute the line parameters of the two closest points
71    if (D < SMALL_NUM):          # the lines are almost parallel
72      sc ← 0.0
73      if (b > c):
```

```
74          tc ← d / b
75        else:
76          tc ← e / c
77      else:
78        sc ← (b*e - c*d) / D
79        tc ← (a*e - b*d) / D
80
81      # get the difference of the two closest points
82      dP ← w + (sc * u) - (tc * v)
83      return norm(dP)
84
85
86  function betaArmSegment(robo):
87      # This implements Equations 1 and 2.
88      parameters: robo, a Robot
89      output: the orientation of the beta arm, a LineSegment
90
91      elbow ← Vector3()
92      elbow.x ← robo.x + alphaArmLen*cos(robo.alphaCurr)
93      elbow.y ← robo.y + alphaArmLen*sin(robo.alphaCurr)
94
95      fiber ← Vector3()
96      fiber.x ← elbow.x + betaArmLen*cos(robo.alphaCurr + robo.betaCurr)
97      fiber.y ← elbow.y + betaArmLen*sin(robo.alphaCurr + robo.betaCurr)
98
99      betaSeg ← LineSegment()
100     betaSeg.v0 ← elbow
101     betaSeg.v1 ← fiber
102
103     return betaSeg
104
105
106 function isCollided(robo):
107     parameters: robo, a Robot
108     output: True when input Robot is collided with a neighbor, otherwise False
109
110     seg1 ← betaArmSegment(robo)
111
112     foreach neighbor in robo.neighbors:
113       seg2 ← betaArmSegment(neighbor)
114       armSeparation ← dist3D_Line_to_Line(seg1, seg2)
115       if armSeparation <= 2*collisionBuffer + maxDispl:  # Equation 6
```

```
116             # the two robots are collided exit now
117             return True
118
119     # not collided with any neighbor
120     return False
121
122 function computeCost(robo):
123     parameters: robo, a Robot
124     output: the cost metric (Equation 8)
125
126     dAlpha ← robo.alphaCurr - robo.alphaDest
127     dBeta ← robo.betaCurr - robo.betaDest
128     return sqrt(dAlpha*dAlpha + dBeta*dBeta)
129
130 function computeEnergy(robo):
131     parameters: robo, a Robot
132     output: the energy metric (Equation 9)
133
134     energy ← 0
135     seg1 ← betaArmSegment(robo)
136
137     foreach neighbor in robo.neighbors:
138         seg2 ← betaArmSegment(neighbor)
139         armSeparation ← dist3D_Line_to_Line(seg1, seg2)
140         energy ← energy + 1/(armSeparation*armSeparation)
141
142     return energy
143
144 function neighborEncroachment(robo):
145     parameters: robo, a Robot
146     output: True when a neighboring robot is encroaching, otherwise False (Equation 10)
147
148     seg1 ← betaArmSegment(robo)
149
150     foreach neighbor in robo.neighbors:
151         seg2 ← betaArmSegment(neighbor)
152         armSeparation ← dist3D_Line_to_Line(seg1, seg2)
153         if armSeparation <= 2*collisionBuffer + 3*maxDispl:  # Equation 10
154             # this neighbor is getting close
155             return True
156
157     # no neighbors nearby
```

```
158   return False
159
160
161 function perturbRobot(robo):
162   parameters: robo, a Robot
163   output: modify state of input Robot
164
165   # if the positioner is at destination, and no neighbor is encroaching do not do anything
166   if computeCost(robo) == 0 and neighborEncroachment(robo) == False:
167     return
168
169   # save the current state of the robot's position
170   alphaCurr ← robo.alphaCurr
171   betaCurr ← robo.betaCurr
172
173   # placeholders for minimization search over perturbations
174   bestAlpha ← robo.alphaCurr
175   bestBeta ← robo.betaCurr
176   bestScore ← 1e16 # a large value to be minimized
177
178   # select the metric to minimize (cost or energy)
179   minimizeEnergy ← rand() < phobia
180
181   # randomize order in which perturbations are tried
182   shuffle(perturbArray)
183
184   foreach dAlpha, dBeta in perturbArray:
185     nextAlpha ← currAlpha + dAlpha
186     nextBeta ← currBeta + dBeta
187
188     # don't allow out of range moves
189     if nextAlpha < 0:
190       nextAlpha ← 0
191     if nextAlpha > 360:
192       nextAlpha ← 359.999
193     if nextBeta < 0:
194       nextBeta ← 0
195     if nextBeta > 360:
196       nextBeta ← 359.999
197
198     # don't overshoot destination coordinates
199     if currAlpha > robo.alphaDest and nextAlpha <= robo.alphaDest:
```

```
200         nextAlpha ← robo.alphaDest
201       if currAlpha < robo.alphaDest and nextAlpha >= robo.alphaDest:
202         nextAlpha ← robo.alphaDest
203       if currBeta > robo.betaDest and nextBeta <= robo.betaDest:
204         nextBeta ← robo.betaDest
205       if currBeta < robo.betaDest and nextBeta >= robo.betaDest:
206         nextBeta ← robo.betaDest
207
208       # set and test the new position
209       robo.alphaCurr ← nextAlpha
210       robo.betaCurr ← nextBeta
211
212       if isCollided(robo):
213         # invalid move, continue to next perturbation
214         continue
215
216       if minimizeEnergy:
217         # minimize energy metric
218         score ← computeEnergy(robo)
219       else:
220         # minimize cost metric
221         score ← computeCost(robo)
222
223       if score < bestScore and rand() < greed:
224         # new best score found
225         bestAlpha ← nextAlpha
226         bestBeta ← nextBeta
227         bestScore ← score
228
229       else if score == bestScore and rand() < 0.5:
230         # score equally good as best seen score
231         # take it with a 50 percent chance
232         bestAlpha ← nextAlpha
233         bestBeta ← nextBeta
234         bestScore ← score
235
236
237     # set the next position for this robot
238     robo.alphaCurr ← bestAlpha
239     robo.betaCurr ← bestBeta
240     return
241
```

```
242 function arrayConverged(robotList):
243   parameters: robotList, a list of Robot instances
244   output: True when all robots have reached destination, otherwise False
245
246   foreach robo in robotList:
247     if computeCost(robo) > 0:
248       # this robot has not converged, exit here
249       return False
250
251   # all robots have converged
252   return True
253
254
255 function recordState(robotList):
256   # a function to record the current positions of all Robot
257   # instances in the array, called throughout the routine
258   # the record the path of each positioner
259   parameters: robotList, a list of Robot instances
260   output: record the current state the Robot array
261
262
263 # --------------------
264 # begin main algorithm
265 # --------------------
266
267 # procedure requires a list of each Robot initialized with:
268 # grid coordinates (x_b, y_b),
269 # current coordinates to a set of non-colliding source coordinates,
270 # and a list of neighboring Robot instances that risk beta arm interference
271 allRobots ← list of initialized Robot instances
272
273 # record the initial state (all robots at targets)
274 recordState(allRobots)
275
276 # set things in motion
277 loopIter ← 1
278 while loopIter < maxIter:
279
280   foreach robo in allRobots:
281     perturbRobot(robo)
282
283   # record new state of robots
```

```
284     recordState(allRobots)
285
286     # check for convergence
287     if arrayConverged(allRobots):
288       # all robots have reached destination, exit loop
289       break
290
291     loopIter ← loopIter + 1
292
293   # --------------------
294   # end main algorithm
295   # --------------------
```

A.2 FVC Loop Algorithm

1: Inputs:
2: $W_T^S \leftarrow [\mathbf{w}_i]$ ▷ 500×2 array of target xy wok coordinates for each robot's Apogee or BOSS fiber
3: $B \leftarrow [\mathbf{b}_i]$ ▷ 500×2 array of calibrated xy beta arm coordinates for each robot's Apogee or BOSS fiber.
4: C $\leftarrow [(x_w^i, y_w^i)]$ ▷ 500×2 array of calibrated xy robot centers in wok coordinates.
5: $\vec{r}^M \leftarrow [r_i^M]$ ▷ 500×1 array of calibrated metrology fiber radii for each robot.
6: $\vec{l_\alpha} \leftarrow [l_\alpha^i]$ ▷ 500×1 array of calibrated alpha arm lengths for each robot
7: $\vec{\alpha}_\Delta \leftarrow [\alpha_\Delta^i]$ ▷ 500×1 array of calibrated alpha angle offsets for each robot.
8: $\vec{\beta}_\Delta \leftarrow [\beta_\Delta^i]$ ▷ 500×1 array of calibrated beta angle offsets for each robot.
9:
10: Outputs:
11: ϵ_1 ▷ 500×1 array of metrology fiber position errors after blind move for each robot
12: ϵ_2 ▷ 500×1 array of metrology fiber position errors after corrective move for each robot using FVC feedback
13: W_F^S ▷ 500×2 array of final measured xy wok coordinates for robot science fibers after FVC feedback correction.
14:
15: Functions:
16: **function** MOVEROBOT(i, α, β) ▷ Command robot i's arms to move to wok coordinate angles α, β
17: $\alpha_{CMD} \leftarrow \alpha - \vec{\alpha}_\Delta[i] + \frac{\pi}{2}$ ▷ Equation 4.17
18: $\beta_{CMD} \leftarrow \beta - \vec{\beta}_\Delta[i]$ ▷ Equation 4.18
19: Command robot i to move to $\alpha_{CMD}, \beta_{CMD}$ arm coordinates
20: **return**
21: **end function**
22:
23: **function** MEASUREROBOT(i) ▷ Measure robot i's metrology fiber location in wok coordinates from an FVC image
24: $\mathbf{p}_i \leftarrow$ extracted centroid location on CCD for robot i's metrology fiber (pixels)
25: $\mathbf{w} \leftarrow F_2(\mathbf{p}_i)$ ▷ FVC Transform, Equation 5.23
26: **return** $\mathbf{w}$

end function

function GETALPHABETA($i, \mathbf{w}, \mathbf{b}$) ▷ Return α, β arm coordinates given wok coordinates $\mathbf{w}$ and a fiber's beta arm coordinates $\mathbf{b}$ for robot i, return NaN if $\mathbf{w}$ is outside of the robot's workspace.

$\mathbf{t} \leftarrow \mathbf{w} - C[i]$

$l_\beta \leftarrow \|\mathbf{b}\|$

if $\|\mathbf{t}\| > l_\beta + \vec{l_\alpha}[i]$ **then**

return NaN ▷ wok coordinate is outside of robot patrol zone annulus, no solution

end if

if $\|\mathbf{t}\| < l_\beta - \vec{l_\alpha}[i]$ **then**

return NaN ▷ wok coordinate is outside of robot patrol zone annulus, no solution

end if

$c_2 \leftarrow \frac{\|\mathbf{t}\|^2 - \vec{l_\alpha}[i]^2 - l_\beta^2}{2\vec{l_\alpha}[i] l_\beta}$

$\theta \leftarrow \arctan2(\mathbf{t}[1], \mathbf{t}[0])$

$\beta \leftarrow \arccos(c_2)$

$\alpha \leftarrow \theta - \arctan2(l_\beta \sin\beta, \vec{l_\alpha}[i] + l_\beta \cos\beta)$

$\beta \leftarrow \beta - \arctan2(\mathbf{b}[1], \mathbf{b}[0])$

return (α, β)

end function

function GETWOKXY($i, \alpha, \beta, \mathbf{b}$) ▷ Return x, y wok coordinates given a fiber's beta arm coordinates $\mathbf{b}$ and α, β angles for robot i

$l_\beta \leftarrow \|\mathbf{b}\|$

$\theta_\beta \leftarrow \arctan2(\mathbf{b}[1], \mathbf{b}[0])$

$\mathbf{t} \leftarrow \begin{bmatrix} \cos\alpha & \cos(\alpha+\beta+\theta_\beta) \\ \sin\alpha & \sin(\alpha+\beta+\theta_\beta) \end{bmatrix} \begin{bmatrix} \vec{l_\alpha}[i] \\ l_\beta \end{bmatrix}$

$\mathbf{w} \leftarrow \mathbf{t} + C[i]$

return $\mathbf{w}$

end function

procedure FVCLOOP ▷ Move, measure, and correct fiber placement for all robots.

$\alpha_T \leftarrow []$ ▷ Target alpha angles for each robot.

$\beta_T \leftarrow []$ ▷ Target beta angles for each robot.

$W_T^M \leftarrow []$ ▷ Target metrology fiber location for each robot in xy wok coordinates.

for $i \leftarrow 0, 499$ **do** ▷ Calculate and command initial move for every robot

$\mathbf{w}_{sci} \leftarrow W_T^S[i]$

$\mathbf{b}_{sci} \leftarrow B[i]$

$(\alpha, \beta) \leftarrow$GETALPHABETA$(i, \mathbf{w}_{sci}, \mathbf{b}_{sci})$

α_T.append(α)

β_T.append(β)

$\mathbf{b}_{met} \leftarrow \begin{bmatrix} \vec{r}^M[i] \\ 0 \end{bmatrix}$

$\mathbf{w}_{met} \leftarrow$GETWOKXY$(i, \alpha, \beta, \mathbf{b}_{met})$

W_T^M.append($\mathbf{w}_{met}$)
MOVEROBOT(i, α, β)
end for

$\epsilon_1 \leftarrow []$ ▷ Initial (blind move) metrology fiber position error for each robot.
for $i \leftarrow 0, 499$ **do** ▷ Measure each robot, apply corrective move
$\mathbf{w}_{met} \leftarrow$MEASUREROBOT($i$)
ϵ_1.append($\|\mathbf{w}_{met} - W_T^M[i]\|$)
$\mathbf{b}_{met} \leftarrow \begin{bmatrix} \vec{r}^M[i] \\ 0 \end{bmatrix}$
$(\alpha, \beta) \leftarrow$GETALPHABETA($i, \mathbf{w}_{met}, \mathbf{b}_{met}$)
$\mathrm{d}\alpha \leftarrow \alpha_T[i] - \alpha$
$\mathrm{d}\beta \leftarrow \beta_T[i] - \beta$
MOVEROBOT($i, \alpha_T[i] + \mathrm{d}\alpha, \beta_T[i] + \mathrm{d}\beta$)
end for

$\epsilon_2 \leftarrow []$ ▷ Final metrology fiber position error for each robot.
$W_F^S \leftarrow []$ ▷ Final xy wok position for science fiber.
for $i \leftarrow 0, 499$ **do** ▷ Measure and record final state of each robot.
$\mathbf{w}_{met} \leftarrow$MEASUREROBOT($i$)
ϵ_2.append($\|\mathbf{w}_{met} - W_T^M[i]\|$)
$\mathbf{b}_{met} \leftarrow \begin{bmatrix} \vec{r}^M[i] \\ 0 \end{bmatrix}$
$(\alpha, \beta) \leftarrow$GETALPHABETA($i, \mathbf{w}_{met}, \mathbf{b}_{met}$)
$\mathbf{b}_{sci} \leftarrow B[i]$
$\mathbf{w}_{sci} \leftarrow$GETWOKXY($i, \alpha, \beta, \mathbf{b}_{sci}$)
W_F^S.append($\mathbf{w}_{sci}$)
end for
end procedure

Appendix B

VITA

CONOR SAYRES

Curriculum Vitae

Contact Information

Telescope Engineering Group
University of Washington
Phys/Astr Bldg Rm. B330A
3910 15th AVE NE
Seattle, WA 98195

E-mail: csayres@uw.edu
github: csayres

Education and Honors

University of Washington
Seattle, WA

Graduate
PhD Candidate, Astronomy: Advanced Data Science Track, June 2021
M.S., Astronomy, June 2020
M.S., Applied Mathematics, June 2014
Undergraduate
B.S., Physics, June 2010
B.S., Astronomy, June 2010
Minor, Applied Mathematics, June 2010
Mary Gates Research Scholar
University Honors Program
Physics Departmental Honors
Astronomy Departmental Honors

Employment

Research Scientist — November 2011 - Present

University of Washington, Dept. of Astronomy
Operations software for the Sloan Digital Sky Survey at Apache Point Observatory and Las Campanas Observatory. SDSS-V Architect and Management Committee member.

Machinist — December 2010 - November 2011

University of Washington, Dept. of Astronomy
Designing, fabricating, and testing telescope components for the Apache Point Observatory and the Sloan Digital Sky Survey.

Data Control Technician November 2010 - April 2011

University of Washington, Dept. of Neurological Surgery
Signal analysis and organization of large datasets of neuro-electrophysiological recordings. Developing experimental paradigms for use on research subjects. PI: Dr. Jeffrey Ojemann

REU Internship January 2010 - March 2010

Cerro Tololo Inter-American Observatory La Serena, Chile
National Science Foundation funded Research Experience for Undergraduates (REU) international research internship. Identify and confirm new nearby white dwarf stars. Operating telescopes. Advisor: John P. Subasavage.

Developer June 2009 - August 2010

University of Washington, Dept. of Astronomy
NASA AISRP funded project designing web-based tools for researchers and public outreach. Interfacing with large scale astronomical databases with an online collaborative framework. PI: Prof. Andrew Connolly.

Engineering Assistant June 2009 - August 2010

University of Washington, Dept. of Astronomy
Manufacturing and testing of telescope components for the Sloan Digital Sky Survey and the ARC 3.5 meter Telescope at Apache Point Observatory.

Teaching

TA for Astro 480. Undergraduate course on astronomical data analysis.

TA for Astro 481. Undergraduate course on observational astronomy with a focus on data acquisition and analysis. Using facilities at Manastash Ridge Observatory.

TA for Astro 581. Graduate course on observational astronomy and data analysis techniques. Using the Apache Point Observatory 3.5m Telescope and instruments.

First Author Publications

C. Sayres et al. SDSS-V Robotic Focal Plane System: Overview of Coordinate Systems and Transforms. Ground-based and Airborne Instrumentation for Astronomy IX, volume 12184, page 121847K. International Society for Optics and Photonics, SPIE, Aug. 2022

C. Sayres et al. SDSS-V Algorithms: Fast, Collision-free Trajectory Planning for Heavily Overlapping Robotic Fiber Positioners. AJ, 161(2):92, Feb. 2021

C. Sayres et al. A Multi-survey Approach to White Dwarf Discovery. AJ, 143(4):103, Apr. 2012

Co-Author Publications

R. W. Pogge et al. On-sky performance of the Robotic Focal Plane Systems (FPS) for the Sloan Digital Sky Survey V. Proc. SPIE 12184, Ground-based and Airborne Instrumentation for Astronomy IX, 1218411, Aug. 2022

M. Engelman et al. SDSS-V Focal Plane System High-Precision Metrology, Proc. SPIE 12184, Ground-based and Airborne Instrumentation for Astronomy IX, 121847J, Aug. 2022

Abdurro'uf et al. The Seventeenth Data Release of the Sloan Digital Sky Surveys: Complete Release of MaNGA, MaStar, and APOGEE-2 Data. ApJS, 259(2):35, Apr. 2022

S. Alam et al. Completed SDSS-IV extended Baryon Oscillation Spectroscopic Survey: Cosmological implications from two decades of spectroscopic surveys at the Apache Point Observatory. PhRvD, 103(8):083533, Apr. 2021

R. W. Pogge et al. A Robotic Focal Plane System (FPS) for the Sloan Digital Sky Survey V. In C. J. Evans, J. J. Bryant, and K. Motohara, editors, Ground-based and Airborne Instrumentation for Astronomy VIII, volume 11447, pages 1731 – 1749. International Society for Optics and Photonics, SPIE, 2020

J. R. Sánchez-Gallego et al. Multi-object spectroscopic operations with the Sloan Digital Sky Survey V. In D. S. Adler, R. L. Seaman, and C. R. Benn, editors, Observatory Operations: Strategies, Processes, and Systems VIII, volume 11449, pages 83 – 96. International Society for Optics and Photonics, SPIE, 2020

L. Grossen et al. Test results of the SDSS-V fiber micro-positioners. In Society of Photo-Optical Instrumentation Engineers (SPIE) Conference Series, volume 11447 of Society of Photo-Optical Instrumentation Engineers (SPIE) Conference Series, page 114478P, Dec. 2020

R. Ahumada et al. The 16th Data Release of the Sloan Digital Sky Surveys: First Release from the APOGEE-2 Southern Survey and Full Release of eBOSS Spectra. ApJS, 249(1):3, July 2020

J. Kollmeier et al. SDSS-V Pioneering Panoptic Spectroscopy. In Bulletin of the American Astronomical Society, volume 51, page 274, Sept. 2019

J. C. Wilson et al. The Apache Point Observatory Galactic Evolution Experiment (APOGEE) Spectrographs. PASP, 131(999):055001, May 2019

D. S. Aguado et al. The Fifteenth Data Release of the Sloan Digital Sky Surveys: First Release of MaNGA-derived Quantities, Data Visualization Tools, and Stellar Library. ApJS, 240(2):23, Feb. 2019

M. R. Blanton et al. Sloan Digital Sky Survey IV: Mapping the Milky Way, Nearby Galaxies, and the Distant Universe. AJ, 154(1):28, July 2017

K. S. Dawson et al. The SDSS-IV Extended Baryon Oscillation Spectroscopic Survey: Overview and Early Data. AJ, 151(2):44, Feb. 2016

S. Kellis et al. Multi-scale analysis of neural activity in humans: Implications for micro-scale electrocorticography. Clinical Neurophysiology, 127(1):591–601, Jan. 2016

J. Huehnerhoff et al. Astrophysical Research Consortium Telescope Imaging Cam- era (ARCTIC) facility optical imager for the Apache Point Observatory 3.5m telescope. In C. J. Evans, L. Simard, and H. Takami, editors, Ground-based and Airborne Instrumentation for Astronomy VI, volume 9908 of Society of Photo- Optical Instrumentation Engineers (SPIE) Conference Series, page 99085H, Aug. 2016

S. Alam et al. The Eleventh and Twelfth Data Releases of the Sloan Digital Sky Survey: Final Data from SDSS-III. ApJS, 219(1):12, July 2015

N. Drory et al. The MaNGA Integral Field Unit Fiber Feed System for the Sloan 2.5 m Telescope. AJ, 149(2):77, Feb. 2015

C. P. Ahn et al. The Tenth Data Release of the Sloan Digital Sky Survey: First Spectroscopic Data from the SDSS-III Apache Point Observatory Galactic Evolu- tion Experiment. ApJS, 211(2):17, Apr. 2014

K. S. Dawson et al. The Baryon Oscillation Spectroscopic Survey of SDSS-III. AJ, 145(1):10, Jan. 2013

C. P. Ahn et al. The Ninth Data Release of the Sloan Digital Sky Survey: First Spectroscopic Data from the SDSS-III Baryon Oscillation Spectroscopic Survey. ApJS, 203(2):21, Dec. 2012

D. J. Eisenstein et al. SDSS-III: Massive Spectroscopic Surveys of the Distant Universe, the Milky Way, and Extra-Solar Planetary Systems. AJ, 142(3):72, Sept. 2011

H. Aihara et al. The Eighth Data Release of the Sloan Digital Sky Survey: First Data from SDSS-III. ApJS, 193(2):29, Apr. 2011